Investigations on Laser Direct Writing and Laser Micro-3D Printing of metals and ceramics towards MEMS Structures Printing for Functional Applications

Ph.D. THESIS

By

Arpit Kumar Singh

Department of Mechanical Engineering

Indian Institute of Technology Indore

June 2025

Investigations on Laser Direct Writing and Laser Micro-3D Printing of metals and ceramics towards MEMS Structures Printing for Functional Applications

A THESIS

Submitted in partial fulfillment of the requirements for the award of the degree

of

DOCTOR OF PHILOSOPHY

By

Arpit Kumar Singh

Department of Mechanical Engineering

Indian Institute of Technology, Indore

June 2025

Indian Institute of Technology

Indore

CANDIDATE'S DECLARATION

I hereby certify that the work being presented in the thesis titled **Investigations on Laser Direct Writing and Laser Micro-3D Printing of metals and ceramics towards MEMS Structures Printing for Functional Applications** in the partial fulfilments of the requirements for the award of the degree of **DOCTOR OF PHILOSOPHY** and submitted in the **Department of Mechanical Engineering, Indian Institute of Technology, Indore** is an authentic record of my own work performed during the time period of July, 2022 to June, 2025 under the supervision of Prof. I. A. Palani, Department of Mechanical Engineering, Indian Institute of Technology, Indore.

The matter presented in the thesis has not been submitted by me for the award of any other degree of this or any other institute.

Signature of the student with date
(Arpit Kumar Singh)

This is to certify that the above statement made by the candidate is correct to the best of my/our knowledge.

Signature of Thesis Supervisor with date.

(Prof. I. A. Palani)

Arpit Kumar Singh has successfully given his Ph.D. Oral Examination held on **15/04/2025** and Ph.D. Viva voce on **07/04/2026**

Signature of Thesis Supervisor with date.

(Prof. I.A. Palani)

-

ACKNOWLEDGEMENTS

First, I would like to express my deepest gratitude and acknowledge My research guide **Prof. I. A. Palani**, Mechatronics, and Instrumentation Lab, for his continuous guidance, patience, motivation, and enthusiasm. His valuable advice, constructive criticism, extensive discussions, and immense knowledge helped me to build a basic understanding of the subject and accomplish my thesis. His research method of developing practical application has been inspiring. During my time of association with him, I learnt a lot of things, both in life and career. He has tremendous multi-tasking and man management skills, which is something I would like to learn and carry with me in life. He has been a mentor who is always true to his position.

I would like to thank **Prof. Suhas Joshi**, Director, IIT Indore, **Dr. S. Dinakaran,** Head of Department, Mechanical Engineering, for supporting me with the sophisticated facilities to conduct my research. I would also like to thank PSPC members **Dr. Indrasen Singh** and **Dr. Jayaprakash Murugesan** for giving their precious time for my assessment and for their valuable comments and suggestions towards enhancing my research work. My sincere thanks **Dr. S. Janakiraman**, DPGC convener for his sincere support.

I would like to thank **Department of Mechanical Engineering**, **IIT Indore** as well as **Department of MEMS, IIT Indore** for allowing access to the facility of various characterization techniques and providing apleasant atmosphere for research.

My appreciation also extends to **my seniors Dr. Jayachandran S., Dr. Nandini Patra, Dr. Sooraj Shiby, Dr. Anshu Sahu, Dr. Kaushal Gangwar, Ms. Diksha Jaurker, Mr. Krishnpal Singh Tomar, Mr. Himanshu Sharma, Mr. Himanshu Sen, Mr. Vivekanand, Mr. Koustubh, Mr. Vishnu** for their dedicated support and stimulating discussions. My special gratitude goes to research collaborators and

guides **Dr. Manish Kumar Srivastava, Ms. Divya Chauhan, Dr. Shailesh M. Kohle and Dr. Santhanam S.** My special regards go to **Dr. Nilesh J. Vasa** sir, IIT Madras who has voluntarily and continuously guided us through his discussions. I would specially like to mention the constant support of office staff **Mr. Ashwin Wagh and Mr. Hemant Raghuvanshi.** Also,I would like to admire my colleagues for their constant care and endorsement through this period. My sincere appreciation extends to my B. Tech inmates Srijan, Piyush, Vijay, Kailash, Soham, Tejal, Sunita, Tannu, Gaurav, Sathwik and others for their help and support during my work. I would also like to acknowledge my school and college friends for being my constant support during my highs and lows. Finally, I would like to express my deepest gratitude and respect to my parents for introducing me to this world and for being an ever-supportive rock in my life with their unflinching support.

I also acknowledge Prime minister research fellowship and IIT Indore for their financial assistance to the research work carried out.

Dedicated to my Peace, Parents & ever supportive Research Supervisor

ABSTRACT

The growing demand for high-performance Microelectromechanical Systems (MEMS) in fields such as biomedical devices, energy harvesting, and flexible electronics necessitates advanced micromanufacturing techniques capable of processing multifunctional materials with sub-micron precision. This thesis investigates two laser-based fabrication methodologies-Laser Direct Writing (LDW) and Laser Micro-3D Printing-to develop metallic and ceramic microstructures tailored for MEMS applications. LDW, employing a 10.6 µm CO_2 laser, is utilized for direct synthesis of porous laser-induced graphene (LIG) on polyimide substrates. Optimized parameters (4.5 W laser power, 15 mm/s scan speed) produced uniform graphene structures exhibiting high conductivity and porous morphology, confirmed by Raman spectroscopy with characteristic D (~1350 cm^{-1}), G (~1580 cm^{-1}), and 2D (~2700 cm^{-1}) peaks. The fabricated LIG-based strain sensors demonstrated excellent mechanical resilience, surviving over 1250 bending cycles without degradation.

The laser Micro-3D Printing was realized via laser decal transfer (LDT) for materials like Aluminum, SiC, and ZnO, enabling layer-by-layer printing of high-aspect-ratio structures. Process optimization showed that SiC ejection was optimal at a 10.5 cm focal distance, with uniform deposition achieved using 4-4.3 W laser power and 60-70% pulse overlap. Profilometry confirmed that 7-layer SiC structures reached a thickness of ~27 µm, while the transformation efficiency for ZnO was measured at 80% under a fluence of 75 J/cm^2, owing to the Gaussian beam profile of the laser.

These two laser-assisted techniques were further integrated to fabricate piezo-triboelectric hybrid nanogenerators (PTENGs) by embedding ZnO within the LIG matrix. Devices based on LIG-ZnO-FEP (fluorinated ethylene propylene) layers exhibited significantly enhanced energy harvesting performance: the hybrid device generated 75 V open-circuit voltage and 1.06 µA short-circuit current, outperforming

individual piezoelectric (9 V, 270 nA) and triboelectric (36 V, 410 nA) configurations. This performance boost, up to 60% increase in current and 40% increase in voltage, was attributed to synergistic effects between ZnO nanostructures and electrostatic charges in the LIG matrix. The findings demonstrate that LDW and laser micro-3D printing not only offer flexible, maskless, and multi-material processing capabilities, but also enable scalable and application-specific MEMS fabrication platforms.

List of Publications

Thesis Publications

S.No.	Journal Publication	Impact Factor
1	Singh, Arpit Kumar, Sooraj Shiby, Anshu Sahu, Piyush Pachori, Manushree Tanwar, Rajesh Kumar, and I. A. Palani. "Parametric investigation on laser interaction with polyimide for graphene synthesis towards flexible devices." Journal of Physics D: Applied Physics 56, no. 1 (2022): 015305.	**3.5**
2	Singh, Arpit Kumar, Anshu Sahu, and Palani Iyamperumal Anand. "Unraveling spatial variations of graphenization of Kapton polyimide via CO2 laser interaction: a comprehensive theoretical simulation and Raman spectroscopy mapping study." Applied Physics A 129, no. 11 (2023): 799.	**2.9**
3	Singh, Arpit Kumar, Vipul Singh, and Palani Iyamperumal Anand. "An Innovative Laser Decal transfer of ZnO Ceramic in LIG for advanced Hybrid Nanogenerator applications." Ceramics International 51, no. 4 (2025): 4957-4970.	**5.1**
4	Singh, Arpit Kumar, Anshu Sahu, and Palani Iyamperumal Anand. "Unraveling the Laser decal transfer-based printing of ZnO ceramic towards FEP-ZnO-based Piezo-Tribo hybrid nanogenerators." Nano Trends (2025): 100079.	**NA**
5	Singh, Arpit Kumar, Anshu Sahu, K. A. Vyvaswath, Kailaash Pandiyan, and Palani Iyamperumal Anand. "Unraveling the Processing Parameters for Selective Positioning of Multi-materials Using Laser Decal Transfer." Journal of Materials Engineering and Performance (2025): 1-9.	**2.2**

6	Singh, A.K., Tomar, K.S. and Anand, P.I., 2025, September. Exploring the Impact of Process Parameters on Laser μ-3D Printing of Silicon Carbide for High-Precision Applications. In International Mechanical Engineering Congress and Exposition-India (Vol. 89145, p. V002T02A045). American Society of Mechanical Engineers.	**NA**

Other than Thesis Publications

S.No.	Journal Publication	Impact Factor
1	Chauhan, Divya, **Arpit Kumar Singh,** Sabatini Tyagi, Palani Iyamperumal Anand, Seeram Ramakrishna, and Manish Kumar Srivastava " Engineering of electrospun lead-free PVDF/Carbon Nanofiber-ZnO nanocomposites for enhanced piezoelectric energy harvesting and wearable sensing applications." Composites Part B: Engineering p.113039	**14.2**
2	Chauhan, Divya, **Arpit Kumar Singh**, Sabatini Tyagi, Palani Iyamperumal Anand, Seeram Ramakrishna, and Manish Kumar Srivastava. "Laser-Induced Graphene-Embedded Electrospun PVDF-ZnO: A Synergistic Piezo-Tribo Nanogenerator for Efficient Energy Harvesting." Carbon (2025): 120521.	**11.6**
3	Sahu, Anshu, **Arpit Singh**, Ayush Singh, Vipul Singh, and Iyamperumal Anand Palani. "Investigation of material ejection in laser decal transfer-based μ-3D printing of ZnO ceramics with microsecond pulsed CO2 laser." The International Journal of Advanced Manufacturing Technology (2024): 1-12.	**2.9**
4	Gangwar, K., Jayachandran, S., Sahu, A., Singh, A. and Palani, I.A., 2022. Influence of pre-strain on	**4.9**

	attributes of Ni-rich NiTi/Kapton polyimide bimorph for flexible mirrors. Sensors and Actuators A: Physical, 341, p.113607.	

Patent Details:

Granted (Thesis Patents)

1. A Method of printing pixelated silicon carbide segments: **Arpit Kumar Singh,** Krishnpal Singh Tomar, Gaurav, I A Palani, Suhas Joshi- Indian Patent No.- 573394, Grant date- 06/11/2025

Granted (Other than Thesis Patents)

2. A gesture-controlled SMA-actuated robotic gripper system and method thereof: I.A. Palani, K.A. Vyvaswath, **Arpit Kumar Singh**, Anshu Sahu, Kaushal Gangwar, Soham Mondal, Tejal uplenchwar- Indian Patent No.-568766, Grant date- 17/07/2025
3. A MULTI-MODAL UNMANNED VEHICLE: Soham Mondal, Tejal Ravindra, **Arpit Kumar Singh**, I.A. Palani- Indian Patent No.-576873, Grant date- 30/12/2025.

Submitted

1. AN INTEGRATED INSOLE FOR HARVESTING ENERGY: I.A. Palani, Anshu Sahu, **Arpit Kumar Singh**, Diksha Jaurker, Suhas S. Joshi, Shailesh M. Kolhe, A. Raju. - Indian Patent No. 202511020242 **(Filed)**

2. An omnidirectional robotic device: Hrishikesh Jawale, Hrishikesh Hiremath, Harsh Sinha, Kaushiki Nanda Duarah, Prathamesh Kawtikwar, Sahil Umale, **Arpit Kumar Singh**, I.A. Palani-Indian Patent No. 202521091366 **(filed)**

3. SYSTEM AND METHOD FOR NAVIGATING MOBILE FURNITURE UNITS: Soham Pandit, Shivam Sharma, Yash Yewale, Poojashree Mishra, Shreya Itlod, **Arpit Kumar Singh**,

I.A. Palani-Indian Patent No. 202521095180 **(Filed)**

4. A RETROFITTABLE METAL PRINTING SYSTEM FOR A LASER MARKING MACHINE: Rajatkumar Vishvakarma, **Arpit Kumar Singh**, Krishnpal Singh Tomar, Anshu Sahu, I.A. Palani-Indian Patent No. 202621041302 **(Filed)**

5. SYSTEM AND METHOD FOR REAL-TIME MONITORING AND PROCESS-STATE CLASSIFICATION IN LASER MICRO THREE-DIMENSIONAL PRINTING APPARATUS: Mukul Raj Ghunawat, **Arpit Kumar Singh**, Suhas S Joshi, I.A. Palani- Indian Patent No. 202621038202 (Filed)

Conferences:

INTERNATIONAL

- Oral presentation on "Unravelling the fabrication of ZnO Ceramics via Laser Micro-3D Printing for Hybrid Piezo-Tribo Energy Harvesting"."- **Arpit Kumar Singh**, Palani Anand Iyamperumal in the **Tribo-Energy & Sensing (TE&S) 2026 Conference,** at **Royal Swedish Academy of Engineering Sciences (IVA) Conference Centre, Grev Turegatan 16, Stockholm, Sweden.** 20th -21st January 2026.
- Oral presentation on "**Investigations on influence of micro and nano pulse laser source for µ-3D printing of ceramics over flexible substrates for functional applications**"- **Arpit Kumar Singh**, Anshu Sahu and Palani Anand Iyamperumal in the **7th Conference on Microactuators, Microsensors and Micro mechanisms 2024** at **Industrial University of Ho chi Minh, Vietnam** 8th -10th November 2024.
- Oral presentation on **"Unraveling the influence of processing parameters towards Aluminum printing using novel µ-3D Printing Technique for functional applications,"- Arpit Kumar Singh,** Anshu Sahu and Palani Anand Iyamperumal in **7th World Congress on Micro and Nano Manufacturing - WCMNM 2024** at **Pattaya, Thailand** 16th -19th September 2024.
- **Oral presentation on "Exploring the Impact of Process Parameters on Laser µ-3d Printing of Silicon Carbide for High-Precision Applications"- Arpit Kumar Singh,** Krishnpal Singh Tomar, Palani Anand Iyamperumal in **ASME**

International Mechanical Engineering Congress & Exposition® India (IMECE- INDIA 2025) 10th- 13th September 2025

NATIONAL

- Oral presentation on "Investigation on Graphene fabrication through laser processing"- Vishnu Varma kamanuri, **Arpit Kumar Singh,** Palani Anand Iyamperumal in **10th International and 31st All India Manufacturing Technology, Design & Research (AIMTDR 2025) Conference- 11-13 December 2025**.
- Oral presentation on "Investigation on laser direct writing for realizing fluorinated laser induced graphene for superhydrophobic applications"- Abhishek Ayushya, **Arpit Kumar Singh,** Palani Anand Iyamperumal, Vipul Singh in **10th International and 31st All India Manufacturing Technology, Design & Research (AIMTDR 2025) Conference- 11-13 December 2025.**
- Oral presentation on "Digital Shadow Development for real-time monitoring of Laser Micro 3D printing"- Mukul Raj Ghunawat, **Arpit Kumar Singh,** Suhas S Joshi**,** Palani Anand Iyamperumal in **10th International and 31st All India Manufacturing Technology, Design & Research (AIMTDR 2025) Conference- 11-13 December 2025**.
- Oral presentation on "Investigation on novel laser decal transfer-based printing of ceramics over conventional non-decal printing for functional applications"- **Arpit Kumar Singh,** Palani Anand Iyamperumal in **33rd DAE-BRNS National Laser Symposium-** 6th -9th March 2025.
- Oral presentation on "**Investigating the laser micro-3D printing of Silicon carbide for functional applications**"- **Arpit Kumar Singh**, Gaurav, Palani Iyamperumal Anand in **International Conference on Additive Manufacturing and Characterization (ICAMC)**at **IIT Bombay** 10th -11th January 2025.
- Oral presentation on "**Investigating the Influence of processing parameters towards laser µ-3D printing of Silicon carbide for critical applications**"- **Arpit Kumar Singh**, Gaurav, Anshu Sahu, Hemant Raghuvanshi, Palani Iyamperumal Anand in **13th International conference on Precision, Meso, Micro and Nano engineering** at **NIT Calicut, Kerala** 13th -15th December 2024.
- Oral presentation on "**Parametric Investigations on Laser**

Cleaning of Biofouling from Ship hulls"- Nandini Patra, Krishnapal Singh Tomar, **Arpit Kumar Singh,** Dinesh Parid, Mr. Rohit Pandya, Mr. Amit Nabira, Dr. Kiran Bala, Dr. I. A. Palani in **13th International conference on Precision, Meso, Micro and Nano engineering** at **NIT Calicut, Kerala** 13th - 15th December 2024.

- Oral presentation on " Development of ZnO Ceramic based Piezo-Tribo Hybrid Nanogenerator using Laser μ-3D printing for sustainable Energy harvesting from Flag Fluttering,"- Arpit Kumar Singh, in 39th MP Young Scientist Congress – MITS Gwalior, M.P. 21st -23rd February 2024.
- Poster presentation on "Unravelling the utilization of laser micro-3D printing towards micron level ceramic printing using novel laser decal transfer technique"- **Arpit Kumar Singh,** Palani Anand Iyamperumal in **32nd DAE-BRNS National Laser Symposium-** Jan 29th -01st Feb 2024.
- Oral presentation on **"Unravelling the processing parameters for selective positioning of multi- materials using Laser decal Transfer based μ- 3D printing,"- Arpit Kumar Singh,** Anshu Sahu, K.A. Vyvaswath, Kailaash Pandiyan, Palani Iyamperumal Anand in **9th International and 30th national All India Manufacturing technology and design, AIMTDR 2023** conference at **IIT (BHU) Varanasi** 8th - 10th December 2023.
- Poster presentation on "Investigation **on the influence of compositional effect of CuAlMn coated on optical fiber for temperature sensor applications**"- **Arpit Kumar Singh**, Nandini Patra, Srivathsan Vasudevan, Palani Anand Iyamperumal in **12th International conference on Precision, Meso, Micro and Nano engineering** at **IIT Kanpur,** 8th -10th December 2022.
- Sathiesh Kumar V, Thangaraja. M, Anshu Sahu, **Arpit Kumar**, I.A. Palani. "Spectroscopy Based Instrumentation Setup to Monitor the Thin Film Deposition Process," **ISBN: 978-93-91930-04-2**, **6th National Conference on Recent Trends in Instrumentation and Control (RTIC 2022).**

TABLE OF CONTENTS

LIST OF FIGURES

LIST OF TABLES

ACRONYMS

S. No.	Acronym	Expansion
1	MEMS	Microelectromechanical systems
2	VLS	Vapor liquid solid
3	HMTA	Hexamethylenetetramine
4	SEM	Scanning electron microscope
5	EDS	Energy dispersive X-ray spectroscopy
6	XRD	X-ray diffraction
7	FEP	Fluorinated ethylene propylene
8	ZnO	Zinc oxide
9	SAED	Selective area diffraction
10	PTENG	Piezo tribo hybrid nanogenerator
11	DLW	Direct laser writing
12	HAZ	Heat affected zone
13	LIG	Laser Induced graphene

Chapter 1

This chapter explains the background and focusses of research work. It elaborates about the thesis outline.

Introduction

1.1 Background and Motivation of MEMS devices

Microelectromechanical Systems (MEMS) have emerged as a transformative technology in the last few decades, impacting a wide range of sectors including automotive, aerospace, healthcare, consumer electronics, and industrial automation. MEMS devices combine mechanical elements, sensors, actuators, and electronics on a common silicon substrate through microfabrication technology [1-6]. This integration allows for highly compact, low-power, and cost-effective systems that are capable of sensing, processing, and actuating at the microscale. The exponential growth of the Internet of Things (IoT), Industry 4.0, and personalized healthcare have amplified the need for advanced MEMS. MEMS evolution has reached the maturity phase for several applications such as accelerometers, gyroscopes, pressure sensors, and microphones, with new opportunities emerging in energy harvesting, biosensing, and autonomous systems. Fig. 1 illustrates the expanding scope of MEMS sensor applications over the decades, reflecting advancements in material science, microfabrication techniques, and system integration. According to projections, the number of MEMS-based connected devices is expected to reach 40 billion by 2025, with approximately 9.27 devices per person.

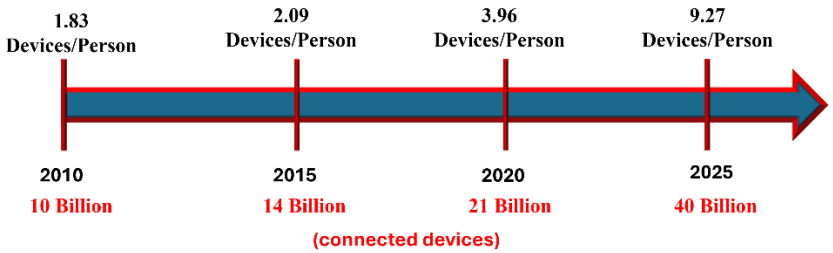

Fig.1.1: Increasing demand for MEMS devices

However, despite these advancements, traditional silicon-based fabrication methods face critical challenges. These include high

costs due to complex photolithographic steps, limited compatibility with non-silicon materials like ceramics and polymers, and the difficulty of constructing non-planar or 3D microstructures. These limitations are particularly restrictive when developing flexible electronics, biomedical implants, or multifunctional systems that require heterogeneous integration. Therefore, there is a strong demand for innovative fabrication strategies that can accommodate diverse materials, offer geometric flexibility, and support rapid prototyping.

1.2 MEMS Fabrication Strategies: Bottom-Up vs. Top-Down

The fabrication of MEMS devices involves highly precise and scalable microfabrication strategies. These methods are typically divided into two major categories: top-down and bottom-up fabrication. Top-down fabrication begins with a bulk material and removes or patterns it to form the desired microstructure. Common top-down techniques include photolithography, wet and dry etching, surface and bulk micromachining, and various forms of milling. These processes provide excellent dimensional control and are well-established in cleanroom environments; however, they often rely on silicon substrates, require multiple processing steps, and are not inherently suited to flexible or non-planar surfaces. On the other hand, bottom-up fabrication builds structures from the molecular or atomic level using methods such as sol-gel processing, chemical vapor deposition (CVD), atomic layer deposition (ALD), and electrochemical deposition. These approaches offer precise control over composition and nanoscale features and are ideal for producing functional thin films and coatings. Nonetheless, bottom-up techniques often suffer from limited spatial precision, difficulties in integration with other materials, and challenges in scaling for practical device fabrication.

While both fabrication strategies have propelled MEMS development over the past three decades, they present significant limitations when applied to the current generation of applications that demand 3D architectures, hybrid material integration, and

flexible substrates. Traditional microfabrication techniques also tend to be costly, time-consuming, and constrained by the need for cleanroom facilities and photomasks. This has driven a growing interest in alternative, adaptive manufacturing technologies that can overcome the material and structural limitations of conventional approaches [7-14].

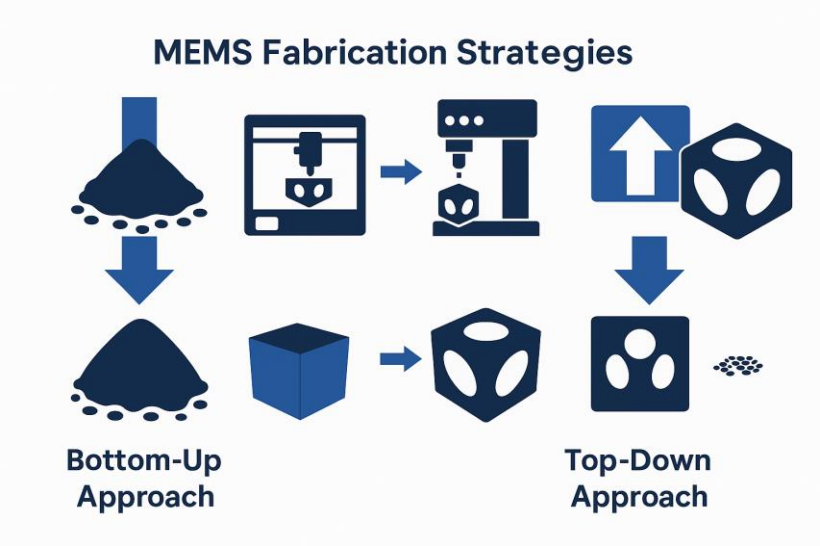

Figure 1.2: Top down and bottom up micro-fabrication technique

1.3 Role of Lasers in MEMS Processing

Laser-based microfabrication has recently emerged as a highly promising direction in MEMS technology. Unlike traditional methods, laser techniques offer maskless, direct-write capabilities that enable rapid and spatially controlled material processing without the need for cleanroom infrastructure [15-16].

Laser Direct Writing (LDW) and Laser Micro-3D Printing allow for non-contact, high-resolution structuring and additive deposition of a wide range of materials, including polymers, ceramics, metals, and nanocomposites. These techniques also support complex 3D geometries and multi-material integration, which are critical for next-generation MEMS applications such as energy harvesters, implantable sensors, and soft robotics.

Laser microfabrication is versatile in that it can serve both subtractive and additive roles. In subtractive applications, lasers are used for precise ablation, drilling, and etching to define features such as microchannels, diaphragms, or resonators. In additive roles, lasers enable the selective transfer or sintering of materials to create microelectrodes, interconnects, and functional coatings. The resolution of these processes can be tuned to the micron or even sub-micron level depending on the laser wavelength, pulse duration, and focusing optics. Moreover, laser systems are compatible with a broad spectrum of substrates, from rigid silicon wafers to flexible polyimide films and biocompatible materials, offering new possibilities in wearable and bio-integrated MEMS design.

1.3.1 Laser direct writing : Laser Direct Writing (LDW) is a versatile and powerful microfabrication technique that enables the precise patterning and functionalization of surfaces through the controlled interaction of laser beams with matter. Unlike conventional photolithographic processes, LDW operates in a maskless, direct-write mode**,** which offers significant advantages in terms of design flexibility, rapid prototyping, and material compatibility. By focusing a laser beam onto a substrate, material transformations such as ablation, photoreduction, or phase conversion can be induced with high spatial resolution. This technique is particularly useful for structuring polymers, ceramics, and carbon-based materials, making it highly relevant for applications in flexible electronics, sensors, and microsystems [17-21].

A prominent application of LDW is in the fabrication of laser-induced graphene (LIG)**.** LIG is produced by irradiating a carbon-rich precursor typically polyimide (PI) film with a CO_2 or near-infrared laser. The laser energy locally decomposes the polymer matrix, initiating a photothermal conversion process that reorganizes the carbon atoms into a porous, three-dimensional graphene-like structure. This transformation occurs under ambient conditions and does not require chemical reagents or post-treatment steps, making it a simple, scalable, and environmentally friendly technique. The resulting LIG exhibits high

electrical conductivity, tunable porosity, and excellent mechanical flexibility, which are essential properties for developing next-generation sensors, energy storage devices, and wearable electronics[22-27].

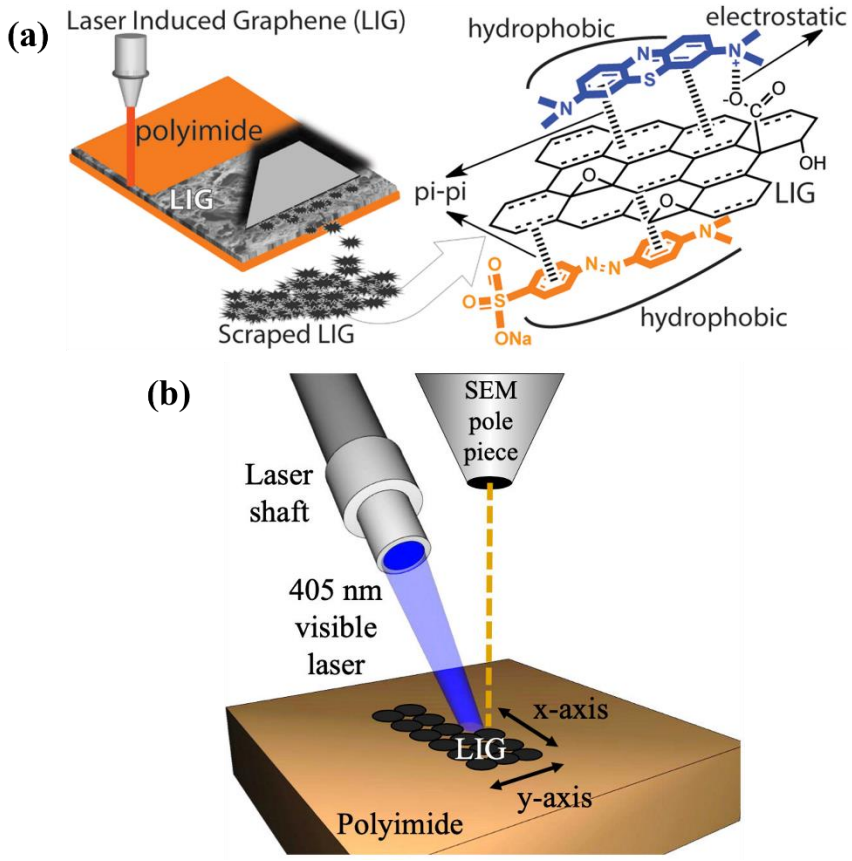

Fig.1.3: (a) direct laser writing over Kapton polyimide using 10.6 µm CO_2 laser, (b) feasibility of direct laser writing using 405 nm laser for LIG fabrication.

The appeal of LIG lies not only in its low-cost, chemical-free synthesis but also in its patternability and integration potential. The laser's trajectory can be digitally controlled to define intricate electrode geometries, interconnects, and microelectrodes directly onto flexible or stretchable substrates. Moreover, the properties of LIG such as sheet resistance, pore structure, and surface roughness can be tuned by adjusting laser parameters like power, scan speed, and pulse duration. This level of control makes LDW a highly adaptable platform for the on-demand fabrication of functional graphene microstructures,

accelerating the development of MEMS devices, strain sensors, electrochemical electrodes, and hybrid energy harvesters.

1.3.2 Laser µ-3D printing: In Laser µ-3D printing, the material to be printed is coated as a thin film on the transparent substrate, and the pulsed laser beam is focused on it, which locally induces high pressure at the interface and ejects the material in the form of droplets or pellets. The ejected material will print on another substrate placed closed to each other. It is a non-contact technique that allows a wide range of metals, compounds, and biomolecules. It does not require the usage of cleanroom equipment or the presence of vacuum making it consider device fabrication with a wide range of substrates and materials for processing. However, the if we compare it with the well -establish ink jet printing, the laser-based process has design freedom for printing high-resolution 2D printing of various functional high viscous ink that can avoid the nozzle clogging problem.

As the result of direct laser interaction with material, the mechanism involves heating, melting, and vaporization of material in a short period which can change in phase and composition and induces a change in the mechanical and thermal behaviour of printed structures. To be fully compatible with the largest possible spectrum of materials, the transfer phase must occur with minimum or no alteration or modification of the donor material when it releases from the donor substrate. This is crucial because many materials, particularly complex multicomponent and multiphase systems, can experience irreversible changes during melting or vaporisation, degrading the functional properties of printed structures. To retain the functionality of the material a sacrificial layer or dynamic release layer can be introduced between the substrate and donor film. The dynamic release layer absorbs the laser energy and forms the high-pressure vapour pocket. These vapours exert pressure force on the donor material to initiate the ejection mechanisms. The process was renamed as DRL-LIFT or Laser decal transfer process for µ-3D printing as shown in Fig. 1.4. The laser energy absorbs the entire energy in the sacrificial

layer and induces the necessary thrust force for the transfer mechanism. Since the laser energy is not interacting with donor film and printing is performed by mechanism thrust which helps to retain the functionalities of printed structure like donor film. Generally, laser decal transfer can be more suitable for different biological molecules and observed the survival and proliferative ability of the deposited proteins, cells and DNAs remain constant after the deposition. A similar phenomenon is observed in the deposition of organic and inorganic polymers where the laser irradiation may damage the structure of the polymers hence the DRL is applied for the deposition of polymers based functional devices for the electronics components. Moreover, the LFT can deposit ceramic materials using the DRL-LIFT phenomenon, but the resolution of ceramics is not as good as in the case of metals and polymers [28-30].

For the microfabrication of sensors and devices, laser μ-3D printing is performed by pixel-by-pixel transfer in a layer-by-layer fashion for a three-dimension microscale structure.

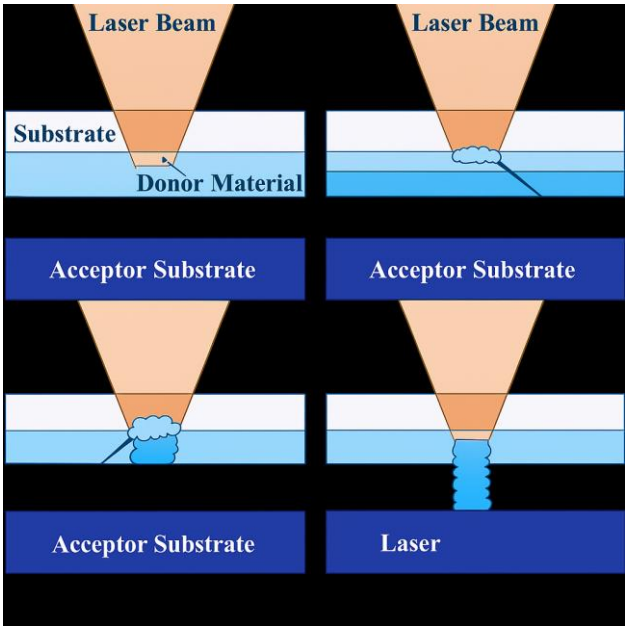

Fig. 1.4: Laser decal transfer based μ- 3D printing mechanism.

The future of MEMS microfabrication lies in merging the precision of traditional top-down processes with the adaptability and material diversity of laser-based and bottom-up techniques. Laser processing not only enables rapid prototyping and low-cost manufacturing but also

provides pathways for digital, scalable, and on-demand fabrication. It opens the door for MEMS devices that are not just small and efficient but also multifunctional, flexible, and customizable for specific applications. As MEMS continue to evolve toward more complex and heterogeneous architectures, the role of laser microfabrication will become increasingly central to their development and commercialization.

1.4 Motivation of Thesis

The motivation for this research arises from the need to address five major bottlenecks in current MEMS fabrication i.e.,

(a) Material Limitation: Conventional MEMS processes are optimized for silicon-based materials, limiting their adaptability to new functional materials like SiC, ZnO, and conductive polymers.

(b) Design Complexity: Photolithographic methods are inherently two-dimensional and require multiple masking and etching steps to realize complex 3D structures.

(c) Process Inflexibility: Cleanroom-dependent techniques are not conducive to rapid prototyping or low-volume customization, which are increasingly important in biomedical and IoT applications.

(d) selective material transfer: Exploring the capabilities of the laser-based system for selectively printing materials that remains a challenge for other processes.

(e) Multi-layered multi-material printing: The present conventional techniques lag in multi-layered multi-material printing that is a requirement for next generation sensors.

While there are multiple processes that follows for micro-fabrication, two major laser processing techniques have been explored in the research work. Laser direct writing that causes direct laser interaction with polyimide and enables direct conversion of carbon-rich polymers into graphene without

chemical treatments, providing spatial control and material independence. It is highly effective for flexible electronics and wearable sensors. Laser micro-3D printing, on the other hand, supports maskless fabrication of complex geometries using a wide variety of materials, including ceramics and metals. It allows selective material transfer and multi-material deposition, opening possibilities for co-fabricating sensors, interconnects, and actuators in a single process.

These laser-enabled methods are aligned with emerging application needs, offering fast, accurate, and versatile microfabrication platforms. The ability to work with non-planar and temperature-sensitive substrates further enhances their appeal for biomedical implants, conformal sensors, and soft robotics. The combination of LDW and laser micro-3D printing thus provides a powerful toolkit for next-generation MEMS development.

1.5 Objectives of Thesis

The core objective of this research is to develop and optimize laser-based microfabrication techniques for the creation of functional metal and ceramic microstructures suitable for MEMS applications. The specific goals include:

- To establish Laser Direct Writing (LDW) as a viable route for patterning conductive and porous laser-induced graphene (LIG) on polyimide substrates, and to analyze its morphological and electrical characteristics.
- To implement Laser Micro-3D Printing using a laser decal transfer (LDT) mechanism for structured deposition of materials such as silicon carbide (SiC), zinc oxide (ZnO), and aluminum, and to optimize printing parameters like laser fluence, overlap, and stand-off distance.
- To investigate material transfer efficiency and structural uniformity of the printed layers, and to correlate these outcomes with laser energy density and pulse control.

- To fabricate hybrid MEMS devices, specifically piezo-triboelectric nanogenerators (PTENGs), integrating both LDW-fabricated LIG and 3D-printed ZnO/SiC layers to evaluate their electromechanical performance.
- To conduct detailed characterization of mechanical robustness, piezoelectric/triboelectric response, and long-term operational stability of the fabricated devices for functional applications.

1.6 Significant contribution

The explored research work has presented significant contributions in the explored field of both direct laser writing as well as laser micro-3D printing. While the physics behind laser material interaction through experiments and simulation is explored, the research outcomes open window for studying depths of direct laser writing through laser material interaction. Further, a detailed investigative exploration towards multiple materials through laser micro-3D printing is explored where metals including aluminum and ceramics including SiC and ZnO is explored for its optimized parameters for lasers-based printing. Finally, the technologies are integrated together towards fabrication of flexible devices for hybrid Nanogeneration and functional applications.

1.7 Organization of Thesis

The thesis is structured to progressively build upon the theoretical background, experimental framework, and practical implementation of laser-based MEMS fabrication techniques:

Chapter 1: Introduction about the MEMS fabrication and its approaches and utilization of lasers for functional applications.

Chapter 2: Literature Review Provides a comprehensive analysis of MEMS technology evolution, conventional microfabrication strategies, and recent advancements in laser-based processing, including comparative assessments of bottom-up and top-down methods.

Chapter 3: Theoretical Framework Discusses the fundamentals of laser-matter interaction, energy absorption mechanisms, and beam shaping techniques relevant to LDW and laser micro-3D printing.

Chapter 4: Laser Direct Writing of Graphene presents the fabrication and characterization of LIG patterns on polyimide films using CO_2 laser, including Raman spectroscopy, SEM imaging, and electromechanical testing of flexible sensors.

Chapter 5: Laser Micro-3D Printing of Functional Materials explores the use of LDT for additive deposition of SiC, ZnO, and aluminum onto target substrates, highlighting process parameters, structural fidelity, and material transformation efficiency.

Chapter 6: Device Fabrication and Hybrid Integration demonstrates the design, fabrication, and testing of PTENGs combining LIG and ZnO layers, with performance metrics.

Chapter 7: Summary and Future Outlook Summarizes the key contributions of the research and outlines future directions for improving laser processing fidelity, integration with flexible substrates, and scaling to industrial platforms.

1.8 flowchart of Thesis

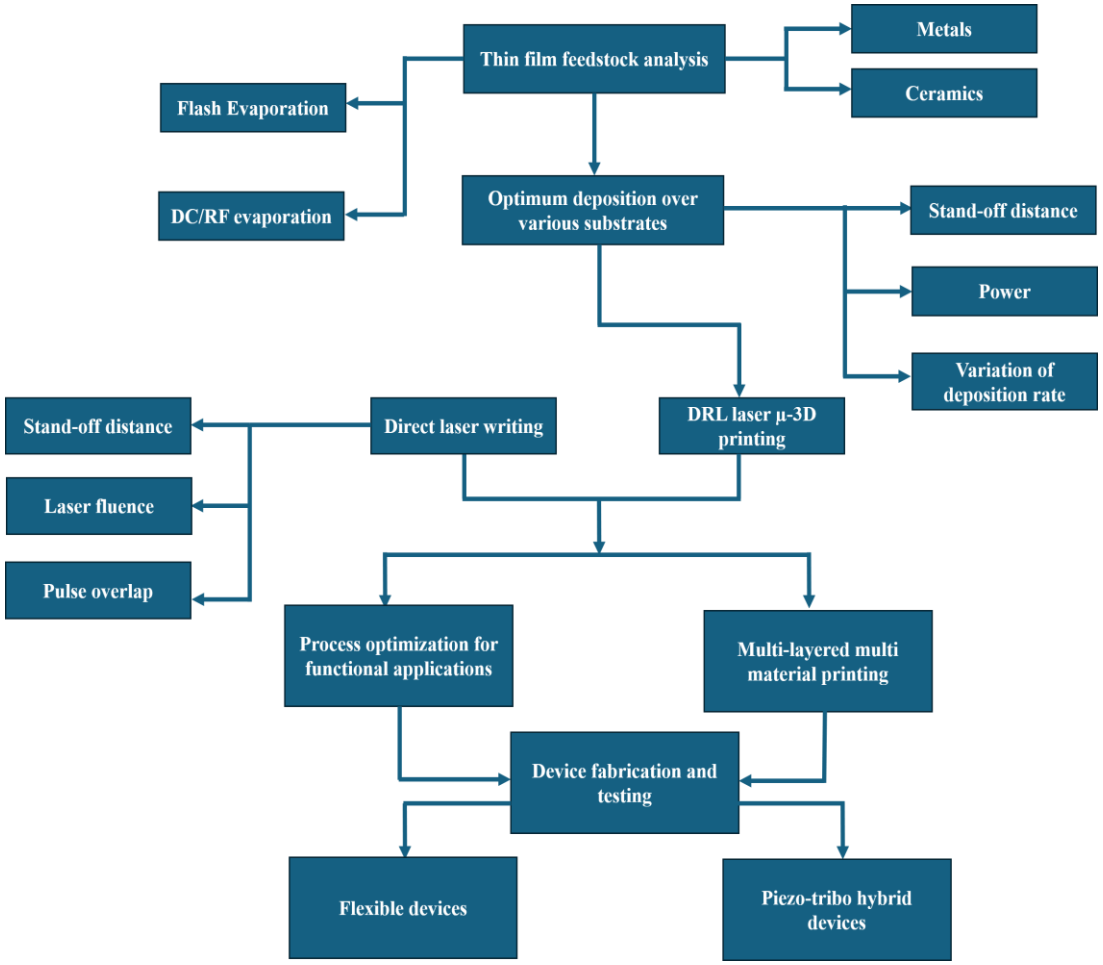

Chapter 2

This chapter consists of comprehensive literature survey of lasers-based microfabrication, microfabrication techniques including top-down and bottom-up approach and laser-based microfabrication techniques.

Review of Literature

2.1 Introduction to laser-based microfabrication

Laser precision engineering has evolved into a highly transformative platform for microscale and nanoscale material processing. As highlighted by Chong et al. (2010), the development of laser-based fabrication methods has enabled the realization of intricate microstructures with feature resolutions ranging from several microns down to tens of nanometres. The transition from traditional laser drilling and cutting to precision micromachining and nano structuring has been largely enabled by advancements in laser sources (especially in the nanosecond, picosecond, and femtosecond domains), beam shaping optics, and precision motion stages. These tools have allowed lasers to become a staple in high-resolution manufacturing for applications in microelectronics, photonics, biomedical engineering, and surface science. For getting better success, there is a need for understanding the laser-matter interaction mechanisms, which vary based on the pulse duration, wavelength, and fluence. For nanosecond pulses, laser energy absorption results in photothermal effects such as melting and vaporization, with thermal diffusion lengths typically around 1 μm for metals.

These laser-induced processes are leveraged across various fabrication scales. At the microscale (1-100 μm), nanosecond or picosecond lasers are often used for patterning metal films or structuring ceramics and polymers. Techniques like laser drilling can produce holes with diameters as small as 10 μm and aspect ratios up to 20:1, while laser micromachining can yield features with edge roughness below 1 μm.

Sub-micron processing (100-1000 nm) is achieved using short pulses and high numerical aperture (NA) optics, enabling direct-write fabrication of trenches, lines, and dots. The diversity of materials processed by laser systems is another key strength. Metals like copper and aluminum, when irradiated with femtosecond pulses (~1 J/cm^2 fluence), exhibit clean ablation with reduced recast layers. Dielectrics such as fused silica require higher peak intensities (10^{13}-10^{14} W/cm^2) to initiate multiphoton breakdown, while polymers can undergo localized decomposition at fluences as low as 0.1-0.5 J/cm^2.

Researchers in the past have provided a foundational understanding of how laser technology has matured into a precise, versatile, and scalable tool for micro- and nano-engineering. The ability to manipulate materials across a wide range of classes and dimensions, coupled with sub-micron spatial resolution and minimal thermal damage, makes laser precision engineering a highly attractive technique for micro-3D printing. The insights gained from this work support the ongoing development of laser-based additive manufacturing platforms for applications in flexible electronics, microsensors, and energy harvesting devices, where material control and geometric fidelity are paramount [31-37].

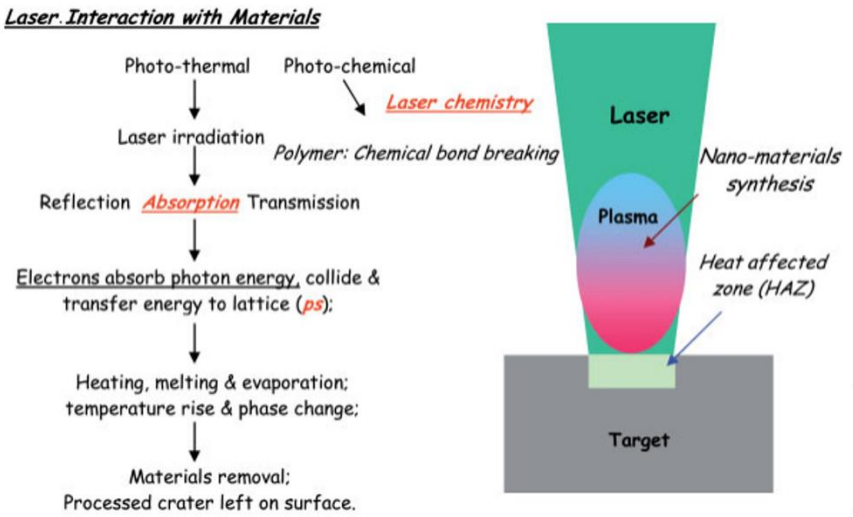

Fig. 2.1: Dynamics of laser material interaction

The laser-based microfabrication process that is taking up shape in recent research has shown its details in various processes as mentioned in the table below.

(a) Stereolithography: Huang et al. (2017) [38] explored the potential of stereolithographic additive manufacturing (SLA) for fabricating high-resolution ceramic components, emphasizing the integration of silicon carbide (SiC) and other ceramic particles into UV-curable photopolymer resins. Their work demonstrated that SLA can successfully print intricate microstructures with resolutions as fine as ~45 μm by carefully controlling resin viscosity and ceramic particle dispersion. They optimized the formulation using ~50 vol% ceramic loading, enabling stable curing and layer-by-layer construction without significant distortion. However, the study also highlighted the importance of post-processing steps such as debinding and high temperature sintering to achieve densification, minimize internal stresses, and preserve dimensional stability. This makes SLA a promising method for producing small-scale, complex ceramic parts suitable for applications in microelectromechanical systems (MEMS) and microfluidic devices. In a broader review, Zocca et al. (2015) analyzed various ceramic additive manufacturing (AM) techniques, with stereolithography being a focal point. Their work provided a critical comparison of SLA with other AM routes in terms of resolution, material compatibility, and process limitations. They emphasized the challenge of light scattering caused by ceramic fillers, which limits the curing depth and resolution, as well as the need to balance high solid loadings with manageable resin viscosity for stable printing. The review reported successful SLA fabrication of complex geometries using materials like SiC and alumina and highlighted the potential for SLA in applications such as biomedical scaffolds, photonic devices, and structural ceramics. They concluded that despite the need for significant post-processing, SLA remains one of the most precise and adaptable AM techniques for ceramic-based microfabrication [39-40].

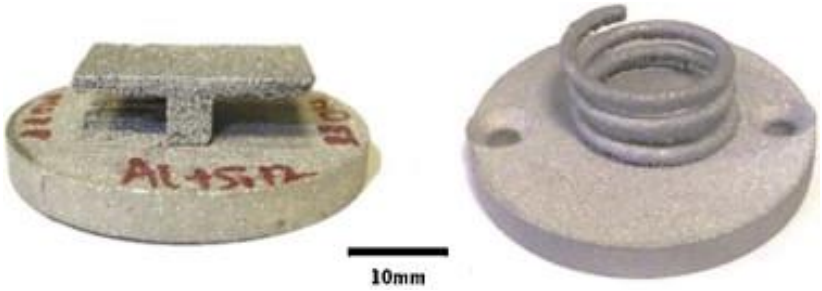

Fig. 2.2: Unsupported overhang components produced using the ASLM process from elemental Al + Si12 powder.

(b) Direct Ink Writing: Saadi et al. introduce a novel approach to DIW by incorporating near-infrared (NIR) assisted photopolymerization. This technique enables the printing of unsupported, multi-scale, and large-span ceramic structures by in-situ curing of the extruded ink. The study demonstrates the fabrication of complex geometries like torsion springs and cantilever beams without the need for additional support structures, marking a significant advancement in DIW capabilities. Wang et a provide a comprehensive review of DIW for ceramic-based porous structures. They discuss the formulation of pseudoplastic inks, solidification strategies, and post-processing techniques. The paper emphasizes the integration of DIW with traditional manufacturing methods to construct hierarchical pore structures, enhancing the functional properties of the ceramics for applications in filtration, catalysis, and biomedical implants [41-42].

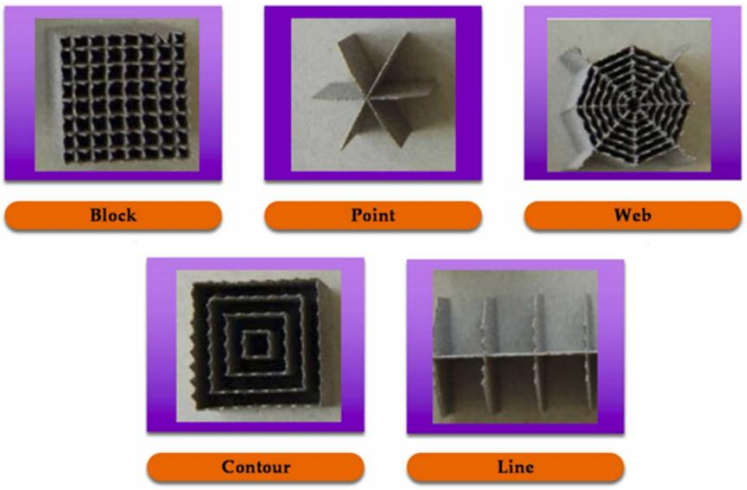

Fig. 2.3: Different support geometries for metallic parts

(c) Laser-Induced Forward Transfer (LIFT): Florian and Serra (2023) discuss the versatility of LIFT as a high-resolution additive manufacturing technique [43]. They highlight its capability to deposit a wide range of materials, including metals, polymers, and biological substances, with precise spatial control. The paper explores the potential of LIFT in digital manufacturing, emphasizing its role in fabricating complex microstructures for electronics and biomedical applications. Zergioti et al. (2012) investigate the application of LIFT for transferring conducting polymers. Their study demonstrates the successful deposition of materials like P3HT:PCBM and polyaniline, which are relevant for organic electronics and biosensors. The research underscores the importance of optimizing laser parameters to achieve high-quality transfers without damaging the functional properties of the materials [44].

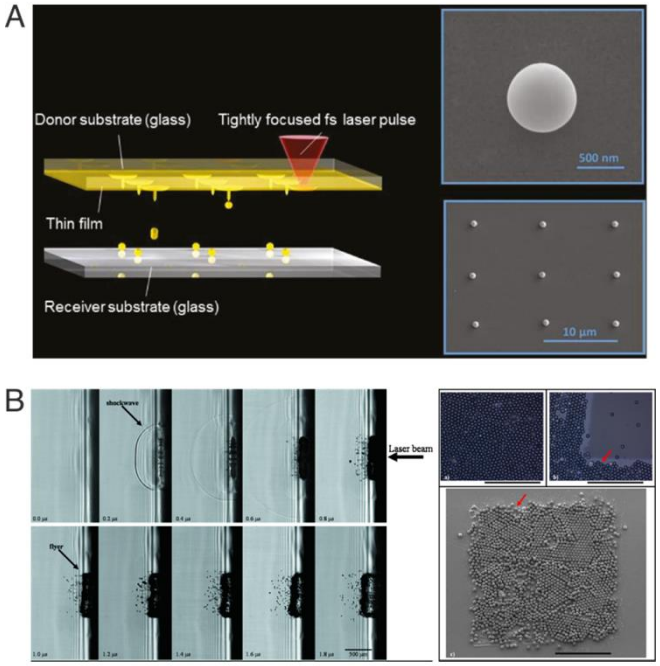

Fig.2.4: Printing of materials starting from a solid donor film following two different scenarios. (A) Melted material, where the final output corresponds to individual spherical particles. (B) In this transfer, the use of a sacrificial layer allowed the printing of an array of microspheres that followed the square shape distribution of the incident laser beam.

(d) Spark Plasma Sintering (SPS): Munir et al. (2011) provide a thorough review of the SPS process, detailing the mechanisms by which pulsed electric currents and uniaxial pressure facilitate rapid

densification of ceramic powders. They discuss the advantages of SPS over conventional sintering methods, including lower sintering temperatures, shorter processing times, and the ability to retain fine microstructures, which are crucial for enhancing the mechanical properties of ceramics [45]. Guillon et al. (2014) delve into the field-assisted sintering technology (FAST), encompassing SPS. Their work examines the influence of various parameters, such as heating rates, pressure, and electric current, on the densification behaviour and microstructural evolution of ceramics. The study also addresses the challenges in scaling up the SPS process for industrial applications, highlighting the need for uniform temperature distribution and control over grain growth [46].

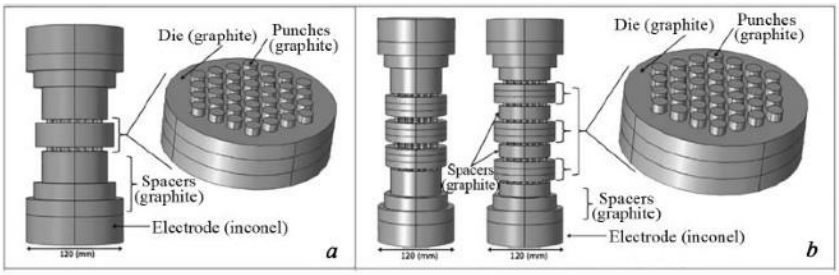

Fig.2.5: Samples in (a) parallel configuration and (b) serial-parallel multiple part configuration with or without intermediate spacer for ceramics printing

2.2 Various micro-fabrication techniques

The processes that follow for micro-fabrication is majorly distributed into two major approaches i.e. Top-down approach and bottom-up approach. The bottom-up approach is a well-established technique and is explored well as well in the past.

2.2.1 Bottom-up approach

1. **Sol-Gel Method:** The sol-gel process offers a versatile and low-temperature route for fabricating micro- and nanostructured materials, particularly useful in oxide film deposition for microfabrication. Hench and West (1990) provided a foundational

overview of sol-gel chemistry, emphasizing its utility in producing homogeneous glass and ceramic coatings with controlled porosity and composition. They highlighted its applicability in micro-scale thin film structures and sensor coatings due to its precise stoichiometric control and processing ease [47]. Complementarily, Brinker and Scherer (1989) elaborated on the physics governing gel formation, aging, and drying, underscoring how these factors affect feature resolution and surface uniformity in sol-gel-derived microstructures [48]. Together, these studies establish sol-gel as an essential bottom-up approach for microfabrication due to its adaptability, chemical tunability, and suitability for flexible substrates.

2. **Chemical Vapor Deposition (CVD):** Chemical vapor deposition (CVD) plays a pivotal role in microfabrication by enabling conformal and high-purity film growth, often used in semiconductors and MEMS. Choy (2003) provided a comprehensive review of CVD techniques thermal, plasma-enhanced, and metal-organic highlighting their capability to deposit complex multi-element films with uniform thickness even on 3D geometries [49]. This is crucial for coating high-aspect-ratio features found in microdevices. Pierson (1999) detailed the practical implementation of CVD in industrial and laboratory environments, emphasizing control over nucleation and film growth mechanisms essential for microstructure resolution [50]. Both works underscore how CVD's scalability and material diversity make it integral for microfabrication, especially in topography-rich device architectures.

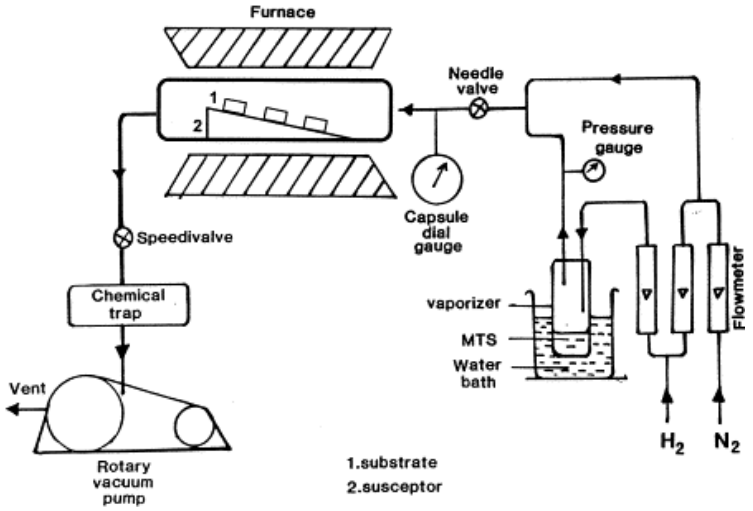

Fig.2.6: A schematic diagram of a typical laboratory CVD equipment for the deposition of SiC coatings.

3. **Electrochemical Deposition:** Electrochemical deposition is widely used in bottom-up microfabrication due to its cost-effectiveness and ability to create 3D metallic microstructures. Modestov and Comninellis (2003) explored the electrochemical principles behind the deposition of nanostructured metals, emphasizing its control over nucleation sites and layer thickness, which is critical for producing high-resolution MEMS structures [51]. In a practical demonstration, Aravamudhan et al. (2005) integrated electrochemical deposition in the fabrication of microcantilever sensors, showcasing the technique's compatibility with surface micromachining and selective material deposition [52]. These studies confirm that electrochemical deposition is not only scalable and low-cost but also enables precise layer-by-layer fabrication, making it suitable for micro-sensor and actuator development.

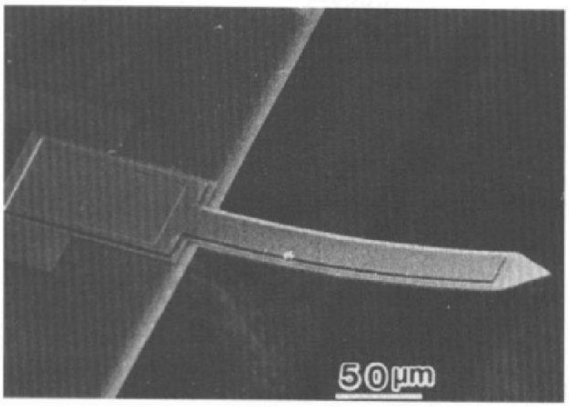

Fig.2.7: A SEM micrograph of a ZnO/SiO 2 piezoelectric microcantilever

4. **Atomic Layer Deposition (ALD):** Atomic Layer Deposition (ALD) is an advanced technique tailored for ultrathin, conformal coating at atomic-level control, essential in microelectronics and nanoscale devices. George (2010) offered an extensive review of ALD's self-limiting surface reactions, which allow for atomic-scale control over film growth, enabling high uniformity in complex microfeatures [53]. Leskelä and Ritala (2012) further emphasized the technique's flexibility across diverse materials (oxides, nitrides, sulfides), supporting its integration into high-density microelectronic structures and nano-MEMS platforms [54]. The precise thickness control and high conformality make ALD a cornerstone technique in bottom-up microfabrication, especially where aspect ratio and dielectric performance are critical.

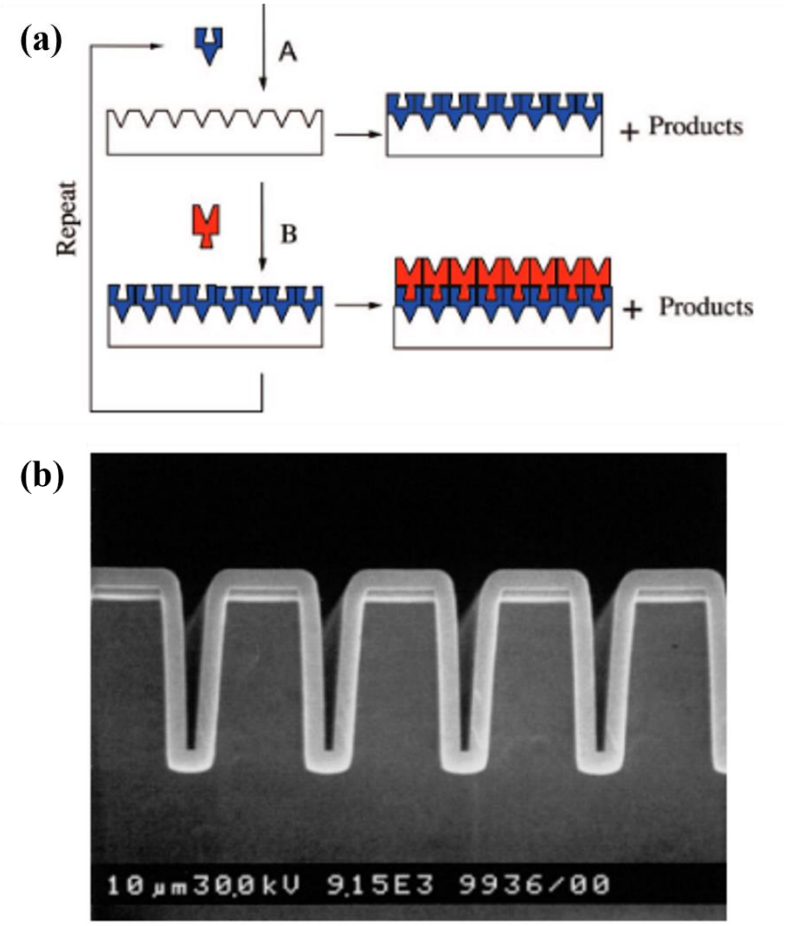

Fig.2.8: (a) Schematic representation of ALD using self-limiting surface chemistry and an AB binary reaction sequence, (b) Cross-sectional SEM image of an Al 2O3 ALD film with a thickness of 300 nm on a Si wafer with a trench structure

2.2.2 Top-down approach

Further is we see through the top-down approaches, there have been recent research reported that includes

(A)Photolithography: Photolithography is the cornerstone of modern top-down microfabrication, enabling precise pattern transfer onto substrates using light-sensitive resists and photomasks. In his comprehensive book, Alam (2015) detailed the step-by-step photolithographic workflow from resist coating and exposure to development and etching highlighting its pivotal role in defining features down to the submicron scale in integrated circuits and MEMS

devices [55]. The text also discussed the challenges of resolution limits and alignment accuracy, particularly when scaling multilayered microstructures. Complementing this, Wynand explored the physics and chemistry of photolithographic processes, including optical diffraction limits, resist chemistry, and resolution enhancement techniques (RET) [56]. These works collectively establish photolithography as a highly mature yet evolving technology essential for manufacturing microscale components with complex geometries and high throughput.

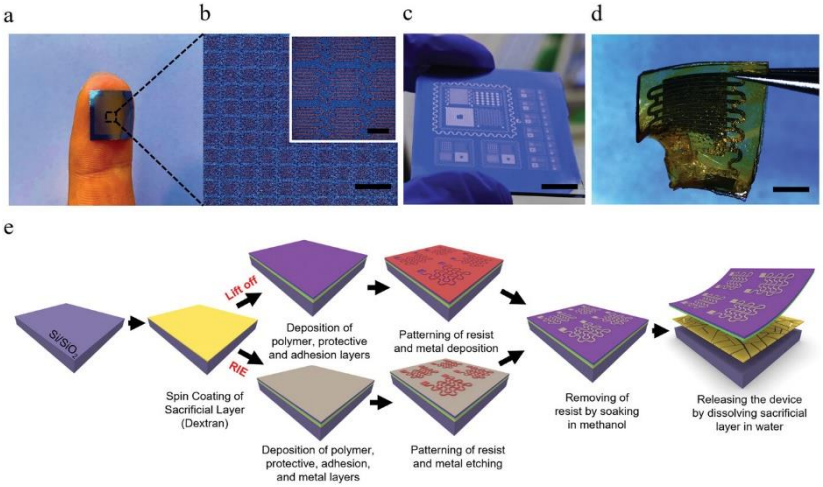

Fig 2.9: Photolithography-based process for fabrication of scalable and highly miniaturized patterns on biodegradable substrates. a) A flexible patch including the 1600 devices in 1 cm^2 placed onto the fingertip. b) Confocal microscope images of IDE capacitor arrays. Inset: Zoomed-in microscopic image of IDE capacitors. c) Photograph of various devices fabricated on PLA on a silicon substrate. d) Partially degraded IDE pattern embedded in PGS stretchable substrate after putting in PBS. e) Schematic illustration of the photolithography-based procedure through lift-off and reactive ion etching (RIE) methods.

(B)Etching (Wet and Dry): Etching processes in top-down microfabrication are critical for defining three-dimensional microstructures, particularly in silicon-based systems. Williams and Xu et al. presented a landmark review on anisotropic wet etching of silicon using potassium hydroxide (KOH) and tetramethylammonium hydroxide (TMAH), showcasing how crystal orientation and doping levels influence etch rates and resulting geometries—critical in MEMS

fabrication [57]. For dry etching, gorowithz et al. pioneered understanding of reactive ion etching (RIE), elucidating plasma-surface interactions that offer superior anisotropy and selectivity compared to wet techniques [58]. These studies demonstrate how wet etching offers simplicity and cost-effectiveness for bulk micromachining, while dry etching supports high-resolution and complex pattern transfer in semiconductor and microsensor fabrication.

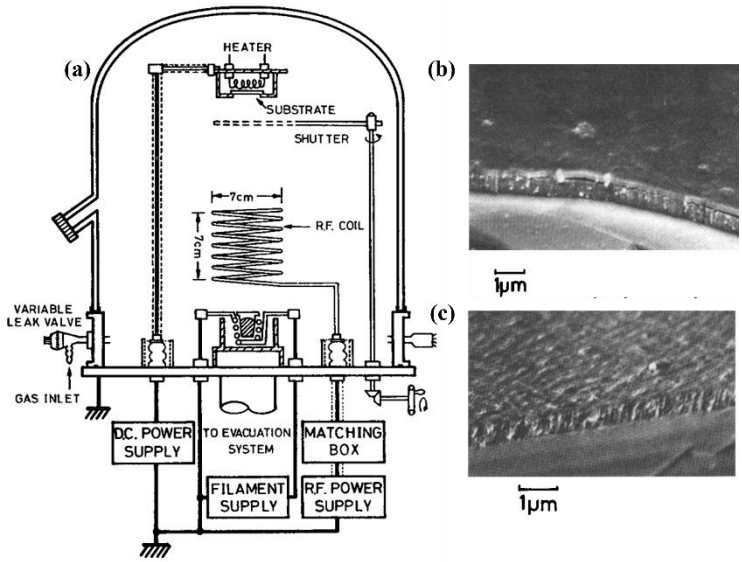

Fig.2.10: (a) Experimental setup of reactive ion etching, (b) and (c) represent SEM micrograph of AlN film coated using RIE.

(C)Erosion and Milling: Mechanical erosion or milling is a physical top-down microfabrication technique commonly used in prototyping or where chemical methods are less effective. Schmid et al. (2000) reviewed ion beam milling and focused ion beam (FIB) techniques for nanoscale patterning and surface engineering, noting their suitability for applications requiring sub-100 nm resolution and direct-write modification of structures [59]. They also highlighted challenges such as material redeposition and substrate damage. Meanwhile, Hata and Neuville (2019) discussed the role of physical abrasion and erosion in microstructured surface formation, especially in creating superhydrophobic or functionalized surfaces using abrasive jets or mechanical rubbing techniques [60]. While generally slower and more

tool-intensive than etching or lithography, erosion methods allow unique control over structure depth and surface texture.

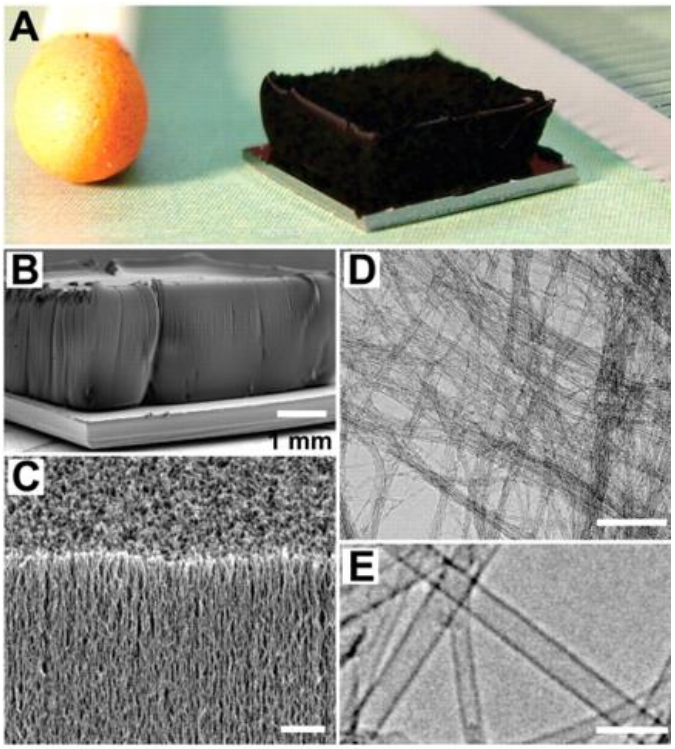

Fig.2.11: SWNT forest grown with water-assisted CVD. (A) Picture of a 2.5-mm-tall SWNT forest on a 7-mm by 7-mm silicon wafer. A matchstick on the left and ruler with millimeter markings on the right is for size reference. (B) Scanning electron microscopy (SEM) image of the same SWNT forest. Scale bar, 1 mm. (C) SEM image of the SWNT forest ledge. Scale bar, 1 µm. (D) Low-resolution TEM image of the nanotubes. Scale bar, 100 nm. (E) High-resolution TEM image of the SWNTs. Scale bar, 5 nm.

One key area that is still under novel research is utilization of lasers for microfabrication process. While there have not been many prominent and established laser-based processes for microfabrication, the major laser-based processes included direct laser writing and laser micro-3D printing. There have been a few reports of certain specific materials explored using the above-mentioned processes i.e., Direct Laser Writing (DLW) is a highly adaptable top-down microfabrication technique that enables maskless, three-dimensional patterning of materials with sub-micron resolution. It uses tightly focused laser pulses to induce nonlinear optical absorption in a photosensitive

material, leading to localized polymerization or ablation. Sun and Kawata (2004) provided a comprehensive account of the DLW process, emphasizing its ability to fabricate complex 3D photonic crystals and micro-architectures inside photoresists using two-photon polymerization. Their work highlighted how focal volume control enables the creation of high-aspect-ratio structures with features as small as 100 nm, suitable for photonics, microfluidics, and MEMS [61]. In a broader application context, Malinauskas et al. (2016) reviewed material compatibility, resolution limits, and emerging applications of DLW in fields such as biomedical scaffolds, metamaterials, and on-chip optical components. They underscored DLW's advantages, such as arbitrary 3D design, multi-material printing, and in situ fabrication, while also discussing challenges like slow writing speeds and voxel elongation [62]. Collectively, these studies position DLW as a pivotal method for high-precision microfabrication, especially where customized, high-resolution geometries and true 3D structuring are required beyond conventional lithography.

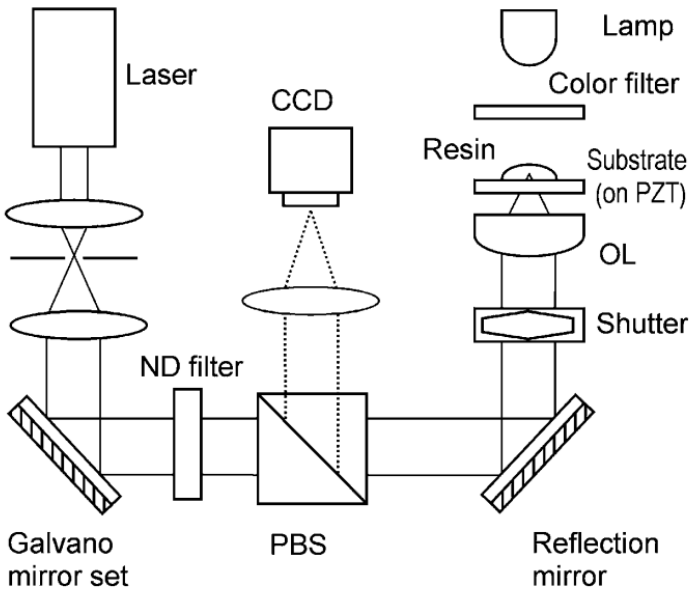

Fig.2.12: Two-photon direct writing laser microfabrication system. The Galvano mirror set is used for scanning the laser beam in the two horizontal dimensions, and along the longitudinal direction a PZT stage is used. The laser power was continuously adjusted by a neutral density (ND) filter. The polarization beam splitter (PBS) lets the laser

beam pass but reflects the illumination light to the CCD monitor for in-situ monitoring of the fabrication process. OL: objective lens

2.2.3 Laser based processing:

Further laser induced forward transfer is also explored in research based on various types of donors used and their laser interactions. This may include

(a)Solid Donor: When the temperature at the interface is not sufficient to melt the solid donor, the transfer happens in the solid phase. The size of the transferred pellets is close to the laser beam diameter. In this condition, two different mechanisms are responsible for the film torn from the donor layers in the solid form (a) Blasting mechanism and (b) Thermomechanical film tearing-off [63]. In the blasting mechanism, the heating of the interface results from desorption by the donor substrate surface defect that creates vapor pockets which exert high pressure on the solid film. When this pressure exceeds the fracture limit of the donor thin film, pellets will be released from the donor substrate and propelled to the receiver substrate.

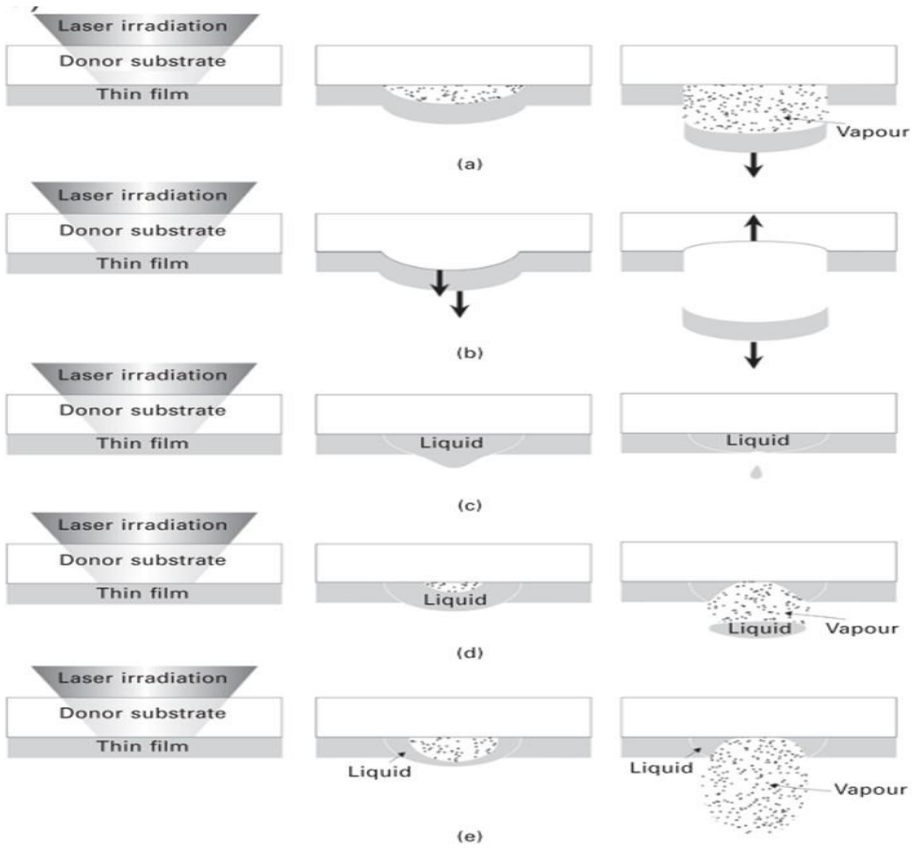

Fig. 2.13: Different mode of transfer mechanisms of LIFT without sacrificial layer at different laser fluences. (a) film fracture & partial vaporization at fluence; (b) thermal expansion and film peel- off at low fluence; (c) phase change melting at threshold fluence; (d) small volume ablation & melting at high fluence, and (e) vaporization at very high fluence

(b) Liquid Donor: One of the advantages of LIFT is that it does not require a nozzle which avoids the clogging problem in inkjet printing, and there is no restriction on the rheological properties and viscosity of the ink or nano pastes. Various biological solutions including mouse fibroblast or storm cell, DNA, protein, inorganic ink or paste and organic polymers. were printed for different functional applications like micro-batteries, solar cells, organic light-emitting diode and biosensors. More literature is available for the parametric investigation of process parameters (laser pulse width. laser fluence, DRL layer thickness, donor film thickness and donor-receiver spacing) on the morphology (deposited shape, volume, and roughness) of the deposited

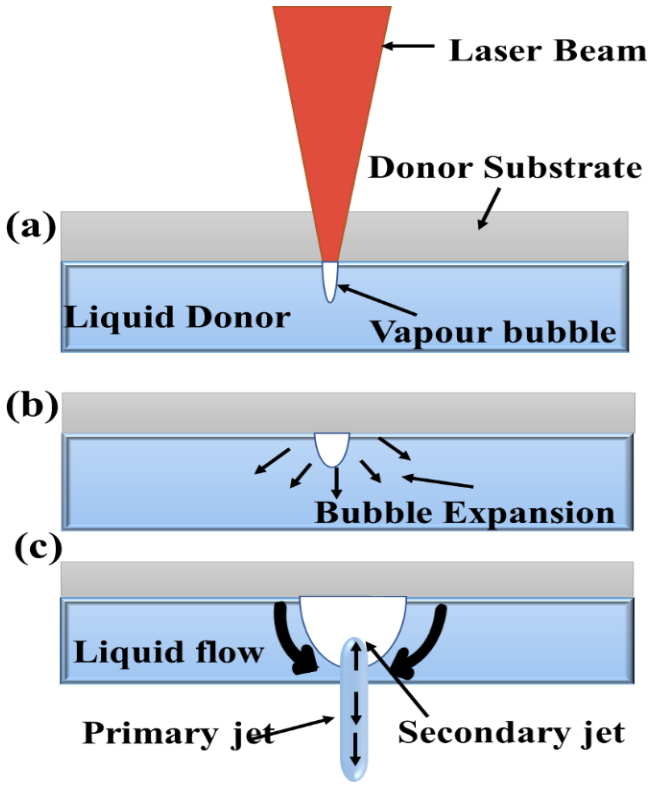

Fig. 2.14: Principle of operation of liquid transfer a) vapor bubble formation due to laser absorption (b) initial expansion of the vapor bubble (c) jet formation.

(c) Dynamic Release Layer (DRL-LIFT): While transferring from the donor to the receiver substrate the donor material undergoes different thermal processes like heating melting and vaporization. This would affect the material characteristics of the transferred deposits with donor thin film. To avoid any thermal effect, the thin sacrificial layer is introduced in between the donor substrate and thin film (known as Dynamic Release Layer) to protect the donor material from the laser pulse heating during the transfer mechanism. The DRL is deposited on the transparent donor substrate with physical vapor deposition (sputtering, and thermal flash evaporation), doctor blade and spin coating. When the laser pulse fluence greater than the threshold fluence interacted with DRL, melting and vaporization takes place. During the expansion of the vaporized layer, it pushes the donor thin film toward the acceptor substrates shown in fig 2.15. Since there is no interaction of laser pulse with donor thin film, hence it deposited without any physical change in the transferred material.

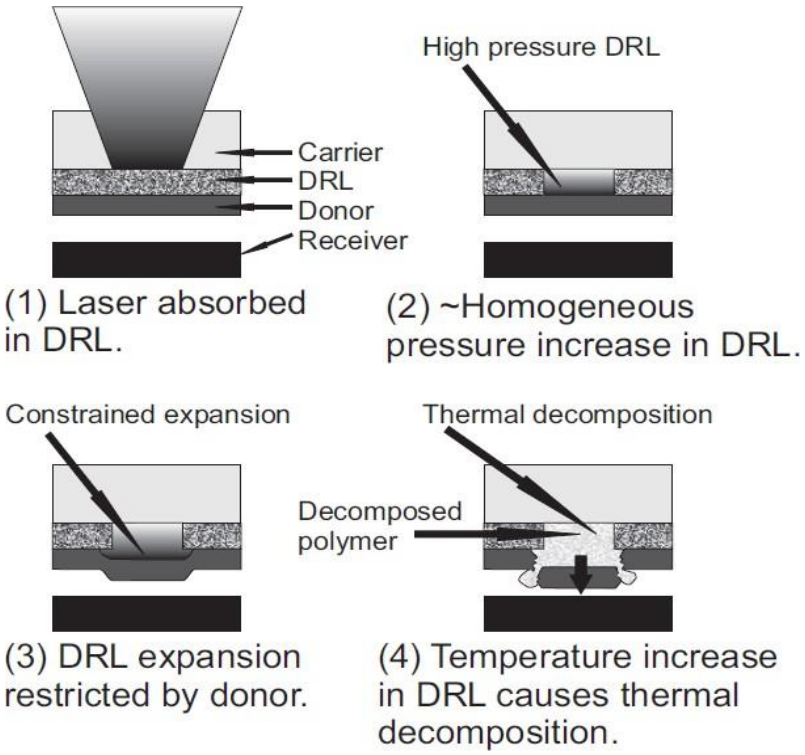

Fig. 2.15: Schematic of Dynamic Release Layer-LIFT (DRL-LIFT).

The metallic DRL is the most used in LIFT for thermal sensitive materials toward laser radiation. These metallic thin films Ti, Au, Pt, Cr are biocompatible and easy to coat using a physical vapor deposition technique or sputtering on the transparent substrate i.e., Quartz substrate. These metals absorb most of the laser radiation within the 100nm thickness for laser wavelengths 532nm and 1064 nm and ensure that the laser radiation is not reaching toward the donor thin films. The first work reported with 60 nm thin Titanium DRL for the transfer of salmon sperm DNA on the poly-L-lysine coated substrate. It revealed that the Titanium does not hinder the adhesion and transfer of DNA to the poly-L-lysine coated substrate. Even though the printing of biomolecules is successful, metallic DRLs have the disadvantage of contamination of transferred material during the melting and vaporization process which affects the fabrication and performance of organic microdevices. Generally, the thickness of metallic DRL and the polymer DRL are in the range of 20-100 nm and 1-5 μm respectively. The thick Polymeric DRLs overcome the limitation of metallic DRLs. In the case of polymeric DRLs, the photothermal and photochemical decomposition of organic molecules gives vapor as a by-product. Photo-decomposing polymer absorbs the laser radiation and decomposes in the gaseous fragments generating high-pressure bubbles for the transfer. Therefore, transferred material is deposited without any physical or phase change with the donor film. Triazene polymer (TP) is a widely used photo-decomposable DRL as a sacrificial layer for thermally sensitive materials (i.e., organic nano pastes, inorganic polymers, and biomolecules) to avoid contamination in transferred material. Due to having a wide range of absorption spectrum, numerous studies focused on different laser wavelengths. A solid disc of GdGaO of 10 μm diameter was deposited using aryltriazene as a DRLs layer with Ti: Sapphire laser (λ = 800 nm and $\tau \approx$ 130 fs) without any shattering at optimal donor-receiver spacing. Aluminium, Gelatine, and Methylcellulose were transferred from the donor substrate using triazene as the sacrificial

layer with a XeCl excimer laser (λ = 308 nm, ζ= 30 ns). It was found that the laser fluence and the DRL thickness are strongly dependent on the mechanical properties of the transferred materials. One of the most significant achievements in the LIFT is the deposition of an Organic Light Emitting Diode using triazene as DRL. The transparent Tin doped indium oxide (ITO) was used as an anode and acted as a receiver substrate. On the donor substrate, cathode, and electroluminescent materials an aluminium of 80nm / MEH-PPV-90nm (poly [2-methoxy-5- (2- ethylhexyloxy)-1,4-phenylenevinylene]) bilayer was deposited over the 100nm TP layer. The laser fluence of 250mJ/cm^2 was applied for the transfer of the cathodic part using the XeCl laser (λ=308nm) [64-71].

2.3 Summary:

The review report presents a detailed and structured exploration of laser-based microfabrication, emphasizing its transformative role in enabling microscale and nanoscale precision manufacturing. The chapter begins by discussing the evolution of laser precision engineering, where advancements in laser systems particularly nanosecond, picosecond, and femtosecond sources have significantly enhanced resolution and control over material processing. The interaction mechanisms between lasers and different materials such as metals, polymers, and dielectrics are described in depth, highlighting how parameters like pulse duration, wavelength, and fluence influence outcomes like melting, ablation, or multiphoton ionization.

The chapter further explores various laser-enabled and laser-assisted fabrication methods. Stereolithography (SLA) is presented as a powerful additive manufacturing technique for printing high-resolution ceramic components using UV-curable resins, with studies by Chen et al. and Zocca et al. underscoring its utility in fabricating microstructures suitable for MEMS and biomedical applications. Direct Ink Writing (DIW), particularly when enhanced by near-infrared photopolymerization, is also discussed for its ability to construct

complex, unsupported geometries. Laser-Induced Forward Transfer (LIFT) is covered extensively across solid, liquid, and dynamic release layer configurations, showcasing its ability to transfer a broad range of materials such as metals, polymers, and biological substances with spatial precision and minimal damage. The Spark Plasma Sintering (SPS) technique is detailed as a rapid densification process for ceramics, with its advantages over conventional sintering being well supported by recent literature.

The chapter transitions into comparing bottom-up and top-down fabrication approaches. Bottom-up techniques such as the sol-gel method, chemical vapor deposition (CVD), electrochemical deposition, and atomic layer deposition (ALD) are presented with relevant references, demonstrating their efficacy in constructing nanostructures with high material tunability and controlled porosity. In contrast, top-down techniques including photolithography, wet and dry etching, and erosion/milling are described as established methods for high-resolution patterning, with applications in microelectronics and MEMS devices. A dedicated section focuses on Direct Laser Writing (DLW), emphasizing its unique ability to perform maskless, three-dimensional micro structuring with sub-micron resolution. Studies by Sun and Kawata, and Malinauskas et al., are cited to show how DLW supports two-photon polymerization for high-aspect-ratio features, making it especially relevant for fabricating photonic crystals, microfluidic components, and biomedical scaffolds. The chapter concludes by positioning DLW and LIFT as cutting-edge laser-based processes that push the limits of current microfabrication capabilities, bridging the gap between material diversity and geometric complexity. The work builds a strong technical foundation for understanding and applying laser-based microfabrication in emerging applications such as flexible electronics, energy devices, and biomedical systems.

Chapter 3

This chapter describes the methodology and relevant equipment involved in laser based processing and finite element modelling in COMSOL Multiphysics Software for laser material interaction followed by experimental setup and fabrication techniques for integrating technologies

Experimental Setup and Theoretical Simulation

3.1 Investigative outcomes on the laser interaction with polyimide towards material transformation

3.1.1 Experimental setup for laser material interaction

A CO_2 laser unit of 10.6 μm wavelength with XY motion control (see Fig. 3.1) is used to fabricate laser dots at varying irradiation duration by varying the frequency or Repetition rate, keeping the duty cycle constant at 2%. Polyimide sheet (Dupont Kapton HN) of sheet thickness 125 μm and of size 25 mm × 10 mm was used for fabricating samples. Before fabrication, the samples were ultrasonicated with ethanol and acetone for 15 min each to remove all the unwanted particles from the surface. The CO_2 laser used in the experiment is designed to operate in both pulse as well as a continuous mode with a maximum power of 50 W. The actual power falling onto the sample is restrained using a pulse width modulator, where the electrical pulse sequence is varied using varying frequencies, i.e., repetition rate and duty cycle. It is to be mentioned that laser irradiation is 2 ms, 2.5 ms and 4 ms, respectively, for samples A, B and C. However, the laser irradiation is calculated based on the varying parameters, i.e., duty cycle and repetition rate, and is calculated using the formula: T(s) = D/R, where T (s) is the pulse duration time or pulse irradiation time, D is the duty cycle and R is the repetition rate. In our analysis, Duty rate is kept constant at 2% and repetition rate is varied accordingly.

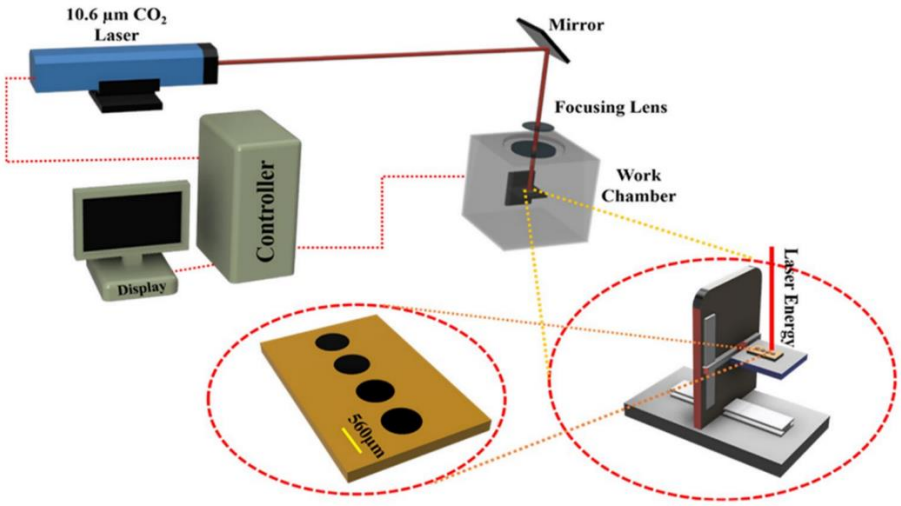

Figure 3.1: Schematic presenting experimental arrangement of 10.6 µm CO_2 laser with auto integrated XY stage for varied applications.

A laser power meter (Field Mate) is used to measure and calibrate the output power. Three samples of specific parameters were fabricated and analyzed to observe the variations in processing parameters. The experiments were carried out in an open atmosphere and hence all the properties thus obtained correspond to their laser interaction with polyimide in an open atmosphere only. The variation in properties of synthesized graphene due to non-uniform energy distribution excessively due to the Gaussian laser beam profile is best analyzed using Raman spectroscopy. In our work, Raman spectroscopic analyses were analyzed using the HORIBA Jobin Yvon Raman spectrometer. The energy used for analysis was a laser beam of 633 nm with spot dimension ~ 2 µm. Raman mapping is performed by recording Raman spectra points across the diameter of the spot so formed by impinging the Raman laser on each fabricated sample for time of integration of 30 s. For further analysis of the spatial variation due to non-uniform Gaussian distributed energy interaction, detailed maps were captured along the diameter of ~ 567 µm carbon dot at ten specific positions spaced evenly at a gap of ~ 50 µm in open atmospheric conditions at normal pressure and temperature. The variation in properties along the spatial direction, i.e., crystalline nature, defect density, and uniformity of the synthesized graphene, is observed due to non-uniform energy

distribution. The thermal pyrolytic behaviour, degradation temperature of polyimide and exothermic enthalpy variation due to the pyrolytic reaction used in the simulation is experimentally calculated with few essential modelling values taken from taken from literature as well.

3.1.2 Numerical simulation of fabricated laser spots

During laser interaction with polymers, multiple complex phenomena, such as laser-induced material ablation, degradation, photo-thermal phase transformation, photo-chemical reaction, and many other evident effects. Laser energy interaction models for metal interaction applications, for instance, laser-assisted welding, laser-assisted drilling and laser ablation models are reported. Due to the apparent variable parameters in lasers as well as the material being interacted with as studied by multiple models reported, it is analyzed that heating and its corresponding carbonization phenomenon is evidently based on Fourier's law of conduction, especially for a long laser pulse duration. A similar case is observed in the case of polyimide transformation into graphene. Based on the above literature study, a similar approach is followed to develop our laser interaction model for the synthesis of graphene, and its detailed information is mentioned below. Numerical simulation is performed on COMSOL Multiphysics, wherein a 3D model wizard is used to analyze the temperature variation on the surface as well as across the sheet depth. The Laser beam used for the experiment is a gaussian beam profile, hence, gaussian beam characteristics are taken while modelling the work. The developed model follows, as mentioned in Fig. 2. Here, important material parameters are fed in for the substrate. Both fixed as well as variable parameters are then added in the model, the variable parameters used for analysis are mentioned in Table 3.1.

Parameter	Value
C, specific heat (J/Kg K),	$1000\left[0.96+1.39\left(\frac{T-300}{400}\right)-0.43\left(\frac{T-300}{400}\right)^{2}\right], 200\ K<T<1500\ K$
k, thermal conductivity (W/m K),	$0.213+3.416\times10^{-5}T, \quad for\ 200\ K<T<729\ K$ $-1.314+2.130\times10^{-3}T, for\ \ 729\ K<T<1500\ K$
α, absorption co-efficient (cm^{-1})	153
R, reflectivity	0.74 for *T<858 K* 0.36 *for T >858 K*
w, beam radius[mm]	0.28 mm

Table 3.1: Various simulation parameters used for analysing temperature profile

The polyimide material used as a substrate is assumed to have uniform properties all around the sheet, i.e., isotropic in nature showing homogeneous properties. The schematic representation in Fig. 3.3 shows the mesh distribution of the developed model. The sheet thickness of the model is taken as 125 µm for its temperature analysis across the depth and the sample size used for analysis is 5 × 5 mm^2. In Fig. 3.3, the

inner rectangular block, where direct laser interaction happens, is taken at 0.5 × 0.5 mm^2. The mesh in this region is extra-fine, whereas the remaining geometry follows the fine mesh configuration. The experimental analysis is performed in an open atmosphere hence, the initial temperature condition is taken as T (m, 0)=298 K, where T (m, t) corresponds to distribution of temperature and m is the laser interaction across the depth of polyimide sheet. Due to the sufficiently large size of the polyimide sheet considered when compared with the actual spot developed, it is assumed that there is no convective heat transfer across the edges and hence and hence zero-flux boundary condition is considered on the left and right side of the substrate. The temperature profile is estimated by considering solid heat transfer with a phase change temperature of 25 K. The model uses tetrahedral mesh with 28,615 elements at a temporal step size of 0.045 ms. The non-uniform temperature distribution profile of the laser causing variation in the properties of synthesized laser-induced graphene is then predicted. The temperature profile of laser Gaussian beam is modelled in cylindrical coordinate system with a falling laser beam acting projecting volumetric heat source and is represented in Eq. 1. There are assumed evident refection losses happening at the polyimide–air interface considered in the analysis and laser energy absorption in the polyimide is calculated based on Beer–Lambert equations formulated by Beer–Lambert law:

$$\boldsymbol{C\frac{\partial T}{\partial t} = \nabla.(k\nabla T) + \alpha(1-R)I_0 e^{-\alpha m}} \qquad \textbf{(1)}$$

Here, C corresponds to specific heat received (J/Kg K), k corresponds to thermal conductivity (W/m K) which is a dependent parameter on varying temperature. Laser energy interaction with polyimide follows a gaussian beam profile and in the cylindrical coordinate system, the heat density based on varying irradiation time follows equation 1. The value of absorption coefficient (α) is calculated experimentally by placing a power meter below the polyimide sheet and hitting unfocused laser energy to measure its value. It is then compared with laser power without

polyimide and based on the comparison, the value of absorption coefficient (α) is presumed for simulation.

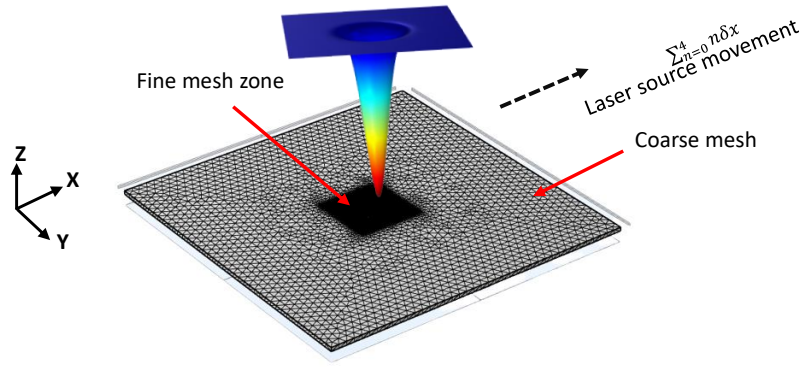

Figure 3.2: Schematic representation of the 3D-moving laser source simulation

The reflectivity of polyimide film at specific wavelength is calculated using literature following complex index $n + i\kappa$. The equations that follow for calculation of R is given in equation Eq.2

$$\boldsymbol{R = R_0 \frac{[1-exp(-\alpha d)]^2+4\exp(-\alpha d)sin^2\beta}{[1-R_0 exp(-\alpha d)]^2+4R_0\exp(-\alpha d)sin^2(\beta+\phi_r)}} \qquad \textbf{(2)}$$

Where,

$$\boldsymbol{R_0 = \frac{(1-n)^2+\kappa^2}{(1+n)^2+\kappa^2}} \quad , \boldsymbol{\beta = \frac{2\pi n d}{\lambda_0}} \text{ and } \boldsymbol{\phi_r = atan\left(\frac{-2\kappa}{1-n^2-\kappa^2}\right)}$$

The term α, i.e., optical absorption coefficient (cm-1), is calculated experimentally, whereas R, i.e., the reflectivity of the polyimide film corresponding to the concerned wavelength of 10.6 µm, is analyzed using the complex refractive index parameter of polyimide, i.e., n+ik. The n and k values of laser interaction with polyimide show a very complicated temperature-to-time dependency due to the physical and chemical changes observed. Based on the literature for laser polyimide interaction, the value of n+ik varies from 1.75+0.03i for temperatures below the decomposition temperature of polyimide and is approximated to 2.5+1.9i for temperature above decomposition temperature for carbonaceous material transformation. I0 is the peak intensity that varies

with varying repetition rates and its corresponding laser irradiation time as mentioned in Table 3.1. The thermal conductivity k (W/mK) and specific heat C (J/KgK) is assumed to be temperature-dependent parameter that follows the relation as mentioned in Table 3.1. As the temperature range exceeds, a constant extrapolation is considered for analysis. It is to be mentioned that due to essentially high heat delivery by a very short laser pulse in the heat affected zone when compared with exothermic enthalpy release due to polyimide carbonization, the heat generation during carbonization is neglected. In addition, convection and radiation losses are neglected in the study. It is also assumed that pyrolysis happens at T ≈ 858 K and the properties of carbonaceous material are considered above this specific temperature.

3.2 Investigative outcomes on the influence of lasers processing parameters towards transformation

3.2.1 Experimental Procedure

Polyimide of 125 µm sheet thickness is used as a base material for the formation of LIG by direct laser irradiation. The samples are ultrasonically cleaned in acetone and ethanol for 30 minutes. The laser is irradiated in an 8mm x 8 mm area with a total sample size of 20 mm x 20 mm. From the laser studies, it is observed that both laser fluence as well as spot overlap % are important parameters towards the synthesis of LIG, and hence study proceeds in a similar fashion. Pulse overlap is the percentage of overlap between successive laser pulses given in eq.3 Laser fluence is the amount of energy per pulse per unit spot area and is given in eq. 4

$$\%\ \boldsymbol{Overlap} = \mathbf{1} - \left(\frac{\boldsymbol{v}}{\mathbf{2}\boldsymbol{w} \times \boldsymbol{r}}\right) \quad \textbf{(3)}$$

$$\boldsymbol{laser\ fluence} = \frac{\boldsymbol{P}}{\boldsymbol{r} \times \boldsymbol{\pi} \times \boldsymbol{w^2}} \quad \textbf{(4)}$$

Where *v* denotes scan speed in mm/s, *w* is the spot radius in mm, *r* is the repetition rate in (1/sec), *P* is average laser power (W).

An in-house fabricated laser engraving setup equipped with a 10.6 µm CO_2 laser is designed to work at low scan speeds (50-150 mm/min) and low laser power (1-3 W) (see fig. 3.2). LIG is fabricated under various working conditions by varying laser fluence, scanning speed (v), and line overlap percentage. The laser intensity is measured using a laser power meter (Field-mate) to measure the average power. The experiments are performed in an open atmosphere. The line overlap is kept constant at 30% throughout the entire experiment.

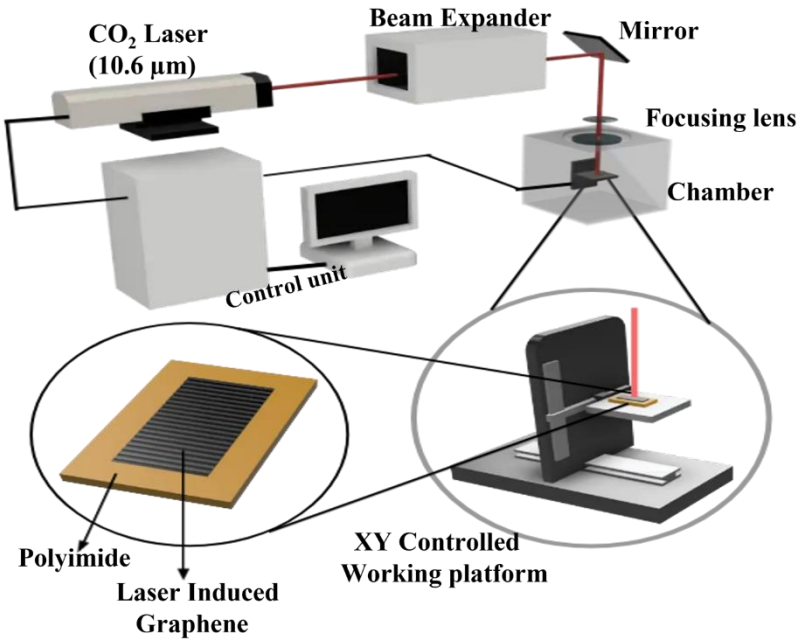

Figure 3.3: Experimental Setup of 10.6 µm CO_2 Laser with automatic controlled XY stage for Low scan speed applications

After successful completion of experiments for all the parameters, the phase formation is analyzed using X-Ray Diffraction. The X-Ray studies are performed with a Cu-K_α radiation source. The surface morphology of specimens is studied using a field emission scanning electron microscope (FESEM) (JEOL JSM-7400F) and stereo-microscope (Leica 300). Raman spectroscopic studies are performed using a HORIBA Jobin Yvon Raman spectrometer at laser excitation of

633 nm with a spot size of ~2 μm. The Raman images are captured by recording multiple Raman spectra along a line scan by shining the Raman laser on each sample for an integration time of 20 s. To check the sheet resistivity of the LIG, a "four-point probe" setup is used in ambient conditions with a Keithley source meter unit (SMU) 2612 for sheet resistance. The full mapping sheet resistance variation across the sheet is performed from t=0 to 10 seconds. The mean and standard deviation are calculated and reported with the standard deviation showing the error bar in the calculation. The influence of contact resistance on the measurement of resistance is ignored since the contact resistance between contact units and LIG is almost negligible (about 1%) compared with an internal resistance of LIG.

3.3 Experimental setup for aluminum deposition for laser micro-3D printing.

3.3.1 Micro-3D printing setup for laser processing:

Fig. 3.4 shows the schematic diagram of components of laser μ-3D printing setup for the continuous printing of pixels. A pulsed CO_2 laser is interfaced with two motion stages i.e. donor stage and acceptor stage with a minimum resolution of 10 μm. The printing is performed by slicing the CAD drawing into multiple layers and converting it into G & M code. Based on the layer-wise G and M code the system sends the command to the laser and motion controller at the same time. The pulse delay generator delays the time between the stage movement and the pulse irradiation between two consecutive pulses. Once the first pixel is transferred the donor stage moves with the 1.5 times the spot diameter while the acceptor's stage follows the G and M code of the specific CAD drawing. As per the CAD model, the pulse generator sends the signal to the laser and motion stages. The laser beam irradiates the donor film as per the signal received and the motion stage follows the same signal with some pulse delay. As the first pixel is printed on the acceptor substrate, the second pulse will irradiate the donor film for the next pixel transfer

and continues till the entire geometry is printed.

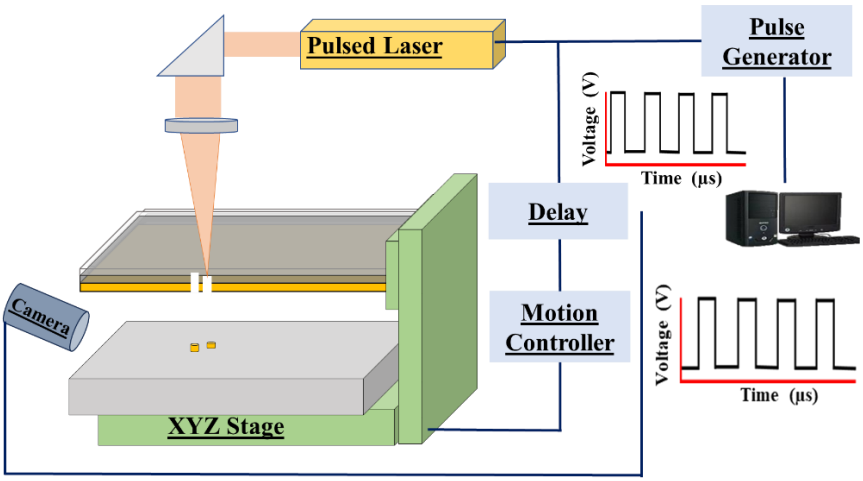

Fig 3.4: System design component for Laser µ-3D printing.

Fig. 3.5 shows the developed laser µ-3D printing setup with CO_2 laser and continuous control of the donor and acceptor stage. The donor stage has 2 degrees of freedom in X and Y directions while the acceptor stage has 3 degrees of freedom in X, Y, and Z for three-dimension printing. The total building volume of the system is 80×80×80 mm^3. The laser spot is focused using different focusing lenses for variable spot sizes on the donor substrate. A substrate heater is also installed at the acceptor stage with a heating capacity of up to 300 ° C to heat the acceptor during the printing process. The developed setup is controlled with user interface software. The software supports the G & M code of the CAD model and then generates the signal as per the CAD geometry. The continuous line cab be printed by a certain pulse overlap of pixels printed on the acceptor substrate. The system is integrated with a carbon dioxide laser working at 10.6 µm laser wavelength. Most of the electronics, optoelectronics, and photonics devices are fabricated on the silicon wafer due to its semiconductor nature, high-temperature resistance, and is chemically stable. It is also having good transmissivity with CO_2 laser in the mid- infrared region at 10.6 µm wavelength.

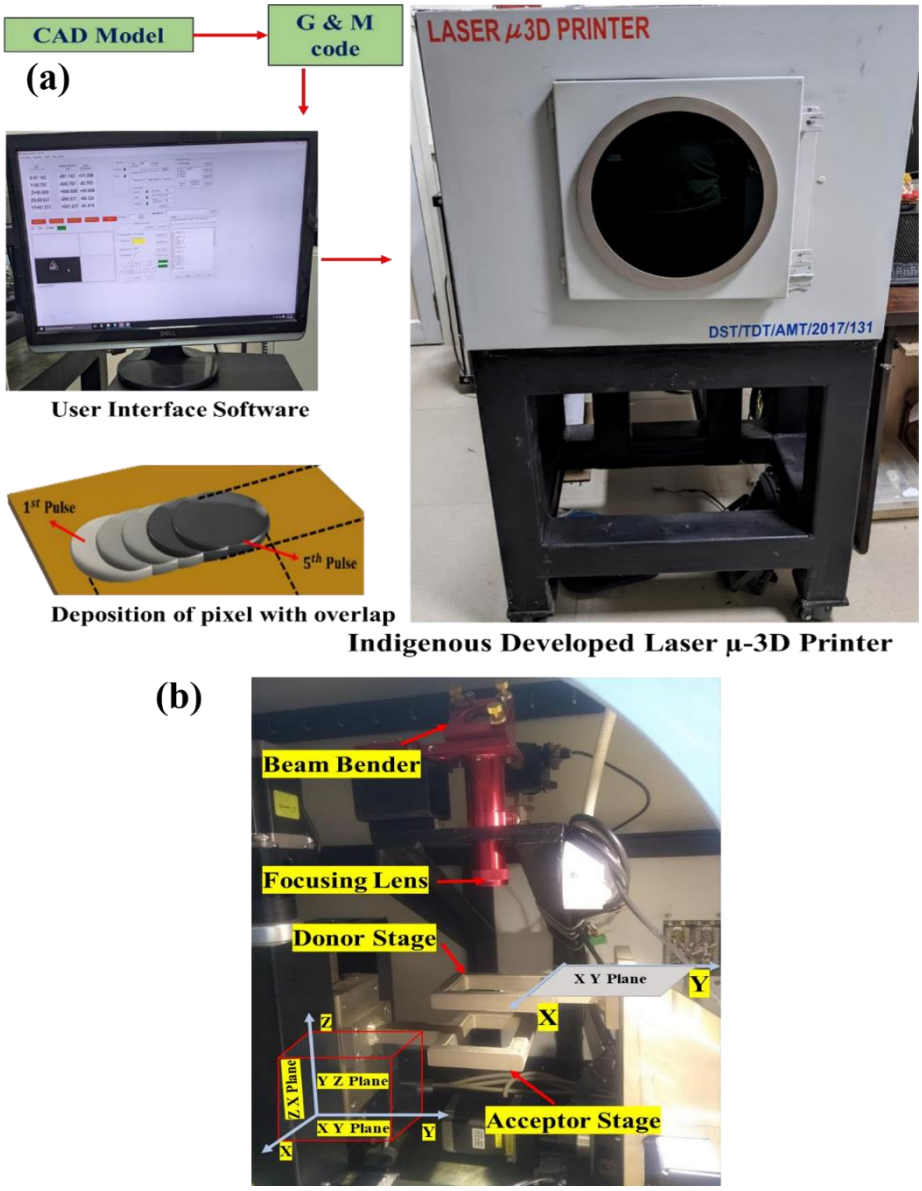

Fig. 3.5: (a) Experimental setup of Laser μ-3D printing and strategy for line printing with pulse overlap, (b) experimental setup with degree of freedom of donor and acceptor stages

3.3.2 Donor Preparation

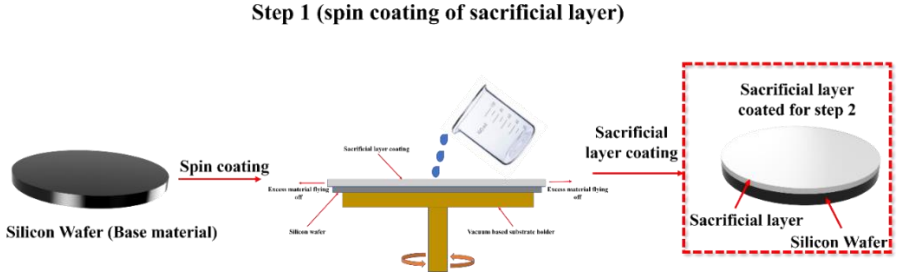

Fig. 3.6 Preparation of donor with sacrificial layer coating and thin film deposition

The transmissivity of the donor substrate should be higher to pass the laser energy through the material. In the case of 10.6 µm laser wavelength, a silicon wafer is having an 80 % transmissivity, hence it is used as donor substrate in this study. Initially, the silicon wafer is dipped in acetone and then rinsing it with deionized water to remove any imperfections or contaminants. The sacrificial layer absorbs the laser energy and vaporizes for the thrust mechanism hence the absorptivity of the sacrificial layer should be good. hence it is used as a sacrificial layer coating in between the donor substrate and donor film. PDMS (Sylgard 184 kit) base (A) polymer and curing agent (B) are mixed in the weight ratio of 10:1, respectively. The mixture kept in a vacuum (0.06 MPa) for 1 min for degassing process ensuring a homogeneous and smooth coating. The mixture is spin- coated on the silicon substrate at 12000 RPM and baked at 60 ºC for 90 min to cure the polymer. Fig.3.6 and 3.7 (a) & (b) show the silicon wafer substrate and PDMS sacrificial layer-coated Silicon substrate respectively.

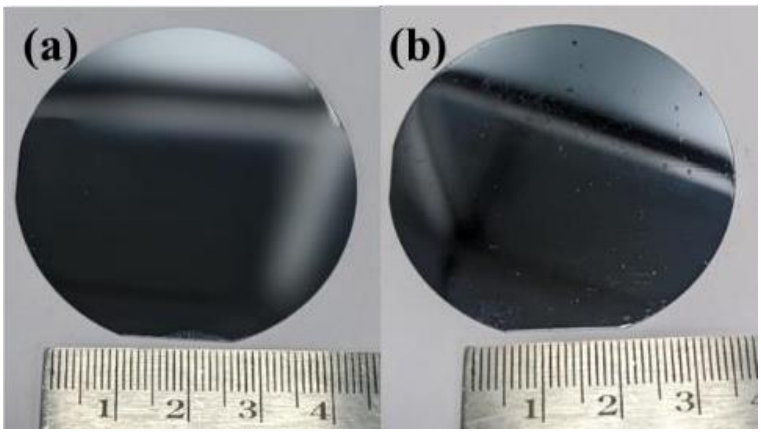

Fig. 3.7 (a) Transparent Silicon substrate at laser wavelength 10.6 µm Sacrificial layer coating on a silicon wafer

3.3.3 Thin film deposition of Aluminum:

To proceed with the deposition process, the PDMS-coated substrate was flash-deposited with aluminum using a tungsten boat. Aluminum wire (1g) was vaporized by applying 460 V and a specific current for 60 seconds. Due to aluminium's low density, the material dispersed uniformly across the chamber. The stand-off distance between the

source and substrate was maintained at 37 cm to ensure a consistent coating thickness on the donor substrate.

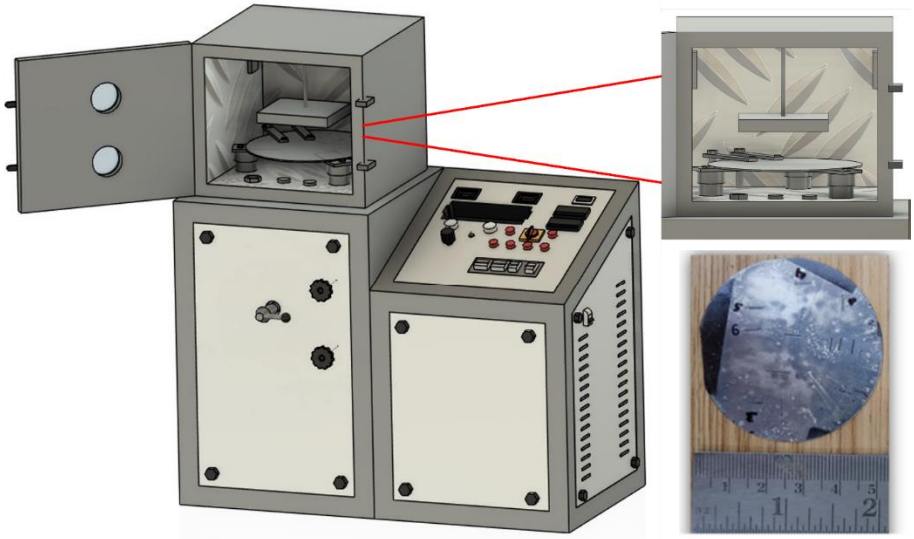

Figure 3.8: Schematic representing experimental setup for preparation of donor material.

A schematic representation of the experimental setup (Fig.3.8) and the principles governing material ejection (Fig.3.9) are provided. Additionally, the processing parameters for the thin-film deposition using laser decal transfer are summarized in Table 3.2.

Table 3.2: Processing parameters followed for deposition of thin film material over sacrificial layer for laser decal transfer.

S.No.	Process Parameters	Flash Evaporation
1.	**Pressure**	**$5*10^{-5}$ mBar**
2.	**Deposition Time**	**60 seconds**
3.	**Voltage**	**460 V**
5.	**Material**	**Aluminum**
6.	**Material Form**	**Wire**
7.	**Stand Off distance**	**37 cm**

8. **Substrate temperature** **100 °C**

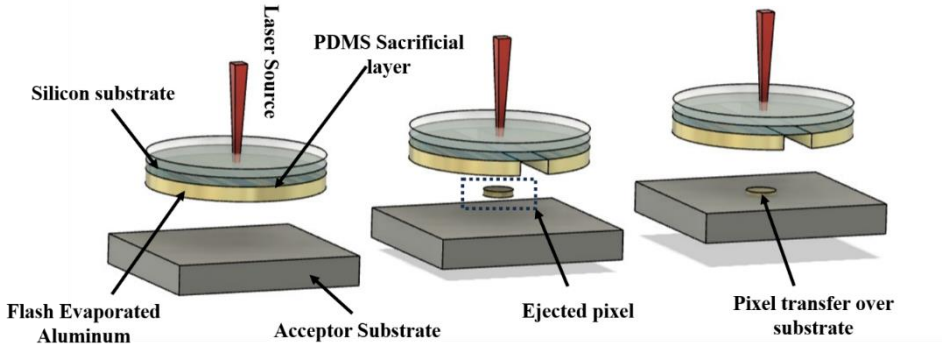

Figure 3.9: Schematic representing underlying principle of material ejection and transfer.

Figure 3.9 illustrates the principle of a laser-assisted pixel transfer process, which operates based on selective ablation and thermal decomposition of a sacrificial polymer layer to enable localized material ejection. In this specific setup, a CO_2 laser with a wavelength of 10.6 µm is used to irradiate a multilayer structure consisting of a silicon donor substrate, a PDMS (polydimethylsiloxane) sacrificial layer, and an aluminum thin film, which acts as the transferrable material. Upon laser irradiation, the CO_2 laser energy is primarily absorbed by the PDMS layer, as it exhibits strong absorption in the mid-infrared region. This causes rapid localized heating, leading to thermal expansion and partial decomposition of the PDMS beneath the laser spot. The sudden buildup of pressure due to gas release from the decomposing polymer generates a mechanical impulse, which propels the aluminum pixel away from the donor surface. The aluminum layer, pre-patterned or continuous, is mechanically ejected in discrete pixel form because of the confined explosive-like force from the PDMS layer. The ejected material travels across a controlled gap and adheres to the acceptor substrate positioned beneath. This process allows for precise, clean, and additive deposition of materials without contaminating the substrate or requiring masks, making it ideal for digital, maskless microfabrication

3.3.4 Experimental setup for SiC and ZnO deposition and Printing for laser micro-3D printing.

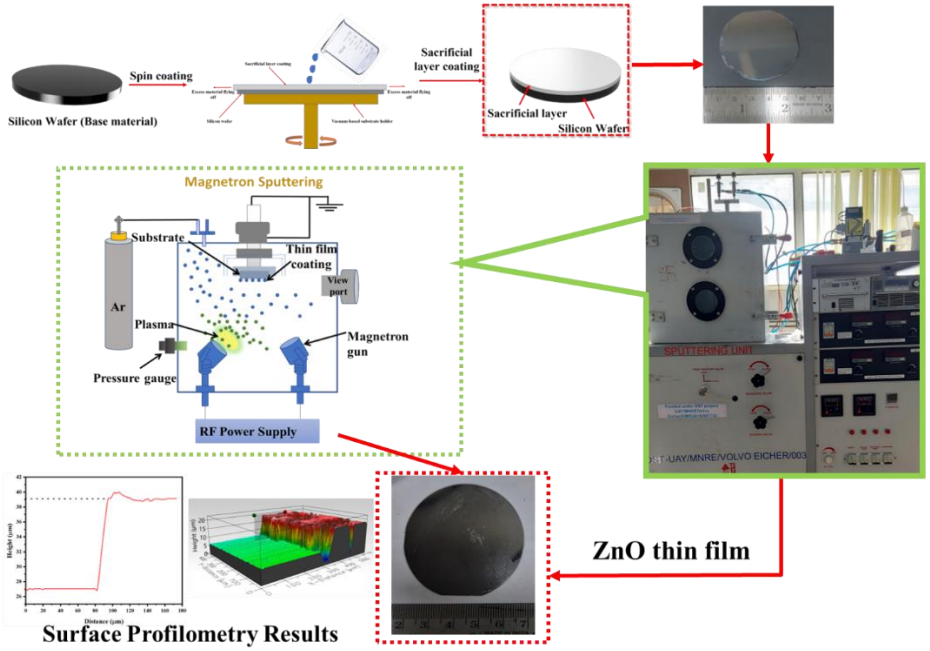

Figure 3.10: underlying process of thin film deposition for laser micro-3D printing

The image illustrates the step-by-step process involved in the fabrication of a thin film-coated donor substrate using RF magnetron sputtering. This donor substrate is subsequently used in laser-assisted micro-3D printing applications. The procedure involves substrate cleaning, metal deposition via sputtering, and characterization of the deposited layer, as detailed below:

The schematic in fig. 3.10 shows the working of a magnetron sputtering unit, which operates under a controlled argon atmosphere. Argon gas is introduced into the chamber and ionized by an RF power supply to create a plasma. These energetic argon ions bombard the target (i.e., SiC and ZnO), causing the ejection of target atoms that then condense onto the rotating wafer substrate, forming a uniform thin film. The actual sputtering process is carried out using the setup shown in the photograph, which includes the vacuum chamber, RF generator, and

associated control units. Deposition parameters such as pressure (typically $5*10^{-5}$ mBar) and power are typically 80 W for ZnO whereas 165 W for SiC. The duration of deposition varies for ZnO and SiC with deposition time of roughly 3 hours for ZnO and approximately 12 hours in steps of 3 hours each. The duration is optimized based on the required film thickness and surface uniformity. Once sputtering is complete, the wafer now contains a metal-coated PDMS layer. The resulting sample is examined for thickness and surface morphology using profilometry and optical imaging**.** The attached graphs show a profilometric scan, confirming a sharp interface between the coated and uncoated regions, and a 3D surface topography plot indicating the uniformity of the deposition. The final donor substrate**,** with its precisely deposited thin film, is now ready for use in subsequent laser micro-3D printing where pixel-by-pixel ejection is enabled through photothermal interaction. This process ensures a clean, adherent, and uniformly deposited film on a soft-release sacrificial interface, which is essential for efficient and reproducible laser transfer in micro-3D printing applications.

3.4 Integrating laser decal transfer and direct laser writing for functional applications

The above-mentioned CO_2 laser is used for dual application viz Direct laser writing (DLW) for laser induced graphene synthesis and Laser μ-3D for selectively printing (see Figure 3.11). The surface profilometry analysis is performed using Filmetrics Profilm 3D non-contact type profilometer. SEM and cross-sectional analysis of the fabricated samples are performed using FESEM JEOL JSM-7400F FEI (model No. TALOS F200S) TEM is used for performing HR-TEM and acquiring SAED Patterns.

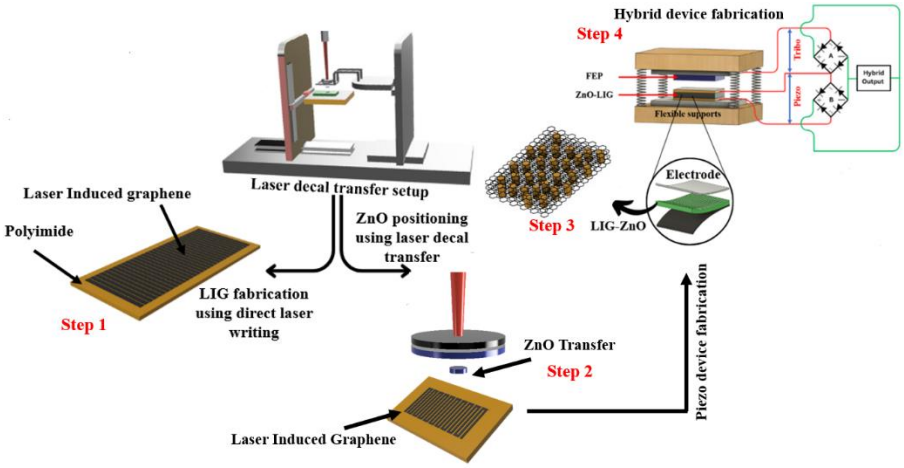

Figure 3.11: Schematic showing utilization of 10.6 µm CO_2 laser for Laser-induced graphene synthesis and selectively doping ZnO ceramic in LIG using laser µ-3D technique for functional applications.

3.4.1 Selective Material transfer using laser decal transfer

As the result of laser-material interaction, the process involves heating, melting, and vaporization of material that needs to be eliminated to maintain the functionality of the material without failure. This is crucial because many materials, particularly complex multicomponent and multiphase systems, can experience irreversible changes during melting or vaporization, degrading the functional properties of printed structures**.** To retain the functionality of the material a sacrificial layer or dynamic release layer can be introduced between the substrate and donor film and the process that follows is same as mentioned in section 3.3.3. The material ejection is analyzed for both ZnO and SiC.

3.4.2 Synthesis of ZnO nanorods

Once the seed layer is grown, the selective positioning of ZnO seed layer was performed in the pores and tracks of laser induced graphene using laser µ-3D technique. The composite thus formed is dipped in a solution for seed layer growth into nano-rods over laser induced graphene. For this purpose, 0.1M of zinc nitrate hexahydrate Zn $(NO_3)_2.6H_2O$ (SIGMA-ALDRICH, 98% Reagent grade) calculated as 0.74375 gm is initially mixed in 25 ml of water. Further 0.1M Hexamethylenetetramine $C_6H_{12}N_4$ ((SIGMA-ALDRICH, ≥ 99.5% Reagent grade) calculated as

0.35 gm was mixed in the solution. The final solution was stirred using magnetic stirrer at 400 rpm for 20 minutes. The equation that follows is

$$(CH_2)_6N_4 + 6H_2O \rightarrow 6HCHO + 4NH_3 \quad (A)$$

$$NH_3 + H_2O \rightleftarrows NH^+ + OH^- \quad (B)$$

$$2OH^- + Zn^{2+} \rightleftarrows ZnO + H_2O \quad (C)$$

Further, 1mM Potassium permanganate $KMnO_4$ (SIGMA-ALDRICH, ≥ 99.5%) calculated as 0.2 gm was placed in the solution and stirred for 5 minutes. Once the solution was made, the selectively transferred ZnO and LIG composite was dipped in the solution and covered with aluminum foil for heat to remain intact. The solution was placed in oven at a temperature of 110 ºC for 3.5 hours and further analysis on growth of ZnO over laser induced graphene was explored using characterization techniques.

3.4.3 Setup for functional realization:

The applicational utility of the proposed laser-based process was explored towards hybrid piezo-tribo nano responses which would effectively play its part for powering up sensors. A LIG-ZnO-FEP based device was fabricated where LIG-FEP response was essentially due to triboelectric Nanogeneration whereas the presence of ZnO introduced piezo-electric response as well. Triboelectric nanogenerator (TENG) works on the principle of triboelectrification and electrostatic induction. A TENG can be fabricated by combining material having tendency to donate the electron (tribo-positive), with a material having an affinity towards electron (tribo-negative). LIG has a strong affinity towards the electron, hence it can act as good tribo-negative material. A TENG device was fabricated with LIG as tribo-positive material and copper as tribo-negative material, as shown in Fig 3.12. The two-electrode design entails a structure featuring a single functional layer that integrates both triboelectric and piezoelectric properties.

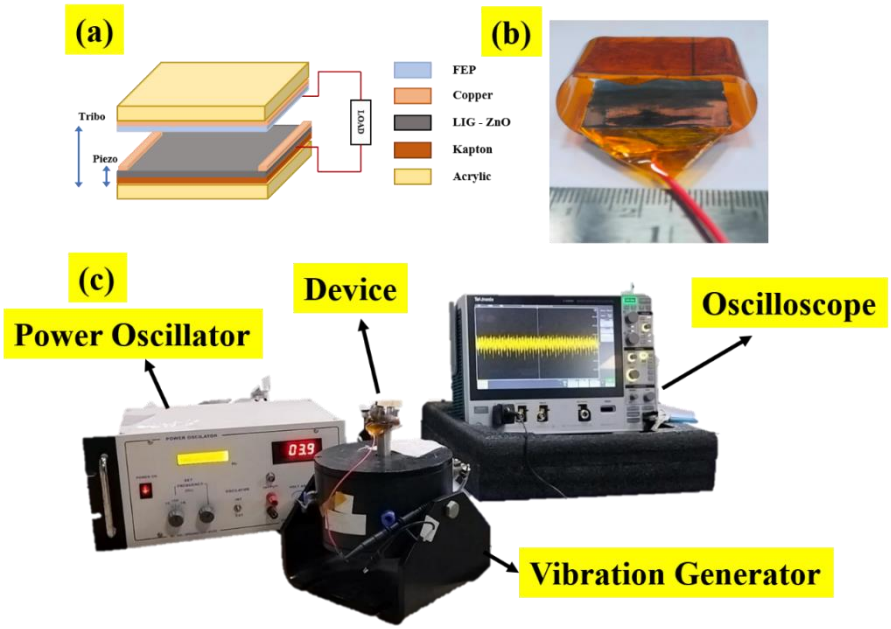

Fig. 3.12: (a) Schematic diagram of piezo and triboelectric hybrid nanogenerator, (b) fabricated devices for response analysis, (c) test setup for device testing and analysis.

3.5 Material characterization

The synthesized graphene is studied using various characterization techniques for material confirmation. The morphological characterization is performed using FE-SEM and physical characterization of material is performed using X-Ray diffraction and Raman Mapping.

3.5.1 X-Ray Diffraction

X-Ray diffraction technique is a non-destructive often used to identify and analyze the crystal structure, degree of crystallinity and availability of impurity phases if any.

It works on the principle that when a high-energy beam falls over a target material, energy absorption happens, and electrons jumps from inner to outer shell thus in an unstable state condition. Due to natural tendency of electrons to reach back to initial stable state, the electrons come back to its original state thus releasing X-rays . The electrons moving from M shell to K shell generates Kβ x-rays and the ones moving from L shell to K shell generates Kα x-rays. The basic principle of analysis of XRD is based on Bragg's law which states that "When a collimated beam of x-rays strikes a crystal, the atoms act as diffraction centers and the diffracted beams combine to give diffraction patterns.

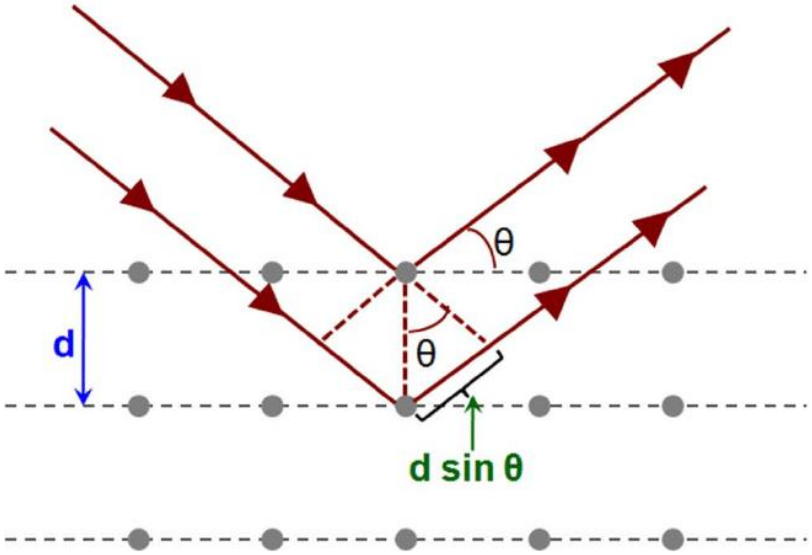

Figure 3.13: Bragg's Law in a 2-D crystal

For the nth order diffraction, using the X-rays of wavelength λ, the Bragg's equation is:

$$n\lambda = 2d \sin\theta \qquad (8)$$

in this work, X-ray diffractometer (Bruker-D2Phaser, with Cu-K radiation) is employed to confirm the crystalline points of graphene synthesized. here XRD patterns are recorded in the range of 10° to 80° for different materials being explored based on varying laser processing.

3.5.2 Field Emission Scanning Electron Microscopy (FESEM):

To study the morphology and its variations over the different energy variations, FE-SEM is used. It is a high-resolution technique where

electron beam emitted by field emission source strikes the surface of the sample placed under it. It is then raster scanned to obtain the microstructure and surface morphology at varying magnifications. The inner arrangement of setup is such that the ejected electron beam passes through an arrangement of magnetic lenses and metal apertures in a vacuum tube for focusing as a thin monochromatic beam. when an incident electron beam interacts with sample, it generates output beams in the form of backscattered electrons, secondary electrons, Auger electrons and characteristic X-rays with different detectors collecting each type of electron and hence produces images of the sample specimen. The elastic interaction between sample and electron beam excelling out of source leads to backscattered electrons creations. However, there are electrons which do not interact with nucleus of the specimen are reflected or backscattered from the sample. it is observed that backscattered electrons depend on the atomic weight of the element. Due to stronger deflection from bigger nucleus, the element with higher atomic mass generates higher number of backscattered electrons. it gives a better information of composition and topography of the sample. the inelastic interaction between sample and electron beam generates secondary electrons. due to loss of inelastic interaction, the energy is less than backscattered electrons. The secondary electron detector is positioned at an angle to the axis of incident beam to improve the efficiency of detector. The secondary electrons help to study the surface morphology of samples. In this study, a Field- emission scanning electron microscope (FE-SEM, JEOL JSM-7400F) is employed to study the morphology of gold coated sample surfaces.

Figure 3.14: Field Emission Scanning electron microscope (FE-SEM)

3.5.3 Raman Spectroscopy:

It is a non-destructive chemical analysis technique which provides detailed information about phase, crystallinity, polymorph and chemical structure. It is a light scattering technique, whereby a molecule scatters incident light from a high intensity laser light source. Most of the scattered light is at the same wavelength (or color) as the laser source and does not provide useful information called Rayleigh Scatter. However, a small amount of light (typically 0.0000001%) is scattered at different wavelengths (or colors), which depend on the chemical structure of the analyte called Raman Scatter.

A Raman spectrum features several peaks, showing the intensity and wavelength position of the Raman scattered light. Each peak corresponds to a specific molecular bond vibration, including individual bonds such as C-C, C=C, N-O, C-H etc., and groups of bonds such as benzene ring breathing mode, polymer chain vibrations, lattice modes, etc. (see fig. 3.15 and fig. 3.16)

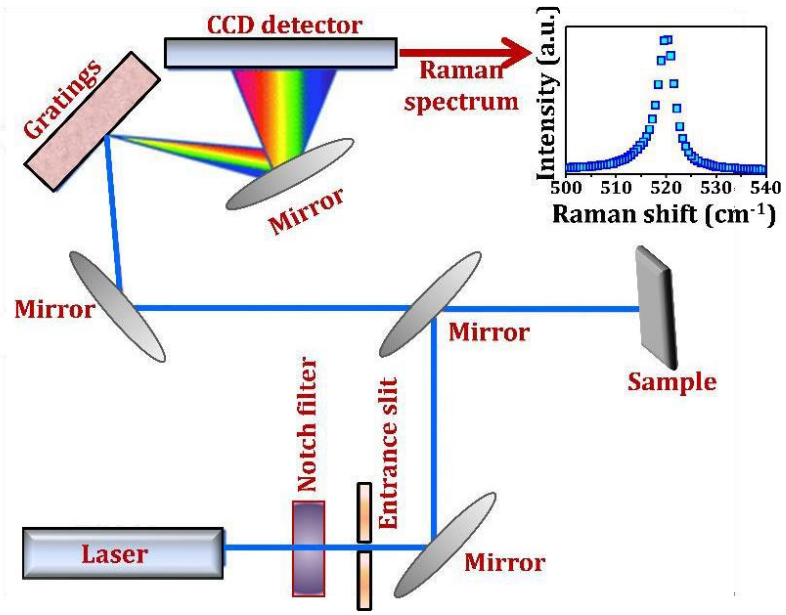

Figure 3.15: Raman spectrometer with its attached units marked

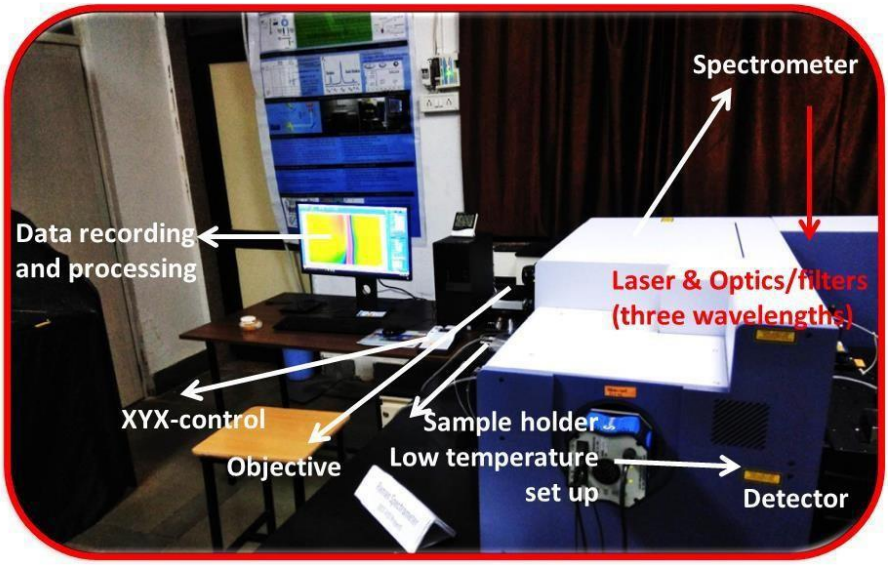

Figure 3.16: Schematic of Raman Microscopy

Chapter 4

This chapter explains the laser polyimide interaction and its transformation into conductive LIG using direct laser writing technique. The associated results with respect to simulation and experiments is discussed in detail followed by flexible sensor applications.

Direct laser writing for functional applications

4.1 laser spot interaction for polyimide to graphene transformation

Laser-induced graphene shows anisotropic material properties in all directions. From the reported literature it was observed that a critical threshold laser energy is required to carbonize polyimide and transform to loosely packed graphene. The governing principle behind synthesizing graphene using a laser source holding potential commercial applications lies in the photothermal effect caused due to source of laser energy over the substrate surface, i.e., polyimide here. As laser irradiation over the surface increases, the energy per pulse (J) and hence energy density changes in the specific area leading to variation in the properties of the synthesized graphene. The laser irradiation variation suggested the presence of sufficiently high temperature gradients along the circular spot spatially. The high temperature gradient on the carbonaceous material is expected to present evident variation in properties. This is mainly due to the non-uniform energy distribution subjected to Gaussian beam profile of the laser. For best analysis of samples concerning spatial variations in synthesized, Raman spectroscopy is performed along the samples. The variation along the spot affects the properties of synthesized graphene ranging from average in-plane crystallinity (La) to defect density (nd) and synthesized material uniformity which is discussed in detail.

4.1.1 Surface temperature and depth of graphenization: Fig. 4.1a–c shows the spatial variation in temperature of a single shot with different irradiation time and laser intensities. The maximum observed temperatures are 1913 °C, 2077 °C, and 2799.93 °C, respectively, for the sample A, B, and C, respectively. The temperature is observed to

increase with an increase in irradiation time of laser pulse with polyimide substrates. The spatial temperature profile over the surface defines the extent of graphenization on the polyimide surface. Fig. 4.2a shows the temperature variation with an increase in irradiation time and of the laser beam on the polyimide substrates. The temperature is increasing sharply within the irradiation time zone and starts decreasing slowly because of natural convection and radiation losses. However, the predicted temperature is slight overestimated because of various assumptions, such as: (1) phase change of the polyimide after the irradiation that will absorb latent heat of energy for the graphenization; (2) the induced porosity of the graphene formed at 585 °C that leads to scattering of laser beam in the materials; (3) the evaporative flux loss is neglected, i.e., during the laser–material interaction, a minor portion of material may undergo ablation, resulting in removal of certain quantity of heat energy and (4) the protruded dome shape formed due to accumulation of gases which causes increase in laser path length with increasing irradiation time is not considered in the simulation model. The assumptions made are highly challenging to experimentally measure and then incorporate in mathematical modelling; however, the developed model paves way for further modifications soon.

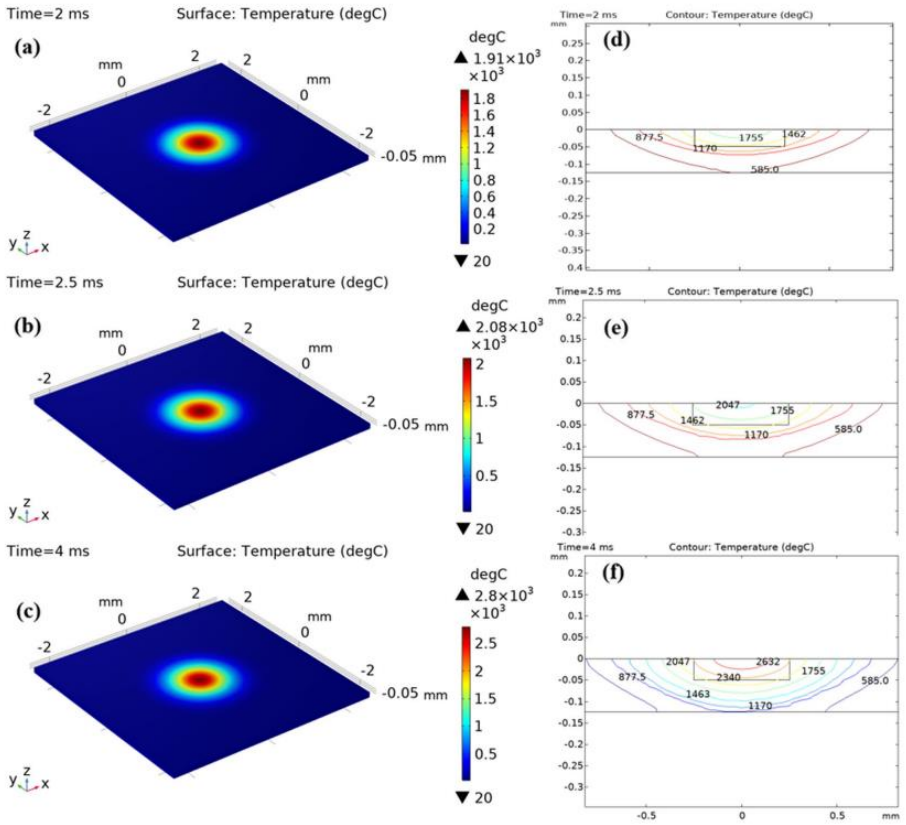

Fig. 4.1: (a–c) Spatial distribution of temperature of single shot for with irradiation time of (a) 2 ms, (b) 2.5 ms, (c) 4 ms, d–f contour plot at the cross-sectional plane of laser beam at (d) 2 ms, (e) 2.5 ms, (f) 4 ms.

Fig. 4.2b shows the temperature over the polyimide surface with a beam diameter of 567 microns. The graphenization area can be observed where the temperature is crossing beyond 585 °C. It can be observed that the temperature is increasing beyond the beam diameter of laser pulse area because of the thermal conductivity of the polyimide hence the effective area of graphenization is also greater than irradiation zone. In addition, it is evident from Fig. 4.1 b that pulse irradiation time has less significance in the extent of graphenization over the polyimide. Laser interaction with polyimide is a highly localized process, where laser energy interaction in the zone causes sudden heating of the localized area causing an increase in temperature at a sudden rate. Based on the simulation results, an experimental analysis was performed using a FLIR A600- series thermal imaging camera to plot it thermal profile.

FLIR Research software was used for analysing the results and to study its reliability and repeatability. The data were recorded for 5 s at laser parameters of repetition rate of 8 Hz and duty cycle of 2% and keeping the frequency of recording as 12 Hz for the camera. The emissivity of the sample for analysis is taken as 0.7 and the standoff distance between surface and camera for measurement is kept at 30 cm. From the simulation results, it was observed that the maximum observed temperature was approximate as 2077 °C, whereas the average analyzed experimental temperature is observed between 1750 and 2060 °C with more peaks hovering around the mid-temperature ranges (see Fig. 4.3). It is, however, observed from the experiments that at times, the laser absorption in formed graphene does not present the necessary emissivity. It is also observed at times that due to excess energy, some material escapes out of the surface which is not considered in simulation thus making the results of simulation over-estimated.

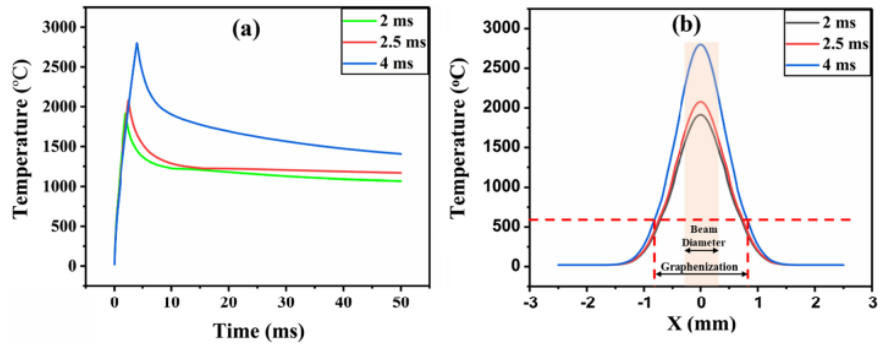

Fig. 4.2 Temporal variation of temperature of single shot for irradiation time of (a) 2 ms, (b) 2.5 ms, and (c) 4 ms

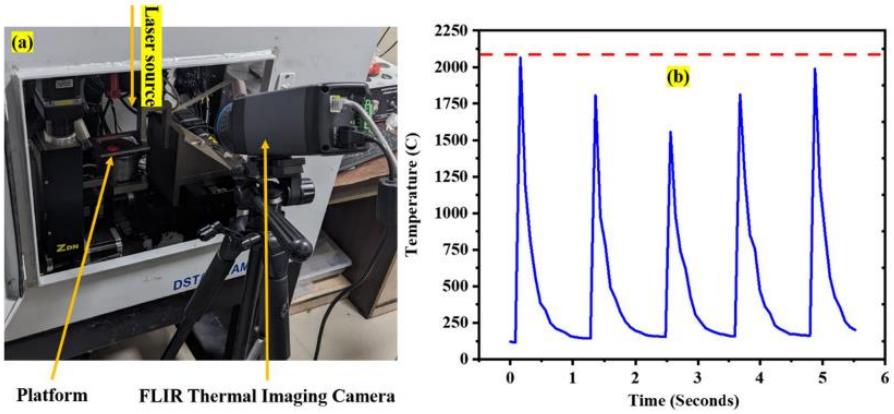

Fig. 4.3 (a) Experimental setup of temperature measurement over surface using FLIR thermal imaging camera and (b) associated temperature for laser parameters at repetition rate of 8 Hz and duty cycle 2%

4.1.2 surface roughness based on laser energy interaction: Fig. 4.4 shows SEM micrographs of polyimide conversed graphene by single laser shot with different irradiation time and laser intensities. It can be observed that as the laser interacts with polyimide the polyimide molecules start dissociating into thin sheets by the release of gaseous product. With further increase in laser irradiation time, the degassing rate increases that leads to the bubble formation in the irradiation zone and converting the thin sheets into porous. The porous graphene shows some crystallinity defects in the graphene structure. With further addition of the laser energy in porous structure, bubbles start growing by degasifcation and converting the porous structure into fibrous nature of graphene. Fig. 4.5 a-c shows the profile generated after the laser irradiation at irradiation time of 2 ms, 2.5 ms, and 4 ms, respectively. The roughness values are 3.64, 4.67 and 5.04 µm. It can be observed that as the temperature increases the roughness value of synthesized graphene increases. This might be due to the high density of the porous graphene formation at elevated temperature that leads to more non-uniformity on the top surface of the polyimide. It is observed that there is a slight rise in the synthesized graphene forming dome-like shape. It is due to a rise in the temperature and its subsequent effect causing pyrolysis of polyimide. Within the irradiated region, as seen from the isothermal contour plot in all cases, the temperature exceeds decomposition temperature causing gasification in the zone with presence of gases as carbon mono-oxide (CO) and carbon-di-oxide (CO_2). As the laser irradiation energy increases, the accumulated gases form positive pressure causing ballooning of fabricated samples eventually causing bursting out and release of gases, as shown in Fig. 4.5c. The pyrolysis of polyimide with the formed dome presents varying properties at varying rates which would present finer structures

in the zone. As the laser irradiation time increases there is a sufficient increase in heat source density eventually causing a rise in temperature. In Fig. 4.4c, a clear and wide-open structure is observed at the center which is due to more intensive extent of reaction and greater pyrolysis kinetics having influence on the properties of the synthesized graphene.

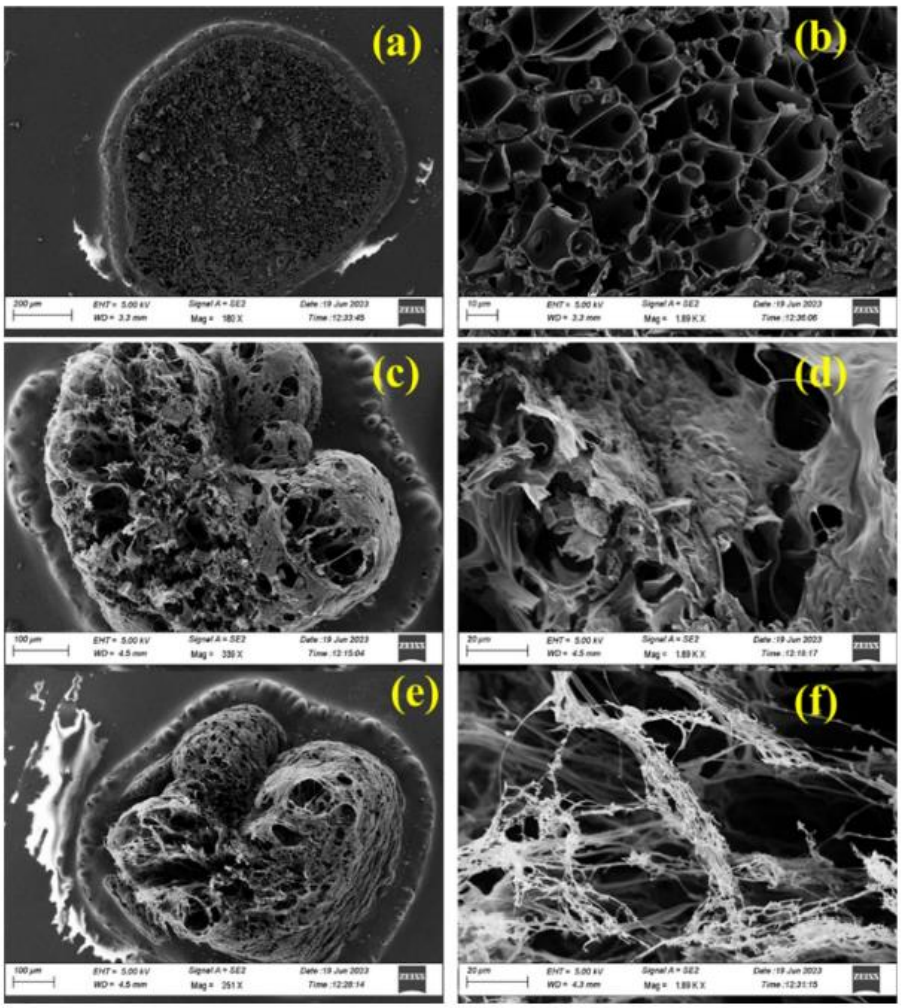

Fig. 4.4 Low and high magnification SEM micrograph shows the dissociation of polyimide into graphene structure at (a, b) 2 ms, (c, d) 2.5 ms, and (e, f) 4 ms, respectively

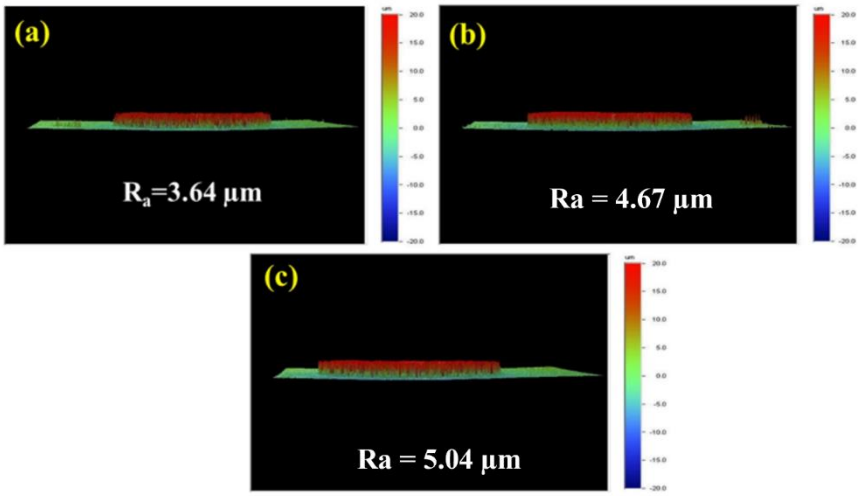

Fig. 4.5 Morphology of fabricated LIG using CO2 at laser interaction time (a) 2 ms, (b) 2.5 ms, (c) 4 ms and d–f surface roughness at (d) 2 ms, (e) 2.5 ms, (f) 4 ms

4.1.3 Raman spectroscopy analysis of irradiated laser spots: Raman spectroscopy, an invaluable non-invasive and non-destructive technique for discerning the composition of materials, plays an equally crucial role in examining the intricate state physics and the resulting defects that emerge. The Raman spectrum of laser interacted polyimide presents two main bands in the range of ~ 1320-1330 cm-1 (D-band) for a laser of excitation wavelength of 633 nm and ~ 1580-1585 cm-1 (G-band). Here, G-band corresponds to the graphitic phase of carbon because of the in-plane stretch of carbon atoms in the tangential direction (E2g mode). The evident D-peaks are associated with the defects along the grain boundaries, edges in the carbon lattice, and vacant sites in the formed structures. The peak corresponds to intervalley scattering. As the laser irradiation time increases, peaks observed at ~ 1610 cm^{-1} due to intra-valley scattering, as shown in Fig. 4.6. Whereas G and 2D bands normally marked for Raman analysis of graphene satisfy the momentum conservation. The presence of D and D′ peaks project the defects representing missing momentum required to conserve the rule of momentum conservation. The D-to-G intensity ratio corresponds to defects formed in graphene lattice as reported in literature and hence the

ratio of intensities is analyzed to quantify the spatial variation of disorder thus observed.

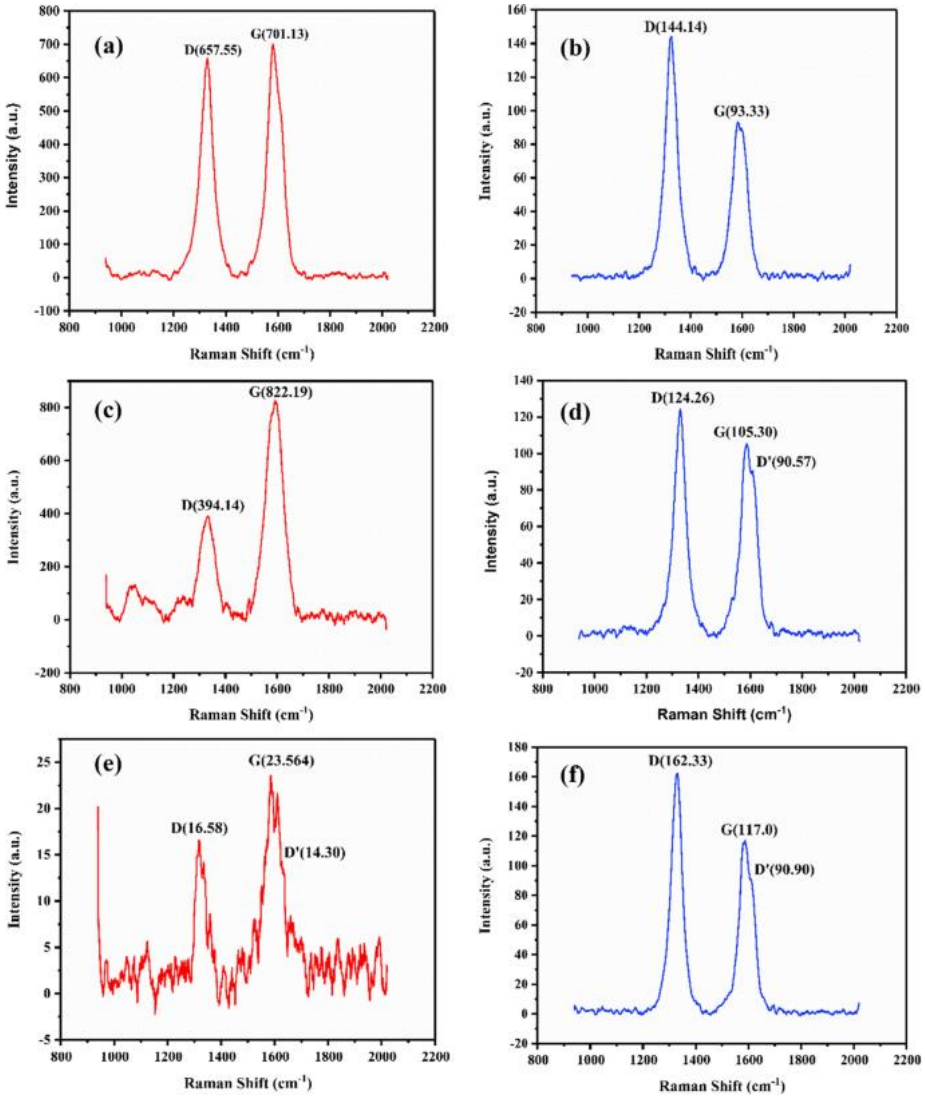

Fig. 4.6: Raman mapping of the LIG and center and circumference of laser spot a, b 2 ms, c, d 2.5 ms, and e, f 4 ms

Laser interaction with polyimide is analyzed at single spot with varying irradiation time and the presence of G and D peak in Raman spectroscopy assures the synthesis of graphene using laser source commonly termed as laser-induced graphene (LIG). Due to Gaussian beam profile of the laser that results in non-uniformity in crystallinity, defect density, as well as spatial non-uniformity of synthesized graphene. Raman Mapping is performed in terms of point across the spot diameter of ~ 567 µm at ten specific positions with a leap of ~ 50 µm.

The position of point analyzed and mentioned in the study are subjected to a variation of ~ ± 5 µm. Apart from G and D peaks, it is observed that D′ peak is in-evident in case A and B in central region, while it shows show in samples C, due to excessively high laser energy interaction restricting the intra-valley scattering around the K point . The high value of the D peak, when compared with G peak, might be due to localized energy density at specific points. A detailed analysis of the variation of energy intensity in laser spot and its variation in the properties of synthesized graphene is presented to correlate the effect of energy intensity. The study is based on positional or spatial analysis. Moreover, it is observed that an improvement in crystalline nature of synthesized graphene as laser energy density increases. However, the excess energy deteriorates the properties of synthesized graphene, and the strength of the film is poor. This is essentially due to excessively high thermal stresses present over the surface.

4.1.3(a) Defect-to-graphitization ratio and defect density with varying laser irradiation

Fig. 4.7a shows of ID/IG ratio at 50 µm spatial distance from the center. The specific Raman spectroscopy plots for all positions are added in the supplementary manuscript for reference. It is observed that for any laser irradiation time, the value of ID/IG increases from the central region to the edges of the circular spot. The variation is evident at every ~ 50 µm which is essentially due to the non-uniform energy variation. The variation shows gradient in the carbon structural synthesized LIG. However, it is also observed that irradiation time has an influence on the variation of defects formed. As the irradiation time variation is not much between sample A and sample B, the defect-to-graphenization ratio is also not much varied except at the extreme peripheral position. The sudden drop in ratio at the extreme end of sample A might be due to more laser energy available that leads to an ablation of the graphene structure at central region.

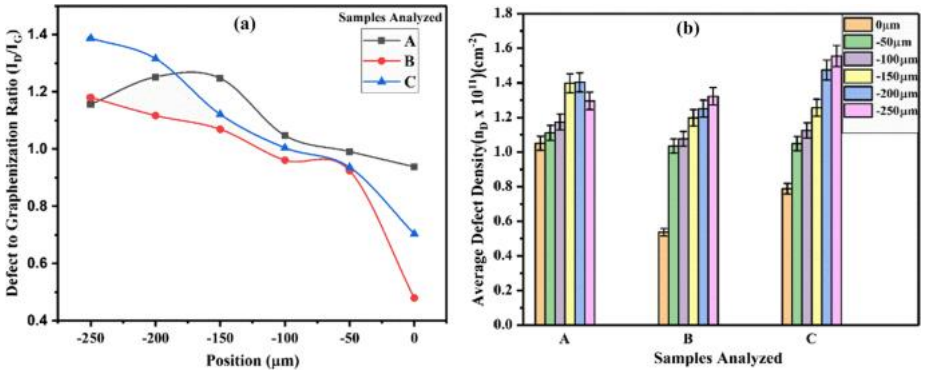

Fig. 4.7: (a) Spatial variation of defect-to-graphenization ratio for varying laser irradiations and (b) average spatial defect density with interval of 50 μm from center at different samples.

For the applications requiring precise control over their electronic and sophisticated geometric control as electrochemical sensors, the understanding of variation of defect density will help fine tune the heterogeneous rate of transfer of electrons for graphene. The presence of defects in graphene leads to scattering of carriers, thereby diminishing conductivity. However, an optimal density of defects serves as active sites for reactions and adsorption, particularly in electro-chemical reactions for fabrication of electronic devices. Defect density (n_D) is calculated using Eq. 1. Fig. 4.7 b shows the defect density (n_D) of the samples based on varied irradiation time. It is observed that sample C shows maximum defect density because of the high temperature induced by the laser source. The defect density of sample A and B shows less significant variation due to the small temperature difference between both the samples:

$$\boldsymbol{n_D(cm)^{-2}} = \left(\frac{(1{\cdot}8{\pm}0.5){\times}10^{22}}{\lambda_L^4}\right) \times \left(\frac{I_D}{I_G}\right) \qquad \textbf{(1)}$$

4.1.3(b) Evaluation of the influence of crystallite size with varying laser irradiation with respect to varying positions

The graphene amorphization trajectory was reported in detail by Ferrari et al. and observed that the presence of defects in sp2 lattice transforms the graphite to tetrahedral amorphous carbon. It is, however, an acceptable study in literature that defects essentially have a positive

impact towards developing electrochemical sensing and charge mobility properties. The average in-plane crystallite size (La) represents the distance between two neighbouring defects for a sp2 crystalline structure. Cançado et al. detailed Tuinstra and Koenig findings and formulated the relation between La and defect-to-graphitization ratio, which is mentioned in Eq. 2. The relation also included the wavelength used for Raman mapping. In our analysis 633 nm wavelength was used and its corresponding energy is 1.96 eV. The final correlation of La with

ID/IG is represented in Eq. 3 where IG and ID correspond to intensity of G- and D-peaks and Eλ represents the laser excitation energy (in eV).

$$L_a(nm) = \frac{560}{E_\lambda^4} \times \frac{I_G}{I_D} \quad (2)$$

$$\frac{I_D}{I_G} = \frac{37 \cdot 945}{L_a(nm)} \quad (3)$$

Fig. 4.8 shows effect of irradiation time on the average in-plane crystallite size with spatial shift of 50 μm from center to the edge. The observed phenomenon can potentially be attributed to the Gaussian beam profile, which inhibits the sp2 crystalline structure conversion. Consequently, as the study is transitioned from center to the edge of synthesized graphene dot structure, an observable amorphous properties rise is evident. Comparing the effect of laser irradiation on the spatial variation of samples with properties averaged out, it is observed that there is an increase in average in plane crystallite size from 34.5 ± 5 nm to 43.5 ± 17 nm in samples A and B, respectively. However, the crystallize size decreases to 37 ± 9 nm in sample C. This might be because the temperature rises very high compared with the crystallization temperature thus causing the bonds of material to break leading to vaporization of the carbon atom from the surface.

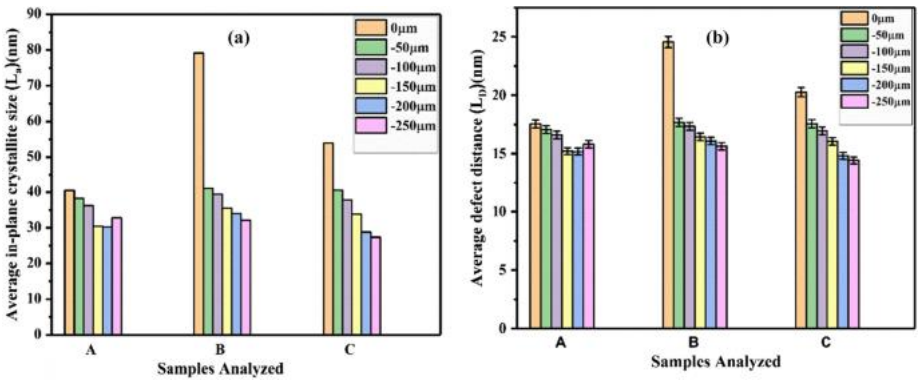

Fig. 4.8: Spatial variation of (a) average in plane crystallite size (L_a) and (b) of average defect distance (L_D) for varying laser irradiations

An increase in the density of defects shall decrease the average travel distance between optical scattering and at a critical value of ~ 3.5 nm, the nano-crystalline graphene might transform to sp3 carbon of amorphous nature. At higher irradiation time the chances of this happening might not be that high as interacting temperature in that case shall be very high and the polyimide surface might not sustain the energy induced as is observed in higher pulse overlap percentages at higher energy interactions. The spatial variation in synthesized graphene across the spot suggests that a better understanding of the carbon gradient due to non-uniform energy will always add up in the optimum utilization of laser energy towards graphene synthesis. The charge mobility and structural uniformity in fabricating processes focus on low-defect density when average distance between defects, LD ≥ 10 nm. The relation that follows is based on the condition that D band scattering area is directly proportional to points defects (eq. 4); therefore

$$(I_D/I_G)^{0.5} \alpha\ 1/L_D \quad (4)$$

The I_D/I_G relation with average defect distance (L_D) for laser excitation wavelength-dependent (λ_L) (in the visible range) as shown in equation (5)

$$L_D^2(nm)^2 = (1 \cdot 8 \pm 0 \cdot 5) \times 10^{-9} \lambda_L^4 \times \left(\frac{I_G}{I_D}\right) \quad (5)$$

From the past study, it is reported that the critical value for activation of graphene maintaining its sp2 network is ~ 2.1 nm. The average defect distance below 2.1 nm would destroy the structural uniformity of fabricated graphene. The average distance between defects is observed to increase from 16.24 ± 0.98 to 17.85 ± 3.3 nm, whereas as laser energy further increases the average value drops to 16.68 ± 2.12 nm suggesting that further enhancement in laser energy would reduce structural uniformity. The presence of these point defects proves to be essentially beneficial in augmenting the characteristics of synthesized graphene, particularly in the realms of electro-chemical and electronic applications.

4.2 Detailed investigation of processing parameters for large area direct laser writing

LIG is generally particulate-filled heterogeneous material in its compositional characteristics. It requires a critical threshold energy interaction of laser with polyimide to carbonize and transform it into porous LIG. The basic principle of preparing graphene by the laser heat source is the photothermal effect of laser irradiation on the surface of polyimide. As laser fluence and pulse laser overlap varies, the unit energy density changes in a particular region. This leads to temperature change over the specific causing carbonization of polyimide. The degree of carbonization affects the morphology, sheet resistance, crystallinity as well as defect density of the LIG as discussed in detail.

4.2.1 Numerical Simulation Results: Fig. 4.9 (a), (b), and (c) shows the spatial distribution of temperature just after the 3rd pulse with 70% spatial overlap between two successive laser spots with 46 J/cm^2, 56 J/cm^2, and 66 J/cm^2, respectively. The maximum observed temperature is 2575 K, 2790 K, and 3052 K for the laser fluences 46 J/cm^2, 56 J/cm^2, and 66 J/cm^2, respectively. It is observed that, at a given laser fluence, there is a sharp rise in the temperature in a very short period, after which it gradually drops down for the remaining irradiation duration. This existing unique feature attributes to the extremely high heat flux which

is almost impossible with conventional heating methods. The theoretically simulated temperature ranges show overestimated due to the following reasons: 1) the porosity of the carbonized material is neglected, porosity can produce scattering of the laser source and give rise to a lesser coupling of the laser energy; 2) the evaporative flux loss is neglected, during the laser-material interaction, a small amount of material can get ablated, and it will take away a certain amount of heat energy.

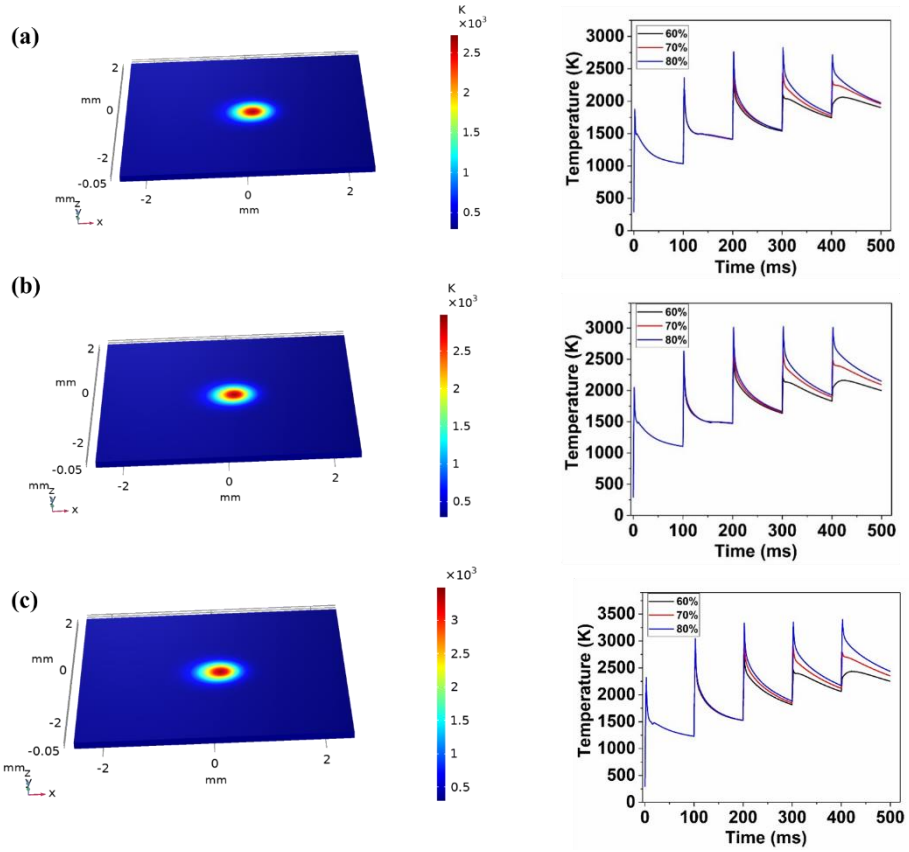

Fig. 4.9: Spatial distribution of temperature with 70% spatial overlap between successive laser spots with laser fluence of (a) 46 J/cm² (b) 56 J/cm² (c) 66 J/cm², and temporal variation of temperature for 5 pulse irradiations with varying overlap with laser fluences (d) 46 J/cm², (e)56 J/cm² , and (f) 66 J/cm²

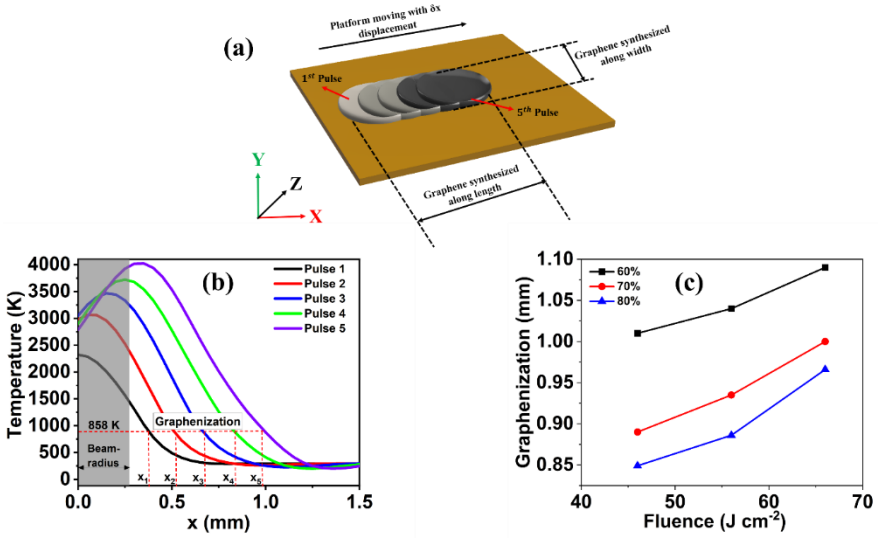

Fig. 4.10 (a) Schematic representation of five pulse overlap, (b) spatial variation of temperature along the scanning direction for 5 pulse irradiations at 66 J/cm^2 of laser fluence, and (c) length of graphene formation as a function of laser fluence for varying overlaps

Fig. 4.9 (d)-(f) shows the time-dependent variation of temperature with varying overlap for the three laser fluences. It is evident that the effective number of pulses irradiating the spot area influences the sample heating. The effective number of pulses for 60%, 70%, and 80% overlap are 2.5, 3.3, and 5 respectively. For a spatial overlap of 60%, the maximum temperature is observed to show a negligible increase after the 2nd pulse. Similarly, with 70% overlap the maximum temperature is observed for the 3rd pulse and with 80% overlap it is observed for the 4th/5th pulse.

Fig. 4.10 (a) shows the schematic representation of 5 pulses overlap-based laser scanning. Fig. 4.10 (b) shows the variation of temperature along the scanning direction in the case of 66 J/cm^2 with 5 laser pulse irradiations at a 10 Hz repetition rate. The grey-coloured square in Fig. 4.10 (b) represents the beam radius of the first laser pulse. It is reported that the pyrolysis will initiate at 858 K and with an assumption of graphene formation at this temperature, the maximum length of graphene formation along the scanning line is estimated as shown in Fig. 4.10 (c). Similarly, the length of graphenization is estimated for the 3 laser fluences with varying overlap and depicted in Fig. 4.10 (c). It is

evident that with an increase in laser fluence the length of graphene formation is increasing. A lesser overlap of 60% is presenting more graphenization due to the maximum displacement of the moving laser pulse. It is, however, to be noted that graphene synthesized is porous and with further increase in pulse overlap the quality of graphene becomes finer due to an increase in heat density for graphenization as evident in experimental results. Hence, the selection of optimum fluence and pulse overlaps control the quality of graphene formation through LIG.

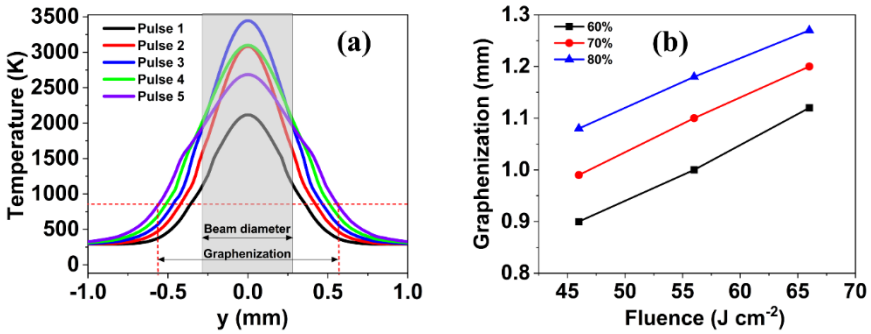

Fig. 4.11: (a) Spatial variation of temperature in the lateral direction and (b) width of grapheme formation

Fig. 4.11 (a) shows the spatial distribution of temperature along the lateral direction in the case of 66 J cm^{-2} with 5 laser pulse irradiations at 10 Hz repetition rate. The width of graphene formed is increasing with an increase in the number of laser pulses. The maximum width is achieved after the 5^{th} pulse and the width is estimated for three laser fluences for three overlaps as depicted in Fig. 4.11 (b). The width of graphene shows an ascending trend with an increase in laser fluence. Also, for a particular laser fluence, the width is increasing with an increase in the spatial overlap between laser pulses. This is due to the fact with the increase in overlap the number of pulses irradiating spot area is increasing.

4.2.2 Morphology & Composition Analysis

It is observed that due to a combination of laser fluence (J cm^{-2}) and laser spot overlap, the LIG formed shows uniform morphology with hills and grooves due to linear scanning of the laser as shown in Fig. 4.12 (a). SEM image shows porous structures where porosities are created by the

gases excelling out due to byproduct of recombination of heteroatoms as observed in Fig. 4.12 (d). As laser intensity over the surface increases, morphology starts converting from porous to fibrous clusters around the overlapping domains that lead to structural changes as well as secondary carbonization of LIG in Fig. 4.12 (e). It is worth noting that most of the region is still porous at a laser fluence of 66 J/cm^2 and 70% pulse overlap in Fig. 4.12 (e). Moreover, the pores are larger as compared with 60% laser pulse overlaps for the same fluence as shown in Fig. 4.12 (d). This shows that the morphology is controlled by laser fluence and pulse overlap. With the increase in overlap percentage, fibrous cluster material extends throughout the surface and transforms from porous to fibrous graphene. This leads to more robust and very tight contact carbon units synthesized as shown in Fig. 4.12 (f). Interestingly it is observed that the fibrous graphene shows more conductive than porous graphene due to the high contact region with the probe electrode.

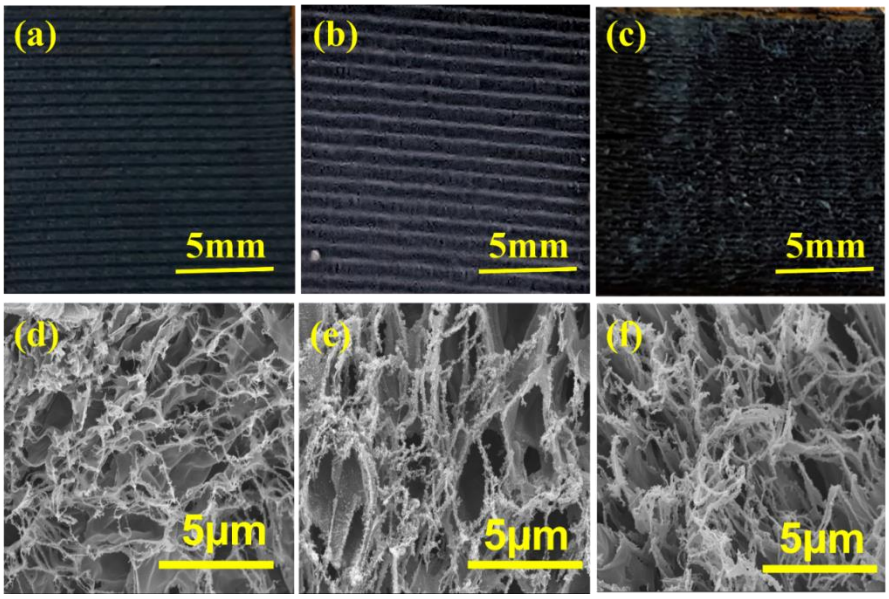

Fig. 4.12: Fabrication of LIG raster patterns on the polyimide surface at 66 J/cm^2 with pulse overlap (a) 60%, (b) 70%, (c) 80% (d-f) respective SEM image shows from porous to fibrous structure at (d) 60%, (e) 70%, and (f) 80%

Fig. 4.13(a-c) shows that EDX results at laser fluence 66 J cm^{-2} with 60, 70, and 80 overlap %. It can be observed that the percentage of carbon increases with increases in overlap % of laser pulse.

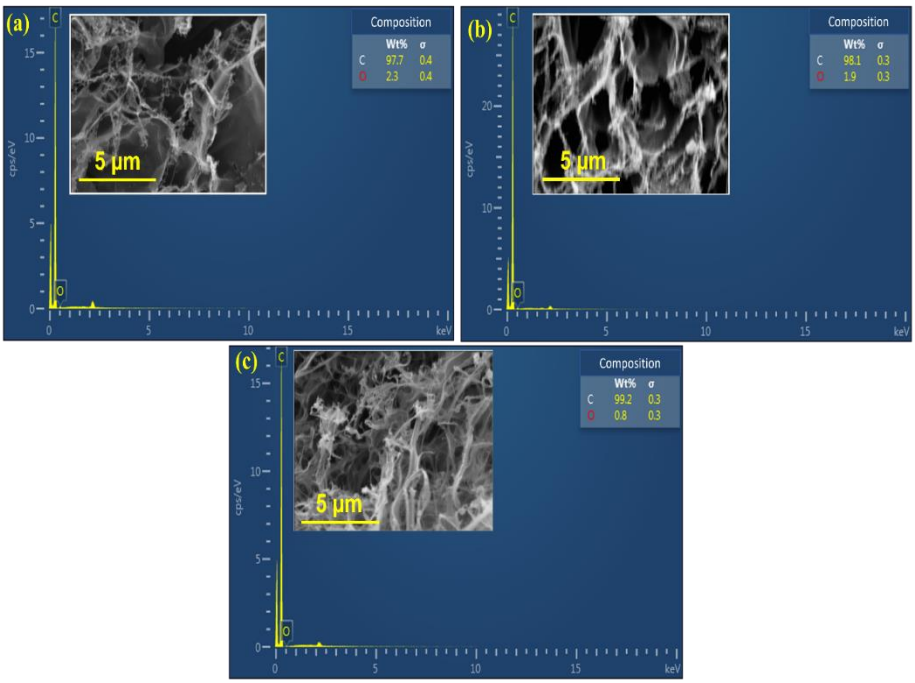

Fig. 4.13: EDX results of LIG raster patterns at laser fluence 66 J cm^{-2} with (a) 60% overlap, (b) 70% overlap, and (c) 80% overlap. The inset shows the respective morphology.

4.2.3 Room Temperature Conductivity Analysis*:* The dependence of sheet resistance R (Ω/sq.) and its corresponding Resistivity(Ω-m) of LIG on laser fluence and laser pulse overlap is investigated using a four-probe setup. A DC power supply is applied through the outer probes to induce a voltage across inner probes. By measuring the voltage drop, the sheet resistance is calculated using eq. 6

$$\boldsymbol{R = \frac{\pi}{ln2} \times \left(\frac{\Delta V}{I}\right)} \qquad \textit{(6)}$$

where ΔV is the voltage drop across inner probes, and I is the current applied across the outer probes.

The measured sheet resistance is used to calculate the resistivity of the LIG using resistivity(ρ)=(R*A)/L. Fig. 4.14 shows the resistivity with overlap percentage at laser fluence 46, 56, 66 J cm^{-2}. It is observed that the resistivity is smallest in the case of 66 J cm^{-2}. This might be due to the fibrous nature of graphene bundles that excelled out and drifted showing more contact with electrodes during the sheet resistance measurement. Moreover, the overlap percentages affect the graphenization of the polyimide which shows less resistivity of the LIG at 80 % overlap. Also, the fibrous nature of graphene leads to a sharp dip in the contact resistance at 66 J cm^{-2} with 80 %.

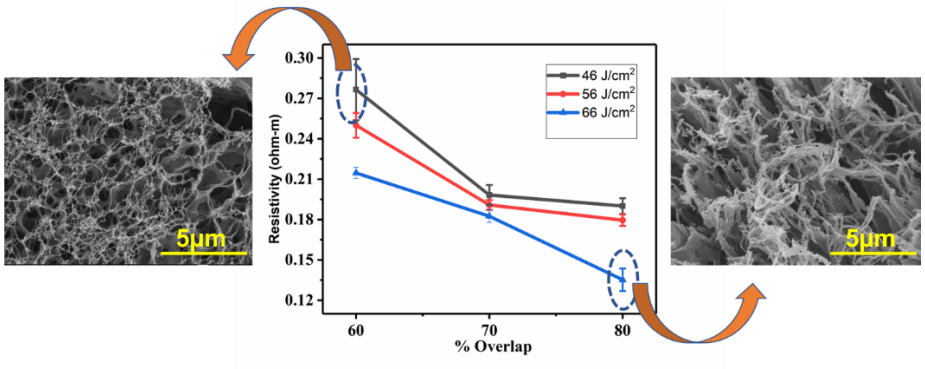

Fig. 4.14: Variation of resistivity with varying pulse overlaps for varying Fluences. SEM images at 5000x

4.2.4 Structural Analysis: The XRD patterns of fabricated LIG with varying overlaps at a laser fluence of 66 J cm^{-2} is shown in Fig. 4.15. The prominent peaks at 2θ = 26° that corresponds to the (002) plane show the presence of LIG. Further, interlayer spacing is calculated by Bragg Formula i.e., nλ= 2dsinθ (λ=1.54 Å corresponds to the wavelength of X-ray), θ =13° corresponds to n=1 i.e., to first-order diffraction. The calculated interspacing is 3.54 Å shows a high degree of graphenization. In the case of 70% and 80% pulse overlap, it is observed that the peak at 26° is more evident when compared with 60% pulse overlap. The peak is fitted with a normal Gaussian fit to calculate FWHM at 2 thetas corresponding to 26°. It is observed that as pulse overlap increases from 60% to 80%, FWHM reduces from 1.425° to 1.030° suggesting an increase in crystallinity. Also, the peak at ~22° is the peak of polyimide on which graphene is synthesized. There is yet another peak at 2θ= 47° which is not very evident in all cases except for 70% pulse overlap and corresponds to (100) reflections associated with in-plane structures.

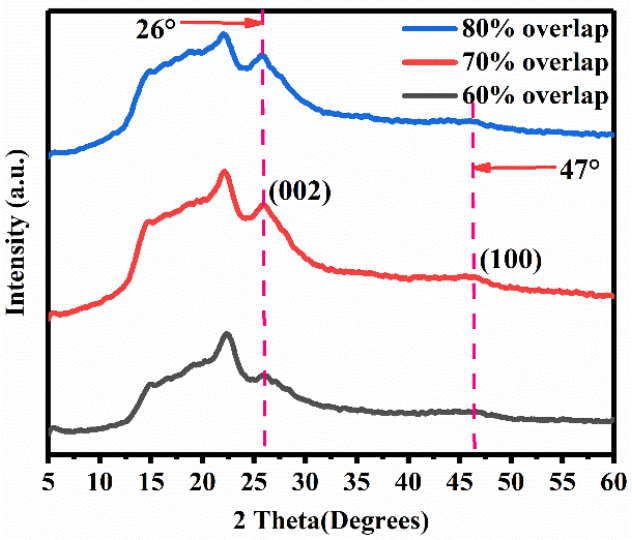

Fig. 4.15: X-ray diffraction (XRD) of LIG synthesized over PI film at a laser fluence of 66 J/cm^2 and varying laser pulse overlap percentage of 60%, 70%, and 80%.

4.2.5 RAMAN SPECTROSCOPY: The Raman spectrum of LIG is known to have two main bands at ~1320 cm^{-1} (D-band) (for 633 nm excitation wavelength laser) and ~1580 cm^{-1} (G-band). G-peak designates graphitic carbon phase arising due to in-plane tangential stretching of carbon atoms (E_{2g} mode), due to the presence of phonons at the center of Brillouin zone. D-peak is evident due to the defects associated with grain boundaries, vacancies, and edges in the lattice of carbon. The disorder associated involves inelastic inter-valley scattering. There are evident D′ peaks at ~1610 cm^{-1} arising due to intra-valley scattering. G and 2D bands are projected to satisfy the momentum conservation whereas D and D′ bands depicting defects project the missing momentum required for the fulfillment of momentum conservation rule. The ratio of the intensity of D to G is proportional to defects formed in the lattice of graphene synthesized hence intensity ratio (I_D/I_G) is studied to quantify disorders in the study. Raman microscopy being a non-destructive and non-invasive spectroscopic technique is used not only to identify material's composition but also to study subtle scale physics, doping levels, and defects. LIG is employed here to study the defects and their corresponding effect on crystallinity and conductivity of synthesized graphene concerning variation in laser pulse overlap. Raman mapping, which amalgamates spatial spectroscopic information in terms of line, area, and point map, is performed for all the samples up to ~5mm at 10 positions with an approximate gap of 0.5 mm. Fig. 4.16 (a) shows a Raman map/image obtained for the sample at 66 J cm^{-2} and 70% laser pulse overlap. It is recorded by taking a line scan along the overlapped area as shown in the inset of Fig.4.16 (a) over ~5 mm. Fig.4.16 (b) shows the Raman spectrum which confirms the D, G, and 2D peaks and hence confirms the formation of LIG. Stacking of Raman plots extracted from the corresponding Raman image provides a better idea of peak positions of D & G at multiple positions across the sample as shown in Fig. 4.16 (c). It is observed that the D peak at various positions hovers around 1320 cm^{-1} with a variation of ±2 cm^{-1} (for 633 nm wavelength) and the G peak is focused around ~1580 cm^{-1}. There are specific D′ peaks at most of the

positions centered around 1610 cm^{-1}. However, D′ peaks are not very evident at a few positions along with the map which might be because of the varying energy interaction due to the Gaussian beam profile of the laser restricting the intra-valley scattering around K point. Fig. 4.16 (d) depicts the calculations of all specific parameters at various positions along the line scan to study the defect analysis which is the basis for discussion in the latter part of the study. By calculation of crystallite size and defect density in different samples, an analysis has been presented to correlate the extent of overlap percentage with the degree of crystallinity of the sample. It is to be noted that based on various positional analyses, a mean value of all calculated parameters is taken for a sample for further study. Along with that, a numerical analysis of structural uniformity has been presented by calculating the I_D/I_G ratio and hence confirming the porous to fibrous structural conversion of LIG.

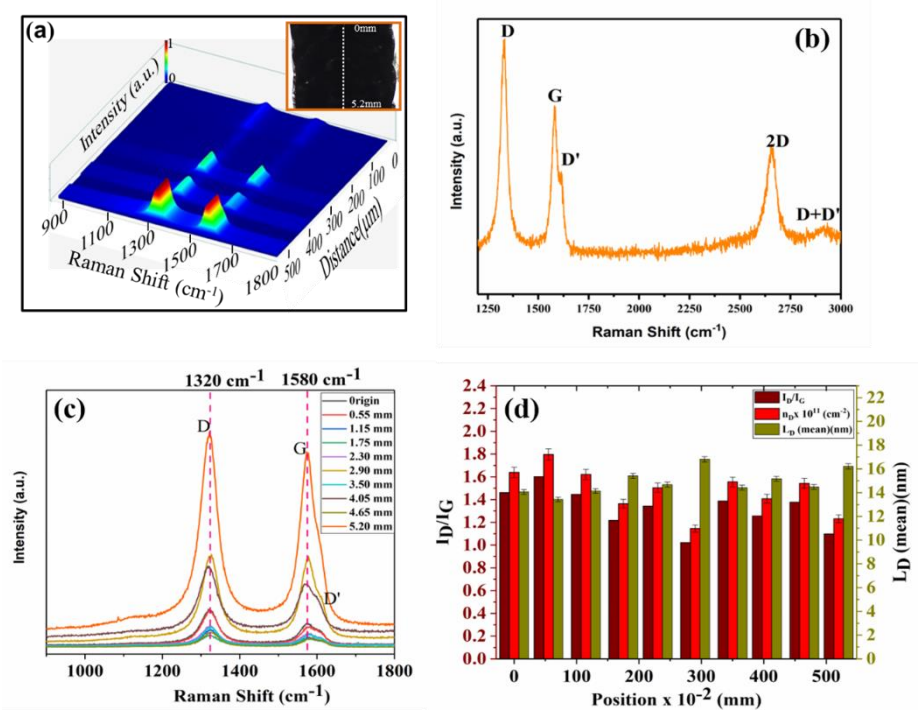

Fig. 4.16: (a) shows an image of Raman mapping obtained for a sample at 66 J/cm² and 70% laser pulse overlap with the right inset showing an optical image of the sample (b) shows the Raman plot projecting all evident peaks at 66 J/cm² and 70% pulse overlap (c) shows the Raman stack plots along the line up to 5 mm at 10 positions

and an interval of ~ 0.5 mm (d) shows the calculations of I_D/I_G, the average distance between defects L_D (mean), and defect density (n_D) at 10 positions across 5 mm line at ~ 0.5 mm position gap.

4.2.5(a) Crystallinity: Ferrari et al. studied the graphene amorphization trajectory for carbon materials in which graphite transforms to tetrahedral amorphous carbon due to defects and disorders present in sp^2 lattice in two different stages. The average in-plane crystallite size (L_a) denotes the preserved length of sp^2 crystalline structure between two neighboring defects. L_a is calculated from Raman spectra using general equation 2. For 633 nm wavelength, it is calculated as 1.96 eV and the final correlation of L_a with I_D/I_G is written in eq. 3

Increasing the defect density reduces the average distance traveled by an electron-hole pair between two Raman scattering events smaller than the distance between two optical scattering events with optical phonon and hence I_D/I_G follows quadratic variation. This usually occurs when L_a reaches a "critical" value ~3.5 nm and is termed the second stage of amorphization trajectory where nano-crystalline graphene transforms to low sp^3 amorphous carbon.

Fig. 4.17(a) reveals that when the overlap percentage increases from 60% to 80% the I_D/I_G ratio reduces from 1.401 ± 0.21 to 1.043± 0.143. Moreover, heat treatment transforms amorphous carbon to sp^2 crystalline structure with increasing crystallite size hence, an increase in the overlap percentage increases the crystallite size (L_a) from 27.732±4 to 37.132 ±6 nm. This in turn leads to more conductivity of the material as shown in the resistivity plot in Fig. 4.14. The above discussion can also be correlated with the XRD plot in Fig. 4.15.

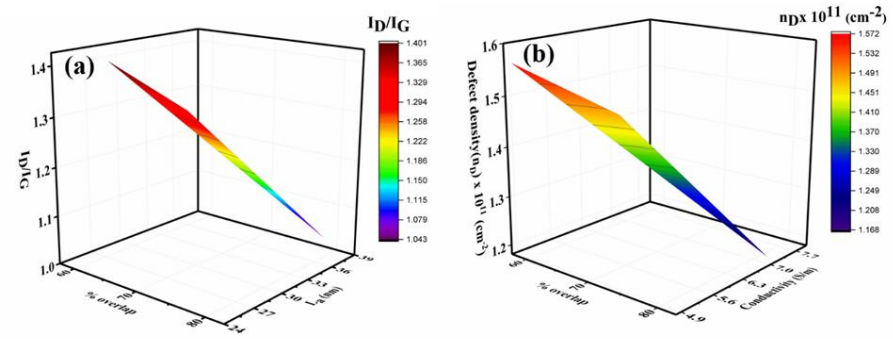

Fig. 4.17: (a) I_D/I_G vs average crystallite size (L_a) for varying pulse overlap (60-80%) at constant laser fluence of 66 J/cm^2. (b) defect density (n_D) vs conductivity (S/m) for varying laser pulse overlap (60-80%) at constant laser fluence of 66 J/cm^2 .

4.2.5(b) Defect Density: Defects in graphene scatter the carriers present in pristine graphene which in turn reduces conductivity. However, an optimum defect density acts as an active site for reaction and adsorption, especially for electrochemical reactions for electronic device fabrication. Fig. 4.16(b) shows the defect density (n_D) and conductivity at laser fluence 66 J cm^{-2} concerning overlap percentage. Defect density (n_D) is calculated using equation 1. It is observed that with the increase in overlap percentage, graphene formed over the surface shows a reduction in defect density from 1.57 x 10^{11}/cm^2 to 1.1696 x 10^{11}/cm^2 due to higher temperature interaction as evident in thermal simulation results. However, the conductivity at the same time shows inverse behaviour from 4.66S/m to 7.4S/m due to the transformation of graphene from porous to fibrous structure inducing more contact points over the surface of the polymer. This implies that optimum balancing of defect sites in LIG always improves the conductivity of synthesized LIG as reported in the literature. It is to be noted that the highest defect density observed by Raman mapping of all samples is still low when compared with fully disordered graphene (defect density ~ 10^{15} /cm^2 approximated as one defect in every four carbon atoms).

4.2.5(c) Structural uniformity: To understand the structural uniformity and mobility in graphene, the study focuses on a low-defect density regime that is based on $L_D \geq 10$ nm. When $L_D \geq 10$ nm, the total area participating in D band scattering is proportional to point defect as followed in equation 4. The I_D/I_G relation with average defect distance (L_D) for laser excitation wavelength-dependent (λ_L) (in the visible range) as shown in equation (5). A value of $L_D \sim 2.1$ nm is a critical value at which all carbon atoms are activated with graphene still maintaining its sp^2 network however any L_D below critical value will structurally destroy the graphene structure. It is observed in the study that for increasing laser pulse overlap, L_D increases from 14.4 ±1 to 16.7 ±1.3 nm with the D-peaks and G-peaks. It suggests an increase in structural uniformity with the expense of a reduction in adhesive property of LIG over polyimide. The availability of point defects can be effective in enhancing the properties of graphene synthesized and hence it can be claimed that synthesis of LIG by varying laser pulse overlap can be helpful in tailored use of electrochemical and electronic applications.

4.2.6. Device Performance: A resistive type of strain sensor is fabricated at 66 J/cm^2 and 70% laser pulse overlap and encapsulated with PDMS, and its performance is measured with repetitive bending loading and relaxation with the frequency of 2 Hz for 1250 number of cycles. The initial resistance of the sensor is 750 ohms and starts increasing with increase in bending angle and reaches 810 ohms for the bending angle of 23°. As the load is applied to the strain sensor, the resistive LIG strain sensor starts bending resulting in an increase in its resistance value. During relaxation the resistance of the sensor returned to its original values. Fig. 4.18(a) shows the fabricated and encapsulated strain sensor with copper wire connection for resistance measurement. The flexibility of the device as observed in Fig. 4.18(b) is more than 60°. Fig.4.18(c) and 4.19 show the bending condition of the sensor in repetitive bending setup and its performance for 1250 cycle stability. At the start of the bending load, the sensor shows high resistance value (>820 ohm) due to sudden catastrophic loading conditions. Furthermore,

the next cycle shows the stability in resistance for incremental change. Moreover, it is also observed that at some point, the resistance values are beyond 820 ohms. This might be due to the thermal stress induced during the graphenization that restricts the flow of charges during that cycle. The gauge factor (G) for the fabricated strain gauge is calculated with a gauge factor of 56 which is similar with the already reported LIG based strain gauges. The obtained value is in line with piezoresistive strain sensors based on graphene sheets having a value between 20 and 200 and are comparable to those of few other works on LIG strain sensors with a GF around 50.

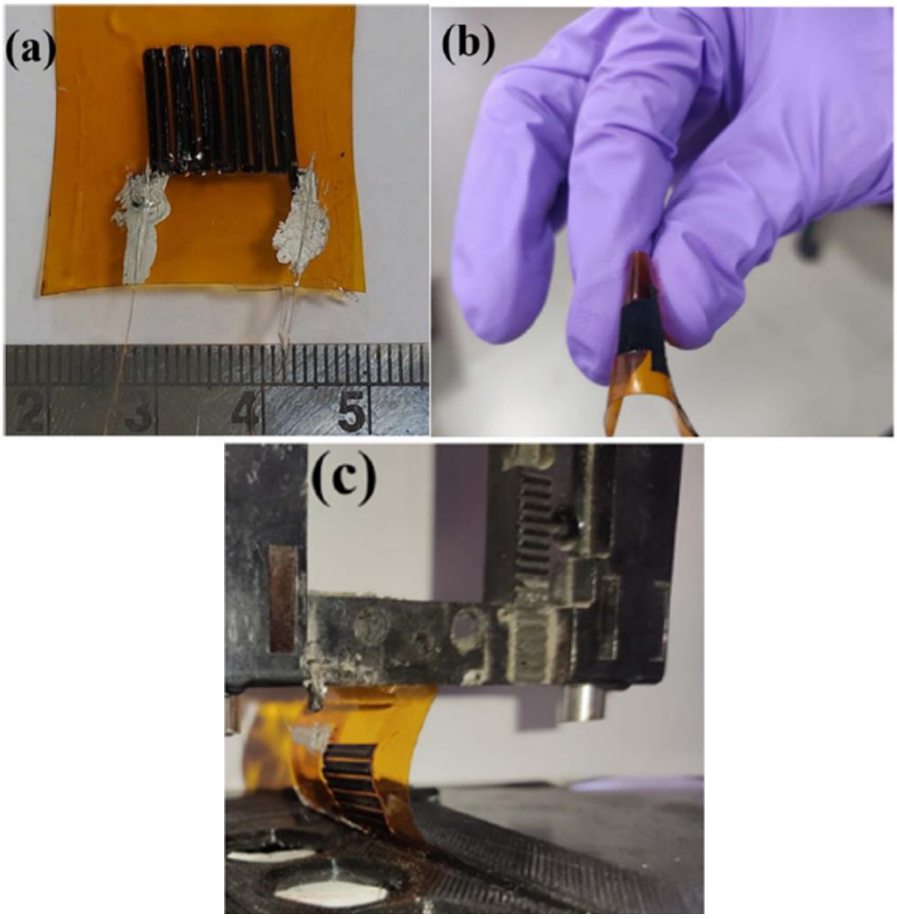

Fig. 4.18. (a) LIG-based resistive type strain sensor (b) intact graphene for the flexible device, (c) strain senor in bending condition, and (d) resistance of the sensor for repetitive bending load for 20◦ for 1250 number of cycles.

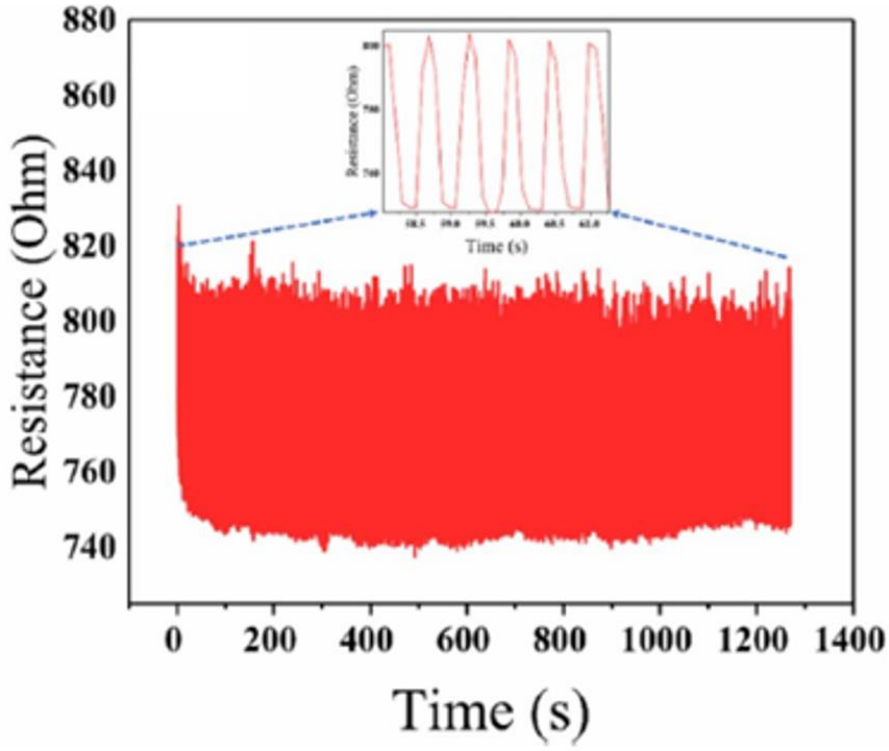

Fig. 4.19. Resistance of the sensor for repetitive bending load for 20◦ for 1250 number of cycles.

4.3 Summary

A detailed exploration of laser interaction with polyimide and its associated variation in the properties of transformed polyimide to laser induced graphene through direct laser writing is explored and its key conclusions are made and mentioned below.

- Laser-induced graphene (LIG) is synthesized from polyimide using a CO_2 laser source through the photothermal effect, causing localized carbonization and structural transformation to graphene.
- Surface temperatures during single-pulse irradiation reach up to 2799.93 °C (sample C), 2077 °C (sample B), and 1913 °C (sample A), depending on irradiation time (2 ms, 2.5 ms, and 4 ms respectively), influencing graphenization depth and quality.
- Thermal profile simulation and FLIR experimental results suggest a strong agreement, with experimental peak

temperatures around 1750–2060 °C, though simulations slightly overestimate due to neglecting evaporation, gas expansion, and porosity effects.

- Surface morphology via SEM imaging shows a progression from flat thin sheets to porous and fibrous graphene with increased irradiation time, due to degassing and pyrolysis-induced bubble formation.
- Surface roughness (Ra) increases with laser exposure: 3.64 µm (2 ms), 4.67 µm (2.5 ms), and 5.04 µm (4 ms), correlating with enhanced porosity and dome formation due to internal gas pressure.
- Raman spectroscopy reveals D and G peaks, with the ID/IG ratio increasing from the center to edges of the laser spot due to Gaussian energy distribution, indicating higher defect density at the periphery.
- Maximum ID/IG ratio and defect density (nD) are observed in sample C (~1.42 and ~6.4×10^{11} cm^{-2}), while samples A and B show lower and comparable defect levels.
- Crystallite size (La) increases from 34.5 ± 5 nm (sample A) to 43.5 ± 17 nm (sample B) but decreases to 37 ± 9 nm in sample C, suggesting over-carbonization at higher energies deteriorates crystallinity.
- Defect distance (LD) initially increases (from 16.24 ± 0.98 nm to 17.85 ± 3.3 nm) but drops slightly (16.68 ± 2.12 nm) at higher fluence, indicating structural non-uniformity due to high energy-induced stress.
- Large-area LIG writing using overlapping pulses shows maximum simulated temperature reaching 3052 K (66 J/cm^2) with 70% overlap, enabling continuous graphene tracks.
- Effective overlap impact: 80% overlap produces the widest and most uniform graphene width and structure, improving lateral and longitudinal graphenization length due to repeated localized heating.

- Morphology changes from porous to fibrous with increasing overlap: 60% overlap forms porous graphene, while 80% overlap yields dense fibrous LIG with enhanced conductivity.
- EDX analysis confirms increasing carbon content with increasing overlap: 82.1% (60%), 85.7% (70%), and 89.2% (80%), indicating improved graphitization.
- Electrical resistivity drops with increasing overlap: from $2.1 \times 10^{-4}\ \Omega\cdot m$ (60%) to $9.8 \times 10^{-5}\ \Omega\cdot m$ (80%) at 66 J/cm² fluence, correlating with fibrous morphology and better contact interface.
- XRD analysis shows sharper graphene (002) peaks with higher overlap (FWHM reduces from 1.425° to 1.030°), and interlayer spacing ~3.54 Å, indicating improved crystallinity.
- Raman mapping across 5 mm line scans confirms lower ID/IG ratios and higher La for higher overlap, showing spatial uniformity and reduced disorder in fibrous LIG structures.
- Crystallite size (La) increases from 27.73 ± 4 nm to 37.13 ± 6 nm as overlap increases from 60% to 80%, while defect density (nD) reduces from 1.57×10^{11} to $1.17 \times 10^{11}\ cm^{-2}$.
- Average defect distance (LD) increases from 14.4 ± 1 nm to 16.7 ± 1.3 nm across overlap variations, confirming improved structural uniformity at higher overlap.
- Device performance of LIG-based strain sensors shows stable resistance variation (750 Ω to ~810 Ω) under cyclic bending (1250 cycles at 2 Hz), with a gauge factor of ~56, validating LIG's flexibility and sensing reliability.

Chapter 5

This chapter describes the investigations of laser processing parameters for micro-3D printing of metals and ceramics over solid and flexible substrates for functional applications.

Laser μ-3D printing of metals and ceramics for functional applications

5.1 Investigation on laser μ -3D printing of low-density aluminum.

Pure aluminum being light and conductive poses greater difficulty in various metal 3D printing processes that are being applied over it. Laser decal transfer-based μ-3D printing presents flexibility towards micron-level controlled printing. However, this would require a greater level of optimization and its effective variation concerning parameters using experimental trials. The same has been discussed in detail in the subsequent sections.

5.1.1 Experimental Results:

The as prepared aluminum coated silicon wafer is placed over holder (donor stage) for its ejection on the acceptor (acceptor stage). To explore the feasibility of material ejection and its localized deposition at the requisite position, it would essentially happen at optimum parameters which were observed in our experimental analysis as well. The influence of distance between laser source and donor substrate, effective energy interaction, laser pulse overlaps and source to substrate distance plays an important role towards micron level printing. A detailed investigation is carried out and is discussed in the subsequent sections.

5.1.1(a) Influence of Stand-off Distance

The laser μ-3D printing process has been extensively studied for materials such as shape memory alloys (e.g., NiTi), which often exhibit consistent ejection characteristics under defocused laser beam conditions due to their high density. However, low-density materials with high conductivity, such as aluminum, require specific optimization

of focusing parameters to achieve effective material ejection and deposition. This section examines the influence of the stand-off distance (SOD) on the distance between the laser source and the donor substrate on the precision and uniformity of material ejection.

Table 5.1: Parameters used for analysing the influence of stand-off distance

S.No.	Rep. rate (Hz)	Duty cycle (%)	SOD (cm)	Source to substrate distance (µm)	Stage speed (mm/min)
A	10	5	9.5	Nil	50
B	10	5	11.5	Nil	50
C	10	5	13.5	Nil	50

The experimental parameters for analysing the influence of SOD are detailed in Table 5.1. All trials utilized a 10.6 µm CO_2 laser, and the duty cycle, repetition rate, and stage speed were held constant to isolate the effect of SOD on material ejection. As shown in the optical micrographs in Fig. 5.1, varying the SOD significantly affects the material ejection and deposition. Fig's 5.1(a) and 5.1(c) depict the donor substrate under defocused laser beam conditions (SOD = 9.5 cm and 13.5 cm, respectively), whereas Fig. 5.1 (b) shows the focused laser beam condition (SOD = 11.5 cm). A focused laser beam enables uniform pixel transfer, as evidenced by the clear and consistent deposition in Fig. 5.1 (b). In contrast, defocused conditions result in uneven pixel deposition and the formation of debris, as seen in Fig's 5.1 (a) and 5.1 (c).

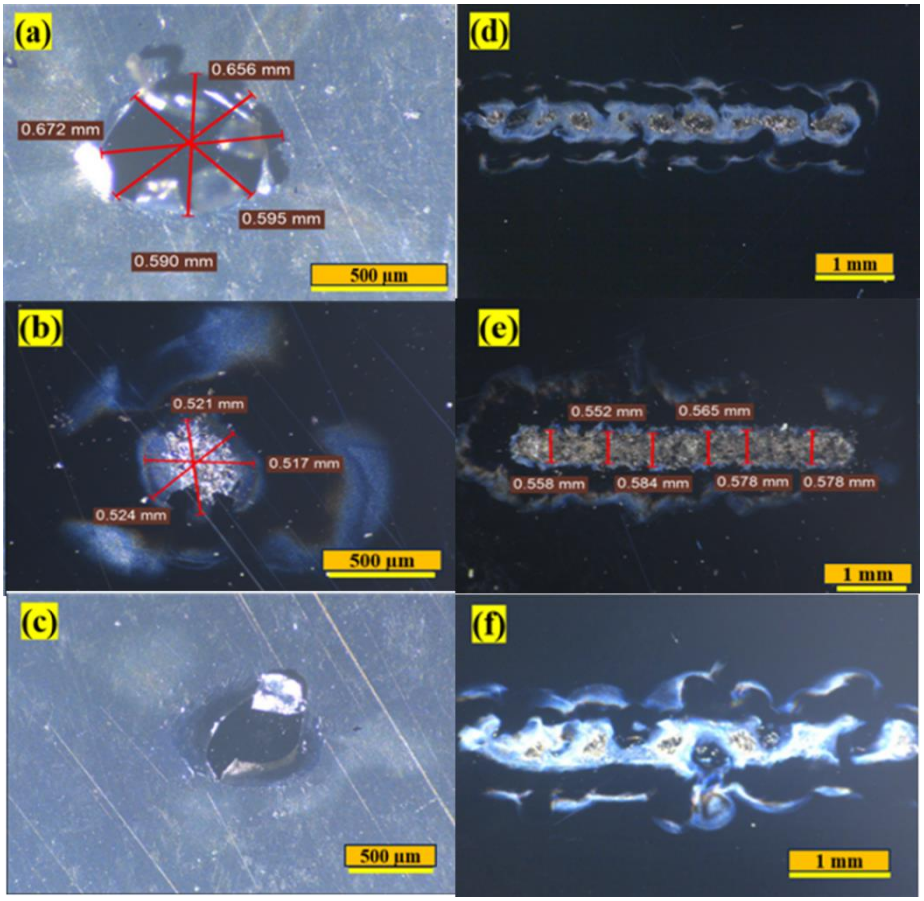

Fig. 5.1: Exploring the influence of stand-off distance on spot as well as line fabrication (a, d) for SOD corresponding to 9.5 cm, (b, e) for SOD corresponding to 11.5 cm, and (c, f) for SOD corresponding to 13.5 cm.

The irregularity observed under defocused conditions is attributed to insufficient gas pressure within the sacrificial layer. When the laser beam is defocused, the adhesive forces between the sacrificial layer and the coated aluminum exceed the thrust forces generated by gas pressure, leading to incomplete or irregular material ejection. At the optimal SOD of 11.5 cm, the thrust force is sufficient to overcome adhesive forces, facilitating precise and uniform pixel transfer.

Fig. 5.2 presents profilometric data comparing the ejected pixel's dimensions on the donor and acceptor substrates. At the focused laser beam position (SOD = 11.5 cm), the ejected pixel exhibits a uniform thickness of approximately 4.7 µm on the donor substrate and 3.5 µm on

the acceptor substrate. The calculated transformation efficiency (η_T) for a single pixel is approximately 74.5%, defined as:

$$\eta_T = \frac{\Delta H}{H_D} \quad (1)$$

Where,

η_T -Transformation efficiency

ΔH - Difference between pixel height of the ejected pixel from donor substrate (H_D) and pixel height of the material transferred on the acceptor substrate (H_A)

H_D - Pixel height of the ejected pixel from donor substrate

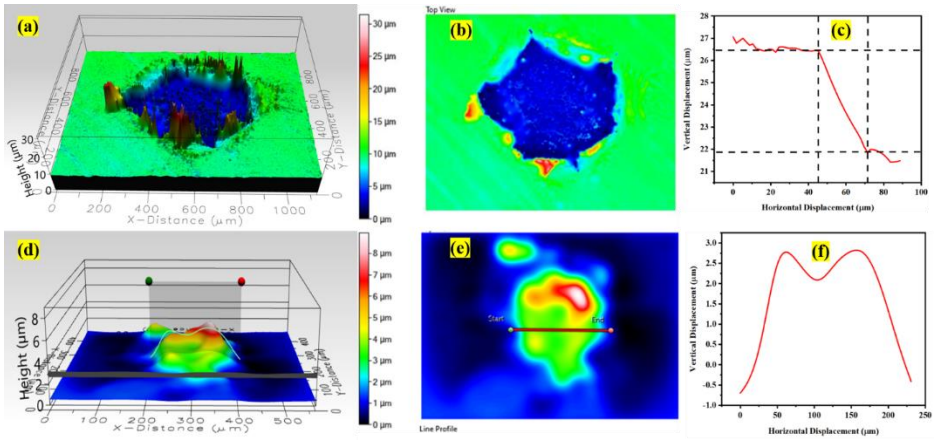

Fig. 5.2: Analysis of material ejection from the donor substrate and its deposition over acceptor state.

The experimental results highlight the critical role of SOD in achieving precise and uniform aluminum ejection during laser µ-3D printing. At an SOD of 11.5 cm, optimal conditions for focused laser beams are achieved, ensuring uniform pixel transfer with minimal debris. These findings emphasize the importance of precise SOD optimization for low-density, high-conductivity materials to enable reliable and efficient micro-3D printing.

5.1.1(b) Influence of Laser Fluence on Aluminum Printing

The hypothesis of heat accumulation and its association towards generating gas pressure for pixelated aluminum ejection would effectively prove its effect at threshold ablation energy. The effective threshold energy would require detailed investigations into the influence of laser fluence towards effective material ejection. The laser fluence, defined as the energy delivered per unit area, plays a critical role in determining the efficiency and quality of material ejection in laser μ-3D printing. For aluminum, a material with high thermal conductivity and low density, achieving the optimal laser fluence is crucial to generate sufficient thermal energy for ablation without causing excessive material damage or splashing. Based on the optimized focal position, the experimental analysis towards varying laser fluence is analyzed.

$$F_L = \frac{P}{R \times \Pi \times d^2} \qquad (2)$$

Where,

F_L = Laser Fluence (J/cm^2)

P = Average laser Power (W)

R = Repetition Rate (Hz)

d = laser spot diameter (mm)

Keeping other parameters such as Repetition rate (Hz), Stand-off distance (cm), donor to acceptor distance (μm) and stage speed (mm/min) constant, the duty cycle (%) is varied and appropriately, the laser power changes which introduces variation in laser fluences. The processing parameters utilized for analysis are mentioned in Table 5.2 below.

Table 5.2: Parameters used for analysing the influence of laser fluence

S.No.	Rep. rate (Hz)	Duty cycle (%)	SOD (cm)	Source to substrate distance (µm)	Stage speed (mm/min)	Laser Fluence (J/cm^2)
A	10	1	11.5	Nil	50	26
B	10	3	11.5	Nil	50	63
C	10	5	11.5	Nil	50	92
D	10	7	11.5	Nil	50	122
E	10	9	11.5	Nil	50	159
F	10	11	11.5	Nil	50	192

The influence of laser fluence on aluminum printing is observed to follow a threshold behaviour. At low fluences (e.g., 26 J/cm²), the energy delivered to the substrate is insufficient to generate the necessary gas pressure within the sacrificial layer. This results in incomplete or irregular material ejection due to the adhesive forces between the aluminum layer and the substrate surpassing the thrust forces. The ejection is weak, and deposition is inconsistent, leading to non-uniform pixel formation on the acceptor substrate. This is corroborated in track widths on both the donor and acceptor substrates are minimal.

As the laser fluence increases to an intermediate range (e.g., 63 to 92 J/cm²), the energy absorbed by the sacrificial layer generates sufficient thermal gradients, causing localized expansion and vaporization of the PDMS layer. This results in controlled thrust forces capable of overcoming adhesion and facilitating uniform aluminum ejection. At this range, both the ejection and deposition processes exhibit high uniformity, with consistent track widths and heights observed across the

substrates. Profilometric analysis confirms the optimal deposition characteristics, with a pixel thickness of approximately 4.8 μm on the donor substrate and 3.6 μm on the acceptor substrate at 92 J/cm². This corresponds to a transformation efficiency (η_T) of nearly 75%.

Beyond this optimal range, at fluences exceeding 122 J/cm², excessive energy delivery leads to rapid expansion and splashing of the aluminum material. The excessive thrust forces result in uneven deposition and material losses, as observed in Fig. 5.3. The Gaussian beam profile of the laser further exacerbates this issue, with high-intensity regions causing localized overheating and non-uniform ejection patterns. Consequently, the track widths on both donor and acceptor substrates begin to decline, accompanied by reduced deposition uniformity. While keeping the stage speed constant and at focused laser beam condition, an aluminum track is ejected out from the donor substrate and at varying laser power thus causing variation in laser fluences.

The observed track width of the material ejected from the donor substrate is higher than the acceptor substrate for all cases (see Fig. 5.3). This might essentially be due to the gaussian beam profile of the laser source that presents sufficient energy near the center and the energy diminishes at the end. The obtained track widths over the donor and acceptor substrate are plotted as observed in Fig. 5.5a. Conventionally, the track width of the acceptor substrate increases as laser fluence increases essentially due to an increase in laser divergence which is observed in the experimental analysis up to 92 J/cm^2 (Fig. 5.3 and Fig. 5.5a). The associated laser divergence generates thrust that forms plume which grows and spreads over the acceptor substrate, however, as the laser fluence further increases, there is a dropping trend in track width, and it keeps on decreasing with further increase in laser fluence. It is because of the excessive thrust force generated in the PDMS layer which ejects the material at a faster velocity thus allowing a part of material to settle down in track and remaining material to splash off. The tendency keeps on growing as the laser energy is increased thus causing reduced track width and more material splashing. It is not just restricted to track

width only but also to the uniformity with which the material is ejected and its deposition thickness over the acceptor substrate as is observed from the profilometric analysis.

Fig. 5.4 represents the 3D surface profilometric analysis of the donor and acceptor material processed at varying parameters as discussed above. While the donor (represented by subscript 1 in all cases) presents aluminum ejection from the coated donor substrate, successful transfer is observed over the acceptor substrate (represented by subscript 2 in all cases). The average height of ejection and transfer is taken into consideration and the graph is plotted as observed in Fig. 5.5b. The obtained outcomes suggest that as the laser fluence increases the material ejection from donor substrate keeps on increasing which is even bound to happen considering the laser energy that would hit the substrate causing higher material ejection. At intermediate fluences, the ejected material exhibits uniform thickness and deposition, forming well-defined tracks on the acceptor substrate. However, at low and high fluences, the deposition is irregular, with uneven height distributions and track widths. The data highlights the importance of operating within an optimal fluence range to balance energy delivery and material transfer efficiency.

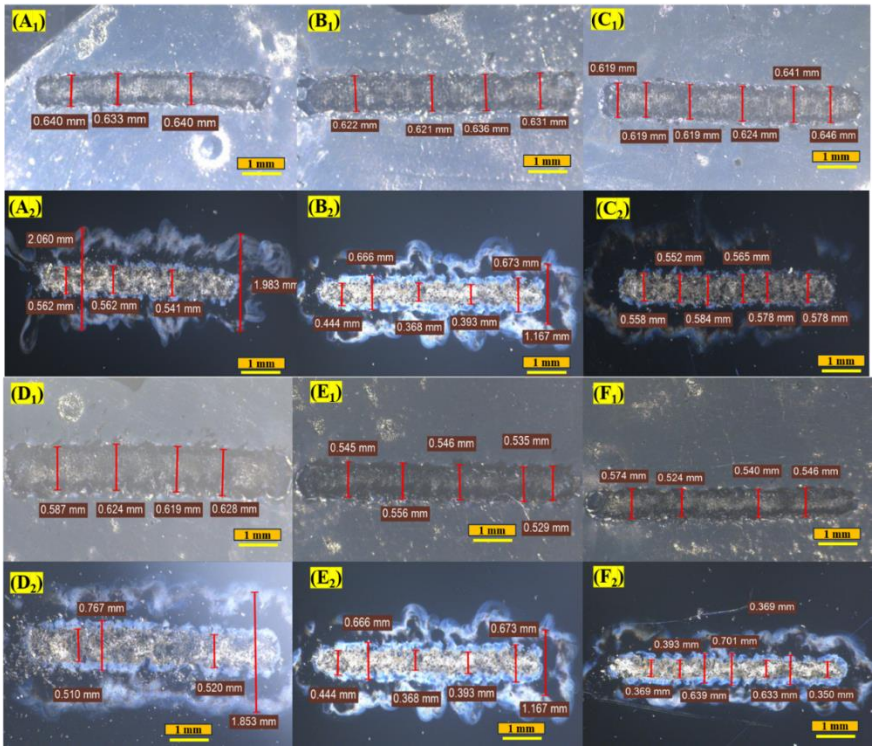

Fig. 5.3: Track ejection at varying laser fluences as per table 2 where subscript 1 and 2 represents donor substrate and acceptor substrate respectively.

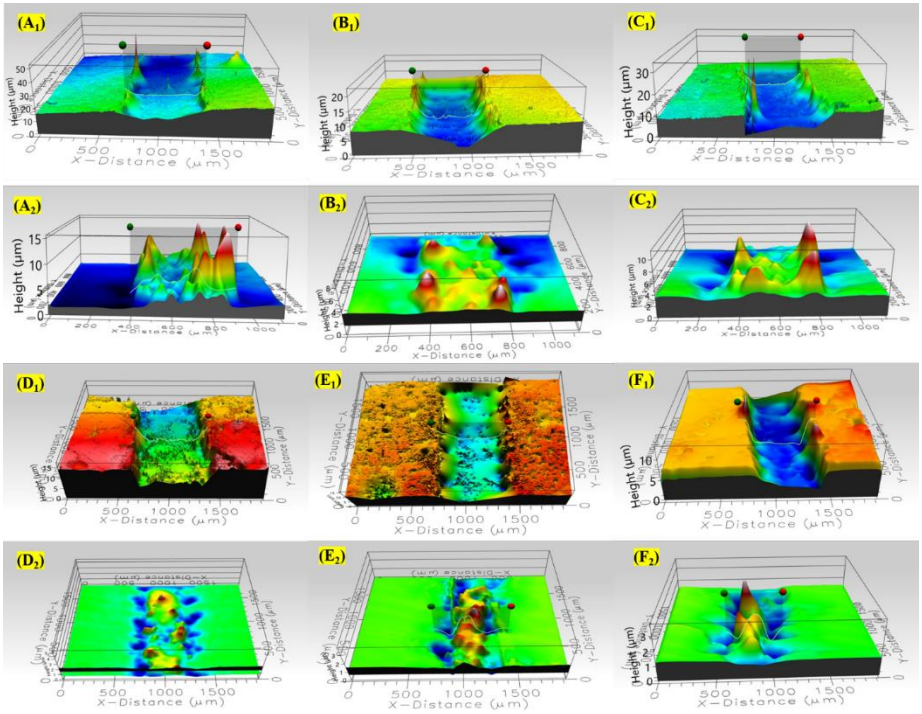

Fig. 5.4: surface profilometric analysis reading the influence of laser fluence towards the material ejection (Subscript 1 represents donor substrate whereas Subscript 2 represents acceptor substrate)

The experimental results demonstrate that laser fluence significantly affects the quality of aluminum ejection and deposition in µ-3D printing. Intermediate fluences, particularly around 92 J/cm², offer the best balance between energy input and material transfer efficiency. These findings emphasize the need for precise energy control and parameter optimization in laser-based additive manufacturing processes to achieve

consistent and reliable outcomes for low-density, high-conductivity materials like aluminium.

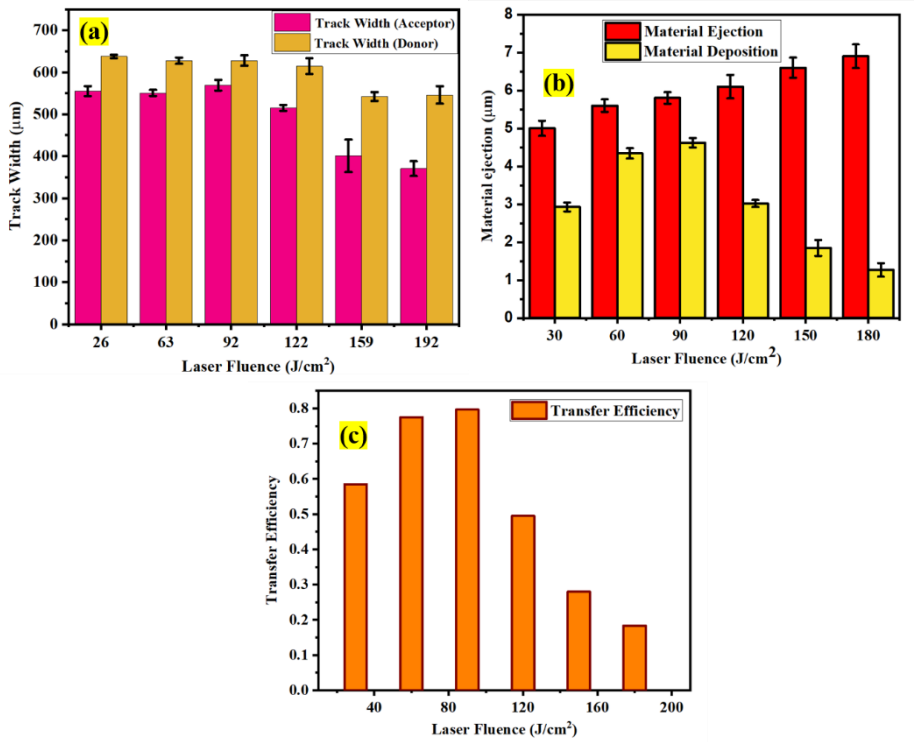

Fig. 5.5: 3D profilometric analysis concerning varying laser fluences

5.1.1(c) Influence of Laser Pulse Overlap on Aluminum Printing

S.No.	Rep. rate (Hz)	Duty cycle (%)	SOD (cm)	Source to substrate distance (µm)	Stage speed (mm/min)	% overlap
A	10	5	11.5	Nil	145	50
B	10	5	11.5	Nil	125	60
C	10	5	11.5	Nil	100	70
D	10	5	11.5	Nil	70	80
E	10	5	11.5	Nil	50	85
F	10	5	11.5	Nil	30	90

Table 5.3: Parameters used for analyzing the influence of laser fluence

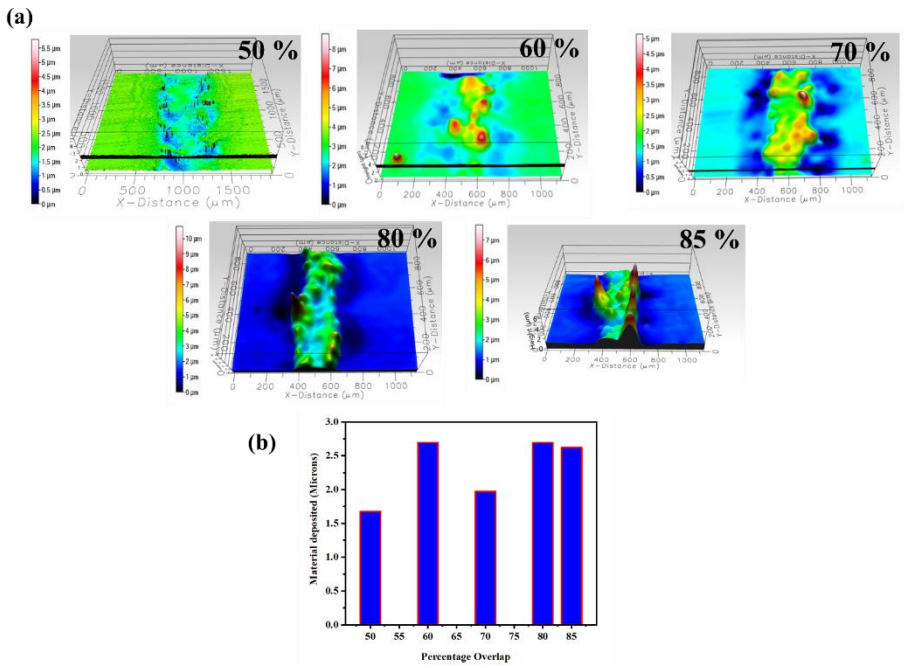

Fig. 5.6: 3D profilometric analysis concerning varying laser pulse overlaps

The influence of laser pulse overlaps on aluminum printing is analyzed in detail keeping the other Processing parameters constant as mentioned in table 5.3 and carrying the stage speed appropriately based on the empirical formula.

$$\% \text{ Overlap} = (1 - V/(D*F)) \quad (3)$$

Where,

V=velocity of stage
D= spot diameter
F=Frequency/repetition rate

The experimental setup maintains a constant repetition rate of 10 Hz, a duty cycle of 5%, and an SOD of 11.5 cm, while the stage speed varies between 30 mm/min and 145 mm/min to achieve different percentages of overlap, ranging from 50% to 90%. As laser pulse overlaps increases, the energy input per unit area changes, affecting the surface morphology, material removal rate, and overall printing quality. Fig.

5.6(a) presents 3D profilometric analyses of the ejected aluminum from the donor substrate at varying pulse overlaps (50%, 60%, 70%, 80%, and 85%). The surface topography indicates significant variations in the material ejection thickness and its associated feature formation based on overlap percentage. At 50% overlap, the surface is although uniform, the ejection thickness is very less suggesting that the energy accumulated due to pulse overlaps is not sufficient material ejection. However, as the overlap increases to 60% and 70%, the ejection of material is improved and is uniform due to high-energy regions becoming evident, signifying increased laser energy interaction causing associated gas pressure in the sacrificial layer for material ejection. This improvement is further observed in 80% and 85% overlap conditions with more uniform and improved ejection thickness however as the pulse overlap increases beyond 80%, extreme energy accumulation in specific domains have presented burning on the samples as well as non-uniform material ejection due to sacrificial layer's inability to hold such high pressure and thus causing laser interaction with coated aluminum causing melting and vaporization of material than its transfer using decal transfer. demonstrate excessive material removal, potentially leading to irregular surface morphology and unwanted thermal effects such as heat accumulation and melting. Thus, the optimum pulse overlap with ejection is uniform and follows the ejection principle is observed at 80% and is hence taken for further analysis.

5.1.2 Design of experiments for aluminum printing based on pilot experiments.

Experimental design begins with defining parameters and their respective levels, a stage known as parameter design. Next, an experimental table is created, outlining the testing procedures and the number of experimental repetitions. Depending on time and cost constraints, either a complete or fractional factorial design is chosen for each optimization process. Statistical techniques such as main effect plots, interaction charts, and ANOVA analysis offer insights within the

chosen designs. However, the effectiveness of these designs in the context of optimizing laser micro-3D printing processes remains unexplored in engineering applications.

The Box-Behnken design (BBD) is employed to explore the experimental design in this study. The most used BBD experimental array was L15, which includes fifteen experiments and three repetitions of the centre point. Typically, BBD uses only the midpoints of the edges and the centre point, meaning it consists of twelve edge points and one center point. With the center point repeated three times, this results in a total of fifteen experiments. Based on the pilot experiments performed to analyze the effects of various processing towards material ejection from donor and its transfer over acceptor for efficient micron level printing, a BBD experimental array was designed as mentioned in Table 5.4 and Table 5.5.

Processing Parameter	**Unit**	**Level 1**	**Level 2**	**Level 3**
Laser Fluence (X)	**(J/cm^2)**	60	90	120
Stand-off distance (Y)	**(cm)**	10.5	11.5	12.5
Pulse overlap(Z)	**(%)**	80	85	90

Table 5.4: Parametric design matrix showing the three-factor, three-level input variables: laser fluence (X), stand-off distance (Y), and pulse overlap (Z) selected for laser-based micro-3D printing, used in L15 experimental design

S.No.	Laser Fluence (J/cm^2)	SOD (cm)	Pulse overlap (%)	Track Width (µm)	Track height (µm)
1	60	10.5	85	562	4.592
2	120	10.5	85	557	4.482
3	60	12.5	85	533	4.321
4	120	12.5	85	540	4.612
5	60	11.5	80	574	4.210
6	120	11.5	80	553	4.460
7	60	11.5	90	559	4.100
8	120	11.5	90	591	4.346
9	90	10.5	80	548.5	4.165
10	90	12.5	80	563.4	4.316
11	90	10.5	90	569.5	4.398
12	90	12.5	90	540.5	4.050
13	90	11.5	85	560.9	4.620
14	90	11.5	85	562.5	4.680
15	90	11.5	85	566.2	4.590

Table 5.5: L15 orthogonal array with measured output values for track width and track height under varying combinations of laser fluence, stand-off distance, and pulse overlap.

5.1.2(a) Mathematical Modelling equations based on Box-Behnken Design

Based on the optimum design outcomes comprising the effect of laser fluence, stand-off distance and laser pulse overlap, the experiments were carried out to analyze the obtained track width and track height relation. The quadratic regression model is a multi-parameter equation that follows linear, quadratic and cross products. Here, the equation obtained from the design presented response surface methodology (RSM) that follows is

$$\mathbf{Y = b_0 + \sum b_i x_i + \sum b_{ij} x_i x_j + \sum b_{ii} x_i^2 \pm e} \quad \mathbf{(4)}$$

Where Y is the response, x_i is the independent variables (here laser fluence, stand-off distance and %age overlap), b is the constant vale and e corresponds to error.

A detailed investigation towards ANOVA and its associated empirical formula is then generated using MINITAB software which is analyzed for its accuracy of fit based on P-value and F ratio. The associated outcomes of the same are discussed in the subsequent sections.

5.1.2(b) Track width analysis

A second-order regression model was developed using response surface methodology (RSM) to capture the influence of laser fluence (X), stand-off distance (Y), and pulse overlap (Z) on the resulting track width.

$$\mathbf{Track\ width\ (\mu m) = 562.390 + 1.303X - 7.548Y + 2.631Z - 0.772X^2 - 13.334Y^2 + 8.112Z^2 + 1.794XY + 12.955XZ - 10.963YZ} \quad \mathbf{(5)}$$

Where X corresponds to laser fluence, Y corresponds to stand off distance and Z corresponds to %age overlap

Source	DF	Adj. SS	Adj. MS	F-Value	P-Value
Regression	9	2656.90	295.211	221.65	0.000

Linear					
X	1	13.58	13.582	10.20	0.024
Y	1	455.81	455.809	342.23	0.000
Z	1	55.39	55.388	41.59	0.001
Square					
X*X	1	2.20	2.199	1.65	0.255
Y*Y	1	656.50	656.501	492.91	0.000
Z*Z	1	242.96	242.956	182.42	0.000
2-Way Interaction					
X*Y	1	12.87	12.874	9.67	0.027
X*Z	1	671.33	671.328	504.05	0.000
Y*Z	1	480.71	480.706	360.92	0.000
Error	5	6.66	1.332		
Lack of fit	3	4.54	1.512	1.42	0.438
Pure Error	2	2.12	1.062		
Total	14	2663.56			
			S		**1.15407**
			R-sq		**99.75%**
			R-sq (adj)		**99.30%**
			R-sq (pred)		**97.10%**

Table 5.6: ANOVA table and second-order regression equation for track width showing the significance of main, square, and interaction

terms. The model demonstrates high statistical reliability with R^2 = 99.75%.

The equation obtained-Track Width (µm) = 562.390 + 1.303X – 7.548Y + 2.631Z – 0.772X^2 – 13.334Y^2 + 8.112Z^2 + 1.794XY + 12.955XZ – 10.963YZ-includes linear, quadratic, and interaction terms that allow a detailed understanding of the parametric effects. The ANOVA results confirm that the model is statistically significant, with an F-value of 221.65 and a p-value less than 0.000. Among the linear terms, stand-off distance (Y) showed the strongest influence (F = 342.23, p = 0.000), followed by pulse overlap (Z) and laser fluence (X). Quadratic terms for Y^2 and Z^2, along with interaction terms XZ *and* YZ, also demonstrated highly significant effects with F-values exceeding 180. These findings indicate that curvature and interaction effects are dominant in defining track width behaviour. The model showed excellent reliability, with R^2 = 99.75%, adjusted R^2 = 99.30%, and predicted R^2 = 97.10%, confirming its accuracy and predictive strength.

Contour Plot	Surface plot
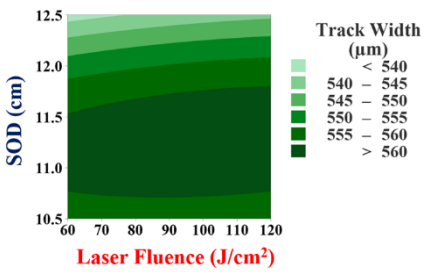	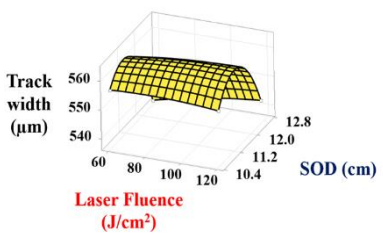
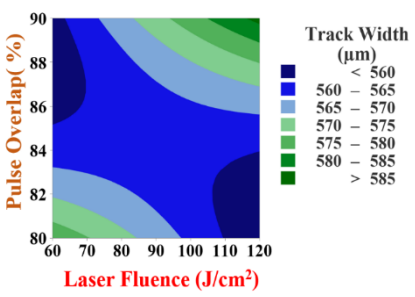	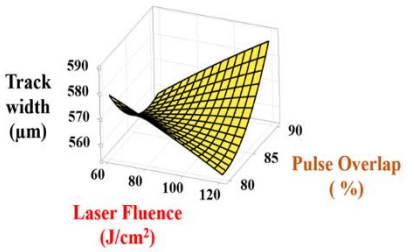

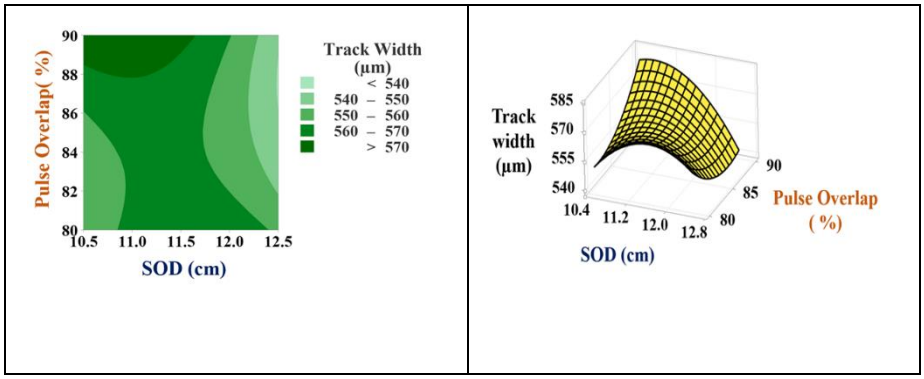

Fig.5.7: Contour and surface plots showing the effect of process parameters on track width: (i) Laser fluence vs. Stand-off distance, (ii) Laser fluence vs. Pulse overlap, and (iii) Stand-off distance vs. Pulse overlap. Optimal track width occurs near moderate fluence (90 J/cm²), SOD (~11.5 cm), and overlap (85-90%).

The contour and 3D surface plots as shown in fig. 5.7 provide visual insights into how the track width varies with changing input parameters:

- Laser Fluence vs. Stand-off Distance: The contour plot shows that lower stand-off distances combined with moderate to high laser fluence yield wider tracks. The corresponding 3D surface plot (top row, right) confirms that track width increases with decreasing SOD, indicating enhanced energy concentration near the focus zone. However, excessively high fluence at low SOD begins to saturate the width response.
- Laser Fluence vs. Pulse Overlap: It is observed that increasing pulse overlap leads to a gradual widening of the track, especially when combined with moderate fluence values (around 90 J/cm²). This behaviour is attributed to enhanced thermal accumulation and overlapping energy zones, which improve material flow and spread.
- Stand-off Distance vs. Pulse Overlap: The plots show that the combination of moderate SOD (~11.5 cm) and higher pulse overlap (85-90%) results in the most uniform and wider tracks. Extremely high overlaps or increased SOD reduce the track width, likely due to reduced effective fluence and beam divergence.

These plots collectively reveal that optimal track width can be achieved at moderate laser fluence, 11.5 cm SOD, and 85-90% overlap, which balance energy input and spot resolution effectively.

To validate the adequacy of the regression model, residual plots were analyzed as seen in fig. 5.8. The normal probability plot exhibited a near-linear distribution of residuals, confirming that the errors follow a normal distribution. The residuals versus fits plot displayed a random spread, suggesting homoscedasticity or constant variance across the prediction range. The histogram of residuals was symmetric and centered around zero, supporting the normality assumption. Furthermore, the residuals versus observation order plot showed no visible pattern, confirming independence of errors across experimental runs. These residual diagnostics support that the regression model is robust, unbiased, and well-suited for predictive analysis. Overall, the analysis establishes a clear and statistically valid relationship between laser parameters and track width, enabling controlled optimization of feature resolution in micro-3D printing.

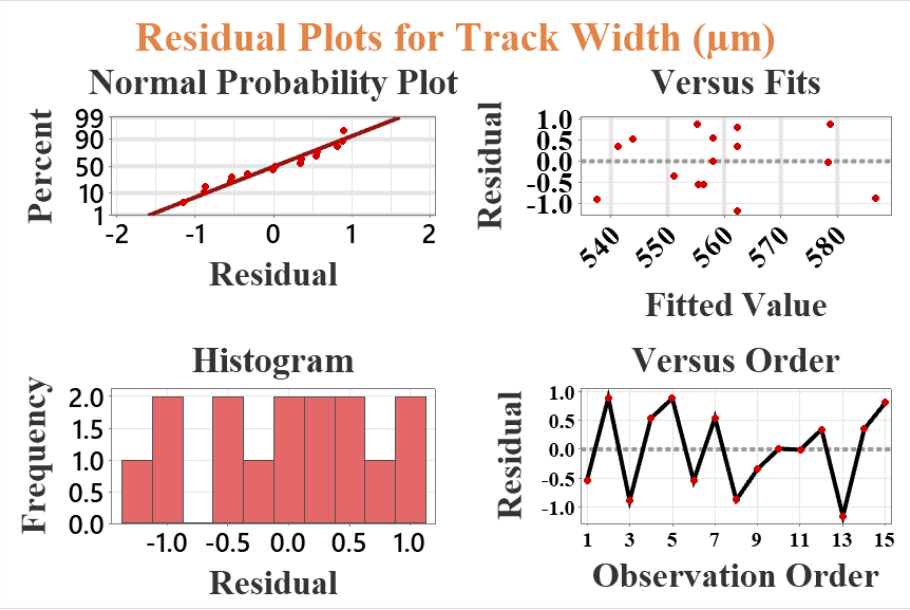

Fig.5.8: Residual plots for track width confirming the model adequacy: (a) normal probability plot, (b) residuals vs. fits, (c) histogram of residuals, and (d) residuals vs. observation order-all validating the statistical assumptions of normality, homoscedasticity, and independence.

5.1.2(c) Track Height analysis

In addition to track width, track height is a critical output parameter in laser-assisted micro-3D printing as it directly governs the vertical resolution and layer stacking fidelity. To model the relationship between process parameters and the resulting track height, a second-order polynomial regression model was developed based on the experimental dataset. The predictive equation obtained is:

$$\textbf{Track height } (\mu m) = 4.63667 + 0.07625X - 0.02125Y - 0.03250Z - 0.05708X^2 - 0.06208Y^2 - 0.31958Z^2 + 0.09250XY + 0.02000XZ - 0.08000YZ \quad (6)$$

Here, X, Y, and Z denote laser fluence (J/cm²), stand-off distance (cm), and pulse overlap (%), respectively. The equation accounts for linear effects, second-order (quadratic) curvature, and two-way interactions among the parameters as observed in figure 5.9 and 5.10. From the equation, it is evident that laser fluence positively influences height in the linear term, but this effect begins to saturate as shown by the negative coefficient of the quadratic term **(**$-0.05708X^2$**).** Similarly, the track height decreases at higher SOD and overlap values individually but gains from coupled effects between parameters are seen in the interaction terms **(**XY and YZ**).** The statistical strength of the model was validated via ANOVA as observed in table 5.7, which returned an overall F-value of 269.68 and $p < 0.000$**,** confirming the model's significance at 99% confidence. Among the linear parameters, laser fluence ($F = 93.72$) and stand-off distance ($F = 223.26$) were highly influential, while pulse overlap ($F = 17.34$, $p = 0.009$) had a moderate but significant effect. Interestingly, the square of the pulse overlap **(**Z^2**)** emerged as the most dominant term **(**$F = 1810.12$, $p < 0.000$**),** indicating that beyond an optimal overlap threshold, additional energy input may lead to remelting, spreading, or even material ejection, thereby reducing the net height. The interaction between laser fluence and stand-off distance (XY) and stand-off distance and pulse overlap (YZ) were also

statistically significant, underscoring the interdependency of spatial and thermal energy distribution in governing vertical buildup.

The coefficient of determination **(**R^2 = 99.79%**)** implies that the model accounts for nearly all variability in the experimental data. The adjusted R^2 (99.42%) and predicted R^2 (96.89%) are also in close agreement, confirming the model's predictive reliability and generalizability. A low standard deviation **(**S = 0.0144**)** and low pure error indicate minimal variation in replicated trials, affirming experimental consistency. The contour and 3D surface plots further illustrate how the input parameters affect the resulting track height. In the laser fluence vs. stand-off distance interaction plot, it is observed that track height increases with higher fluence and lower SOD. This behavior can be attributed to enhanced energy coupling at closer distances, which enables greater melt pool formation and vertical growth. However, if fluence exceeds the threshold at low SOD, it may induce material splashing or degradation. In the laser fluence vs. pulse overlap plots, the peak track heights occur at mid-to-high overlaps (85-90%) and moderate fluence, suggesting optimal thermal accumulation that promotes deposition without excessive remelting. The stand-off distance vs. pulse overlap plots reveal that the maximum height is achieved at an intermediate SOD (~11.5 cm) and high overlap, likely due to balanced laser fluence density and pulse superposition at this configuration.

Residual plots were analyzed to validate the model's statistical assumptions. The normal probability plot exhibited a near-linear alignment of residuals along the diagonal, indicating that the residuals follow a normal distribution. The residuals vs. fitted values plot displayed random scattering around zero, which confirms homoscedasticity or equal variance. The histogram of residuals showed a symmetric, bell-shaped curve, reinforcing the normality assumption. Additionally, the residuals vs. observation order plot confirmed the independence of errors across experimental runs, as there was no observable trend or autocorrelation.

The track height model accurately captures the complex interdependence between laser fluence, stand-off distance, and pulse overlap. It reveals that vertical feature formation is optimized under conditions of high fluence (~120 J/cm²)**,** intermediate stand-off distance (~11.5 cm), and pulse overlap in the range of 85-90%**.** This behavior is primarily driven by efficient energy localization and effective melt pool dynamics, which are crucial for achieving consistent layer stacking and dimensional precision in micro-3D printed structures. The model provides a predictive tool to guide future process tuning for optimal vertical resolution.

Source	DF	Adj. SS	Adj. MS	F-Value	P-Value
Regression	9	0.505652	0.056184	269.68	0.000
Linear					
X	1	0.058575	0.019525	93.72	0.000
Y	1	0.046512	0.046512	223.26	0.000
Z	1	0.003613	0.003613	17.34	0.009
Square					
X*X	1	0.012031	0.012031	57.75	0.001
Y*Y	1	0.014231	0.014231	68.31	0.000
Z*Z	1	0.377108	0.377108	1810.12	0.000
2-Way Interaction					
X*Y	1	0.034225	0.034225	164.28	0.000
X*Z	1	0.001600	0.001600	7.68	0.039
Y*Z	1	0.025600	0.025600	122.88	0.000
Error	5	0.001042	0.000208		
Lack of fit	3	0.000975	0.000325	9.75	0.094
Pure Error	2	0.000067	0.000033		
Total	14	0.506693			
			S		**0.0144338**
			R-sq		**99.79%**
			R-sq (adj)		**99.42%**
			R-sq(pred)		**96.89%**

Table 5.7: Regression model and ANOVA summary for track height analysis showing statistically significant contributions of linear, square, and interaction terms.

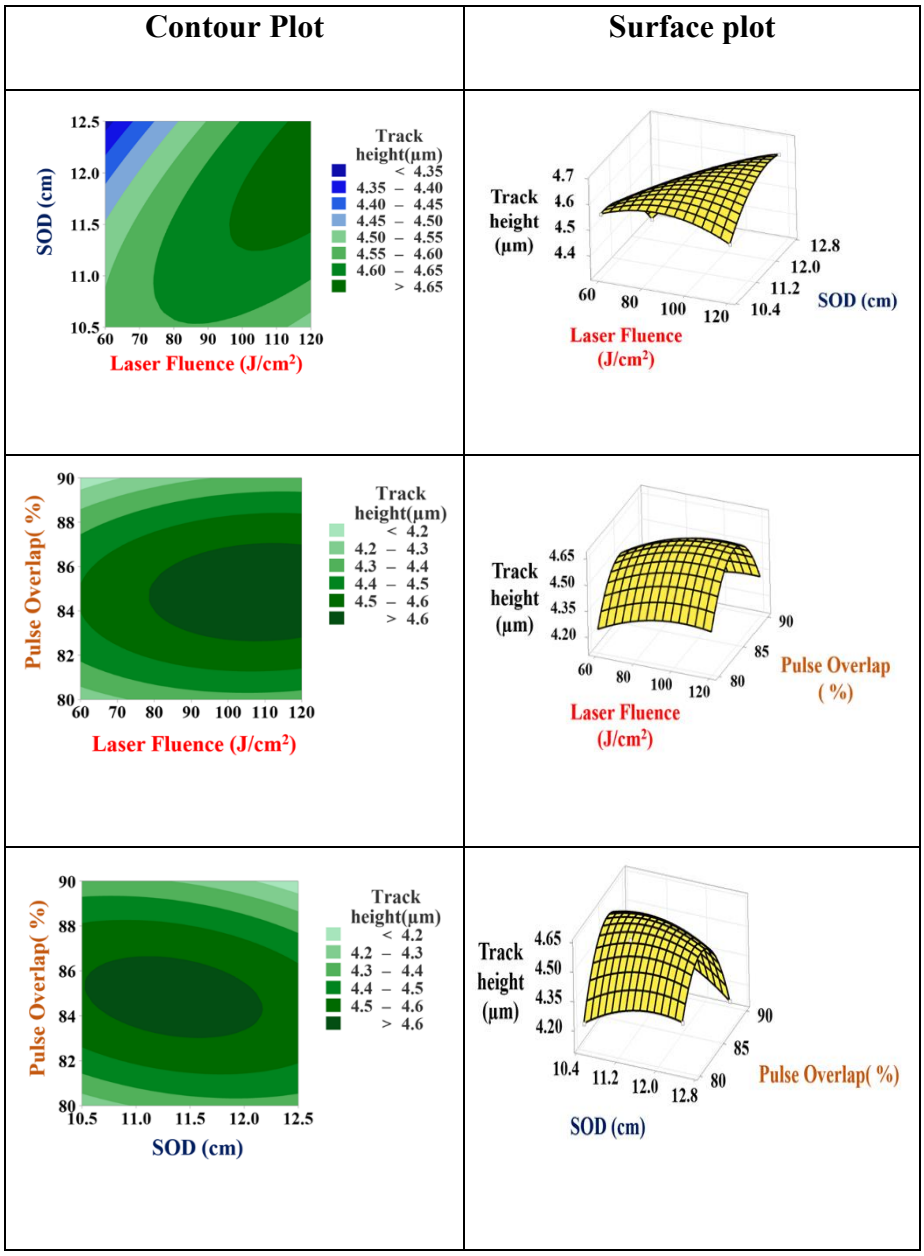

Fig.5.9: Contour and 3D surface plots representing the effect of process parameters on track height: (top row) Laser Fluence vs. Stand-off Distance, (middle row) Laser Fluence vs. Pulse Overlap, and (bottom row) Stand-off Distance vs. Pulse Overlap.

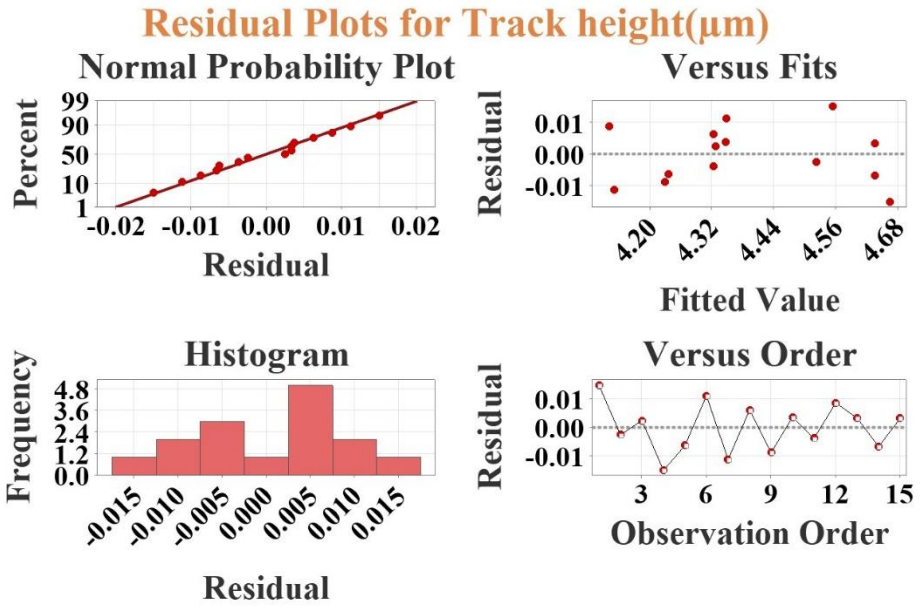

Fig. 5.10. Residual plots for track height analysis validating model adequacy: (a) Normal probability plot confirms normal distribution of residuals, (b) Residuals vs. fits verifies homoscedasticity, (c) Histogram shows symmetric residual distribution, and (d) Residuals vs. observation order confirms independence across trials.

5.1.3 Overall optimization for optimum outcomes

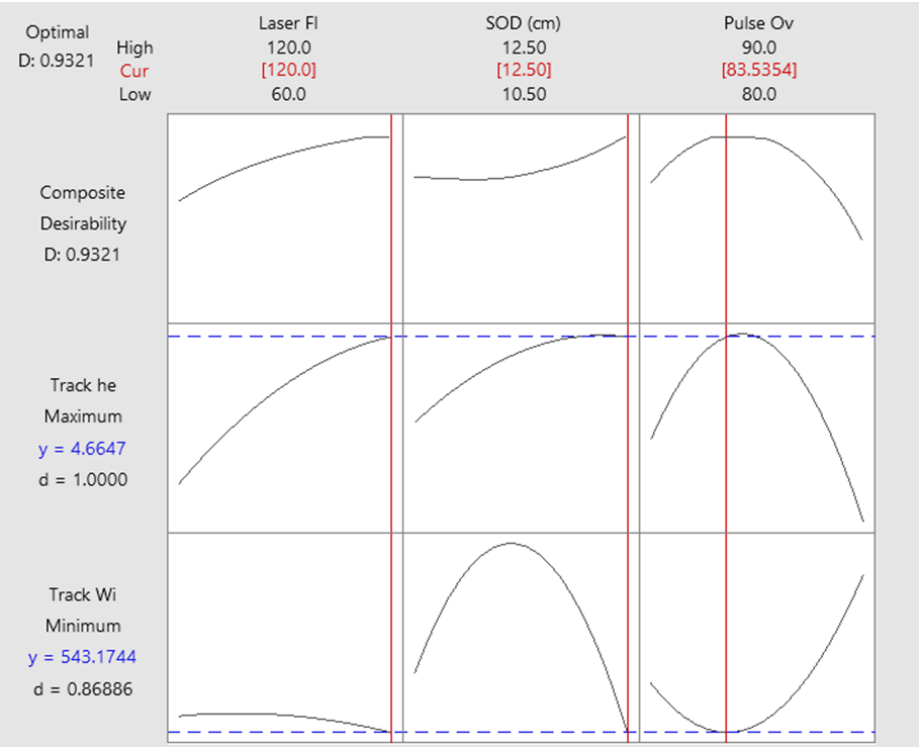

Fig.5.11. Multi-response optimization plot shows the composite desirability function for maximizing track height and minimizing track width. Optimal parameter settings (laser fluence = 120 J/cm²,

SOD = 12.5 cm, pulse overlap = 90%) yield a maximum height of 4.6647 µm and minimum width of 543.17 µm with an overall desirability score of 0.9321.

To identify the optimal set of laser processing parameters that simultaneously maximize track height and minimize track width, a multi-response optimization was conducted using desirability function analysis as seen in fig. 5.11. The aim was to achieve tall, narrow tracks—ideal for high-resolution micro-3D printing—with the most favorable trade-off between vertical and lateral growth. The composite desirability function, which combines individual response desirability into a single scalar index, was employed to guide the optimization. The desirability plot presented shows that the optimal parameter set consists of a laser fluence of 120 J/cm², stand-off distance of 12.5 cm, and pulse overlap of 90%. Under these conditions, the track height reaches a maximum value of 4.6647 µm, while the track width is minimized to 543.1744 µm. The composite desirability (D) value achieved is 0.9321, indicating a highly favorable solution where both response objectives are satisfactorily met. A desirability value close to 1 reflects the model's ability to find a global optimum where conflicting goals—such as increasing height while constraining lateral spread—are balanced effectively. The desirability curves plotted for each input parameter reveal additional insights. Track height shows a strong positive dependence on laser fluence and moderate sensitivity to pulse overlap, with a peak at the highest fluence and overlap settings. In contrast, track width demonstrates a nonlinear response, minimizing at high overlap and maximum stand-off distance, likely due to controlled energy dispersion and reduced beam convergence. These plots suggest that high laser fluence combined with longer stand-off and maximum overlap promotes sufficient energy density for melt accumulation without excessive lateral diffusion.

The identified optimal condition (120 J/cm² fluence, 12.5 cm SOD, 90% overlap) offers the best compromise between vertical growth and lateral confinement, thus enabling structurally robust, vertically stacked micro-

tracks with improved resolution. This optimization framework not only validates the predictive capabilities of the developed regression models but also provides a practical guideline for tuning laser parameters to achieve high-quality micro-3D printed features.

5.1.4 Morphological Analysis:

The morphological and elemental characteristics of the donor substrate were analyzed to confirm the surface structure and elemental composition prior to laser-induced material transfer. Fig. (a) shows the macroscopic view of the sputtered donor wafer, revealing a uniform metallic appearance with no macroscopic defects. The SEM micrograph in Fig. (b), captured at higher magnification, shows a densely packed granular microstructure with interconnected nano-islands and shallow valleys, typical of a sputtered aluminum-based thin film. These features are advantageous for controlled laser-material interaction, as the granularity supports energy absorption and localized material ejection. The EDX spectrum (Fig. c) confirms the elemental composition of the donor material, where a dominant peak corresponding to aluminum (Al) is observed, accompanied by minor peaks for oxygen (O) and gold (Au). The presence of gold is attributed to the conductive coating used for SEM imaging, while oxygen arises from minor surface oxidation during ambient exposure.

5.1.4(a) Morphological Analysis of donor material

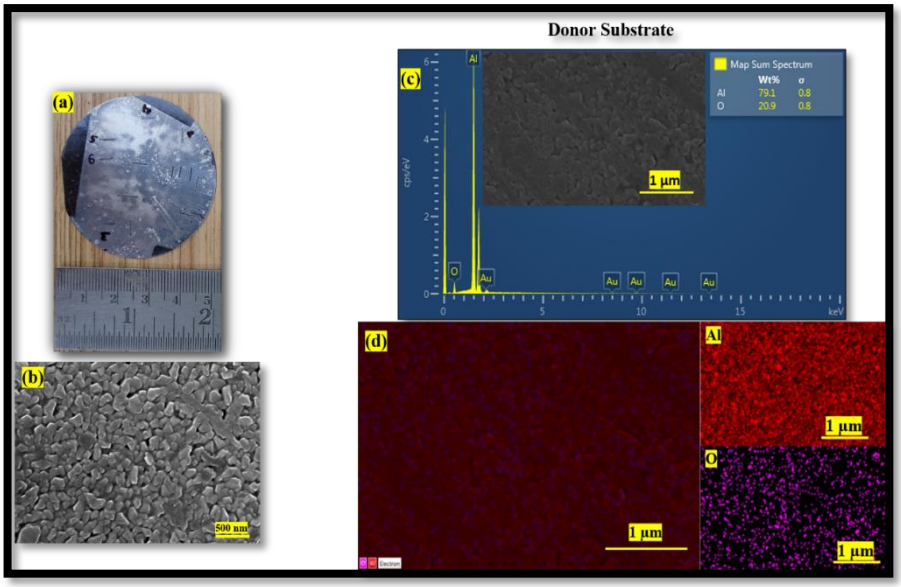

Fig.5.12. Morphological characterization of donor substrate: (a) Macroscopic image of the sputtered donor wafer, (b) SEM microstructure showing dense and uniform nano-grains, (c) EDX spectrum showing Al and minor O and Au peaks, and (d–f) EDX elemental maps confirming uniform distribution of Al and O over the donor surface.

The atomic percentages of Al (71.8%) and O (20.9%) as seen in fig. 5.12 are consistent with the deposition parameters used in aluminum thin-film sputtering. Additionally, EDX elemental mapping (Fig's d–f) reveals a uniform spatial distribution of Al and O across the scanned region, confirming the compositional homogeneity of the donor layer. No localized agglomerates or contaminants were detected, validating the purity and suitability of the donor film for clean laser-based transfer. Overall, the donor surface exhibited a continuous metallic layer with micro-scale uniformity, which supports efficient and reproducible material transfer upon laser interaction.

5.1.4(b) Morphological analysis of acceptor substrate

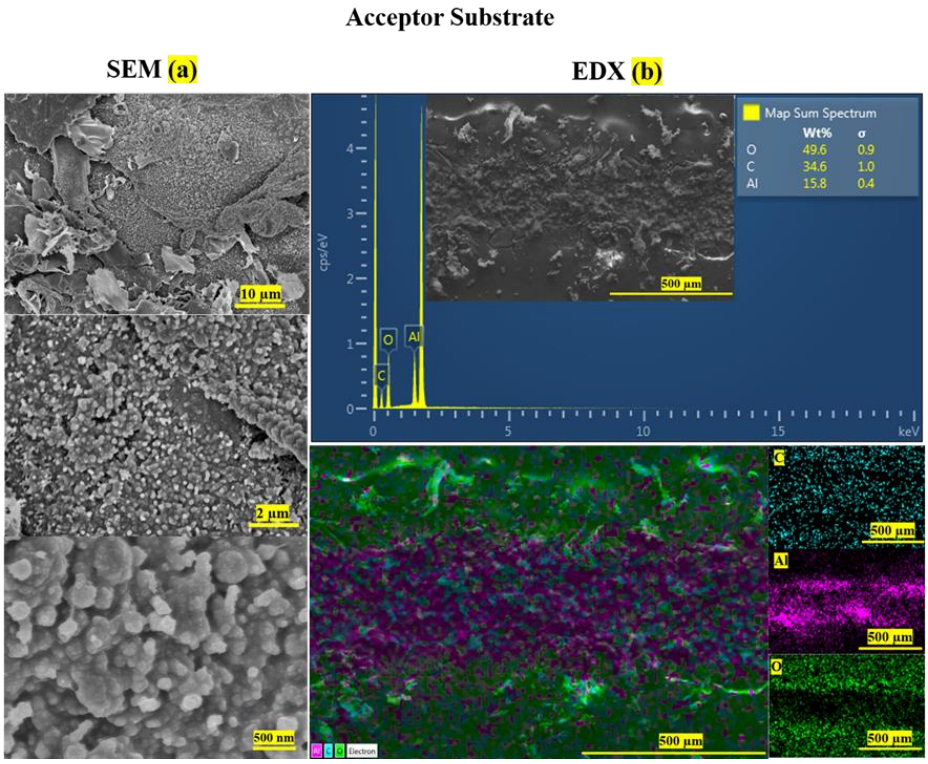

Fig.5.13. Morphological and compositional analysis of acceptor substrate after laser-assisted transfer: (a) SEM images at different magnifications show transferred and partially fused particles forming granular topography, and (b) EDX spectrum and elemental mapping indicating the spatial presence of Al, O, and C, confirming successful donor-to-acceptor transfer.

Post-transfer morphological analysis was performed on the acceptor substrate to investigate the quality and integrity of the material received. SEM imaging (Fig. 5.13 a) at multiple magnifications illustrates the multiscale topography of the transferred features. At low magnification, a wrinkled and fragmented surface morphology is observed, suggesting partial melting and solidification effects during laser decal transfer. The intermediate and high magnification images reveal densely packed micro-aggregates and partially fused particles, indicating localized spinning of the transferred material. These features confirm successful deposition and redistribution of donor particles onto the acceptor surface.

Elemental composition was assessed through EDX analysis (Fig. 5.13 b). The acquired spectrum displays strong peaks for O (oxygen, 49.6%), C (carbon, 34.6%), and Al (15.8%), indicating that aluminum from the donor substrate was effectively transferred to the acceptor while also showing some degree of oxidation and carbonaceous contamination. The presence of carbon is attributed to either atmospheric exposure or interaction with organic residues on the flexible substrate surface. The EDX elemental maps confirm the spatial distribution of Al, O, and C, with Al being concentrated in well-defined regions, confirming targeted material transfer and partial embedding into the polymeric acceptor. Oxygen and carbon are more diffusely spread, indicating surface reactions or existing background content of the substrate.

Together, these analyses confirm that the laser-assisted material transfer process successfully moved material from the donor to the acceptor with consistent elemental presence and identifiable morphological features. The particle sintering, uniform Al mapping, and defined surface features suggest that the process is not only effective but also repeatable. Minor surface oxidation and roughness are inherent to the localized thermal gradients but do not hinder the structural integrity or electrical potential of the transferred tracks.

5.1.5 Pattern Reproducibility and Geometrical Versatility

To evaluate the geometrical flexibility and reproducibility of the developed laser-assisted micro-3D printing platform, complex 2D patterns were fabricated on rigid substrates using a pre-programmed pixelated feed code. As shown in the image, the system successfully replicated diverse geometries with high fidelity, including linear comb-like tracks (fig 5.14 a, d), gear patterns (fig 5.14 b, e), and a spiral square configuration (fig 5.14 c, f). These designs were selected to test the ability of the printing mechanism to handle sharp corners, curves, and repetitive parallel paths, all of which are essential features in real-world

microsystem applications such as antennas, electrodes, and microsensors.

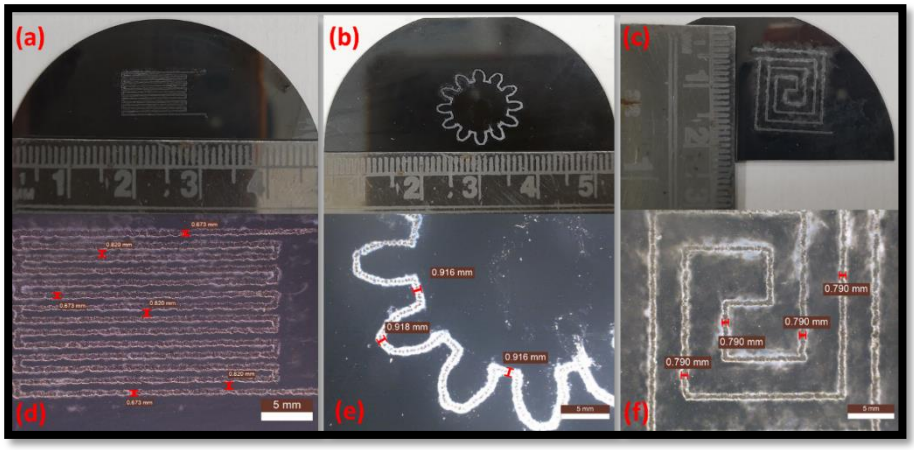

Fig.5.14. Demonstration of geometric versatility in laser-assisted micro-3D printing. (a-c) Optical images of line array, sinusoidal, and spiral square patterns fabricated on rigid substrates. (d-f) Corresponding magnified views showing consistent track widths across geometries: 0.673-0.820 mm for linear, ~0.916 mm for sinusoidal, and ~0.790 mm for spiral patterns, validating the resolution and reproducibility of the printing system.

In the linear pattern (fig 5.14 a, d), uniform track spacing and consistent widths were observed across multiple lines. The measured track widths ranged from 0.673 mm to 0.820 mm, indicating low variation and robust control of the beam translation and energy delivery. The geared pattern (fig 5.14 b, e) further validated the system's capability to handle curved features without geometric distortion. The track width was consistently measured around 0.916-0.918 mm, demonstrating the laser's ability to maintain precision even in dynamic path changes.

The spiral square pattern (fig 5.14 c, f) was employed to assess angular resolution and the ability to print nested, sharp-angled loops. The track widths remained constant at 0.790 mm, with well-defined corners and no visible material discontinuities. The consistent edge sharpness and dimensional conformity in all three geometries highlight the system's digital controllability and high repeatability. Furthermore, the absence of material splattering, edge tapering, or breakage indicates well-optimized pulse overlap and fluence parameters during printing.

These results confirm that the proposed laser-based microprinting approach enables reliable fabrication of arbitrary geometries without loss of resolution, making it well-suited for integration into functional microdevices. The programmable control over geometry, in combination with the physical consistency observed across patterns, provides strong evidence of the system's scalability and applicability in customized device prototyping.

5.2 Investigation on laser micro-3D printing of high density SiC ceramics.

Silicon carbide (SiC) has emerged as a highly attractive material for sensor applications operating in extreme environments due to its wide bandgap, high thermal conductivity, excellent chemical inertness, and superior mechanical properties. Despite its remarkable potential, the conventional fabrication of SiC based microdevices faces significant technical challenges across various domains, including substrate quality, material properties, manufacturing processes, and integration complexity. These hurdles are further amplified when scaling the process for large-area or commercial production. The advent of micro-3D printing presents a promising pathway to address these issues by enabling direct, maskless, and layer-wise fabrication of complex SiC structures at the microscale. The key challenges in Conventional SiC Sensor Fabrication include the fabrication of SiC sensors typically relies on high-temperature chemical vapor deposition (CVD) techniques. However, this approach is constrained by several limitations:

- High Manufacturing Costs and Substrate Quality Constraints: SiC substrates are expensive and difficult to process due to their high hardness. Achieving high-quality substrates involves complex growth procedures, making them economically non-viable for many commercial applications. The size and quality of SiC wafers significantly affect defect densities, yield, and scalability.

- Material Property Challenges – Hardness, Brittleness, and High-Temperature Requirements: SiC is inherently hard and brittle, which, while beneficial for mechanical robustness, introduces substantial difficulties in micromachining and patterning using traditional subtractive processes. Moreover, the CVD growth of high-quality SiC requires extreme temperatures in the range of 1000°C to 1800°C, leading to significant packaging strain and thermal expansion mismatch with other device components. These thermal constraints further limit material choices for sensor integration and encapsulation.
- Device Manufacturing and Growth Process Challenges: Achieving uniform film thickness, controlling the growth rate, and suppressing defects during CVD are major challenges. These issues directly impact the reproducibility and sensitivity of the sensor devices. Furthermore, the high thermal budget restricts the compatibility of the SiC layer with low-temperature electronics or flexible substrates. The inherent difficulties in doping SiC and controlling its conductivity further complicate device fabrication.
- Sensor-Level Challenges - Integration and Cost Impact: SiC's properties, while advantageous, make integration with standard MEMS and CMOS platforms complex. Packaging SiC-based sensors without inducing stress or delamination, especially in miniaturized or flexible formats, is a critical issue. Additionally, the overall cost impact of SiC device fabrication remains high due to expensive substrates, slow deposition rates, and high-energy process requirements.

Micro-3D printing, also known as additive micromanufacturing, offers a novel, maskless, and low-waste alternative to conventional methods. It enables the direct writing of functional or structural materials in a layer-by-layer fashion, allowing the construction of intricate geometries with sub-micron resolution. In the context of SiC, micro-3D printing provides several critical advantages:

- Bypassing High-Temperature Growth Requirements: Micro-3D printing enables the deposition of SiC-containing inks or precursors at significantly lower temperatures than those required for CVD. This is particularly beneficial for fabricating sensors on flexible or polymeric substrates that would otherwise degrade at high temperatures. Laser-based sintering or localized thermal curing methods used in 3D printing can provide sufficient energy for densification without damaging the surrounding material.
- Improved Material Utilization and Custom Geometry Fabrication: Instead of starting with a bulk wafer and etching away material, additive methods build the structure only where needed. This reduces material waste and supports the fabrication of non-planar or freeform sensor geometries, which are difficult or impossible to produce with lithography. Such geometries can enhance sensitivity by increasing surface area or improving mechanical strain distribution.
- Mitigation of Brittleness and Interface Challenges: Micro-3D printing allows the creation of composite SiC structures, where SiC is blended with binders or flexible matrices that reduce brittleness and improve mechanical resilience. Moreover, interfacial compatibility between layers can be enhanced by controlling printing of gradient structures or interlayers that minimize delamination or cracking during thermal cycling.
- Enabling Multi-Material and Embedded Sensor Fabrication: Micro-3D printing supports the integration of multiple materials within a single fabrication step. This means electrodes, interconnects, and sensing elements can be co-fabricated with the SiC layer, reducing assembly steps and improving alignment precision. Such integration is particularly useful for embedded sensor applications in aerospace, biomedical, or harsh industrial environments.

- Scalability and Customization: Unlike batch-based photolithography, 3D printing is inherently scalable and adaptable. It is particularly suited for low-volume, high-value, or custom sensor production, such as wearable electronics or implantable devices where design flexibility is paramount.

5.2.1 Sputtering-Based Deposition and Process Optimization for SiC Micro-3D Printing

Following the material preparation stage, where high-purity SiC targets are fabricated (as shown in the Fig.), the deposition process is carried out using physical vapor deposition (PVD) techniques primarily sputtering to realize functional microstructures suitable for sensor fabrication. In this work, sputtering is employed to deposit thin films of SiC onto pre-treated substrates, which are then patterned and consolidated using laser-based micro-3D printing methods.

- **Sputtering Deposition of SiC**

RF magnetron sputtering is preferred due to the insulation nature of SiC and the requirement for uniform, high-density film formation. The sputtering process involves the bombardment of the SiC target with energetic ions (typically Ar^+), causing ejection of SiC atoms that subsequently condense onto the substrate. The key considerations during sputtering include:

(a) Target purity and compaction: The solidified target (as shown in the center image) must be uniform and crack-free to avoid arc formation and non-uniform deposition.

(b) Substrate pre-conditioning: Shown in the left image, the substrate is held at elevated temperatures or exposed to plasma pre-treatment to enhance adhesion and film density.

(c) Film Thickness and Surface Morphology: Surface profiling (bottom image) reveals a SiC layer thickness of ~5.5 µm, indicative

of a stable and repeatable sputtering process with minimal delamination or curvature-induced stress.

- **Process Optimization in Micro-3D Printing**

To achieve functional and high-fidelity SiC microstructures, laser-based patterning is applied post-sputtering. The optimization of various laser processing parameters is critical to controlling the resolution, feature definition, and uniformity of the printed structures. The following aspects were systematically investigated:

a) Influence of Stand-off Distance: The distance between the laser focusing optics and the substrate (stand-off distance) governs the spot size and energy density. A reduced stand-off distance enhances spatial resolution but may lead to substrate overheating, while excessive distance causes beam divergence and reduces resolution. An optimal trade-off must be established to maintain precision without compromising material integrity.

b) Influence of Laser Power on Feature Size: Laser power plays a direct role in local melting, ablation, or sintering of the SiC layer. Too low power results in incomplete patterning, while excessive power leads to material degradation or unintended etching. Experimental optimization revealed that feature dimensions shrink or broaden non-linearly with power, necessitating real-time control or pre-calibrated parameters.

c) Laser Pulse Overlap and Uniformity Analysis: Uniform energy delivery is essential for consistent pattern thickness and morphology. By controlling the overlap of laser pulses, the system ensures minimal ridges or valleys between adjacent scan lines. Overlap percentages between 50-80% were evaluated, with higher overlaps improving smoothness but increasing thermal load.

d) Influence of Substrate Heating: Maintaining a controlled substrate temperature during printing can reduce thermal gradients and improve interfacial bonding. Pre-heating the substrate promotes

stress relaxation and densification, reducing the likelihood of cracking or delamination. However, excessive substrate heating can lead to grain coarsening or out-of-plane warping.

5.2.2 Detailed investigations into processing parameters for optimized SiC printing

5.2.2(a) Influence of Stand-off distance: To optimize the laser-based material transfer process post-SiC deposition, a detailed parametric study was conducted to evaluate the influence of **stand-off distance**, the gap between the laser nozzle and the substrate-on the quality of material ejection and transfer fidelity. With repetition rate and duty cycle held constant at **10 Hz** and **3%**, respectively, three stand-off distances (8.5 cm, 10.5 cm, and 11.5 cm) were investigated as seen in table 5.8.

S. No.	Repetition Rate (Hz)	Duty Cycle (%)	Stand-off Distance (cm)	Observation
A	10	3	8.5	No material transfer
B	10	3	10.5	Uniform material transfer
C	10	3	11.5	Non-uniform material transfer

Table 5.8: Processing parameters for optimizing SiC printing based on influence of stand-off distance

A detailed analysis of the laser-assisted material transfer process revealed the critical influence of stand-off distance on the quality and consistency of SiC film deposition as shown through the microscopic image in Fig. 5.15.

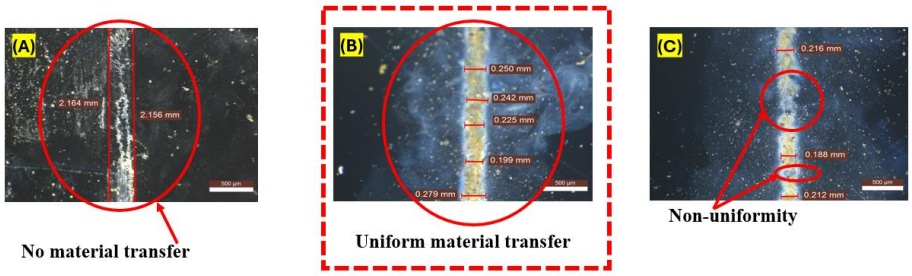

Fig. 5.15: Microscopic images of track ejection at mentioned processing parameters. (a) material ejection based on S.No. A, (b) material ejection based on S.No. B and (c) material ejection based on S.No. (c) in table 5.8.

At a reduced stand-off distance of 8.5 cm, corresponding to a defocused condition, no significant material ejection was observed. Microscopy images confirmed that the laser energy density was insufficient to overcome the surface adhesion of the SiC layer, leading to incomplete ablation and a complete absence of transfer despite visual disturbance along the laser path. The excessive proximity of the laser head resulted in energy dispersion over a broader area, thereby reducing the peak fluence below the material ejection threshold. In contrast, the optimal condition was achieved at a stand-off distance of 10.5 cm, where the laser was precisely focused, allowing effective energy delivery to the substrate. This led to uniform and controlled material transfer, with consistent strip widths ranging from 0.199 mm to 0.279 mm, indicative of minimal beam divergence and excellent process reproducibility. The focused laser energy at this position was sufficient to trigger clean ablation and transfer without collateral damage to surrounding regions, making 10.5 cm the ideal stand-off distance for process optimization. However, when the distance was increased to 11.5 cm., the resulting material transfer was non-uniform. Although some depositions occurred, the patterns were inconsistent, with feature widths varying from 0.188 mm to 0.216 mm. This irregularity is attributed to the decreased energy density caused by excessive beam divergence, which disrupted the thermal and mechanical coupling at the substrate-film interface and led to scattered deposition and unconfined material ejection.

These findings highlight the critical importance of laser focusing on micro-3D printing processes. Even minor deviations from the optimal stand-off distance can lead to substantial variations in transfer efficiency, feature definition, deposition uniformity, and thermal stress distribution. The focused condition at 10.5 cm not only ensures precise and efficient energy transfer but also maximizes material utilization and dimensional accuracy. Therefore, strict control over optical alignment and beam geometry is essential in future automated or high-precision micro-3D printing systems to achieve reliable, scalable, and repeatable fabrication of SiC microstructures. In conclusion, the parametric study confirms that focused laser delivery at a stand-off distance of 10.5 cm is necessary for obtaining uniform and high-fidelity material transfer in laser-assisted printing of SiC films. Both under-focused (8.5 cm) and over-focused (11.5 cm) conditions result in suboptimal outcomes-either due to insufficient fluence or uncontrolled scattering-underscoring the need for carefully optimized laser parameters in standardized sensor manufacturing workflows.

5.2.2(b) Influence of laser power: To evaluate the effect of laser power on the quality of SiC material transfer during micro-3D printing, a systematic study was conducted by maintaining a constant stand-off distance of 10.5 cm and duty cycle of 7%, while varying the repetition rate and laser power between 3.5 W and 5.5 W as seen in table 5.9. The results indicate that both underpowered and overpowered laser settings lead to suboptimal material ejection, whereas moderate power values result in uniform and controlled transfer. At the lower end of the power spectrum, cases A and B (3.5 W and 3.8 W, respectively) resulted in non-uniform material ejection. In case A (5 Hz), the transfer occurred in a pulsed and inconsistent manner, with irregular track widths ranging from 0.279 mm to 0.307 mm, accompanied by gaps and poor continuity. While case B (7 Hz) showed marginally improved strip definition, it still exhibited numerous voids within the transferred path, indicating insufficient energy to induce continuous ablation and ejection of the SiC layer.

Conversely, at higher power settings such as cases E and F (4.8 W and 5.5 W), excessive energy input led to increased ejection velocity, resulting in material splattering and degraded pattern definition. In case E (15 Hz), although the material transfer occurred, it was accompanied by splashing at the edges and irregular feature boundaries, with measured widths ranging from 0.261 mm to 0.311 mm. This became more pronounced in case F (20 Hz), where the transferred features were considerably narrower (as low as 0.170 mm) and surrounded by significant overspray and debris, indicating that excessive power led to uncontrolled expulsion of material rather than focused transfer.

The optimal material ejection behaviour was observed in cases C and D (4.0 W and 4.3 W), corresponding to repetition rates of 9 Hz and 11 Hz, respectively. In these cases, the laser energy was sufficient to induce localized and stable ablation without causing excessive thermal damage or splashing. The transferred lines displayed uniform widths ranging from approximately 0.199 mm to 0.316 mm and demonstrated minimal void formation. Case D showed a highly consistent deposition with clean boundaries, indicating that 4.3 W power at 11 Hz offered the best trade-off between energy delivery, thermal confinement, and mechanical ejection forces.

These observations underscore the importance of laser power optimization in micro-3D printing of SiC films. While low power settings fail to initiate continuous transfer, excessive power results in high-velocity ejection, splattering, and poor dimensional control. Therefore, maintaining the laser power in the moderate range of 4.0–4.3 W, as demonstrated in cases C and D, is essential for achieving reproducible, uniform, and high-fidelity material transfer in laser-based additive fabrication processes for sensor-grade SiC structures.

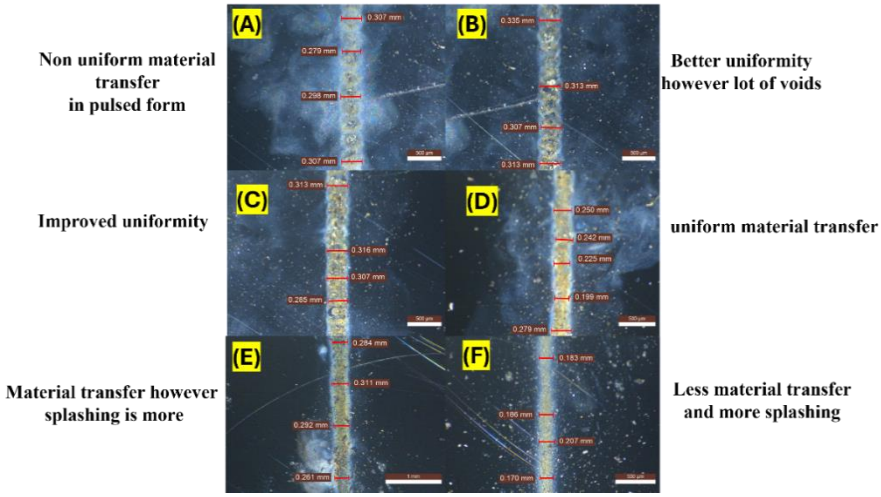

Fig. 5.16: Microscopic images (a–f) showing track ejection corresponding to the processing parameters listed in Table 5.9.

S. No.	Repetition Rate (Hz)	Duty Cycle (%)	Stand-off Distance (cm)	Power (W)	Observation
A	5	7	10.5	3.5	Non-uniform material transfer (pulsed, irregular)
B	7	7	10.5	3.8	Slightly better uniformity, but with voids
C	9	7	10.5	4.0	Improved uniformity in material transfer
D	11	7	10.5	4.3	Uniform and clean material transfer
E	15	7	10.5	4.8	Material transfer with splashing and overspray
F	20	7	10.5	5.5	Less material transfer, more splashing

Table 5.9: Processing parameters for optimizing SiC printing based on influence of laser power

5.2.2(c) Influence of laser pulse overlap: To examine the effect of laser pulse overlap on material transfer quality in micro-3D printing of SiC films, a study was performed by keeping repetition rate (10 Hz), duty cycle (1%), and stand-off distance (10.0 cm) constant, while systematically varying the overlap percentage and corresponding stage

speed. Four overlap conditions 50%, 60%, 70%, and 80% were analyzed, which corresponded to stage speeds of 130 mm/min, 115 mm/min, 100 mm/min, and 85 mm/min respectively. The results revealed that laser pulse overlap plays a critical role in defining the uniformity, continuity, and edge quality of the transferred material track.

At a lower overlap of 50% (A), material transfer was observed to be non-uniform. The higher stage speed (130 mm/min) reduced the effective energy input per unit area, leading to incomplete and uneven ejection, as reflected by inconsistent track widths ranging from 0.270 mm to 0.332 mm. This condition resulted in irregular ablation and poor surface definition, making it unsuitable for precision fabrication. In contrast, at moderate overlaps of 60% and 70% (B and C), corresponding to reduced speeds of 115 mm/min and 100 mm/min respectively, the material transfer improved significantly. Both cases exhibited better uniformity, smoother edges, and consistent line widths. S.No. B displayed widths in the range of 0.298 mm to 0.318 mm, while S.No. C maintained values from 0.257 mm to 0.305 mm. These conditions appear to offer the best balance between energy deposition and spatial coverage, indicating that overlaps in the range of 60-70% are optimal for achieving uniform and reproducible SiC transfer (see figure 5.17).

However, at the highest overlap of 80% (D), where the stage speed was reduced to 85 mm/min, the material transfer began to degrade again. Although the track was continuous, visible signs of material splashing and localized over-burning were noted, with widths varying between 0.232 mm and 0.325 mm. The high pulse overlap resulted in excessive localized energy deposition, which promoted thermal damage, increased splatter, and introduced roughness.

These results emphasize that while increasing pulse overlap generally enhances track uniformity, excessive overlap can lead to detrimental thermal effects due to cumulative heating and laser energy concentration. Hence, there exists an optimal window specifically between 60% and 70% overlap that yields the most desirable balance

between uniform transfer and minimal thermal side effects. This study highlights the necessity of fine-tuning pulse overlap and stage speed together to maintain high-quality pattern fidelity in laser-assisted micro-3D printing of SiC films.

S. No.	Repetition Rate (Hz)	Duty Cycle (%)	Stand-off Distance (cm)	% Overlap	Speed (mm/min)	Observation
A	10	1	10.0	50%	130	Less uniformity due to low overlap and high stage speed
B	10	1	10.0	60%	115	Improved uniformity with minimal voids
C	10	1	10.0	70%	100	Improved uniformity with better edge quality
D	10	1	10.0	80%	85	Splattering and thermal damage due to over-exposure

Table 5.10: Processing parameters for optimizing SiC printing based on influence of laser pulse overlap

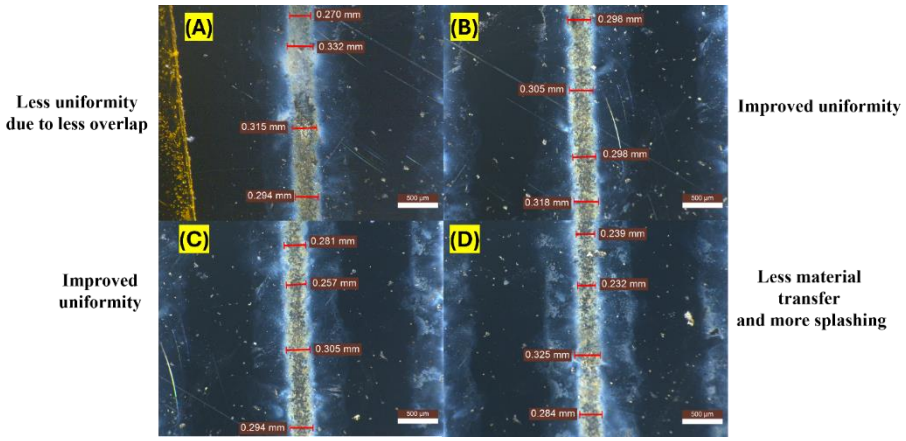

Fig. 5.17: Microscopic images (a–d) showing track ejection corresponding to the processing parameters listed in Table 5.10.

5.2.2(d) Influence of Acceptor Substrate heating: To evaluate the role of substrate heating in laser-assisted micro-3D printing of SiC, a comparative study was performed under two different thermal conditions i.e. (a) printing without acceptor substrate heating, and (b) printing with controlled acceptor substrate heating at 100 °C. In unheated conditions, three SiC layers were deposited. Microscopic examination and profilometry data showed that the line widths ranged from 0.333 mm to 0.373 mm with an average height fluctuation of approximately 0.8 µm (see fig.5.18). The corresponding 3D surface plot revealed irregular peak-valley formations with poor layer stacking, indicating weak interfacial adhesion and inefficient energy coupling during successive laser passes. Thickness profiling showed a maximum build height of 12 µm for 3 printed layers, confirming insufficient vertical growth and inconsistent fusion across layers. When the substrate was heated to 100 °C, the process stability and deposition quality improved substantially. A total of five layers were printed under this condition, and the resulting line widths showed more consistent values ranging from 0.200 mm to 0.316 mm. The 2D thickness profile captured a significantly higher peak value of 22 µm, indicating improved densification and layer-by-layer growth (fig.5.19). The 3D surface topography showed a smoother, more homogenous structure with minimized voids, demonstrating enhanced interfacial bonding and better control overheat distribution during deposition. The elevated substrate temperature helped reduce thermal gradients and facilitated localized softening of the material, promoting effective fusion between successive layers and minimizing delamination.

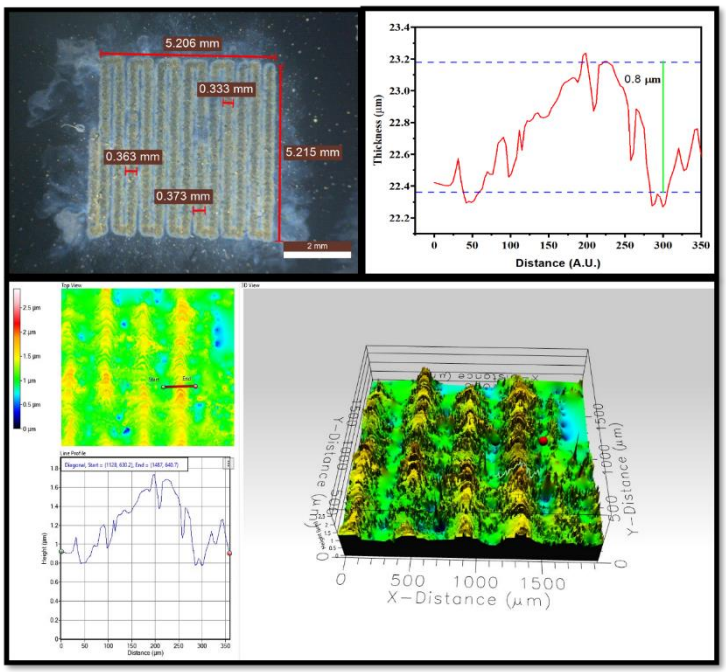

Fig. 5.18: 3 layers SiC transfer over acceptor substrate without substrate heating.

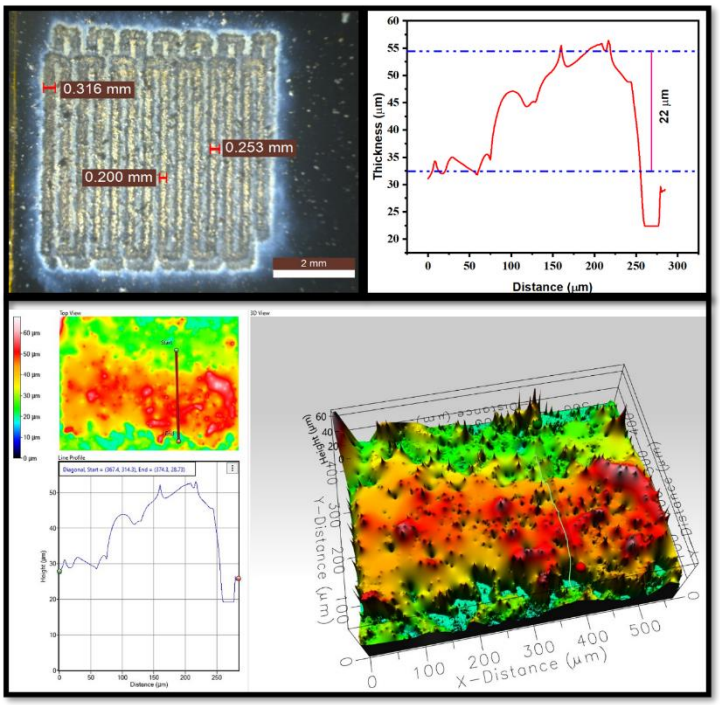

Fig. 5.19: 5 layers SiC transfer over acceptor substrate with controlled substrate heating at 100 °C

Further experiments with increased layer count under heated conditions confirmed the layer-dependent thickness gain. As shown in the profilometer data, 3 layers without heating produced a maximum height of 12 µm, while 5 layers with heating achieved 22 µm, and 7 layers extended the height to 26 µm *(fig.5.20)*. These measurements confirm the linear progression of thickness with increasing number of layers, while also highlighting the amplifying effect of substrate heating on vertical growth efficiency. The consistency and fidelity of multi-layer stacking were clearly enhanced under thermal assistance, as demonstrated by the smoother elevation profiles and fewer surface irregularities.

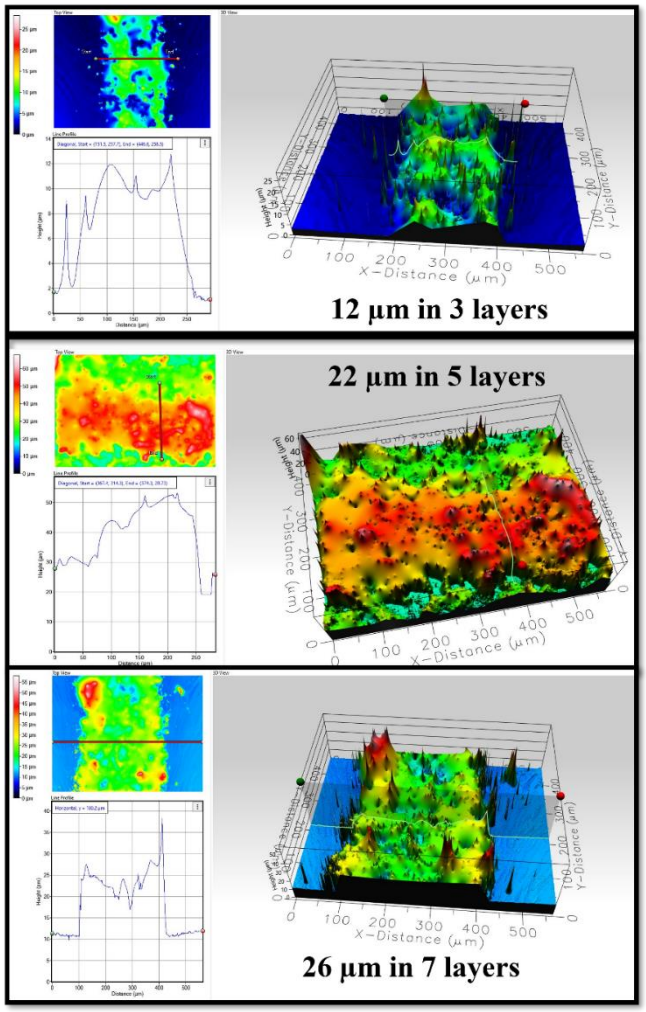

Fig. 5.20: profilometric analysis of multiple layers transferred with increasing thickness of overall sensor structure formed.

These results underscore the critical role of substrate heating in enhancing the quality and vertical resolution of laser printed SiC

structures. By enabling better layer adhesion, controlled ejection dynamics and more uniform energy absorption, substrate heating at moderate temperatures such as 100 °C can significantly improve the structural integrity, surface finish, and overall performance of printed microstructures. This process proves essential for applications requiring precise layer control, such as sensor fabrication or functional ceramic integration in microelectromechanical systems (MEMS).

5.2.3 Compositional and morphological Characteristics: The material confirmation was performed using XRD and SEM Analysis for the sputtered and transferred samples using laser micro-3D printing as is discussed in subsequent sections.

5.2.3(a) X-Ray Diffraction (XRD) Analysis: XRD analysis was performed to evaluate the phase purity, crystallographic orientation, and structural transformation of the SiC material throughout the fabrication process-from the initial target to the sputtered and laser-transferred layers.

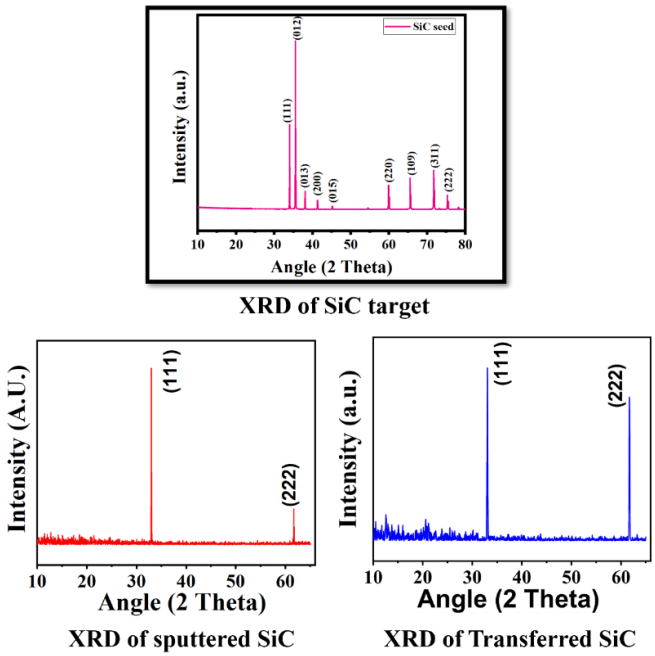

Fig. 5.21: XRD analysis of SiC target, sputtered SiC and transferred SiC over acceptor substrate

The XRD spectrum of the original SiC target displays multiple sharp peaks corresponding to various crystallographic planes. Major

reflections were observed at 2θ values around 35.7° (111), 41.4° (200), 60.1° (220), and 72.0° (311), which are characteristic of the β-SiC cubic phase (3C-SiC) with a zinc blende structure (fig.5.21). The presence of multiple well-defined peaks indicates a high degree of crystallinity and confirms the polycrystalline nature of the target material. These peaks match well with the standard JCPDS card for β-SiC (Card No. 29-1129), validating the purity and suitability of the target for thin-film deposition. Following RF magnetron sputtering, the resulting SiC thin film was analyzed, revealing two prominent peaks at approximately 35.7° and 60.1°, corresponding to the (111) and (222) planes, respectively. The appearance of these two reflections indicates that the deposited film retains the β-SiC crystal phase, albeit with lower intensity and broader peaks compared to the target. This suggests that the sputtered SiC possesses a nanocrystalline or partially amorphous structure, which is typical for low-temperature PVD processes where limited atomic mobility suppresses long-range ordering. The preferred orientation along (111) further suggests a growth bias under the applied sputtering conditions. After laser- micro-3D printing, the transferred SiC layer also exhibited peaks at (111) and (222), although the intensity was slightly enhanced and peak widths narrowed compared to the sputtered film. This change indicates partial crystallization or reorganization of SiC grains during laser exposure, as localized thermal energy may enhance grain coalescence and lattice ordering. The consistency of phase signatures across the sputtered and transferred states confirms that the laser process preserves the structural integrity of SiC while marginally improving its crystallinity. No secondary phases (such as SiO_2 or free carbon) were detected, affirming the phase purity of the printed structures.

5.2.3(b) Scanning Electron Microscopy (SEM) Analysis: SEM imaging was conducted at various magnifications to evaluate the surface morphology, grain distribution, and microstructural evolution of the SiC samples at different stages of the fabrication process (fig.5.22). The SEM micrograph at 15,000× magnification reveals a fine, granular

microstructure with relatively uniform grain distribution across the surface. The grain boundaries appear diffused, indicating partial densification and nanostructured surface features typically seen in sputtered ceramic films. The absence of large pores or cracks suggests good film continuity, although the surface remains rough at the nanoscale due to incomplete atomic rearrangement during deposition. The SEM images (taken at 5,000× and 10,000× magnifications) show the surface of SiC after laser transfer. Compared to the sputtered film, the laser transferred SiC exhibits larger agglomerated clusters and denser packing. The texture is more compact and appears smoother at micro-level, suggesting that the laser energy helped in sintering or fusing the nanograins into a cohesive structure. Fine particulate bridges between grains indicate improved intergranular connectivity, which is essential for mechanical integrity and functional performance in sensor applications. Notably, no signs of thermal damage such as microcracking, delamination, or carbon-rich residue were observed, confirming the compatibility of the laser parameters with the thermal threshold of SiC. The observed microstructure supports the hypothesis

that laser-assisted transfer can slightly reconfigure grain boundaries while maintaining phase stability and improving interfacial cohesion.

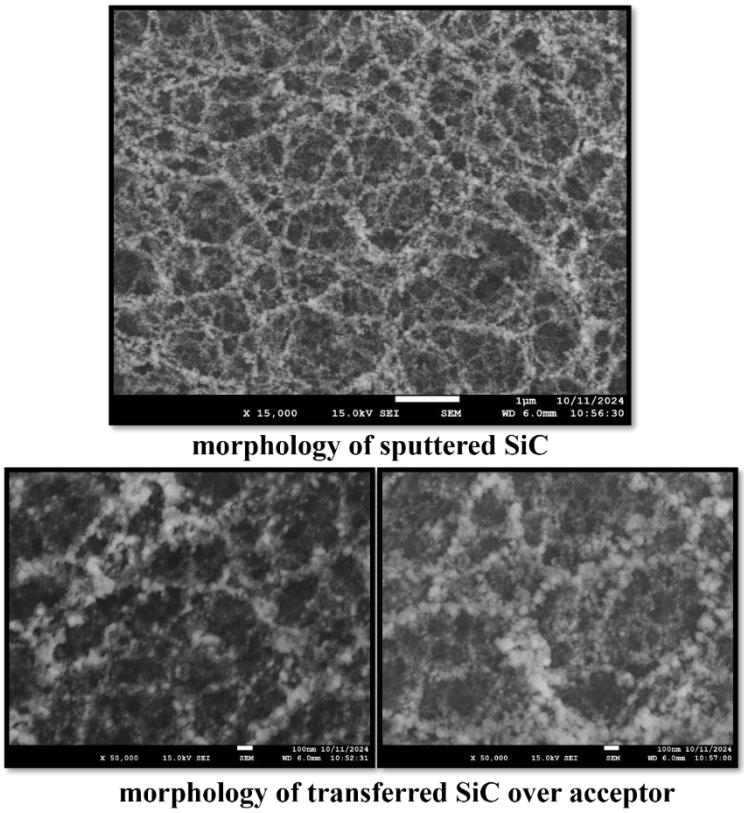

Fig. 5.22: Morphological analysis of sputtered and laser transferred SiC sample over acceptor substrate

5.2.4 Shape Printing Capability of SiC Using Laser-Assisted Micro-3D Printing

The developed laser-assisted micro-3D printing technology demonstrates significant versatility in fabricating custom-shaped SiC structures with high spatial precision. The system utilizes a programmable feed code approach that translates CAD-generated pixelated patterns into precise laser scanning paths. As shown in Fig. 5.23, SiC was successfully printed in various complex geometries including square, semicircular, and quadrant shapes highlighting the system's ability to operate with diverse spatial codes and generate patterns in accordance with customized design inputs.

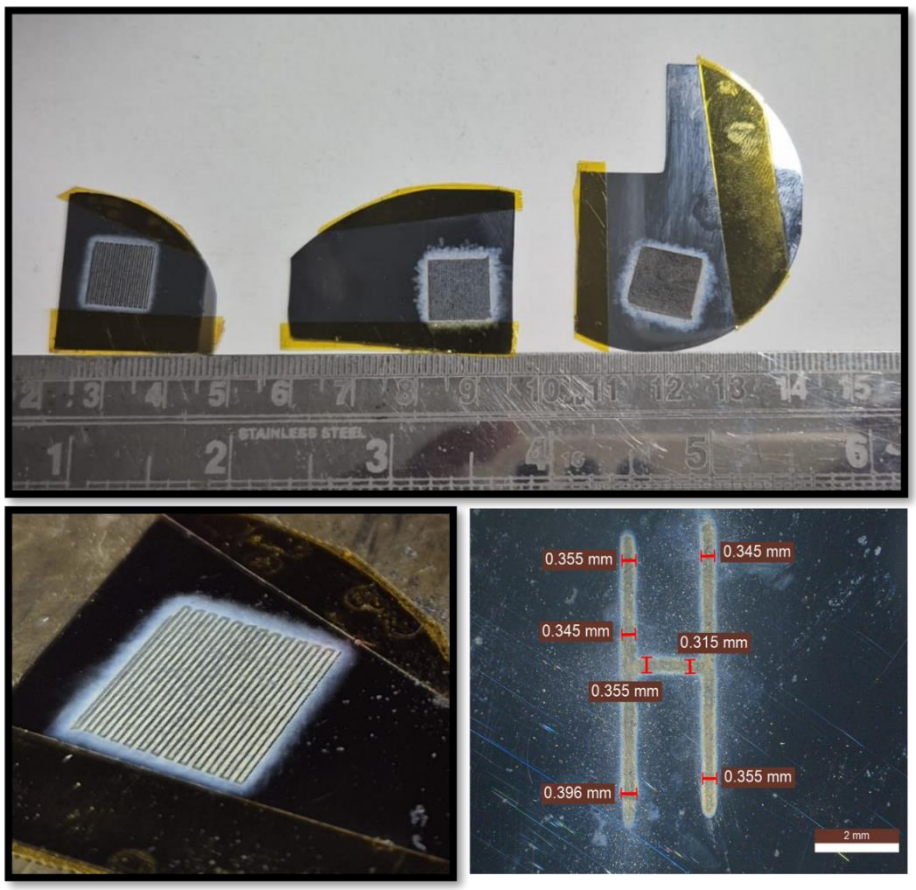

Fig. 5.23: Laser-printed SiC in various geometries (square, quadrant) using pixelated feed codes, demonstrating high design flexibility with consistent line widths (0.315-0.396 mm).

Each of these shapes maintains a highly uniform microstructure and consistent feature dimensions, validating the system's resolution and process reliability. Notably, the zoomed-in views reveal consistent line widths ranging between 0.315 mm and 0.396 mm, indicating high pattern fidelity and reproducibility across different shape boundaries. The fine, grid-like array observed within the printed region further confirms the capability of the system to deposit in tightly packed, pixel-by-pixel fashion, without distortion at corners or curves. This pixelated control enables high-precision layer stacking and supports anisotropic designs, making it ideal for sensor arrays, interconnects, and patterned micro-coatings. The successful printing of these diverse shapes without post-processing or masking steps underscores the maskless, digital nature of the platform. The SiC films were directly patterned on substrates using a controlled laser-material interaction mechanism,

wherein the laser beam modulated by scanning speed, power, and standoff distance selectively transferred the material onto desired locations. The programmable toolpath ensures accurate laser dwell time and spacing between pulses, leading to highly uniform deposition even at micro-scale curvature and edge zones. The demonstrated ability to fabricate SiC in arbitrary 2D geometries illustrates the flexibility and scalability of the laser-based microprinting system. This shape customization capability is critical for device-specific applications, especially in the fabrication of SiC-based sensors, microsystems, and interdigitated electrodes where the footprint and alignment geometry directly affect performance. Future implementations could incorporate multilayered or embedded designs, further expanding the utility of this technology for functional ceramic integration in MEMS, biomedical, or harsh-environment electronics.

5.3. Detailed investigations on optimized printing of ZnO on flexible substrate

Zinc oxide (ZnO) is a multifunctional semiconductor material widely known for its excellent piezoelectric, optoelectronic, and chemical sensing properties. To harness these characteristics in microscale devices, a hybrid fabrication approach combining RF sputtering and laser-assisted micro-3D printing has been developed. Initially, high-purity ZnO thin films are deposited using radio frequency (RF) magnetron sputtering, a physical vapor deposition method ideal for insulating targets like ZnO. In this process, argon plasma is ignited under vacuum, and energetic Ar^+ ions bombard the ZnO ceramic target, ejecting zinc and oxygen species that condense onto the substrate to form a uniform thin film. The deposition parameters such as RF power (typically 80 W), working pressure (5×10^{-5} mbar), and optional oxygen flow are precisely controlled to ensure stoichiometric growth, good adhesion, and crystalline orientation.

Once the ZnO film is deposited, laser micro-3D printing is employed to define high-resolution patterns directly onto the film surface without the

need for masks or etching. This is achieved by scanning a focused laser beam across the substrate in accordance with a preprogrammed feed code or pixelated design. The laser locally modifies the ZnO layer through controlled thermal interaction, enabling pattern transfer. This digital approach allows the fabrication of finely defined structures with widths ranging from a few microns to several hundred microns, maintaining excellent fidelity to the intended geometry. The ability to vary laser parameters such as power, pulse overlap, and scanning speed provides additional control over material removal rate and edge quality, enabling the printing of interdigitated electrodes, sensor layouts, or functional microgrids with high precision. The combination of RF sputtering and micro-3D laser printing offers several advantages. It enables maskless and direct patterning, reduces processing steps, and supports the fabrication of complex geometries with excellent spatial resolution. Furthermore, the localized heating effect of the laser can improve the densification and adhesion of ZnO microstructures, enhancing their mechanical robustness and functional performance. This hybrid approach is particularly promising for the fabrication of flexible or miniaturized devices such as gas sensors, UV photodetectors, nanogenerators, and piezoelectric-based microelectromechanical systems (MEMS). The precision and adaptability of this process also make it well-suited for rapid prototyping and scalable production of next-generation ZnO-based microscale components. The processing parameters for the same has been studied in detail for its pixelated transfer over solid as well as flexible substrate and its further exploration towards selective transfer for hybrid devices fabrication.

5.3.1 Processing parameters for optimized printing of ZnO on solid substrate:

To analyze the selective material transfer, a detailed analysis on control over parameters was performed. For that purpose, the process optimization for ZnO seed layer transfer was analyzed and based on experiments the influence of laser fluence towards material transfer,

stand-off distance and effect of laser pulse overlap is analyzed in detail in the below segment.

5.3.1(a) Sputtered ZnO Seed Layer Analysis:

To grow ZnO nanorods, there are multiple methods of synthesis being explored which includes electro-chemical deposition, chemical vapor deposition and vapor-liquid-solid (VLS) growth. It is however observed that severe conditions or catalysts are required for ZnO growth. Hydro-thermal method allows the nano-rods growth at low temperatures and is an effective method for nano-devices fabrication. By growing a highly oriented ZnO with improved length and diameter of growth, the surface area per unit area increases thus improving the performance of the devices. In hydrothermal process, temperature as well as solution concentration and seed layer are major effective parameters for high quality ZnO nanorods growth and its orientation. The size of nanoparticles and the presence of seed layer on the substrate determines the size of growing ZnO nanorods. The PDMS sacrificial layer coated over silicon wafer was sputtered with ZnO seed layer for its selective positioning and further hydrothermal growth. As observed in the morphology (see Fig. 5.24a) and EDX analysis (see Fig. 5.24 (b, c)), ZnO seed layer is coated all along the surface on a silicon wafer which marks the presence of it in the spectrum as well.

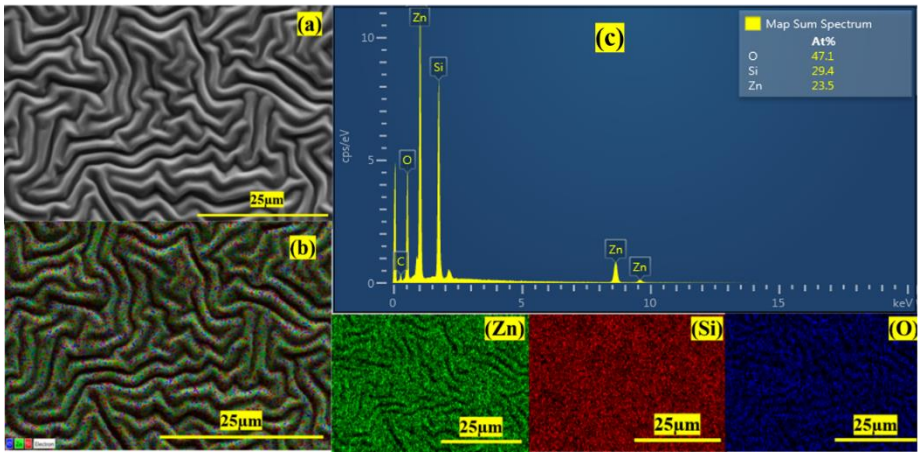

Fig. 5.24: (a) SEM analysis, (b) EDX mapping and (c) EDX spectrum (wt.%) of sputtered ZnO seed layer.

5.3.1(b) Influence of laser fluence towards ZnO seed layer transfer

The coated material is ejected out uniformly from the surface essentially due to sufficient gas pressure that gets generated in the sacrificial layer and the gas pressure forms due to laser energy interaction. To optimize the energy required for material transfer, a stand-off distance was fixed at near focus condition i.e., Z=11.5 cm and the obtained spot diameter was ~720 µm, however, further experimental results suggested that the effective diameter were material transfer was observed was in the range of 400-450 µm. This might essentially be due to the gaussian beam profile of laser energy sources. Table 5.11 defines the processing parameters used to analyze the sufficiency of energy required for material transfer.

Sample Name	Processing Parameters			
	Repetition Rate (Hz)	Duty (%)	Power (W)	Laser Fluence (J/cm^2)
A	10	1	0.56	15
B	10	3	1.60	40
C	10	6	3.0	75

Table 5.11. Laser processing parameters for analysing the sufficiency of material transfer for selective positioning

From Fig. 5.25, it is observed that as laser fluence increases, the material ejection also increases. However, the donor substrate presented some black burning marks in sample C and further increase in laser fluence would lead to burning of the material to be transferred due to puncture of the generated gas pressure in the sacrificial layer.

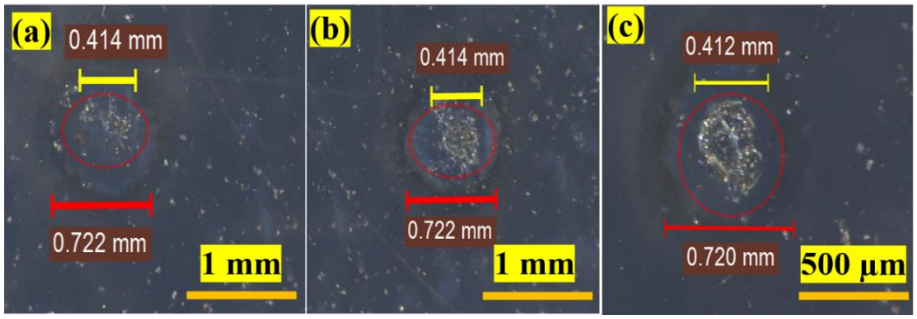

Fig. 5.25: Microscopic images representing variation of laser fluence towards material transfer analysis.

5.3.1(c) Influence of stand-off distance towards ZnO seed layer transfer: The influence of stand-off distance on ZnO seed layer transfer in Fig. 5.26 demonstrates its critical role in material ejection and associated feature size. At a near-focus condition (Z = 11.5 cm), the laser beam achieved an optimal balance between energy density and spot size, leading to effective material transfer with a heat-affected zone of ~720 µm and a material transfer region of ~412 µm. In contrast, at under-focus (Z = 9.8 cm) and over-focus (Z = 13.2 cm) conditions, material transfer was significantly reduced or absent due to insufficient or excessive energy dispersion. The over-focused condition (Z = 13.2 cm) resulted in a larger spot diameter (~800 µm) but lacked effective material ejection, while the under-focused condition (Z = 9.8 cm) had a smaller spot size but insufficient energy to propel the material. These findings highlight that a controlled stand-off distance (~11.5 cm to 12.5 cm) is essential for precise material transfer, minimizing unwanted heat effects while ensuring accurate feature formation in laser decal transfer-based multi-material microfabrication.

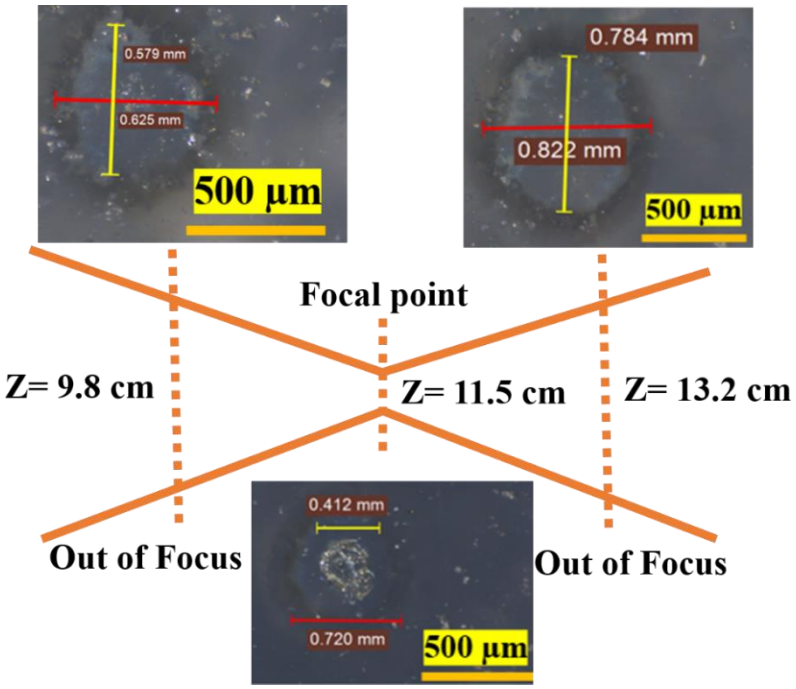

Fig. 5.26: Characteristic variation of stand-off distance towards material ejection and its associated feature size

5.3.1(d) Influence of laser pulse overlaps towards selective ZnO seed layer transfer

Based on laser fluence and stand-off distance as fixed in above section, the variation of laser pulse overlap is analyzed, and the associated varying parameters are mentioned in the table 5.12 below.

Sample details	Processing Parameters			
	Spot dia. (mm)	Rep rate (hz)	Velocity (mm/min)	overlap (%)
A	0.720	10	50	90
B	0.720	10	85	80
C	0.720	10	115	70
D	0.720	10	145	65

Table 5.12: Laser processing parameters for analysing the influence of laser pulse overlap

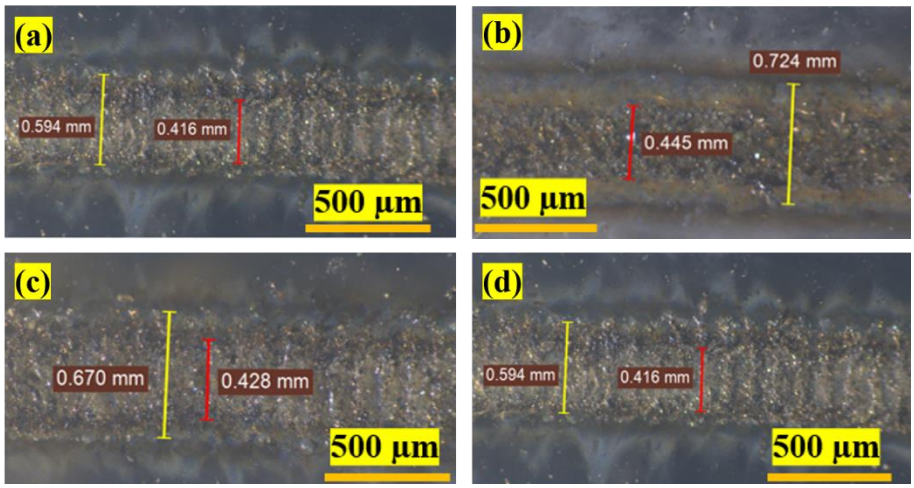

Fig.5.27: Microscopic analysis of influence of pulse overlaps towards effective material transfer and generated heat affected zone.

The material ejected at various parameters as mentioned in table 3 was analyzed using microscope to analyze the effective material ejection zone and total trach width thus formed. It was observed that pulse overlaps have a major impact on both effective material ejection zones as well as heat effective zone formation. From the analysis, it was observed that as laser pulse overlap decreased from 90% to 65%, the effective area of material transfer also reduces. However, the formed heat affected zone drastically drops down and pose great control in feature size as well. It is however also observed that continuity of the transferred material also dropped down hence the study was restricted to 65% pulse overlapping.

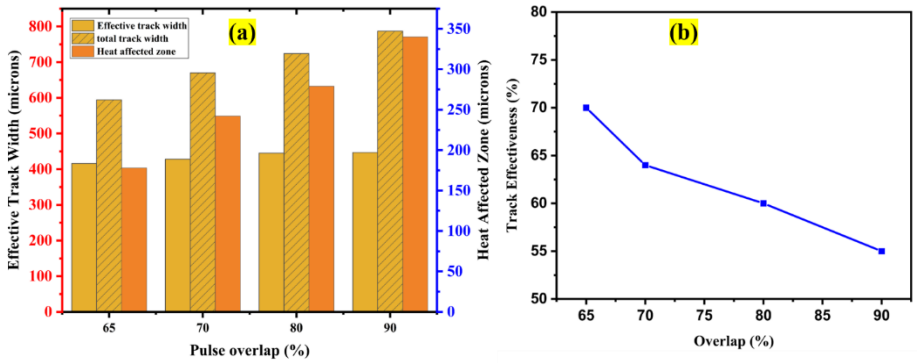

Fig. 5.28. (a) plots the effective track width, heat affected zone and total track width formed with increasing pulse overlap and (b) represents plot of % effectiveness in track vs % pulse overlap.

Fig. 5.27 and Fig. 5.28 represent the microscopic images and its associated plots to analyze the influence of pulse overlap. Track effectiveness is calculated as the ratio of effective area where material is transferred to the total track width observed. It is observed that as the % overlap increases, the track effectiveness decreases, and more heat affected area is formed when compared with the effective material transfer area. It is essentially because the energy interaction in a zone keeps on increasing as pulse overlaps increases which in turn would affect the sacrificial layer melting as well and thus causes higher heat affected zone formation when compared with lower pulse overlaps.

Based on the above analysis, an optimum stand-off distance of 12.5 cm, laser fluence of 75 J/cm^2 and a pulse overlap of 65% was used for

selectively positioning ZnO seed layer as a layer of material in multi-material transfer.

5.3.2 Morphological and compositional characterization: To confirm the transfer of ZnO seed layer, a SEM micro-graph was taken for both spots as well as for line formed at above optimized parameters as mentioned in Fig.5.29 and was then hydro-thermally grown further. It was observed that hexagonal nano-rods were formed uniformly grown all along the track (see Fig. 5.29).

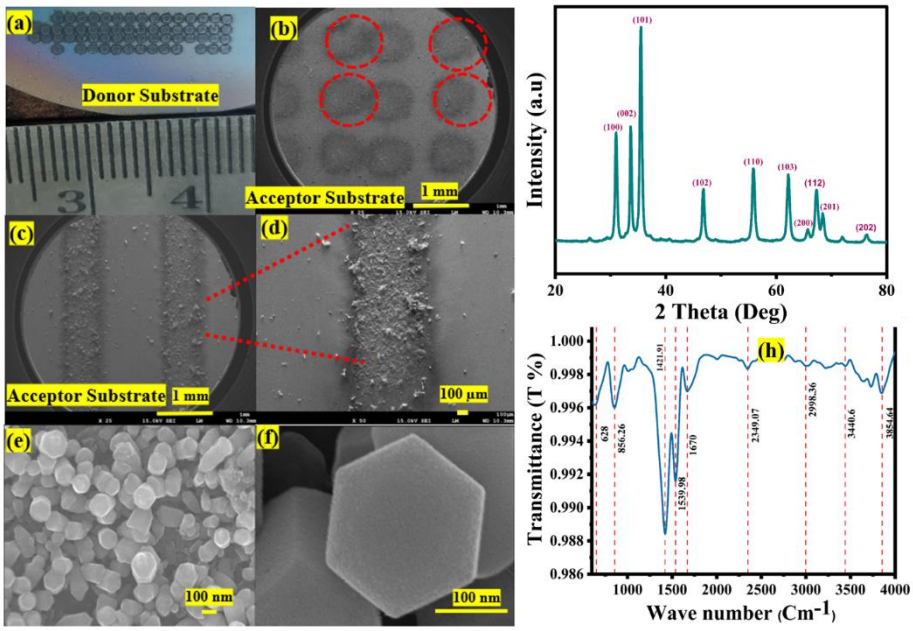

Fig. 5.29. (a-d) Control parameters for fabrication of dot and line structure at feature sizes ranging between (420-460 µm), (e-f) represents SEM micrograph of ZnO nanostructure at 100 nm scale, (g) represents XRD plot of ZnO being transferred and grown and (h) represents its FTIR plot.

The X-ray diffraction (XRD) analysis reveals diffraction peaks that are indicative of zinc oxide (ZnO) in its hexagonal wurtzite crystal structure, recognized as the most thermodynamically stable form of ZnO. The patterns display distinct diffraction peaks at specific 2θ angles, approximately 31.7°, 34.4°, 36.2°, 47.5°, 56.6°, 62.8°, 66.3°, 68.0°, and 69.2°, which correspond to the (100), (002), (101), (102), (110), (103), (112), (200), and (201) crystallographic planes, respectively. These observations are consistent with the standard diffraction data for hexagonal ZnO (JCPDS No. 36-1451), thereby confirming that both

samples crystallize in the well-established wurtzite phase. The most prominent peak in both samples is noted at approximately 36.2°, aligning with the (101) plane. This finding suggests that the transferred ZnO demonstrates a preferred orientation along this specific crystallographic plane, a characteristic often observed in ZnO nanostructures due to the inherent properties of the wurtzite structure. The relative intensity of the (101) peak, in comparison to other peaks, indicates a significant preferential growth along this plane, particularly in the c-axis direction.

The Fourier Transform Infrared Spectroscopy (FTIR) analysis of the sputtered ZnO seed layer reveals transmittance across a broad spectrum of wavenumbers (4000–500 cm^{-1}), which indicates the existence of functional groups and chemical bonds related to Zinc Oxide (ZnO) as well as other potential constituents within the sample matrix. In the FTIR spectrum illustrated in Fig. 5.29h, several distinct peaks are identified at various wavenumbers, reflecting the vibrational modes of different chemical bonds. Noteworthy peaks at 628 cm^{-1} and 856.26 cm^{-1} are typically linked to Zn–O stretching vibrations, thereby affirming the presence of ZnO matrix in the sample. The peak observed at 1421.91 cm^{-1} is likely attributed to C–O stretching vibrations, suggesting the potential absorption of atmospheric CO_2 or other carbon-based entities on the ZnO surface. Additionally, a significant peak around 1539.98 cm^{-1} may correspond to bending vibrations of adsorbed water molecules or hydroxyl groups (-OH) present on the surface. The broad absorption band at 1670 cm^{-1} further corroborates the existence of surface -OH groups, likely due to atmospheric moisture. Other peaks at 2349.07 cm^{-1} and 2998.36 cm^{-1} may indicate residual organic materials or the stretching vibrations of C–H bonds, possibly originating from organic molecules that persist from the synthesis process or surface adsorption. The peak near 3854.64 cm^{-1} could signify O–H stretching vibrations of surface hydroxyl groups or physically adsorbed water.

5.3.3 Multi-layer multi-material transfer analysis

To further analyze the functional capability of dynamic release layer based micro-3D printing towards multi-material printing, initially NiTi which was coated using belt deposition technique was transferred on a thin film of conductive ITO over glass substrate. After transfer, it is observed that the conductivity of material remains undisturbed, and no such material variation happened in ITO. To perform this process, the glass substrate was continuously heated up to 100 ºC while material transfer happened and then was left for normal cooling in ambient condition for the coating particles to settle down. Fig 5.30 (a-b) represents the material transfer in interdigitated form from the coated silicon wafer suggesting that material has escaped out of the donor substrate. Fig 5.30 (c-d) represents the uniform material transfer observed on the ITO coated glass without hampering the properties of ITO.

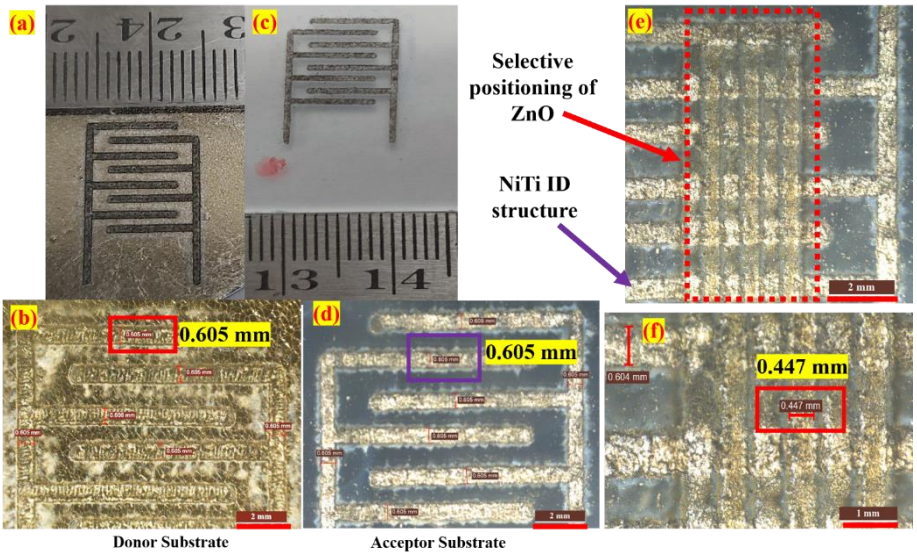

Fig.5.30. (a-b) represents NiTi interdigitated shape material transfer from donor and Fig. (c-d) shows NiTi interdigitated structures on Acceptor substrate (ITO). Fig.(e) represents selective positioning of ZnO tracks transversely over NiTi Interdigitated structures with feature size of 600 µm for ID structure and 400 µm for ZnO raster pattern and Fig. (f)representing zoomed in image of Fig. (e).

For the coating of ZnO over NiTi Interdigitated structure, substrate was heated to 100 ºC while three layers of ZnO seed layers were coated over

each other to obtain necessary thickness of coating as observed in the microscopic image (see Fig 5.30e) and it's zoomed in image is shown in figure 8f. While it is observed that for an optimized laser fluence, the obtained track width of NiTi was uniform throughout of 650 µm whereas for ZnO, it was observed in the range of 400-450 µm. It might essentially be due to expansion of metal due to energy interaction and pressure generated in the PDMS while for ceramic, the expansion is not much observed. Positioning errors were minimized by maintaining a near-focus stand-off distance of 11.5 cm, preventing material misalignment. The heat-affected zone (HAZ) was carefully controlled by adjusting pulse overlap and fluence, ensuring effective material transfer without excessive thermal damage. The material characterization discussed in the above sections were performed to confirm its intact properties and characteristics. The experimental analysis suggested that using the principle of laser decal transfer, we can essentially trace multiple material stacked one over the other in various alignments and laser as an energy source would prove great potential in future scope of technology in terms with electronics printing. This research demonstrates the feasibility of multi-layer, multi-material micro-3D printing using laser decal transfer, which holds great potential for fabricating complex sensors and electronic devices with controlled material gradients and high structural precision.

5.4 Detailed investigations on optimized printing of ZnO on flexible substrate

5.4.1 Investigation on ejection analysis: A detailed investigation on material ejection over flexible ITO coated PET for its utilization for functional applications. This Fig. illustrates the process and results of a laser decal transfer technique used to eject and redeposit ZnO material from a sputtered ZnO layer. The 3D profile image in Fig. 5.31a shows the ZnO ejection process, where laser energy is applied to a sputtered ZnO layer, causing a portion of the material to detach and form a cavity. The profilometry scan captures the depth, shape, and overall structure of this cavity, indicating the effectiveness of the laser energy in transferring

the ZnO material. The corresponding 2D profile in Fig. 5.31b shows the height profile across a horizontal cross-section of the ejected ZnO region, confirming the thickness of the ejected layer. A significant drop in height can be observed, which gives a quantitative measurement of the ZnO layer removed by the laser.

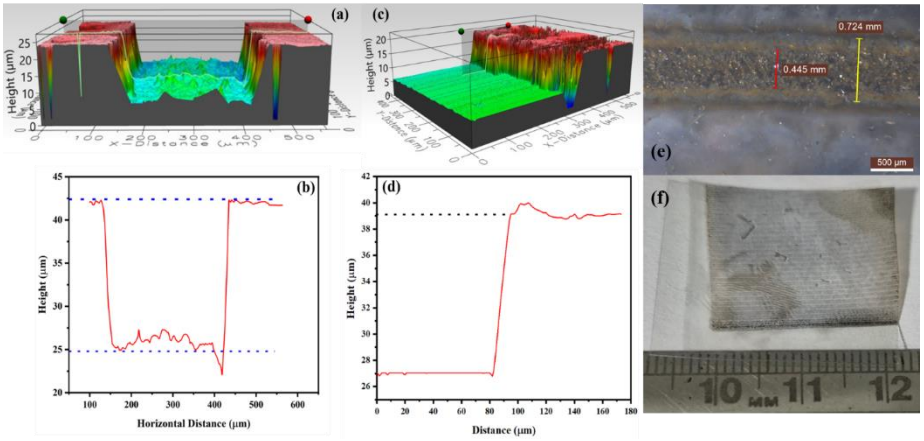

Fig. 5.31: (a) 3D surface profile of ZnO ejection from donor substrate, (b)2D profile of ZnO ejected presenting material ejection, (c) 3D surface profile of ZnO sputtered on donor substrate, (d) 2D profile of sputtered ZnO, (e)optical microscopy image of transferred single track and, (f) a 2.5cm × 2.5 cm ZnO mat printed for piezo energy sensing and harvesting.

After ejection, the ZnO material is redeposited on a substrate, as shown in the 3D profilometry scan in Fig. 5.31c. This scan reveals the morphology and thickness of the transferred ZnO material, now in a controlled deposition pattern. The 2D profile in Fig. 5.31d further confirms the deposited layer's thickness by plotting the height across a horizontal distance. The thickness measured here aligns with the depth of the ejected region in Fig. 5.31b, verifying that a consistent layer of ZnO was successfully transferred and deposited.

In Fig. 5.31e an optical microscope image displays the deposited ZnO track on the substrate. Measurements overlaid on the image indicate a track width of approximately 0.724 mm and a thickness of 0.445 mm, providing a visual confirmation of the uniformity and accuracy of the deposited material along the intended path. Lastly, Fig. 5.31f shows a photograph of a larger, rectangular mat of ZnO printed using the same

laser transfer technique. The mat is placed next to a ruler for scale, showcasing the flexibility of this technique to print ZnO over different geometries and dimensions. Together, these images and profiles highlight the potential of laser decal transfer as a precise method for patterning and depositing ZnO layers with controlled thickness and structure. The resolution of the laser-assisted sputtering process was measured at approximately 724 μm for line patterns, as shown in Fig. 5.31e.

5.4.2 Compositional and morphological analysis:

5.4.2(a) XRD and SEM analysis: The image presents a comprehensive analysis of Zinc Oxide (ZnO) nanostructures, combining morphological observation via Scanning Electron Microscopy (SEM) and elemental identification through Energy Dispersive X-ray Spectroscopy (EDS). In Fig. 5.32a, the SEM image reveals the intricate surface morphology of the ZnO nanostructures. The observed formations appear as densely packed, needle-like, or flake-like structures, indicative of nanostructured ZnO. These formations are characteristic of ZnO, a material known for its versatile nanostructured configurations, which include nanorods, nanosheets, and nanoflowers. The structures seen here are likely synthesized using chemical or physical deposition methods, which are commonly employed in ZnO preparation for use in fields like photocatalysis, gas sensing, and optoelectronic devices. The scale bar indicates that the structures are on the order of 1 μm, suggesting a nanoscale arrangement that could provide a high surface area-to-volume ratio. This nanoscale morphology is crucial for enhancing the performance of ZnO in applications such as solar cells or sensors, where surface interaction plays a significant role. Fig.5.32b features the EDS spectrum, which complements the SEM analysis by providing a quantitative elemental composition of the ZnO nanostructures. The EDS analysis focuses on identifying the elements present within the scanned area of the sample. The spectrum shows prominent peaks for zinc (Zn) and oxygen (O), confirming the presence of ZnO. The quantitative analysis, displayed in the upper-right corner of the spectrum, shows that

the material consists of 75.4% zinc by weight and 24.6% oxygen. These values closely match the expected stoichiometry of ZnO, where the zinc-to-oxygen atomic ratio is ideally 1:1. Minor peaks, such as the one for carbon (C), could indicate either surface contamination or residuals from the sample preparation process, such as carbon tape or organic solvents used during sample handling.

The combined SEM and EDS analysis presented in this image effectively validates the successful synthesis of ZnO nanostructures. The SEM image shows a well-defined, high surface area structure, while the EDS confirms the composition to be predominantly zinc and oxygen, with minor impurities. The needle-like or sheet-like morphology and the confirmed presence of Zn and O suggest that these ZnO nanostructures could be suitable for applications in gas sensors, UV detectors, photocatalysts, or antimicrobial agents. The high surface area provided by the nanostructures, coupled with the elemental purity indicated by the EDS analysis, underscores the material's potential for effective performance in these domains.

This extensive analysis highlights both the structural and compositional properties of ZnO, showcasing the importance of combining imaging techniques like SEM with elemental analysis like EDS to fully characterize nanomaterials for advanced technological applications.

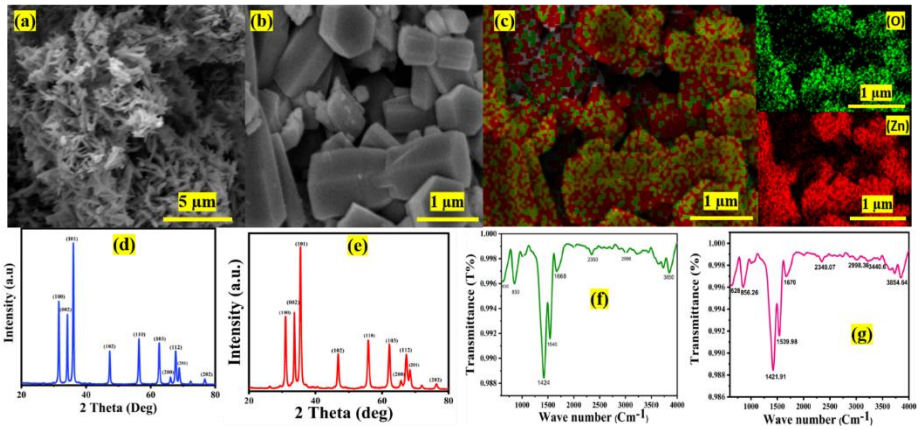

Fig. 5.32: (a,b) SEM analysis of transferred ZnO,(c) EDX mapping of transferred ZnO over ITO-coated PET sheet, (d,e) represents XRD analysis of sputtered seed layer and laser decal transferred ZnO over ITO-coated PET respectively and, (f,g) represents FTIR spectroscopy

suggesting various functional groups in sputtered ZnO seed layer and transferred ZnO seed layer over ITO-coated PET substrate respectively.

The X-ray diffraction (XRD) patterns shown for the sputtered seed layer (fig. 5.32d) and laser-transferred and systematically grown sample (fig. 5.32e) depict the diffraction peaks characteristic of zinc oxide (ZnO) in its hexagonal wurtzite crystal structure, which is the most thermodynamically stable form of ZnO. Both patterns exhibit well-defined diffraction peaks at distinct 2θ angles, located at approximately 31.7°, 34.4°, 36.2°, 47.5°, 56.6°, 62.8°, 66.3°, 68.0°, and 69.2°, which correspond to the (100), (002), (101), (102), (110), (103), (112), (200), and (201) crystallographic planes, respectively[21]. These peaks align with the standard diffraction data for hexagonal ZnO (JCPDS No. 36-1451), confirming that both samples crystallize in this well-known wurtzite phase.

The most intense peak in both samples is observed at approximately 36.2°, corresponding to the (101) plane. This indicates that both samples exhibit a preferred orientation along this crystallographic plane, which is common for ZnO nanostructures due to the intrinsic properties of the wurtzite structure. The relative intensity of the (101) peak compared to other peaks suggests a strong preferential growth along this plane, particularly in the c-axis direction, often occurring during the synthesis process.

Despite the similarity in peak positions, which suggests that both samples possess similar lattice constants and have not undergone significant strain or lattice distortion, there are notable differences in the intensities and sharpness of the peaks between the sputtered seed layer and laser-transferred and solvothermal grown ZnO. The peaks in sputtered ZnO are more intense and sharper than in laser-transferred ZnO. Peak intensity is directly related to the material's crystallinity: higher intensities typically indicate better crystallinity, meaning fewer structural defects such as dislocations, grain boundaries, or vacancies. The sharper peaks in sputtered ZnO suggest that the crystallite size in

this sample is larger than ZnO grown. This is consistent with the Scherrer equation, which relates the broadening of diffraction peaks to the crystallite size; broader peaks indicate smaller crystallites, while sharper peaks indicate larger crystallites.

Moreover, the absence of any noticeable shift in the 2θ positions of the peaks between the two patterns indicates that the lattice parameters are consistent in both samples. Any such shifts would imply lattice distortion, often caused by factors such as doping or external stress. In this case, the identical peak positions suggest that no significant compressive or tensile strain is present, and both samples maintain the same unit cell dimensions, likely without any incorporation of foreign elements.

Overall, both XRD patterns confirm that the samples are ZnO with a hexagonal wurtzite structure, but they exhibit differences in crystallinity and crystallite size. Fig. 5.32e demonstrates superior crystallinity, with sharper and more intense diffraction peaks, likely due to larger crystallites and fewer defects. In contrast, fig. 5.32d shows broader and less intense peaks, indicating smaller crystallite sizes and potentially more defects. The similarities in peak positions imply that both samples have identical lattice parameters, with no evident strain or phase changes. These differences could be due to variations in the synthesis or post-synthesis treatments, such as annealing conditions, solvent types, or reaction times, which play a critical role in determining the structural properties of ZnO Nanomaterials.

5.4.2(b) FTIR analysis: Fig.5.32(f,g) represents Fourier Transform Infrared Spectroscopy (FTIR) spectra of sputtered ZnO seed layer and transferred seed layer over ITO-coated PET substrate, both exhibiting transmittance over a wide range of wavenumbers (4000-500 cm^{-1}), indicating the presence of functional groups and chemical bonds associated with Zinc Oxide (ZnO) and other potential components in the sample matrix. In this FTIR spectrum of Fig. 5.32f, multiple characteristic peaks are observed at different wavenumbers, signifying

the vibrational modes of various chemical bonds. Key peaks are observed at 630 cm^{-1} and 850 cm^{-1}, which are typically associated with Zn–O stretching vibrations. These bands confirm the presence of the ZnO matrix in the sample. The peak at 1424 cm^{-1} is likely due to the presence of C–O stretching vibrations, indicating the possible absorption of atmospheric CO_2 or other carbon-based species on the surface of ZnO. Another notable peak is observed around 1540 cm^{-1}, which could be related to bending vibrations of adsorbed water molecules or hydroxyl groups (-OH) on the surface. The broad absorption band at 1668 cm^{-1} further supports the presence of surface-OH groups, likely resulting from atmospheric moisture. Other peaks are observed at 2350 cm^{-1} and 2996 cm^{-1}, which may correspond to residual organic components or the stretching vibrations of C–H bonds, possibly from organic molecules that remain from the synthesis process or surface adsorption. The peak near 3850 cm^{-1} could represent the O–H[24] stretching vibrations of surface hydroxyl groups or physically adsorbed water.

The FTIR spectra of Fig. 5.32g presents vibrational modes that appear like the FTIR of the ZnO seed layer but with slight variations in peak intensities and positions. The Zn-O stretching bands are again identifiable at lower wavenumbers, notably at 628 cm^{-1} and 856 cm^{-1}, indicating the presence of ZnO nanostructures. The close similarity between these bands and those in the ZnO seed layer suggests a consistent ZnO composition in both samples.

The peak at 1421.91 cm^{-1} in Fig. 5.32 g is nearly identical to the 1424 cm^{-1} peak, again corresponding to the C–O stretching vibration. Similarly, the peak around 1539.98 cm^{-1} may be attributed to water molecules or hydroxyl group vibrations, closely mirroring the peak observed in Fig. 5.32 f around 1540 cm^{-1}. A distinct peak at 1670 cm^{-1} suggests some slight difference in the amount or type of hydroxyl groups or water content when compared to Fig. 5.32 f. At higher wavenumbers, we observe peaks at 2349 cm^{-1}, 2998 cm^{-1}, 3640.6 cm^{-1}, and 3854.64 cm^{-1}, which correspond to the stretching vibrations of O-H and C-H

bonds. These peaks are consistent with the presence of surface-bound hydroxyl groups and potential organic residues on the ZnO surface. The higher wavenumber peaks could also reflect atmospheric contamination or unreacted precursors from the synthesis process.

Both FTIR spectra reflect the typical signature of ZnO, with distinct Zn-O stretching vibrations at low wavenumbers confirming the structural integrity of the ZnO matrix. The variations in peak intensity and slight shifts in wavenumber between the two spectra may indicate differences in surface chemistry, such as varying levels of hydroxylation, water content, or surface-adsorbed organic species. These differences could arise from different synthesis conditions, sample treatments, or environmental exposure, affecting the surface properties of the ZnO nanostructures. The hydroxyl and carbon-based groups identified by the characteristic vibrational peaks suggest that the ZnO surface may have undergone functionalization or adsorption, influencing its potential applications in areas such as catalysis, sensing, or biomedical use.

It is however worth mentioning that while photolithography achieves superior resolution and is widely used for MEMS fabrication, it requires multiple processing steps, including resist deposition, exposure, development, and material etching. Additionally, photolithography often requires specific substrate compatibility and introduces challenges in transferring functional materials without altering their properties. In contrast, the laser-assisted transfer method demonstrated here simplifies fabrication by enabling direct deposition of functional materials onto diverse substrates without intermediate processing steps. However, it is acknowledged that the resolution of the current technique is limited compared to photolithography, and strategies to improve precision and scalability are part of ongoing research.

The demonstrated process ensures the preservation of the chemical and functional properties of ZnO, a thermodynamically stable material, under the applied laser processing conditions. However, it is recognized that the transfer of thermodynamically metastable materials may result

in phase transitions or alterations due to the localized thermal effects of the laser. Addressing these challenges requires further investigation into optimized laser parameters or alternative material systems.

5.4.2(c) XPS analysis: Fig. 5.33 presents the X-ray Photoelectron Spectroscopy (XPS) analysis of sputtered ZnO seed layers on PDMS coated silicon and transferred ZnO on polyethylene terephthalate (ZnO-PET), highlighting the differences in their chemical environments and bonding characteristics. The wide-scan spectra in Fig. 5.33(a) reveals the elemental composition and binding energy peaks for Zn and O, which are the key constituents of ZnO. Notably, the intensity of the Zn 2p and O1s peaks is significantly higher for donor substrate compared to ZnO-PET (acceptor). This observation suggests a denser and more uniform ZnO layer formation on the donor substrate, attributed to the better adhesion and chemical interaction. In contrast, the lower peak intensity for ZnO-PET reflects weaker ZnO bonding and comparatively reduced material absorption on the polymeric substrate. It is however noted that there is effective transfer and growth of ZnO over PET substrate for analysing its functional properties.

The high-resolution Zn 2p spectra is shown in Fig. 5.33(b), which is decomposed into two peaks corresponding to Zn 2p3/2 and Zn 2p1/2. For ZnO seed layer, the Zn 2p3/2 peak is observed at 1042.9 eV, while the Zn 2p1/2 peak appears at 1019.8 eV. These peaks are consistent with Zn–O bonding in ZnO. Interestingly, for ZnO-PET, the same Zn 2p3/2 and Zn 2p1/2 peaks are shifted to slightly higher binding energies. The shift, typically attributed to changes in the local chemical environment and bonding strength suggesting presence of ZnO bonding to the PET substrate. The shift could be due to the lower polarity and weaker surface interactions of the organic PET substrate compared to the seed layer.

Fig. 5.33(c) and Fig. 5.33(d) present the high-resolution O 1s spectra for ZnO-over PDMS coated Silicon and ZnO-PET, respectively, providing deeper insights into the oxidation states and chemical bonding. For ZnO-Si (Fig. 5.33(c)), the O 1s peak is deconvoluted into two components: a

dominant peak at 529.3 eV corresponding to lattice oxygen (O2-) in Zn-O bonding and a smaller peak at 531.4 eV attributed to surface hydroxyl groups (O-H or Zn-OH bonding). In contrast, for ZnO-PET (Fig. 5.33(d), the peak corresponding to O2 shifted to a slightly higher binding energy of 529.5 eV, while the 531.4 eV peak is notably more intense. This enhancement in the hydroxyl-related peak suggests an increase in surface oxygen-related defects and weaker lattice bonding of ZnO on PET. The shift in the O 1s peak for lattice oxygen and the relative intensity changes indicate that the bonding strength and structural quality of ZnO on PET is comparatively less than on donor substrate.

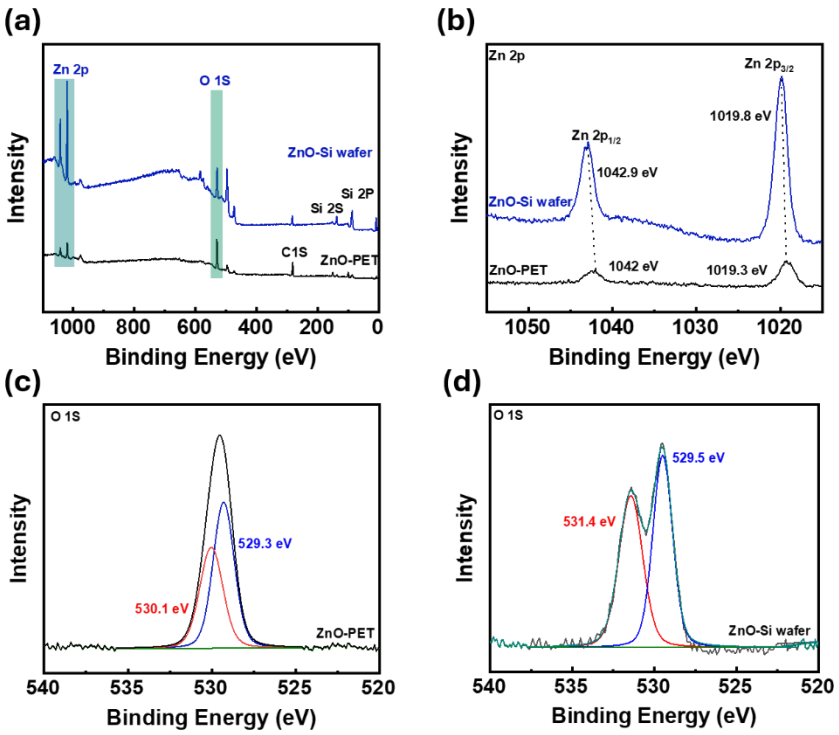

Fig. 5.33: XPS plot of sputtered ZnO seed layer and transferred and grown ZnO over PET.

The XPS analysis reveals that ZnO exhibits stronger adhesion robust bonding over both donors (PDMS coated silicon wafer) and acceptor (PET) substrate. This is evident from the higher peak intensities, lower binding energy shifts, and reduced hydroxyl defect states observed for ZnO-Si. These findings highlight the superior material integration of ZnO and its successful transfer which is crucial for applications

requiring high-performance optical and electronic interfaces. The weaker bonding on PET, while potentially advantageous for flexible applications, might necessitate further surface treatments or interlayers to enhance the stability and adhesion of ZnO on polymeric substrates.

5.5 Summary

A laser-assisted micro-3D printing technique was developed that utilized the laser micro-3D printing technique to enable precise deposition of less dense metals such as aluminum and high dense ceramics such as SiC and ZnO on flexible and rigid substrates for its functional applications. Based on the above discussion, key points are summarized below.

Aluminum Printing

- The parametric study established that at a stand-off distance (SOD) of 10.5 cm, the laser beam is optimally focused, resulting in highly uniform pixel ejection and clean deposition with minimal edge distortion.
- At a reduced SOD of 8.5 cm, no material transfer occurred due to beam defocusing, while an increased SOD of 11.5 cm led to scattered and inconsistent transfer with lower track quality.
- The optimal laser fluence was found to be 92 J/cm², providing sufficient thrust force to overcome adhesion without damaging the donor layer, achieving a maximum material transfer efficiency of ~75%.
- Pulse overlaps significantly influenced deposition quality. The best results were observed at 80-85% overlap, ensuring uniform energy delivery and minimizing unfilled zones or overburned regions.
- A design of experiments (DOE) approach using Box-Behnken Design (BBD) evaluated the effects of fluence, SOD, and overlap on track dimensions across 15 experimental runs.

- Regression modelling and ANOVA for track width revealed that SOD (F = 123.74) and pulse overlap (F = 88.95) were dominant factors, while laser fluence had a moderate impact (F = 33.02). The model achieved R^2 = 99.75%, Adj. R^2 = 99.17%.
- The optimal track width was predicted to be 543.17 µm at 120 J/cm² fluence, 12.5 cm SOD, and 90% overlap, with a composite desirability of 0.9321 from the multi-response optimization.
- For track height, the regression model also showed high accuracy (R^2 = 99.79%, Adj. R^2 = 99.42%), with pulse overlap square (Z^2) being the most significant term (F = 1810.12), indicating sensitivity to energy stacking.
- The maximum track height was obtained as 4.6647 µm at the same optimal parameters, validating the coupled optimization of height and width for ideal micro-feature formation.
- Various geometries linear (0.673–0.820 mm), sinusoidal (~0.916 mm), and spiral square (~0.790 mm) were printed with consistent width and resolution, demonstrating the system's flexibility and control in complex pattern fabrication.

SiC Printing

- Laser transfer of sputtered SiC thin films was also achieved. The optimal SiC transfer occurred at 10.5 cm SOD, 4.3 W power, and 70% overlap, producing continuous tracks with widths ~0.35–0.45 mm and sharp edge definition.
- Thermal assistance via substrate heating to 100°C improved vertical stacking of SiC features by enhancing melt pool stability and reducing surface tension effects.
- XRD analysis of printed SiC confirmed the presence of polycrystalline β-SiC peaks while SEM showed granular structures that supported efficient laser energy absorption and uniform ejection.

ZnO Printing

- ZnO thin films were first deposited using RF sputtering onto a donor wafer, producing uniform crystalline layers with strong adhesion and consistent surface coverage suitable for laser-induced transfer.
- The laser decal transfer technique was applied to print ZnO micro-patterns onto both rigid (Si) and flexible (PET) substrates. The process relied on precise control of laser fluence, stand-off distance, and overlap to achieve clean pixel detachment without damaging the underlying donor film.
- On solid substrates, optimal transfer was achieved at a laser fluence of ~92–100 J/cm², stand-off distance of ~11.5 cm, and pulse overlap of ~80–85%, resulting in sharply defined tracks with widths in the range of 400–600 µm and minimal debris.
- The printed ZnO features on glass showed strong adhesion and retained their original crystalline morphology, as confirmed by SEM and XRD, with peak positions corresponding to the hexagonal wurtzite structure.
- On flexible substrates, the laser-induced transfer process was successfully adapted by optimizing the energy input to avoid substrate warping. Clean ZnO pixel deposition was achieved with slightly reduced fluence (~85–90 J/cm²) to account for lower thermal tolerance.
- SEM analysis on flexible PET/PI substrates revealed wrinkle-free deposition with good line continuity and well-retained microstructures. The transferred features maintained lateral resolution (~500–550 µm) with minimal edge diffusion.
- EDX mapping confirmed the uniform distribution of Zn and O on both substrate types, with no detectable contamination or degradation, indicating the non-destructive nature of the transfer process even for thermally sensitive flexible materials.
- The results demonstrated that laser-assisted ZnO printing is highly versatile and scalable for both rigid and flexible electronics, enabling selective deposition, spatial resolution

control, and material compatibility across diverse substrate platforms.

The developed technique offers sub-millimeter resolution, high repeatability, design flexibility, and material compatibility, making it suitable for the prototyping of MEMS structures, sensor tracks, and patterned electrodes.

Chapter 6

This chapter describes the integration of laser direct writing and laser micro-3D printing for fabrication of functional hybrid energy harvesting devices and sensors.

Integrating Laser direct writing and laser µ-3D printing for hybrid nanogenerators

6.1 Integration of Laser µ-3D printing of ZnO Ceramic in LIG

The dual-utilization of single laser source for fabrication of laser induced graphene (LIG) by direct laser writing (DLW) technique as well as selective doping of ZnO in fabricated laser Induced graphene using laser decal transfer technique is explored and as mentioned in figure 6.1. The schematic illustrates the integrated fabrication approach for a hybrid piezo-triboelectric nanogenerator (PTENG) that utilizes a combination of direct laser writing (DLW) and micro-3D printing via laser decal transfer**.** The device is composed of a flexible layered architecture where the active material, a ZnO-LIG (Laser-Induced Graphene) composite**,** is sandwiched between an FEP tribo-layer and compliant mechanical supports. This configuration enables simultaneous harvesting of piezoelectric and triboelectric energy under mechanical stimuli, with each transduction mechanism contributing through a rectified bridge circuit to a unified hybrid output.

The fabrication process begins with the laser-induced conversion of polyimide (Kapton) into graphene by direct laser writing. Using a CO_2 or near-infrared laser, the surface of the Kapton substrate is selectively photothermally reduced to create porous, conductive graphene structures known as LIG. This step offers maskless, high-resolution, and scalable patterning of electrode layers with tunable sheet resistance and mechanical flexibility. Subsequently, ZnO nanostructures are transferred and positioned precisely onto the LIG surface using **a** laser decal transfer technique**.** This micro-3D printing method involves laser-mediated pick-and-place deposition of ZnO from a donor substrate onto

the pre-patterned LIG, enabling clean, localized placement without the need for wet chemical processing or adhesive bonding. The laser decal transfer setup, shown in the center of the figure, allows for micro-level positioning accuracy and integration of ZnO features in customized shapes and densities. The final assembly integrates the LIG-ZnO composite as an electrode material, capable of enhancing charge transfer due to the synergistic interaction between ZnO's piezoelectric properties and LIG's high conductivity and surface area. The modular design enables not only geometric control over the active layer but also mechanical robustness for flexible energy harvesting. This dual-laser strategy-direct laser writing for in-situ graphene synthesis and laser micro-3D printing for ZnO integration-demonstrates a fully digital and scalable route for the fabrication of multifunctional hybrid nanogenerators. A detailed investigation on its graphene synthesis and selective transfer of coated ZnO at optimized parameter is explored in this study followed by piezo-electric and tribo-electric performance and its utilization towards hybrid piezo-tribo applications.

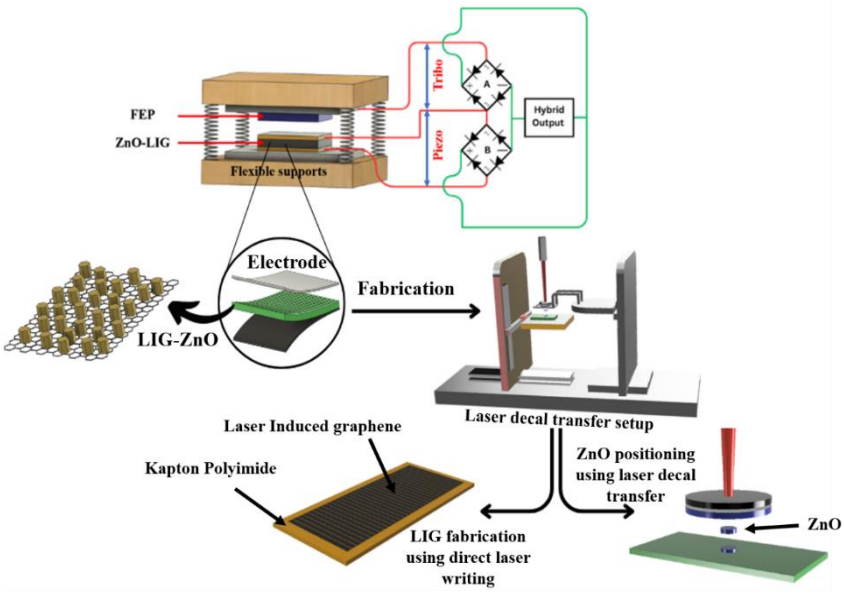

Figure 6.1: Schematic showing utilization of 10.6 µm CO_2 laser for Laser induced graphene synthesis and selectively doping ZnO ceramic in LIG using laser µ-3D technique for functional applications.

6.1.1 Microscopic and profilometric analysis for Transfer efficiency calculations:

The coating thickness was analyzed using Filmetrics non-contact type optical surface profilometer and it was observed that the PDMS sacrificial layer which was spin coated presented a thickness of ~ 2 µm. The transfer efficiency of laser µ-3D was calculated as the ratio of volume of deposited pixel over acceptor to the volume of transferred pixel from the donor substrate.

Here transfer efficiency is given by

$$\eta_{transfer} = \frac{volume\ of\ deposited\ pixel\ over\ acceptor}{Volume\ of\ transferred\ pixel\ from\ donor\ substrate}$$

Or

$$\eta_{transfer} = \frac{Thickness\ over\ acceptor\ x\ \frac{\pi}{4}(track\ width\ of\ acceptor)2}{Thickness\ over\ donor\ x\ \frac{\pi}{4}(track\ width\ of\ donor)2}$$

At optimum Percentage overlap of 65%, the processing parameters i.e. laser fluence which is dependent on varying laser duty cycle and repetition rate was varied and appropriately all the essential calculations were performed. Figure 6.2 (1) presents the microscopic image of donor substrate (left) from where sputtered ZnO is ejected and acceptor substrate (right)presenting ZnO transfer over the substate at varying processing parameters as mentioned in table 6.1. Based on the processing parameters, the average track width for donor and acceptor was measured to calculate the area coefficient for volume calculations. Similarly, surface profilometry analysis is performed to measure the thickness of material ejected from donor substate and transfer over acceptor substrate. Figure 6.2 (3) depicts the surface profilometric analysis of donor (subscript as D i.e. A_D, B_D and C_D) and acceptor substrate (subscript as A i.e. A_A, $B_A$and C_A) presenting material ejection from donor and transfer over acceptor substrate. A bar chart for both track width and track height/depth are presented in figure 6.2 (2).

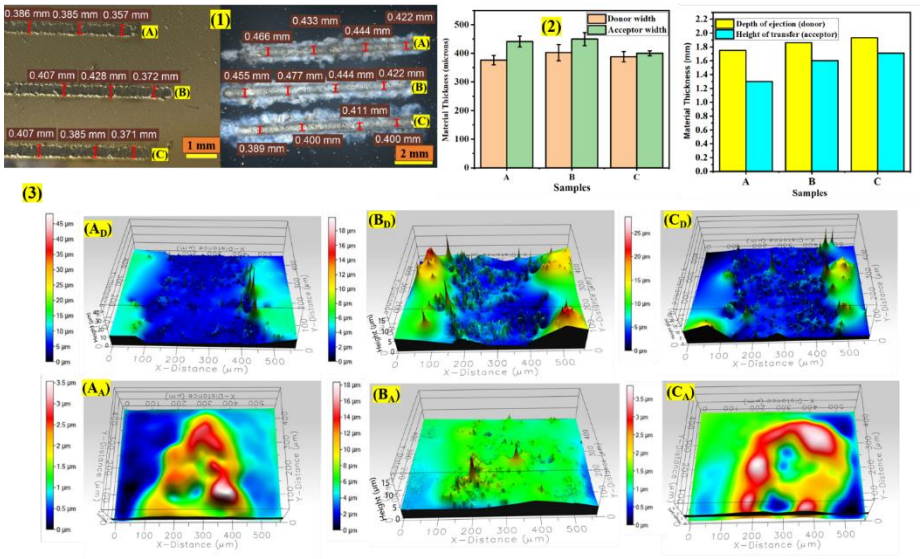

Figure 6.2: Microscopic results of (1) Material ejected from donor material(left) and material transfer over acceptor(right), (2)track width calculation of material ejected from donor and material transfer over acceptor (left) and thickness of material ejection from donor and transfer on acceptor(right), (3) surface profilometric analysis of material ejection from donor(subscript D) and material transfer over acceptor (subscript A) with A,B,C at varying processing parameters.

Sample No.	Processing parameters		Track width		Material height/depth		Transfer efficiency (%)
	Rep Rate (Hz)	Duty cycle (%)	Donor (microns)	Acceptor (microns)	Donor (microns)	Acceptor (microns)	
A	10	3	398.2	441.0	1.75	1.10	73
B	10	6	402.3	449.5	1.86	1.30	86.75
C	10	9	387.8	400.0	1.93	1.52	83.70

Table 6.1: Track width and Track height/dept measurement for transfer efficiency calculations

Based on the experimental outcomes, it is observed that the effective transfer efficiency was observed at laser fluence of 75 J/cm^2 corresponding to the repetition rate of 10 Hz and duty cycle of 6% with effective value of 86.75% and hence is used for further experimental analysis.

6.1.2 Selective positioning of ZnO Seed layer in LIG:

To analyze the selective positioning of ZnO seed layer, the material ejection and its adhesion with the substrate was analyzed by transferring it in the form of dots and track over glass slide. The material ejection from the donor substrate occurs due to sufficient gas pressure that is induced in the PDMS sacrificial layer.

Processing Parameters	Units	Optimized values (LIG)	Optimized values (ZnO)
Repetition Rate	Hz	10	10
Duty cycle	%	2	6
Spot diameter	µm	~567 (effective)	~720 (effective)
Laser fluence	J/cm^2	56	75

Extent of focus	cm	11.5	11.5
% pulse overlap	%	70	65

Table 6.2: Optimized process parameters for LIG fabrication and laser μ-3D-based material transfer for selective position.

The LIG was synthesized over Kapton polyimide, and selective ZnO positioning was achieved using optimized parameters, as shown in Figure 7. The process parameters, listed in Table 6.2, were set to a laser fluence of 75 J/cm² and a pulse overlap of 70% to ensure uniform and controlled material transfer. Figure 6.3(c) demonstrates the controlled ejection and selective transfer of the ZnO seed layer at three distinct positions on the LIG surface, with varying transfer lengths of 1.5 mm, 2.0 mm, and 2.5 mm. This selective transfer process allows precise placement of ZnO seeds layers. ZnO nanorods were then hydrothermally grown on the selectively transferred ZnO seed layer using a hexamethylenetetramine (HMTA) hydrothermal solution. The selective growth of ZnO nanorods within the graphene matrix was analyzed via SEM imaging and Energy Dispersive X-ray Spectroscopy (EDX) mapping, as shown in Figures 6.3(d) and 6.3(e). EDX confirmed the presence of Zn, O, and C at the transition zone between the selectively positioned and non-transferred areas. The SEM images in Figures 6.3(e) and 6.3(f) reveal a dense growth of ZnO nanorods in the selectively transferred regions, while only sparse traces of ZnO were observed in the non-transferred zones. This minimal ZnO presence in the non-transferred areas likely results from slight deposition during the hydrothermal growth process, where the sample was exposed to the solution. The morphology of the grown nanorods is clearly visible in the SEM images, with Figure 6.3(e) displaying detailed structural analysis of the ZnO nanorods, confirming successful selective growth on the laser-induced graphene.

Based on the optimized process parameters, the synthesis of LIG by direct laser writing using CO_2 laser follows selective seed layer positioning of ZnO using novel laser µ-3D technique for functional devices applications.

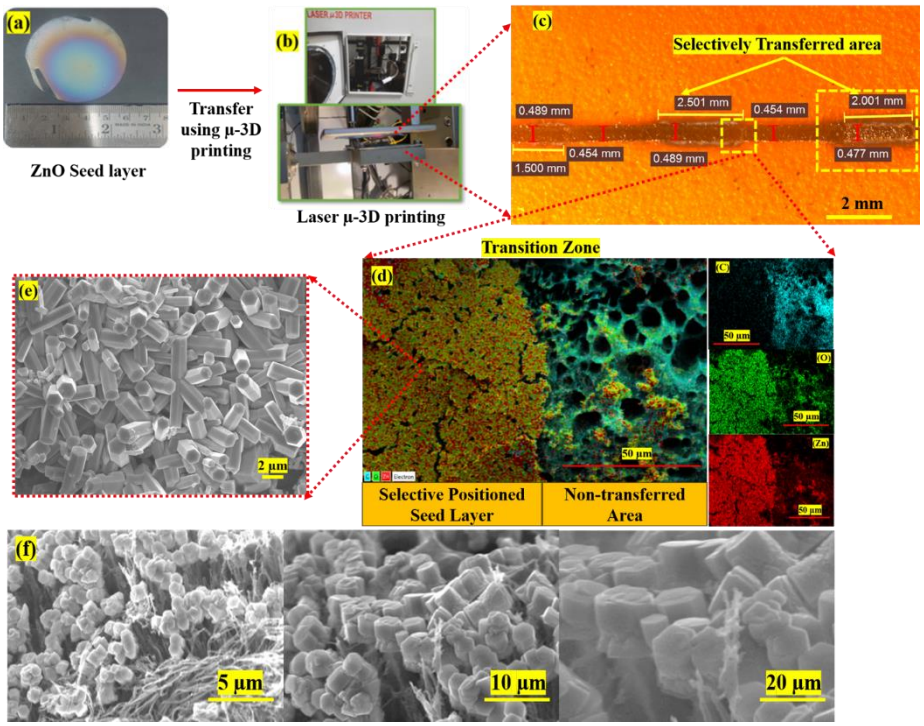

Figure 6.3: Experimental analysis for material ejection and selective ZnO positioning in LIG (a) sputtered ZnO seed layer, (b) laser µ-3D using laser µ- 3D printing, (c) depicting ZnO material ejection selectively in selective zones at different lengths(d) EDX mapping in transition Zone between selectively positioned seed layer and non-transferred area (e) morphological analysis of the hydrothermally grown ZnO and, (f) Low magnification and High magnification morphological representation of ZnO growth in the pores of Laser Induced graphene.

6.1.3 Compositional and Morphological Analysis:

The XRD analysis of sputtered thin film is represented in Figure 6.4a and as per previous reports, it generally shows polycrystalline nature with hexagonal structures as observed in morphological results (JCPDS 00-003-0888). There are many evident peaks in both sputtered seed layer (Figure 6.4) as well as grown ZnO nanorods in LIG (Figure 6.4b), however two major prominent peaks representing (002) at 34.2° and (103) at 62.7° is observed all through the thin film samples.These peaks

are thermodynamically suitable in ZnO based composites because of their least surface energy. It is evident that peak (002) sharpness increases in grown ZnO (Figure 6.4b) when compared with seed layer. This is essentially due to uniform crystalline growth because of the the composite being hydrothermally grown in $KMnO_4$-HMTA solution. It is also noticed that there is an evident drop in peak intensity of (103) when compared in composite (Figure 6.4b) with seed layer (Figure 6.4a). It is found that (103) plane predominates over (002) plane at high thickness film which is even observed in this case. The higher film thickness in sputtered seed layer the peak (103) at 62.7° is highly evident when compared with (002) peak at 34.2° whereas in LIG-ZnO composite, intensity of (103) peak is reduced when compared with (002) peak. Although ZnO nano-rods are grown and uniformly aligned, the intensity is reduced because the seed layer is selectively transferred in specific position and the material grows accrodingly at specific positions in LIG pores.

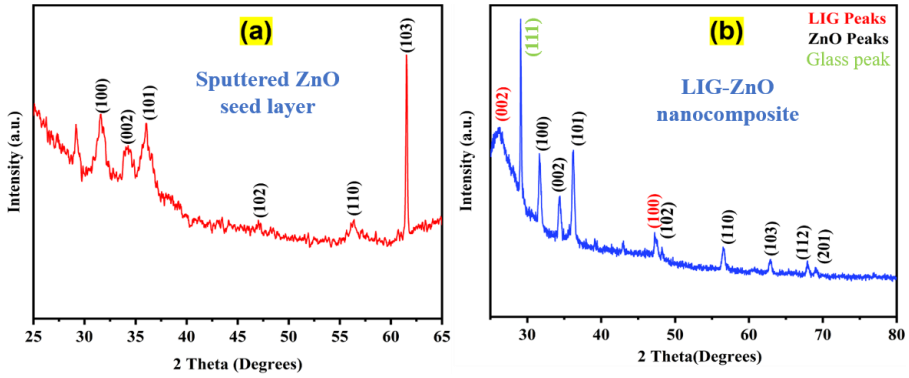

Figure 6.4: (a) XRD results of sputtered seed layer, and (b) XRD results of selectively transferred ZnO in LIG pores.

The other evident peaks confirm all diffraction peaks to be indexed to ZnO with wurtzite structure [space group: p63mc (180): a = 3.2512 Å and c = 5.2109 Å] and is in closer agreement with JCPDS file of ZnO (JCPDS 01-089-7102). The intense and sharp peak as observed demonstrates the crystallinity of grown ZnO. There are two evident LIG peaks at ~26° corresponding to (002) and ~47° corresponding to (100). Thus XRD suggests that there is successful transfer and growth of ZnO nanorods in LIG for its funtional analysis.

The surface morphology and structure of LIG-ZnO nanoparticle composites is characterized using scanning electron microscopy (SEM) and transmission electron microscopy (TEM). The micro-structures showed hexagonal close packed (HCP) crystal structure of ZnO, and porous graphene sheets are clearly identified. It is observed that LIG skeleton is fully and well wrapped by ZnO nanoparticles, especially at the edge of LIG fibrous flakes as observed. SEM results at higher magnification presents generation of mesoporous structures allowing ZnO to penetrate and react at their interfaces. The size of the nanorods were measured in ImageJ software and it was observed that the average length of ZnO nanoparticles was 2.92 ± 0.45 μm whereas the average diameter of the grown nanorods were 2.14 ± 0.40 μm. The density of distribution and growth of selectively positioned ZnO seed layer, and its growth followed thresholding technique, and it was observed that the gap between two ZnO nanorods were ~ 50 nm suggesting dense growth of nanorods. The cross-sectional SEM analysis presents that 3D structure of LIG and hexagonal shaped ZnO nanoparticles well deposited over the surface of fibrous ZnO. The Energy dispersive spectrometer (EDS) mapping analysis clearly demonstrates the presence of carbon, zinc and oxygen evenly distributed within the LIG-ZnO nanoparticle composite. Additionally, the cross-sectional results even suggest the nanoparticle composite successfully formed over flexible PI substrate and presents a better understanding towards composite fabrication in figure 6.5.

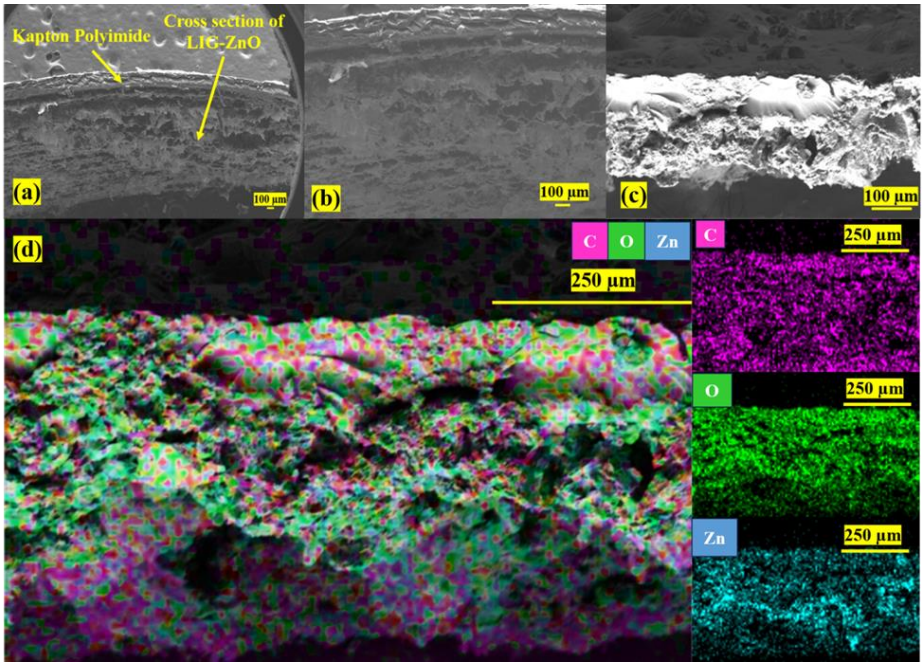

Figure 6.5: Cross sectional SEM and EDX result of fabricated sample (a-c) cross sectional SEM result, (d) EDX mapping and its elemental distribution confirming the presence of Zn, O and C.

The TEM images as observed in figure 6.6 (A-C) shows LIG film with d spacing of 3.796 Å and its selective area diffraction (SAED) pattern shows XRD corresponding to (002) at ~26° and (100) at ~47°. Figure 6.6 (D-F) presents even distribution of ZnO nanoparticles embedded in LIG flake with normal distribution size. The high-resolution TEM images present formation of few-layered graphene with ripple-like wrinkled polycrystalline structure at the edges due to laser energy interaction and its thermal expansion and distinct well-oriented lattice fringes in LIG. The fast Fourier transform (FFT) of HRTEM lattice fringes (Figure 6.6e, inset), LIG and ZnO nanoparticles obtain lattice fringes with spacings of $D_{(002)}$= 3.62 Å and $D_{(101)}$= 2.346 Å respectively. The ring like SAED Pattens (Figure 6.6 F) reveals polycrystalline structure of LIG (marked in blue) and ZnO (marked in yellow). The diffraction rings of LIG is indexed at (002) and (100) whereas that of ZnO is (100), (002), (101), (102), (200) and (112) planes, respectively of ZnO which is in good agreement with the results obtained from XRD patterns (JCPDS 01-089-7102). There are several weak asymmetric spots in (002) planes in synchronization with previous results.

Compared to the traditional hexagonal lattice structure of graphene, the TEM results of LIG shows a mixture of hexagon and Pentagon-heptagon hybrid lattice. It is essentially because there is no time for equilibration to the standard hexagonal lattice because of rapid cooling following laser irradiation.

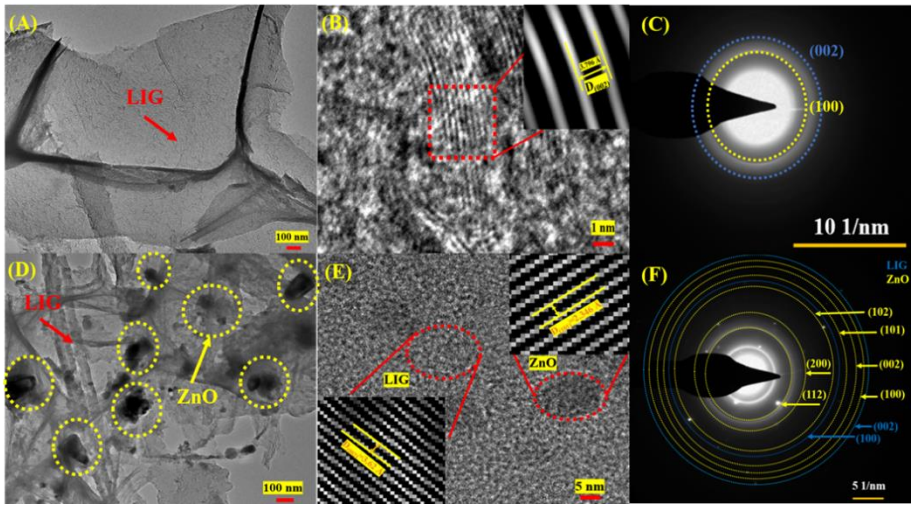

Figure 6.6: TEM images of LIG-ZnO nanocomposite formed by direct laser writing and laser decal transfer, (a-c) TEM, HR-TEM with FFT in inset and SAED pattern of LIG respectively and (e-f) TEM, HR-TEM with FFT in inset and SAED pattern of LIG-ZnO nanocomposite respectively.

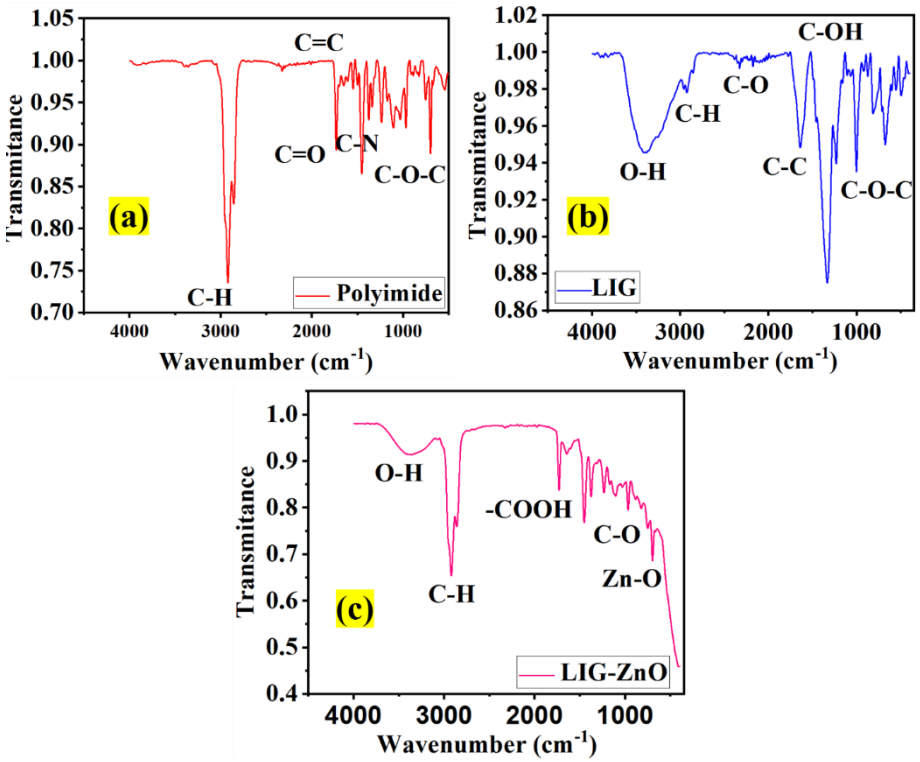

Figure 6.7: FTIR spectroscopy suggesting various functional groups

in (a) Plain/Pristine polyimide (b) Laser induced graphene and (c)LIG-ZnO nanocomposite.

To explore the LIG-ZnO nanocomposite formation and to investigate about the functional group thus formed over the surface of composite, FTIR spectroscopy was used for investigation. The FTIR spectra of plain polyimide, Laser Induced graphene and LIG-ZnO nanocomposite is shown in figure 6.7. There are evident oxygen functional groups peaks in the range of 1800 to 400 cm^{-1} in all the cases corresponding to different functional groups in the polyimide, LIG and LIG-ZnO nanocomposite thus formed. As seen in Figure 6.7(a) i.e., for plain polyimide, the presence of aromatic =C-H stretching in polyimide at 2981 cm^{-1} depends upon the thickness of polyimide and is intense in case of 125 μm thick sheet. The other evident peaks as observed are mentioned in the table below. As the laser energy is exposed on the polyimide, it transforms to conductive laser induced graphene thus forming evident peaks as seen in Figure 6.7(b). The absorption peak in the range 3600-3400 cm^{-1} is attributed to the presence of O-H groups and the peaks at 2928 and 2327 cm^{-1} are essentially due to asymmetric and symmetric C-H stretching bonds. There are C=C aromatic stretching peaks observed 1636 cm^{-1}. In addition to this, the peaks evident in the range 1263-1032 cm^{-1} and 914-600 cm^{-1} depict the stretching vibrations of C-OH and C-O-C respectively. The FTIR spectrum of LIG-ZnO nanocomposite presents a series of absorption peaks between 4000-400 cm^{-1} (see Figure 6.7 c). The presence of Zn-O bond is evident at 480 cm^{-1} which is its characteristic absorption peak. The absorption peak from 1600-1300 cm^{-1} is attributed to the stretching mode of -COOH acetate group. The presence of carbon-hydrogen (C-H) stretching bonds are evident due to 2960 and 2850 cm^{-1} peaks. The observed peaks and their associated bonds are mentioned in Table 6.3.

Peak position (cm^{-1})	Identified functional group
3560-3350	—OH bonds
3068-2910	=C—H aromatic stretching
1750-1730	C═O stretching
1617, 1481	=C═C aromatic stretching
1449-1456	skeleton vibrations of the observed phenyl rings
1376-1370	stretched cyclic imide (=C—N—)
1234-1240	Asymmetric stretching of aromatic ether (C—O—C)
1167, 1115, 1091 and 1016	Para substituted phenyl, in-plane hydrogen rocking
883	out of plane waging vibration of isolated hydrogen in (1, 2, 4, 5)
818	out of plane waging vibration of two adjacent hydrogens
723-713	cyclic imide
690-600	bending vibration of C—O—C
635	C=O deformation
567-532	rocking band of cyclic imide
517	out of plane ring bending

Table 6.3: Transmission wavenumbers in FT-IR spectroscopy results of plain/Pristine polyimide

6.1.4 Functional characteristics

The explored novel technique presenting dual utilization of laser has shown its capability in the selective deposition/ transfer of materials to form nano-composites structures, it is essentially required to explore the applicability for its utilization in real world applications. Due to the

natural tendency of Piezo-electric properties of ZnO and tribo-electric properties of LIG, hybrid piezo-tribo-tribo functional Nanogeneration properties is explored which can efficiently be used in powering up sensors especially when the technological world is pacing up towards Industry 4.0 and Industry 5.0 revolution.

6.1.4 (a) Piezo-electric Response:

Before analysing the hybrid piezo-tribo response of the designed device for its functional application, the piezoelectric properties were explored. Pristine Polyimide, LIG and LIG-ZnO nanocomposite were coated with silver paste on both sides to provide continuous conductive surface. The piezoelectric coefficient or piezoelectric modulus i.e., d_{33} which quantifies the change in volume when a piezoelectric material is subjected to an electrical stimulus. It was observed that for pristine polyimide as well as for LIG, the displayed d_{33} value was 0 pC/N projecting there is no piezoelectric response. Further, laser μ-3D based selectively positioned ZnO in LIG hydrothermally grown was tested for its piezoelectric response and a value of 9 pC/N was obtained. The experiment was repeated 5 times, and the response was the same every time. While the theoretically reported d_{33} value for defect free ZnO is 8.6 pC/N, its value enhances by addition of dopants or due to certain defects. Our experimental values suggested the response very near to defect free growth which is also observed in other characterizations. It was also concluded that the piezo response thus observed was only due to ZnO nanorods grown over LIG and not due to LIG or polyimide.

6.1.4 (b) Hybrid Piezo-Tribo Response:

Hybrid piezo-triboelectric nanogenerators represents an innovative category of self-powered systems that combines potential of piezoelectric and triboelectric mechanisms. This synergy aims to enhance energy harvesting efficiencies and cater to the energy and power requirements of portable and wearable electronic devices. The distinctive electrical coupling mechanisms coming up because of the synergy between piezoelectric and triboelectric effects result in

amplified electric outputs and improved energy conversion efficiency for hybrid generators. This enhancement goes beyond a simple linear summation of contributions from individual triboelectric and piezoelectric mechanisms. Nanomaterials, characterized by their expansive surface-area-to-volume ratios and exceptional mechanical, electronic, and thermal properties, serve as advantageous building blocks for the construction of these hybrid nanogenerators. They constitute a diverse family of flexible structures and devices for electronic energy harvesting, offering a promising avenue for addressing the evolving landscape of energy needs in electronic applications.

The operational cycle of the two-electrode hybrid device comprises four stages, guided by the interaction of the piezoelectric layer and the electrodes. Initially, the upper electrode approaches the pre-rubbed generator, establishing contact with the piezoelectric layer. During this phase, increasing electrostatic induction between the piezoelectric layer and the upper electrode prompts positive charges to flow from the lower electrode through the external circuit to the upper electrode. This generates a triboelectric current from top to bottom in the external circuit. Simultaneously, as pressure intensifies, piezoelectric bound charges emerge within the piezoelectric layer due to the piezoelectric effect. Electrostatic induction of the piezoelectric charges causes negative charges in the upper electrode to flow to the lower electrode, creating a piezoelectric current from top to bottom in the external circuit. Upon pressure release, the piezoelectric charge dissipates, and charges produced by the piezoelectric effect in the electrode revert to their original positions, restoring electrostatic balance. This phase yields a piezoelectric current opposite to the initial one. Lastly, as the distance between the upper electrode and the piezoelectric layer gradually increases, weakening electrostatic induction between them prompts excess positive charge to flow from the upper electrode to the lower electrode. This results in a triboelectric current in the external circuit opposite the initial triboelectric current.

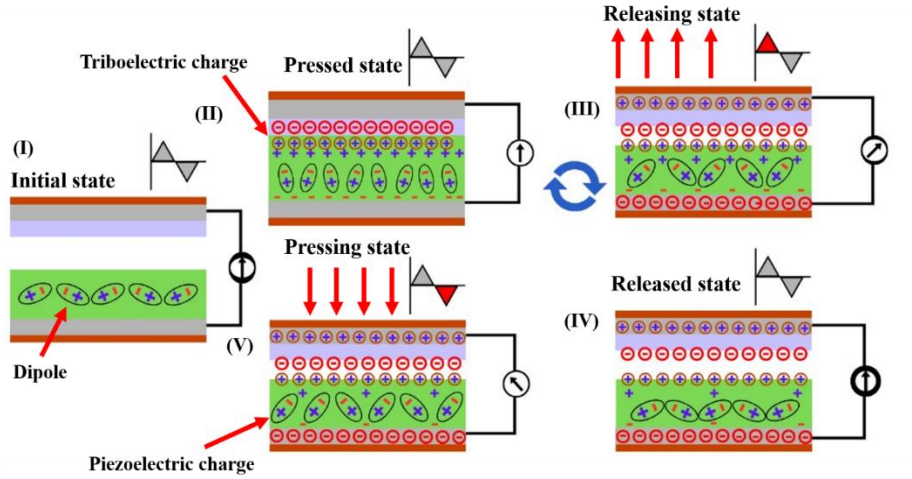

Figure 6.8: Working principle of ITO coated PET/ZnO/FEP Piezo-Tribo hybrid nanogenerator.

Based on the above-mentioned principles, devices were fabricated. Initially ZnO was transferred over conductive LIG base and piezo device was fabricated and tested for voltage and current output. It was observed that open circuit voltage was 9V and shot circuit current was 260 nA Further a LIG-FEP (Fluorinated ethylene propylene) device was fabricated to analyze its tribo performance and it was observed that the open circuit voltage was 36V whereas the shot circuit current was 410 nA Further the selectively positioned ZnO ceramic in LIG was tested with FEP as tribo-negative layer. The fabricated hybrid device presented remarkable results i.e., open circuit voltage increased by almost 50% when compared with plain tribo device and the current increased by almost ~ 60%. The hybridization of the piezoelectric and triboelectric effects does not merely result in a simple summation of their output performance. This has been proved in many previous studies on hybridization between piezoelectric and triboelectric effects. The amalgamation of piezoelectric and triboelectric effects goes beyond a simple summation of their individual output performances, as demonstrated in numerous prior studies on their hybridization. The enhancement of piezoelectric properties is an outcome of triboelectric charge accumulation. The tribo-charges establish an electric field in the piezoelectric layer, influencing the polarization of the piezoelectric materials. Consequently, when the intrinsic poling direction of the piezoelectric material aligns with the electric field generated by the

triboelectric charges, the overall output of the hybrid device experiences enhancement, and vice versa.

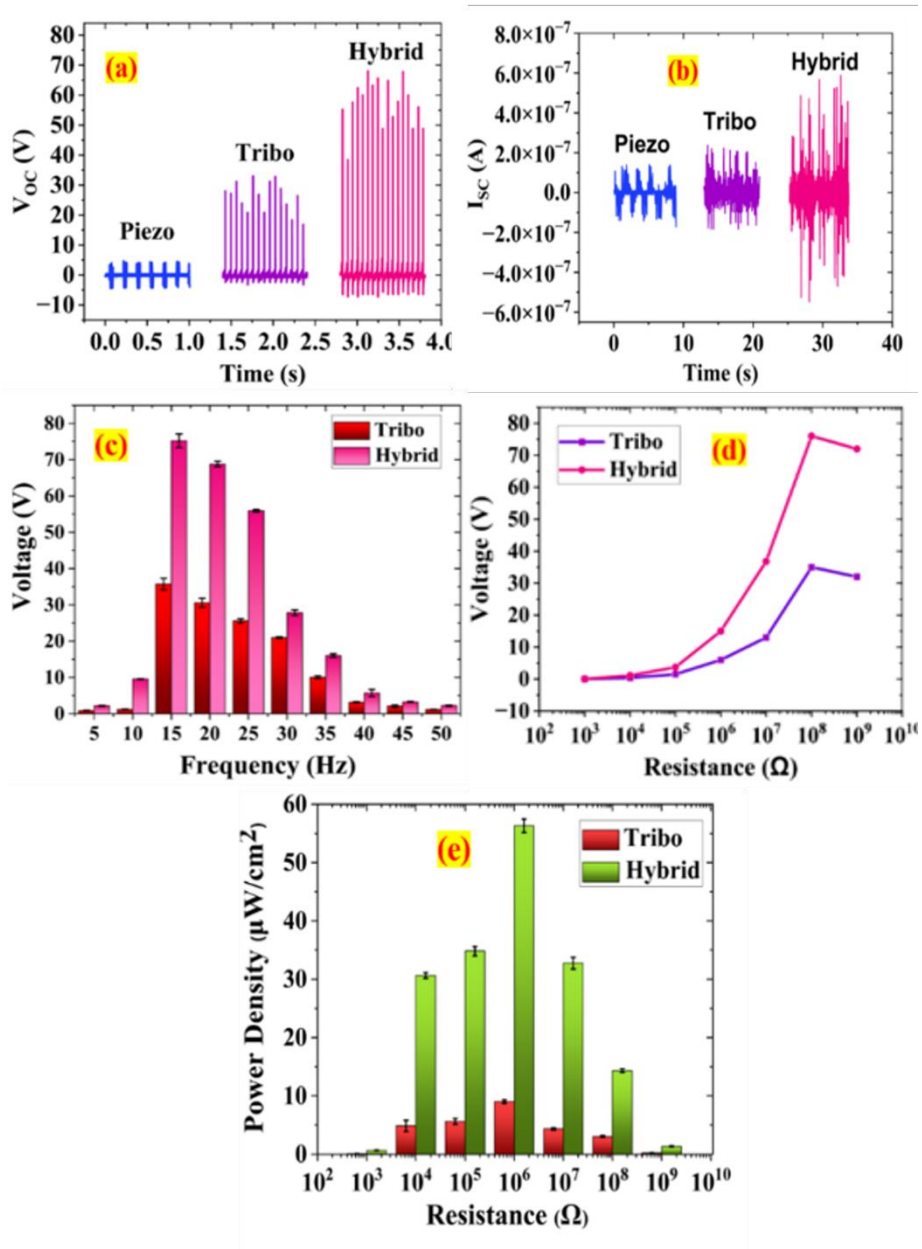

Figure 6.9: Performance analysis of the fabricated piezo, tribo and hybrid devices (a)V_{oc} vs time, (b) I_{sc} vs time, (c) performance of devices at variable frequency, (d) V_{oc} of fabricated tribo and hybrid device with variation in load resistance, and (e) overall power density generated by device at variable load resistance.

It is however to be noted that before reaching the maximum output points obtained, the maximum response was observed at a frequency of 15 Hz up to which the voltage kept on increasing, however, as the frequency increased further the effective contact and separation between

layers reduces thus presenting reduced voltage output (see figure 6.9c). Primarily, the rise in frequency led to an escalation in the contact and separation cycles, resulting in higher voltage and current outputs. However, as the frequency continued to increase, it became apparent that there was insufficient contact and separation. This limitation hindered the smooth flow of charge during the contact and separation cycles and thus presenting lower voltage and current output. While the impact of contact and separation at varying frequencies plays a vital role in energy generation, another important parameter is matching impedances. Normally the associated impedance of such devices is very high in the range of MΩ and hence the fabricated devices are tested for varying resistances. It was observed that at 100 MΩ (see Figure 6.9 d), the response was maximum for both tribo as well as hybrid devices whereas the associated power density was maximum in the range of 1-10 MΩ (see Figure 6.9 e) resistance. After analysing the associated responses, the finally fabricated device was attached to a bridge rectifier and tested for its effective output at optimized parameters. The effectiveness of the fabricated hybrid device was tested in charging up and discharging the capacitor as well and it was effectively suggested variation in adding LED load.

The final outcomes of the study not only paved a way for fabricating piezo-tribo hybrid devices, but it also marked a pathway towards utilizing laser as a source of energy for selectively positioning materials and thus can effectively be used for fabricating various flexible sensors for multiple applications.

6.2 Exploring the performance of ZnO printed over ITO coated PET for hybrid applications

The laser-based process has been examined for its potential applications in hybrid piezo-tribo nanogenerators, which can effectively power sensors. A device was developed using zinc oxide (ZnO) efficiently printed over flexible ITO-coated PET where ZnO sandwiched between PET and aluminum acts as a piezoelectric pair whereas aluminum

interacting with fluorinated ethylene propylene (FEP) formed a triboelectric pair thus making it a hybrid pair all-together. Triboelectric nanogenerators (TENGs) operate on the principles of triboelectrification and electrostatic induction. A TENG is created by pairing materials with different electron affinities: one that readily donates electrons (tribo-positive) and one that tends to accept them (tribo-negative). In our device, aluminum is utilized as the tribo-positive material, and fluorinated ethylene propylene (FEP) paired with copper acts as the tribo-negative material, as illustrated in Figure 6.10.

The device features a two-electrode design that incorporates a single functional layer, seamlessly integrating both triboelectric and piezoelectric properties. This combination allows the device to harness energy from both mechanical movements and contact electrification, enhancing its efficiency and making it suitable for powering a variety of sensor applications.

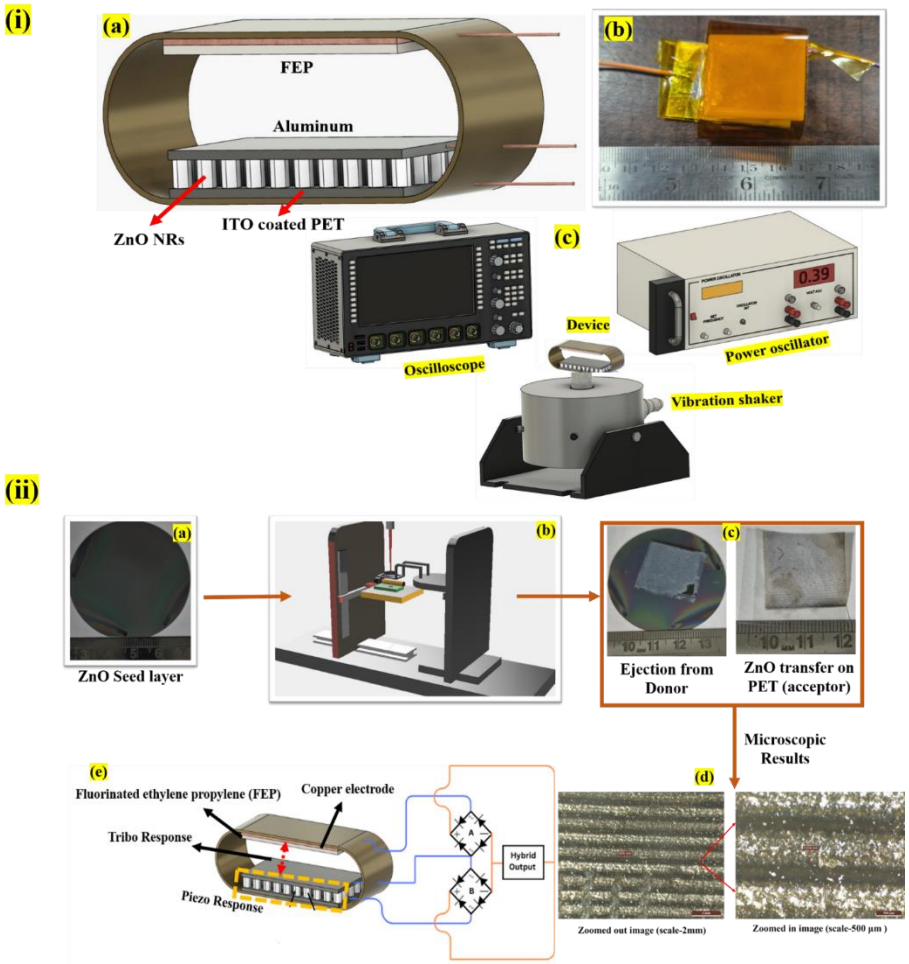

Figure 6.10: (i) (a) Schematic diagram of piezo and triboelectric hybrid nanogenerator (b) fabricated devices for response analysis (c) test setup for device testing and analysis and (ii) Experimental analysis for material ejection and printing of ZnO over ITO coated PET (a) sputtered ZnO seed layer, (b) laser decal transfer using laser μ- 3D printing technique, (c) depicting ZnO material ejection from donor and transfer on ITO coated PET(d) microscopic images of transferred ZnO and (e) schematic suggesting hybrid device fabrication based on printed structure.

6.2.1 Functional Application of the fabricated device

The investigated novel technique involves laser decal transfer printing, which allows for the selective deposition and transfer of materials to create nano-composite structures. This method needs to be further explored for its potential real-world applications. The inherent piezoelectric properties of ZnO, combined with the triboelectric properties of FEP-Al, enable the development of hybrid piezo-

triboelectric nano-generators. These generators could play a crucial role in powering sensors, especially as we advance toward Industry 4.0 and Industry 5.0 revolutions.

6.2.1 (a) Piezo-electric Response:

Before investigating the hybrid piezo-triboelectric response of the designed device for functional applications, the piezoelectric properties were first evaluated. Plain ITO-coated PET and ZnO nanocomposite samples were made conductive by applying silver paste on both sides. The piezoelectric coefficient, or piezoelectric modulus (d33), which quantifies the volume change in a piezoelectric material in response to an electrical stimulus or stress, was measured. The results indicated that the transferred and solvo-thermally grown ZnO displayed a piezoelectric response with a d33 value of 9 pC/N. This experiment was repeated five times, consistently yielding the same result. Although the theoretical d33 value for defect-free ZnO is reported as 8.6 pC/N, this value can be increased by introducing dopants or specific defects. Our findings suggest that the response closely matches that of defect-free ZnO growth, which is consistent with other characterization results. It was also determined that the observed piezoelectric response was solely due to the ZnO nanorods grown on the ITO-coated PET, not the PET itself. The piezoelectric response observed in the fabricated ZnO structures arises from the intrinsic alignment of the ZnO nanorods along the c-axis ([0001] direction) during hydrothermal growth. This preferential alignment is facilitated by the wurtzite crystal structure of ZnO and the use of a ZnO seed layer, which acts as a nucleation site, directing the vertical growth of the nanorods. While the dipoles of individual nanorods are not deliberately aligned through an external poling process, their collective orientation contributes to the generation of piezoelectric signals under mechanical deformation.

It is important to note that ZnO is not ferroelectric, and no poling procedure was applied in this study. The piezoelectric properties of ZnO result from its wurtzite crystal structure and the intrinsic displacement

of ionic charges under mechanical stress, which generates a piezoelectric response.

Under mechanical deformation, the ZnO nanorods experience a relative displacement of Zn^{2+} and O^{2-} ions within the wurtzite lattice, generating an electric dipole moment and thus a piezoelectric signal. This phenomenon is well-documented in the literature for ZnO nanostructures, where the vertical growth orientation contributes to a consistent piezoelectric response. The lack of ferroelectric properties in ZnO does not hinder its ability to generate piezoelectric signals as the effect is rooted in the intrinsic lattice structure rather than domain alignment.

6.2.1 (b) Hybrid Piezo-Tribo Response:

Hybrid piezo-triboelectric nanogenerators represent an advanced class of self-powered systems that leverage both piezoelectric and triboelectric effects to boost energy harvesting efficiency. This combination enhances the energy output to meet the power demands of portable and wearable electronics. The unique electrical interactions created by the synergy between piezoelectric and triboelectric mechanisms result in amplified electric output and improved energy conversion efficiency, achieving more than just the simple addition of each effect's contribution. Nanomaterials, with their high surface-area-to-volume ratios and excellent mechanical, electronic, and thermal properties, serve as ideal building blocks for these hybrid nanogenerators. They form a versatile range of flexible structures for electronic energy harvesting, offering a promising solution to the growing energy needs in electronics.

Figure 6.8 illustrates the fundamental operational principle of charge generation and interaction mechanisms within the ITO coated PET/ZnO/FEP device. The electrical output produced by this device arises primarily from two significant power generation phenomena: electrostatic induction and triboelectricity, which occur during vertical contact separation. Additionally, piezoelectric charges are generated due

to the pressure applied to the ZnO, placing it in a state of compression. This interaction between piezoelectric and triboelectric effects enhances the overall electrical output performance of the device. Initially, ZnO[35] was transferred over ITO coated PET sheet with a conductive side on top and the piezo device was fabricated with aluminum placed over and tested for voltage and current output (see Fig. 6.10a). The graphs in Fig. 6.11 provide a comprehensive analysis of the voltage and current responses of three types of energy harvesting generators: a standalone piezoelectric generator, a standalone triboelectric nanogenerator and a hybrid piezo-triboelectric (Piezo-Tribo) generator. Each graph illustrates the benefits and performance differences between the two setups under similar conditions, showcasing the effectiveness of combining piezoelectric and triboelectric mechanisms for enhanced energy output.

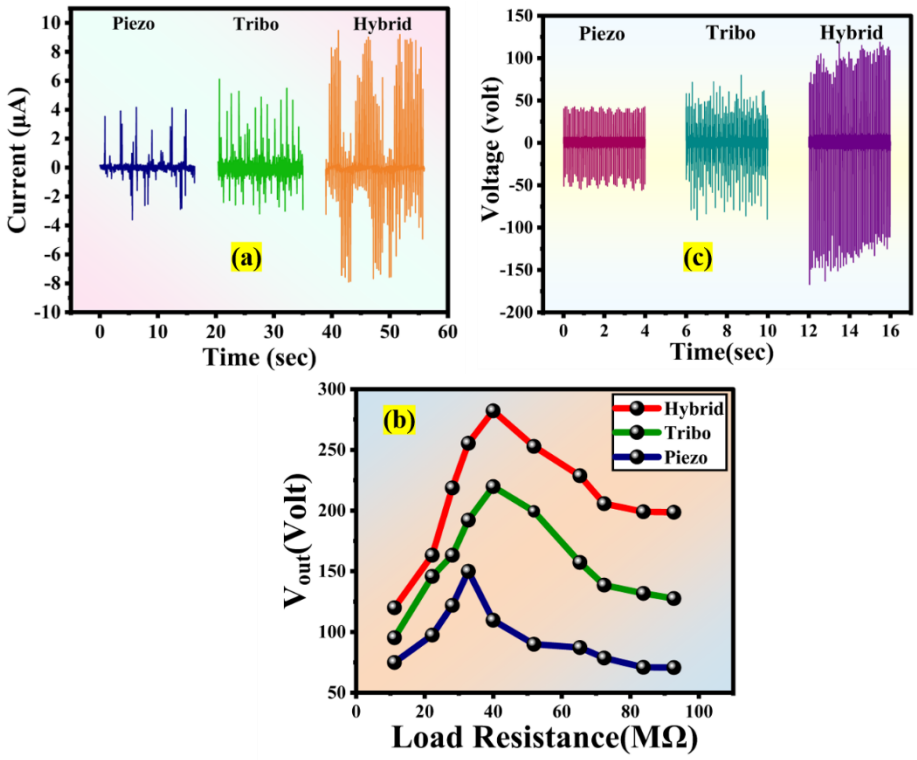

Figure 6.11: Performance analysis of the fabricated piezo, tribo, and hybrid devices (a)Voc vs time, (b) performance of devices at variable loads, (c) Voc of fabricated tribo and hybrid device with variation in load resistance

Fig. 6.11 a projects the current output over time for piezo, tribo as well as hybrid nanogenerators. The standalone piezoelectric generator produces a relatively low and steady current, with minor fluctuations, which is visible in the first half of the graph with the output range of ~ ± 3 μA whereas standalone tribo response for current is however improved to ~ ± 4.5 μA, it is still not sufficient. In contrast, the hybrid generator's current output is significantly higher and more variable, with pronounced peaks and valleys ranging in ~ ± 8 μA, an improvement of ~ 60 %. This indicates that the hybrid generator can deliver a much larger current output, making it more suitable for applications that require higher current levels or operate under more demanding load conditions. The current is measurement with electrometer 6514 and voltage is measured with oscilloscope. Since the Sampling rate of oscilloscopes is more when compared with that of electrometer, the voltage signals observed are uniform throughout the process while the current is non-uniform during the tapping process. Due to low sampling rate of electrometer, there is mismatch between the compression of ZnO piezoelectric and the current acquisition from the piezoelectric devices. Hence the peak current is used for maximum performance of the devices rather than smaller peak. The enhanced current output in the hybrid generator demonstrates the combined effect of piezoelectric and triboelectric mechanisms, which allow it to harvest more energy compared to the piezoelectric generator alone.

The response associated with maximum output is associated with the matching impedances and essentially depends on matching impedances. Fig. 6.11b illustrates the output voltage as a function of load resistance for the Hybrid, tribo and Piezo configurations. For all setups, the output voltage initially increases with load resistance, peaking at certain points before gradually declining as the resistance continues to rise. The Hybrid configuration achieves a higher maximum output voltage of approximately 270 volts at around 40 MΩ while the Piezo configuration reaches its peak output voltage of about 140 volts at a similar load resistance value. After these peaks, the output voltage for both

configurations decrease and stabilizes as load resistance approaches 100 MΩ. This indicates that the Hybrid configuration generally yields a higher output voltage compared to the Piezo and tribo configuration alone across the tested load resistance range.

Fig. 6.11c displays the piezoelectric nanogenerator, triboelectric nanogenerator and hybrid device's voltage output, showing a periodic oscillation with a relatively consistent amplitude between ± 80 volts for piezoelectric device and -150 V to +100 V for hybrid device. This sinusoidal behaviour is typical of piezoelectric materials, which generate voltage in response to mechanical stress, such as bending or compression. The graph highlights that the piezoelectric generator alone can produce a significant voltage output, although the range is somewhat limited when compared to the hybrid system. The periodic nature of the voltage indicates that it is highly responsive to mechanical inputs, making it suitable for applications where regular mechanical movement is available for energy harvesting. An increased voltage and current response are observed in triboelectric tests as well. In case of hybrid devices, the output voltage is noticeably higher, demonstrating that the hybrid system enhances the voltage output significantly increasing it by approximately 50% compared to the piezoelectric generator alone. The hybrid approach combines both piezoelectric and triboelectric effects, effectively harnessing two distinct mechanisms for generating electrical energy. This combination results in a more complex oscillation pattern, as seen in the irregular peaks and valleys, suggesting that the hybrid system may respond to a wider range of mechanical stimuli, thereby increasing the overall energy harvested. The increased amplitude of the voltage in the hybrid system highlights the advantage of using both mechanisms to boost performance in energy generation applications.

Figure 6.12 illustrates a practical and innovative application of walking-based energy harvesting using hybrid energy systems. The image depicts a human walking, highlighting the incorporation of energy-harvesting technologies into the shoe's sole. The inset shows a close-up of the shoe

with integrated components that likely include piezoelectric and triboelectric mechanisms. These technologies generate electrical energy from mechanical motion, such as the pressure and friction exerted during walking. The hybrid system exhibits a higher and more stable voltage output, demonstrating the synergy between the two mechanisms. Further, the fabricated hybrid device was tested on a treadmill to investigate how variations in speed affect voltage generation. The speeds evaluated were 0.8 km/hr, 2 km/hr, 4 km/hr, and 6 km/hr, with the voltage and current signals recorded for each speed, as shown in the graph. At the lowest speed of 0.8 km/hr, the voltage as well as current signals displayed the highest amplitude, indicating significant voltage and current output. However, as the speed increased, a noticeable reduction in the signal amplitude was observed. By the time the speed reached 6 km/hr, the signals had significantly diminished, with much smaller peaks and troughs compared to those at lower speeds. This clear trend demonstrates that voltage and current generation decrease as the treadmill speed increases. The observed reduction in voltage and current at higher speeds can be explained by the mechanics of foot impact. At lower speeds, the user's steps are slower but exert greater force, allowing more pressure to be applied to the hybrid device's piezoelectric components. This higher pressure results in greater deformation of the material, leading to a stronger voltage output. Conversely, at higher speeds, the steps become quicker, with reduced impact forces due to shorter foot contact durations and less concentrated pressure. This reduced mechanical engagement limits the piezoelectric material's ability to generate voltage, resulting in weaker signals. Thus, the experiment highlights the dependence of piezoelectric performance on mechanical pressure, particularly in energy harvesting and sensing applications.

This hybrid energy-harvesting technology has significant potential in various real-life scenarios. For example, the electrical energy generated can power portable electronics such as fitness trackers, smartwatches, and wearables, ensuring continuous functionality without reliance on

frequent battery recharges. In healthcare, this system could sustain medical devices like biosensors or prosthetics, enhancing patient mobility and convenience. Military applications stand to benefit as well, as soldiers equipped with energy-harvesting footwear can charge essential devices such as communication tools, GPS units, and surveillance equipment while in remote or challenging environments. This reduces the logistical burden of carrying spare batteries and improves operational efficiency. The hybrid energy-harvesting system depicted in figure 10 also holds transformative potential for future applications. In smart city initiatives, similar technology could be embedded into pavements or walkways, allowing pedestrians to generate energy to power streetlights, traffic sensors, or public charging stations. Furthermore, this innovation aligns with the growth of the Internet of Things (IoT), where distributed, self-powered sensors could enable widespread environmental monitoring, smart agriculture, or infrastructure management. The high output demonstrated by the hybrid system makes it especially suitable for powering such low-energy, always-on IoT devices. Beyond these applications, this technology offers a sustainable alternative to conventional batteries, reducing electronic waste and contributing to a greener energy ecosystem. By leveraging advancements in hybrid systems walking-based energy harvesting has the potential to revolutionize both real-life and future technological landscapes, driving innovation and sustainability.

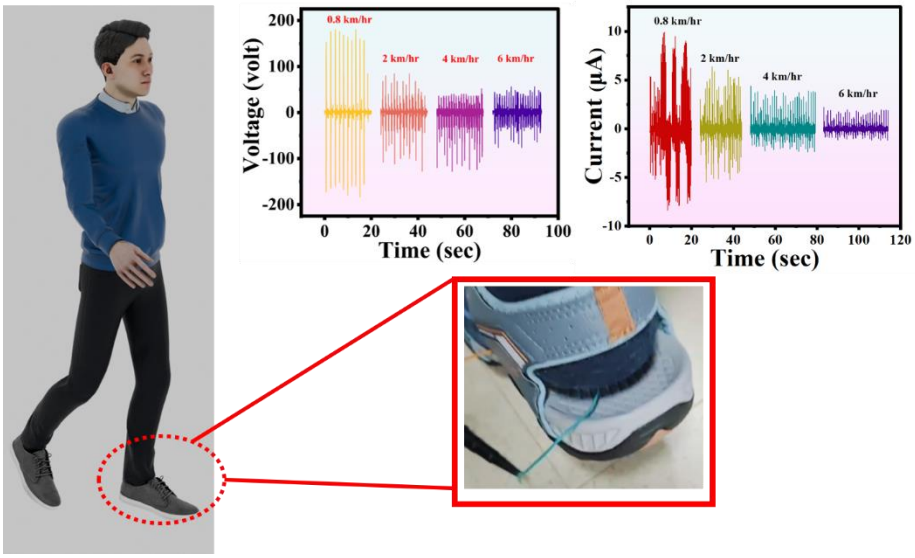

Figure 6.12: Hybrid Energy Harvesting via Piezo-Tribo Systems in Footwear for functional applications

Overall, these outcomes present the advantages of the hybrid Piezo-Tribo generator over the standalone piezoelectric generator in terms of both voltage and current output. The hybrid generator's increased voltage and current capabilities make it a more efficient and versatile option for applications in energy harvesting, where maximizing output is crucial. The results suggest that the hybrid approach leverages the strengths of both piezoelectric and triboelectric effects to produce a more robust and adaptable energy source. The outcomes of the study not only paved the way for fabricating piezo-tribo hybrid devices, but it also marked a pathway towards utilizing a laser as a source of energy for selectively positioning materials and thus can effectively be used for fabricating various flexible sensors for multiple applications.

6.2 Summary

The utilization of lasers for direct laser writing and laser micro-3D printing is explored for its practical and functional applications as discussed in the chapter. Based on the explored outcomes, the key concluding outcomes are mentioned here in points.

1. A dual-laser strategy was successfully employed-CO_2 laser (10.6 µm) for direct laser writing (DLW) to synthesize LIG from Kapton and a laser micro-3D (µ-3D) system for transferring ZnO seed layers, enabling a fully digital, maskless process with micro-level precision for hybrid device fabrication.
2. On LIG substrates, ZnO was selectively deposited using a PDMS sacrificial layer, achieving a maximum transfer efficiency of 86.75% at optimized laser fluence of 75 J/cm², repetition rate of 10 Hz, and 6% duty cycle, as confirmed through profilometry and microscopy.
3. The transferred ZnO enabled hydrothermal growth of vertically aligned ZnO nanorods with dense packing (~50 nm inter-rod gap), exhibiting average rod lengths of 2.92 ± 0.45 µm and

diameters of 2.14 ± 0.40 µm, indicating well-defined morphology essential for functional applications.

4. XRD analysis of the LIG-ZnO composite showed enhanced crystallinity with a dominant (002) peak at 34.2°, confirming wurtzite ZnO structure; a noticeable reduction in (103) peak intensity indicated selective growth confined to laser-defined pores in LIG.
5. FTIR and EDX confirmed successful integration and chemical bonding of ZnO with graphene, while TEM revealed lattice fringes corresponding to d-spacing of 3.62 Å for LIG (002) and 2.346 Å for ZnO (101), validating crystal phase and interfacial integration.
6. Piezoelectric coefficient (d_{33}) of 9 pC/N was recorded for selectively grown ZnO on LIG, with both pristine Kapton and bare LIG showing no piezo response, confirming that the signal arises solely from ZnO.
7. A standalone piezo device using LIG-ZnO delivered 9 V open-circuit voltage and 260 nA short-circuit current, while a triboelectric-only LIG-FEP device achieved 36 V and 410 nA, respectively.
8. When hybridized (ZnO/LIG-FEP), the device showed significant enhancements: voltage increased by ~50% and current by ~60% compared to tribo-only devices, indicating synergistic performance due to polarization coupling between piezo and tribo layers.
9. Voltage output peaked at 15 Hz frequency due to optimal contact-separation cycles; further increase in frequency led to reduced output due to inadequate contact time and pressure.
10. Load resistance analysis revealed maximum output voltage at 100 MΩ, with peak power density in the 1–10 MΩ range; beyond this, impedance mismatch reduced effective energy transfer.
11. On flexible ITO-coated PET substrates, ZnO was printed using the same laser µ-3D method and hydrothermally grown, yielding

a consistent d_{33} value of 9 pC/N across trials, suggesting reproducibility and uniformity in ZnO alignment.

12. The ITO-ZnO-FEP hybrid device achieved ±8 µA peak current, a ~60% improvement over standalone tribo or piezo devices (which showed ~ ±4.5 µA and ±3 µA, respectively), validating the dual-mechanism efficiency.
13. The hybrid generator demonstrated peak output voltage of ~270 V at 40 MΩ compared to 140 V for the piezo-only device, illustrating higher output due to effective superposition of piezoelectric and triboelectric mechanisms.
14. Walking-based energy harvesting experiments using a shoe-integrated hybrid system revealed maximum voltage at 0.8 km/h walking speed, with output decreasing at higher speeds due to reduced mechanical impact duration.
15. This laser-enabled, flexible, and modular hybrid nanogenerator platform offers promising applications in wearables, IoT devices, smart footwear, and next-generation self-powered sensors, leveraging scalable and maskless laser processing methods for material integration.

These conclusions emphasize the technological novelty, material performance, and application potential of integrating laser-based processes on diverse substrates for functional applications.

Chapter 7

This chapter covers the key conclusions and probable windows that can be explored further in future research

Conclusion and Future Scope

7.1 Conclusions

Various laser-based manufacturing techniques were explored for multi-layered multi-material printing. A detailed exploration of laser direct writing and laser micro-3D printing is conducted, which is further integrated for its essential utilization in functional applications. Based on the explored work, the overall summary of the thesis is as follows:

Research Objective 1

- Laser-induced graphene (LIG) was successfully synthesized from commercial Kapton films using CO_2 laser irradiation. The process leveraged the photothermal effect to achieve localized graphenization, with surface temperatures experimentally reaching over 2000 °C. The structural transition from polymer to porous fibrous graphene was confirmed through SEM, Raman, and XRD analyses.
- The Gaussian distribution of the laser beam induced variable crystallinity across the irradiated region, with the center showing high graphitic quality and the periphery displaying more disorder. Raman mapping revealed an increasing ID/IG ratio from the center outward, indicating controlled defect engineering. These properties were strongly correlated with the spatial energy profile.
- Electrical conductivity of LIG improved significantly with increased laser pulse overlap. At 80% overlap, the resistivity dropped to 9.8×10^{-5} Ω·m, and carbon content rose to 89.2% as confirmed by EDX. This demonstrates that laser parameter

tuning is critical for maximizing conductivity and structural integrity of printed graphene.

- The fabricated LIG-based strain sensor demonstrated high mechanical durability and sensitivity, with a gauge factor of ~56. The device maintained stable performance to over 1250 bending cycles. This confirms the potential of LIG for flexible electronics, wearable sensors, and dynamic mechanical monitoring.

Research Objective 2

- Micro-3D printing of silicon carbide (SiC) was carried out using a pixel-wise laser transfer approach, where sputtered SiC films were selectively ejected from donor substrates. The laser-mediated ablation ensured precise deposition without chemical processing, showcasing a clean and efficient route for material transfer.
- A parametric study revealed that stand-off distance (SOD), fluence, and pulse overlap greatly affect transfer efficiency and feature quality. Optimal results were obtained at 120 J/cm² fluence, 12.5 cm SOD, and 90% overlap. Under these settings, uniform line widths and excellent interlayer fusion were achieved.
- Design of Experiments (DOE) using a Box-Behnken model enabled quantitative optimization of process parameters. The regression models yielded R^2 values above 99.7%, indicating excellent predictive capability. This statistical approach provided a framework for scalable, repeatable microfabrication.
- The SiC printing method could produce complex geometries such as spirals, sinusoidal paths, and interdigitated patterns. Substrate heating at 100 °C further enabled vertical stacking and improved interlayer adhesion. These features expand the method's applicability to MEMS and 3D microelectronic platforms.

Research Objective 3

- ZnO thin films were transferred via laser decal printing onto both rigid (LIG) and flexible (ITO-coated PET) substrates, maintaining structural fidelity. Post-transfer hydrothermal growth led to the formation of vertically aligned ZnO nanorods with average dimensions of 2.92 µm in length and 2.14 µm in diameter.
- On LIG substrates, the ZnO-LIG devices exhibited a piezoelectric coefficient (d_{33}) of 9 pC/N and produced a voltage output of 9 V and a current of 260 nA. When integrated with a triboelectric layer, these values improved significantly to 15 V and 410 nA, highlighting the synergistic effect of hybrid energy harvesting.
- On flexible PET substrates, ZnO retained its structural and electrical functionality, achieving ±8 µA current and 270 V voltage in hybrid mode. The performance was consistent with rigid devices, confirming the reliability and adaptability of the laser transfer process on flexible substrates.
- Electrical characterization showed optimal power transfer at a load resistance of 40 MΩ, with frequency response peaking at 15 Hz. This tuning is crucial for real-world applications where mechanical excitation varies dynamically, such as in human motion or ambient vibrations.
- The shoe-integrated hybrid energy harvester confirmed practical applicability, generating higher output at low walking speeds (~0.8 km/h). This result is attributed to prolonged contact time between the foot and surface, allowing for more complete charge transfer cycles.
- Overall, the research established a scalable, maskless, and lithography-free method for printing functional materials with micron-scale resolution. The use of laser energy as a tool for precise material patterning enables rapid prototyping and on-

demand fabrication without hazardous chemicals or vacuum packaging.

- This work lays the foundation for modular microfabrication of multi-material systems suited for flexible electronics, energy harvesting, and MEMS devices. Future directions include expanding material compatibility, exploring adaptive laser control, and scaling up to roll-to-roll manufacturing platforms.

7.2 Future scope

Based on the explored outcomes of the research work, it opens key areas that can be explored in future as mentioned below.

- **Multi-Material and Functional Ink Integration**: Future work can explore integrating additional functional materials such as MXenes, perovskites, or polymer composites to enable tuneable electrical, optical, and thermal responses. This will expand the platform's utility toward multifunctional sensing, energy storage, and optoelectronic applications.
- **Real-Time Adaptive Laser Control Systems**: Developing real-time feedback mechanisms using optical sensors or machine learning algorithms can enable dynamic control of laser fluence, pulse overlap, and beam shape. Such closed-loop systems will ensure consistent print quality and compensate for surface non-uniformities or substrate curvature.
- **Hybrid Device Stacking and 3D Architectures**: The vertical stacking approach demonstrated with SiC can be extended to build multi-layered devices incorporating piezoelectric, triboelectric, and conductive layers. These 3D microsystems could form the basis of self-powered micro-sensors, logic units, or integrated circuits at the microscale.
- **Wearable and Biocompatible Applications**: Future research could adapt the laser printing techniques for biocompatible substrates (like PDMS or cellulose), enabling applications in wearable health monitors, implantable devices, or electronic

skin. The low thermal load and selective material transfer make this particularly suited for soft and living tissues.

- **Scale-Up and Roll-to-Roll Manufacturing**: To transition toward commercial applications, roll-to-roll laser systems with synchronized motion stages and high-speed scanning optics can be developed. This will allow continuous patterning of flexible materials for large-area electronics, smart textiles, and distributed energy harvesting systems.

References

1. Kim, Seong H., David B. Asay, and Michael T. Dugger. "Nanotribology and MEMS." Nano today 2, no. 5 (2007): 22-29.

2. Gad-el-Hak, Mohamed, ed. The MEMS handbook. CRC press, 2001.

3. Huang, Yunhan, Arvind Sai Sarathi Vasan, Ravi Doraiswami, Michael Osterman, and Michael Pecht. "MEMS reliability review." IEEE Transactions on Device and Materials Reliability 12, no. 2 (2012): 482-493.

4. Bogue, Robert. "MEMS sensors: past, present and future." Sensor Review 27, no. 1 (2007): 7-13.

5. Spearing, S. M. "Materials issues in microelectromechanical systems (MEMS)." Acta materialia 48, no. 1 (2000): 179-196.

6. Epstein, Alan H., S. D Senturia, G Anathasuresh, A. Ayon, K. Breuer, K-S. Chen, F. Ehrich et al. "Power MEMS and microengines." In Proceedings of International Solid-State Sensors and Actuators Conference (Transducers' 97), vol. 2, pp. 753-756. IEEE, 1997.

7. Persano, Luana, Andrea Camposeo, and Dario Pisignano. "Integrated bottom-up and top-down soft lithographies and microfabrication approaches to multifunctional polymers." Journal of Materials Chemistry C 1, no. 46 (2013): 7663-7680.

8. Mijatovic, D., Jan CT Eijkel, and Albert Van den Berg. "Technologies for nanofluidic systems: top-down vs. bottom-up—a review." Lab on a Chip 5, no. 5 (2005): 492-500.

9. Schaffner, Manuel, Grant England, Mathias Kolle, Joanna Aizenberg, and Nicolas Vogel. "Combining Bottom-Up Self-Assembly with Top-Down Microfabrication to Create

Hierarchical Inverse Opals with High Structural Order." Small 11, no. 34 (2015): 4334-4340.

10. Hobbs, Richard G., Nikolay Petkov, and Justin D. Holmes. "Semiconductor nanowire fabrication by bottom-up and top-down paradigms." Chemistry of materials 24, no. 11 (2012): 1975-1991.

11. Khanna, Vinod Kumar, and Vinod Kumar Khanna. "Bottom-up nanofabrication." Integrated Nanoelectronics: Nanoscale CMOS, Post-CMOS and Allied Nanotechnologies (2016): 397-417.

12. Ruiz-Zambrana, César L., Magdalena Malankowska, and Joaquín Coronas. "Metal organic framework top-down and bottom-up patterning techniques." Dalton Transactions 49, no. 43 (2020): 15139-15148.

13. Zhang, Xiang, Cheng Sun, and Nicholas Fang. "Manufacturing at nanoscale: Top-down, bottom-up and system engineering." Journal of Nanoparticle Research 6 (2004): 125-130.

14. Chen, Songyue, Johan G. Bomer, Wilfred G. van der Wiel, Edwin T. Carlen, and Albert van den Berg. "Top-down fabrication of sub-30 nm monocrystalline silicon nanowires using conventional microfabrication." ACS nano 3, no. 11 (2009): 3485-3492.

15. Rahim, Kaysar, and Ahsan Mian. "A review on laser processing in electronic and MEMS packaging." Journal of Electronic Packaging 139, no. 3 (2017): 030801.

16. Holmes, Andrew S. "Laser fabrication and assembly processes for MEMS." In Laser Applications in Microelectronic and Optoelectronic Manufacturing VI, vol. 4274, pp. 297-306. SPIE, 2001.

17. Liu, Jianlei, Haijie Ji, Xiaoyan Lv, Chijia Zeng, Heming Li, Fugang Li, Bin Qu, Feiyun Cui, and Qin Zhou. "Laser-induced

graphene (LIG)-driven medical sensors for health monitoring and diseases diagnosis." Microchimica Acta 189 (2022): 1-14.

18. Ye, Ruquan, Dustin K. James, and James M. Tour. "Laser-induced graphene." Accounts of chemical research 51, no. 7 (2018): 1609-1620.

19. Xia, Sheng-Yuan, Yunfeng Long, Zhengyong Huang, Yunlong Zi, Lu-Qi Tao, Chang-Heng Li, Hao Sun, and Jian Li. "Laser-induced graphene (LIG)-based pressure sensor and triboelectric nanogenerator towards high-performance self-powered measurement-control combined system." Nano Energy 96 (2022): 107099.

20. Ye, Ruquan, Dustin K. James, and James M. Tour. "Laser-induced graphene: from discovery to translation." Advanced Materials 31, no. 1 (2019): 1803621.

21. Le, Truong-Son Dinh, Hoang-Phuong Phan, Soongeun Kwon, Sangbaek Park, Yeongju Jung, Jinki Min, Byung Jae Chun et al. "Recent advances in laser-induced graphene: mechanism, fabrication, properties, and applications in flexible electronics." Advanced Functional Materials 32, no. 48 (2022): 2205158.

22. Palaniappan, Raghavan UM, Yung-Fu Chang, Chao-Fu Chang, M. J. Pan, C. W. Yang, Peter Harpending, Sean P. McDonough et al. "Evaluation of lig-based conventional and real time PCR for the detection of pathogenic leptospires." Molecular and cellular probes 19, no. 2 (2005): 111-117.

23. Liu H, Tang Y, Xie Y, Lu L, Wan Z, Tang W, Yang L, Yang D. Effect of pulsed Nd: YAG laser processing parameters on surface properties of polyimide films. Surf Coat Technol. 2019 Mar 15; 361:102–11.

24. Nam KH, Abdulhafez M, Najaf Tomaraei G, Bedewy M. Laser-Induced fluorinated graphene for superhydrophobic surfaces with

anisotropic wetting and switchable adhesion. Appl Surf Sci. 2022 Feb 1;574.

25. Hiraoka H, Lazare S. Surface modifications of Kapton and cured polyimide films by ArF excimer laser: applications to imagewise wetting and metallization. Vol. 46, Applied Surface Science.

26. Duy, Luong Xuan, Zhiwei Peng, Yilun Li, Jibo Zhang, Yongsung Ji, and James M. Tour. "Laser-induced graphene fibers." Carbon 126 (2018): 472-479.

27. Huang, Libei, Jianjun Su, Yun Song, and Ruquan Ye. "Laser-induced graphene: En route to smart sensing." Nano-micro letters 12 (2020): 1-17.

28. Barner-Kowollik, Christopher, Martin Bastmeyer, Eva Blasco, Guillaume Delaittre, Patrick Müller, Benjamin Richter, and Martin Wegener. "3D laser micro-and nanoprinting: challenges for chemistry." Angewandte Chemie International Edition 56, no. 50 (2017): 15828-15845.

29. Piqué, Alberto, Raymond CY Auyeung, Heungsoo Kim, Nicholas A. Charipar, and Scott A. Mathews. "Laser 3D micro-manufacturing." Journal of physics D: applied physics 49, no. 22 (2016): 223001.

30. Gonzalez-Hernandez, Diana, Simonas Varapnickas, Andrea Bertoncini, Carlo Liberale, and Mangirdas Malinauskas. "Micro-optics 3D printed via multi-photon laser lithography." Advanced Optical Materials 11, no. 1 (2023): 2201701.

31. Piqué, Alberto, Raymond CY Auyeung, Heungsoo Kim, Nicholas A. Charipar, and Scott A. Mathews. "Laser 3D micro-manufacturing." Journal of physics D: applied physics 49, no. 22 (2016): 223001..

32. Meunier, Michel, Bruno Fisette, Alexis Houle, Andrei V. Kabashin, Sergey V. Broude, and Pascal Miller. "Processing of

metals and semiconductors by a femtosecond laser-based microfabrication system." In Commercial and Biomedical Applications of Ultrafast Lasers III, vol. 4978, pp. 169-179. SPIE, 2003.

33. Zhao, Lili, Zhen Liu, Duo Chen, Fan Liu, Zhiyuan Yang, Xiao Li, Haohai Yu, Hong Liu, and Weijia Zhou. "Laser synthesis and microfabrication of micro/nanostructured materials toward energy conversion and storage." Nano-Micro Letters 13 (2021): 1-48.

34. Armon, Nina, Ehud Greenberg, Eitan Edri, Ornit Nagler-Avramovitz, Yuval Elias, and Hagay Shpaisman. "Laser-based printing: from liquids to microstructures." Advanced Functional Materials 31, no. 13 (2021): 2008547.

35. Kim, Joohan, and Xianfan Xu. "Laser-based fabrication of polymer micropump." Journal of Micro/Nanolithography, MEMS and MOEMS 3, no. 1 (2004): 152-158.

36. Weidenfeller, Laura, Johannes Kirchner, Martin Hofmann, Michael Kühnel, Carsten Reinhardt, Ivo Rangelow, and Eberhard Manske. "Laser-microfabrication with accurate positioning and metrological traceability." In Advanced Fabrication Technologies for Micro/Nano Optics and Photonics XII, vol. 10930, pp. 29-36. SPIE, 2019.

37. Zhou, Weiping, Denzel Bridges, Ruozhou Li, Shi Bai, Ying Ma, T. X. Hou, and Anming Hu. "Recent progress of laser micro-and nano manufacturing." Sci. Lett. J 5 (2016): 228.

38. Huang, Jigang, Qin Qin, and Jie Wang. "A review of stereolithography: Processes and systems." Processes 8, no. 9 (2020): 1138.

39. Schmidleithner, Christina, and Deepak M. Kalaskar. "Stereolithography." IntechOpen, 2018.

40. Corbel, Serge, Olivier Dufaud, and Thibault Roques-Carmes. "Materials for stereolithography." In Stereolithography: Materials, processes and applications, pp. 141-159. Boston, MA: Springer US, 2011.

41. Saadi, M. A. S. R., Alianna Maguire, Neethu T. Pottackal, Md Shajedul Hoque Thakur, Maruf Md Ikram, A. John Hart, Pulickel M. Ajayan, and Muhammad M. Rahman. "Direct ink writing: a 3D printing technology for diverse materials." Advanced Materials 34, no. 28 (2022): 2108855.

42. Lewis, Jennifer A., James E. Smay, John Stuecker, and Joseph Cesarano. "Direct ink writing of three-dimensional ceramic structures." Journal of the American Ceramic Society 89, no. 12 (2006): 3599-3609.

43. Florian, Camilo, and Pere Serra. "Printing via laser-induced forward transfer and the future of digital manufacturing." Materials 16, no. 2 (2023): 698.

44. Zergioti et al. (2012) investigate the application of LIFT for transferring conducting polymers.

45. Munir, Zuhair A., and Manshi Ohyanagi. "Perspectives on the spark plasma sintering process." Journal of Materials Science 56, no. 1 (2021): 1-15.

46. Grippi, Thomas, Elisa Torresani, Andrii L. Maximenko, and Eugene A. Olevsky. "Additive manufacturing-assisted sintering: low pressure, low temperature spark plasma sintering of tungsten carbide complex shapes." Ceramics International 50, no. 19 (2024): 37228-37240.

47. Hench, Larry L. Sol-gel silica: properties, processing and technology transfer. William Andrew, 1998.

48. Nishida, Fumito, John M. McKiernan, Bruce Dunn, Jeffrey I. Zink, C. Jeffrey Brinker, and Alan J. Hurd. "In situ fluorescence

probing of the chemical changes during sol–gel thin film formation." Journal of the American Ceramic Society 78, no. 6 (1995): 1640-1648.

49. Choy (2003) provided a comprehensive review of CVD techniques—thermal, plasma-enhanced, and metal-organic.

50. Pierson, Hugh O. Handbook of chemical vapor deposition: principles, technology and applications. William Andrew, 1999.

51. Brillas, Enric, Birame Boye, Ignasi Sirés, José Antonio Garrido, Rosa María Rodríguez, Conchita Arias, Pere-Lluís Cabot, and Christos Comninellis. "Electrochemical destruction of chlorophenoxy herbicides by anodic oxidation and electro-Fenton using a boron-doped diamond electrode." Electrochimica Acta 49, no. 25 (2004): 4487-4496.

52. Yan, Jun, and Shyam Aravamudhan. "2 Nano-Electro-Mechanical." Nanoscience and Nanoengineering: Advances and Applications (2014): 13.

53. Lu, Junling, Jeffrey W. Elam, and Peter C. Stair. "Atomic layer deposition—Sequential self-limiting surface reactions for advanced catalyst “bottom-up” synthesis." Surface Science Reports 71, no. 2 (2016): 410-472.

54. Leskelä and Ritala (2002) further emphasized the technique’s flexibility across diverse materials (oxides, nitrides, sulfides),

55. Madou (2011) detailed the step-by-step photolithographic workflow—from resist coating and exposure to development and etching

56. Wynand, Lambrechts, Sinha Saurabh, and Abdallah Jassem. "Photolithography Enhancements." In Extending Moore's Law through Advanced Semiconductor Design and Processing Techniques, pp. 101-140. CRC Press, 2018.

57. Muller (1996) presented a landmark review on anisotropic wet etching of silicon using potassium hydroxide (KOH) and tetramethylammonium hydroxide (TMAH),

58. Coburn and Winters (1979) pioneered understanding of reactive ion etching (RIE), elucidating plasma–surface interactions

59. Stanishevsky, Andrei V. "Focused ion beam nanofabrication." In Encyclopedia of nanoscience and nanotechnology, vol. 3, no. 483, pp. 469-483. American Scientific Publishers, 2004.

60. Neuville, Stephane. "Selective carbon material engineering for improved MEMS and NEMS." Micromachines 10, no. 8 (2019): 539.

61. Takada, Kenji, Hong-Bo Sun, and Satoshi Kawata. "Improved spatial resolution and surface roughness in photopolymerization-based laser nanowriting." Applied Physics Letters 86, no. 7 (2005).

62. Malinauskas, Mangirdas, Albertas Žukauskas, Satoshi Hasegawa, Yoshio Hayasaki, Vygantas Mizeikis, Ričardas Buividas, and Saulius Juodkazis. "Ultrafast laser processing of materials: from science to industry." Light: Science & Applications 5, no. 8 (2016): e16133-e16133.

63. Veiko, V. P., E. A. Shakhno, V. N. Smirnov, A. M. Miaskovski, and G. D. Nikishin. "Laser–induced film deposition by LIFT: Physical mechanisms and applications." Laser and Particle Beams 24, no. 2 (2006): 203-209.

64. Serra, Pere, and Alberto Piqué. "Laser-induced forward transfer: fundamentals and applications." Advanced Materials Technologies 4, no. 1 (2019): 1800099.

65. Serra, P., M. Duocastella, J. M. Fernández-Pradas, and J. L. Morenza. "Liquids microprinting through laser-induced forward transfer." Applied surface science 255, no. 10 (2009): 5342-5345.

66. Fernández-Pradas, Juan Marcos, C. Florian, Francesc Caballero-Lucas, P. Sopeña, J. L. Morenza, and P. Serra. "Laser-induced forward transfer: Propelling liquids with light." Applied Surface Science 418 (2017): 559-564.

67. Sopeña, P., J. M. Fernández-Pradas, and P. Serra. "Laser-induced forward transfer of low viscosity inks." Applied Surface Science 418 (2017): 530-535.

68. Fernández-Pradas, J. Marcos, and Pere Serra. "Laser-induced forward transfer: a method for printing functional inks." Crystals 10, no. 8 (2020): 651.

69. Munoz-Martin, David, C. Frederik Brasz, Yu Chen, M. Morales, Craig B. Arnold, and C. Molpeceres. "Laser-induced forward transfer of high-viscosity silver pastes." Applied Surface Science 366 (2016): 389-396.

70. Delaporte, Philippe, and Anne-Patricia Alloncle. "Laser-induced forward transfer: A high-resolution additive manufacturing technology." Optics & Laser Technology 78 (2016): 33-41.

71. Serra, P., M. Duocastella, J. M. Fernández-Pradas, and J. L. Morenza. "The laser-induced forward transfer technique for microprinting." Advances in Laser Materials Processing (2010): 367-393